

**MODELING OF INTERIOR BEAM-COLUMN JOINTS FOR
NONLINEAR ANALYSIS OF REINFORCED CONCRETE FRAMES**

by

Zhangcheng Pan

A thesis submitted in conformity with the requirements

for the degree of Master of Applied Science

Graduate Department of Civil Engineering

University of Toronto

© Copyright by Zhangcheng Pan (2016)

Modeling of Interior Beam-Column Joints for Nonlinear Analysis of Reinforced Concrete Frames

Zhangcheng Pan

Master of Applied Science

Graduate Department of Civil Engineering

University of Toronto

2016

ABSTRACT

Beam-column connections are often assumed rigid in traditional frame analysis, yet they undergo significant shear deformations and greatly contribute to story drifts during earthquake loading. Older frame joints designed prior to the 1970's with little or no transverse reinforcement are more vulnerable to earthquakes. Numerical simulation methods are needed to identify existing vulnerable buildings as well as to design new buildings for performance-based earthquake engineering. Although local joint models are available in the literature for the investigation of single, isolated joints, there is a lack of holistic frame analysis procedures simulating the joint behavior in addition to important global failure modes such as beam shear, column shear, column axial, and soft story failures.

The objective of this study is to capture the impact of local joint deformations on the global frame response in a holistic analysis by implementing a joint model into a previously-developed global frame analysis procedure. The steps taken in this study include: a comprehensive literature review, identification of a suitable joint model from the literature, simplification, implementation into the global analysis procedure, and verification of this model with an experimental database. The implemented joint element simulates joint shear deformations and bar-slip effects. Concrete confinement effects are also considered so that both older and new joints can be modeled. The developed procedure provides better overall load-deflection response predictions including the local joint response.

TABLE OF CONTENTS

ABSTRACT.....	ii
TABLE OF CONTENTS.....	iii
LIST OF TABLES.....	v
LIST OF FIGURES.....	vii
CHAPTER 1: INTRODUCTION.....	1
1.1 Motivations for the Study.....	1
1.2 Nonlinear Frame Analysis Program, VecTor5.....	3
1.3 Objectives of the Study.....	5
1.4 Thesis Organization.....	6
CHAPTER 2: MODELING OF BEAM-COLUMN JOINTS.....	8
2.1 Chapter Layout.....	8
2.2 Beam-Column Joint Behavior.....	8
2.3 Review of Existing Behavior Models for Beam-Column Joints.....	12
2.3.1 The Modified Compression Field Theory.....	13
2.3.2 The Strut-and-Tie Model.....	19
2.3.3 Bond Stress-Slip Relationship.....	22
2.4 Review of Existing Beam-Column Joint Models.....	28
2.4.1 Rotational Hinge Models.....	28
2.4.2 Component Models.....	30
CHAPTER 3: IMPLEMENTED JOINT ELEMENT MODEL.....	36
3.1 Chapter Layout.....	36
3.2 Joint Element Formulation.....	36
3.3 Modeling Bond Slip Response.....	41
3.4 Modeling Joint Shear Response.....	46
3.5 Modeling of Interface Shear Response.....	49
3.6 Computation Schemes.....	50
CHAPTER 4: JOINT IMPLEMENTATION IN VECTOR5.....	52
4.1 Chapter Layout.....	52
4.2 Global Frame Modeling.....	52

4.3 Joint Analysis Algorithm	57
4.3.1 Subroutine: Local Joint Element	57
4.3.2 Subroutine: Bar Slip Spring.....	68
4.3.3 Subroutine: Shear Panel.....	70
4.4 Modifications of the Global Frame Analysis Procedure.....	75
4.4.1 Detection of Interior Joints	75
4.4.2 Assembly of the Global Stiffness Matrix	76
4.4.3 Solution to the Global Frame Analysis.....	77
4.5 Guidelines for Modeling Beam-Column Joints	78
4.6 Interpretation of Results	79
4.6.1 Output Files	79
4.6.2 Graphical Representation	81
CHAPTER 5: MODEL EVALUATION AND VERIFICATION	83
5.1 Chapter Layout.....	83
5.2 Beam-Column Subassemblies.....	83
5.2.1 Summary.....	83
5.2.2 Shiohara and Kusuhara (2007)	87
5.2.3 Park and Dai (1988).....	98
5.2.4 Noguchi and Kashiwazaki (1992)	109
5.2.5 Attaalla and Agbabian (2004).....	119
5.3 Parametric Study for Beam-Column Subassemblies	132
5.4 Frame Structures	138
5.4.1 Summary.....	138
5.4.2 Xue et al. Frame (2011).....	138
5.4.3 Ghannoum and Moehle (2012).....	144
5.4.4 Pampanin et al. (2007).....	150
CHAPTER 6: SUMMARY, CONCLUSIONS AND RECOMMEDATIONS	157
6.1 Summary	157
6.2 Conclusions	157
6.3 Recommendations for Future Research	159
REFERENCES	161

LIST OF TABLES

Table 3.1: Average bond stress for various rebar conditions	44
Table 4.1: List of input variables required by local joint element subroutine	60
Table 4.2: Iterations to convergence for selected stiffness values	64
Table 5.1: Material behavior models and analysis parameters used in VecTor5.....	84
Table 5.2: Summary of the specimen properties and analytical results of interior beam-column subassemblies.....	85
Table 5.3: Material properties of Specimens A1 and D1	88
Table 5.4: General material specifications of Specimen A1	91
Table 5.5: Reinforced concrete material specifications of Specimen A1	91
Table 5.6: Longitudinal reinforcement material specifications of Specimen A1	92
Table 5.7: Comparison of experimental and analytical results of Specimen A1	92
Table 5.8: Stress in the longitudinal bars at the joint panel interface of Specimen A1	96
Table 5.9: Comparison of experimental and analytical results of Specimen D1	97
Table 5.10: Material properties of Specimens Unit 1 and Unit 2	101
Table 5.11: General material specifications of Specimen Unit 1	103
Table 5.12: Reinforced concrete material specifications of Specimen Unit 1	103
Table 5.13: Longitudinal reinforcement material specifications of Specimen Unit 1	104
Table 5.14: Comparison of experimental and analytical results of Specimen Unit 1	105
Table 5.15: Stress in the longitudinal bars at the joint panel interface of Specimen Unit 1	107
Table 5.16: Comparison of experimental and analytical results of Specimen Unit 2	108
Table 5.17: Material properties of Specimens OKJ2 and OKJ6	110
Table 5.18: General material specifications of Specimen OKJ2	113
Table 5.19: Reinforced concrete material specifications of Specimen OKJ2.....	113
Table 5.20: Longitudinal reinforcement material specifications of Specimen OKJ2	114
Table 5.21: Comparison of experimental and analytical results of Specimen OKJ2.....	114
Table 5.22: Stress in the longitudinal bars at the joint panel interface of Specimen OKJ2.....	117
Table 5.23: Comparison of experimental and analytical results of Specimen OKJ6.....	118
Table 5.24: Material properties of Specimens SHC1, SHC2 and SOC3	121

Table 5.25: General material specifications of Specimen SHC1	123
Table 5.26: Reinforced concrete material specifications of Specimen SHC1	123
Table 5.27: Longitudinal reinforcement material specifications of Specimen SHC1.....	123
Table 5.28: Comparison of experimental and analytical results of Specimen SHC1	124
Table 5.29: Stress in the longitudinal bars at the joint panel interface of Specimen SHC1	126
Table 5.30: Comparison of experimental and analytical results of Specimen SHC2	126
Table 5.31: Comparison of experimental and analytical results of Specimen SOC3	129
Table 5.32: Material properties of Specimen HPCF-1.....	140
Table 5.33: Comparison of experimental and analytical results of Specimen HPCF-1.....	143
Table 5.34: Material properties of Ghannoum and Moehle Frame.....	145
Table 5.35: Material properties of Pampanin et al. Frame.....	152

LIST OF FIGURES

Figure 1.1: Common failure modes of frames subjected to seismic loading (Google Images).....	1
Figure 1.2: Contributions of displacement factors to story drift for an older type joint, Specimen CD15-14, subjected to reversed cyclic loading (Walker, 2001).....	3
Figure 1.3: Experimental and analytical load-displacement responses of Specimen SHC2 tested by Attaalla and Agbabian (2004).....	5
Figure 2.1: Three types of beam-column connections in a reinforced concrete frame (Kim and LaFave, 2009).....	9
Figure 2.2: Forces expected to develop at the perimeter of an interior joint in a frame under seismic actions (Mitra, 2007).....	10
Figure 2.3: Load distribution at the joint region (Hakuto et al., 1999).....	10
Figure 2.4: Major shear resisting mechanisms: (a) the concrete strut mechanism and (b) the truss mechanism (Pauley et al., 1978).....	11
Figure 2.5: Deformed reinforced concrete joint with bond slip and bar pullout (Altoontash, 2004).....	12
Figure 2.6: Reinforced concrete element subjected to normal and shear stresses (Vecchio and Collins, 1986).....	13
Figure 2.7: Stress-strain relationship for concrete under (a) uniaxial compression and (b) uniaxial tension (Vecchio and Collins, 1986).....	15
Figure 2.8: B Regions and D Regions in a reinforced concrete frame structure (Schlaich et al., 1987).....	19
Figure 2.9: The strut-and-tie model: (a) single-strut model, (b) distributed-truss model, (c) combined strut-truss model, and (d) definition of the strut width in combined strut-truss mechanism (Mitra, 2007).....	21
Figure 2.10: Test setup in the bond experiment conducted by Viwathanatepa et al. (1979): (a) the elevation view of the specimen and (b) the testing apparatus.....	23
Figure 2.11: Formulation of bond model proposed by Viwathanatepa et al. (1979): (a) monotonic skeleton bond stress-slip Curve, (b) finite soft layer elements, and (c) load-displacement relationship of a #8 (25M) bar.....	24
Figure 2.12: Proposed analytical model for local bond stress-slip relationship for confined concrete subjected to monotonic and cyclic loading. (Eligenhausen et al., 1983).....	26
Figure 2.13: Monotonic envelope curve of bar stress versus loaded-end slip relationship (Zhao and Sritharan, 2007).....	27

Figure 2.14: Joint model proposed by Alath and Kunnath (Alath and Kunnath, 1995; figure adopted from Celik and Ellingwood, 2008).....	28
Figure 2.15: Joint model proposed by Altoontash (Altoontash, 2004).....	29
Figure 2.16: Joint model proposed by Shin and LaFave (Shin and LaFave, 2004).....	30
Figure 2.17: Joint model proposed by Lowes and Altoontash (Lowes and Altoontash, 2003)...	31
Figure 2.18: Joint model proposed by Ghobarah and Youssef (Ghobarah and Youssef, 2001)..	32
Figure 2.19: Joint model proposed by Fleury et al. (Fleury et al., 2000).....	33
Figure 2.20: Joint model proposed by Elmorsi et al.: (a) proposed element and (b) details of the bond slip element (Elmorsi et al., 2000).....	34
Figure 2.21: Joint model proposed by Shiohara (Shiohara, 2004).....	35
Figure 3.1: Implemented interior beam-column joint model (Mitra and Lowes, 2007).....	37
Figure 3.2: Definition of displacements, deformations and forces in the model: (a) external displacements and component deformations and (b) external forces and component forces.....	38
Figure 3.3: Compatibility equations of the implemented joint model (Mitra and Lowes, 2007)	40
Figure 3.4: Bond stress and bar stress distribution along a reinforcing bar anchored in a joint..	43
Figure 3.5: Bar stress versus slip relationship from various studies and experiments.....	44
Figure 3.6: Sectional analysis of a frame member at the nominal flexural strength: (a) member cross-section, (b) strain distribution, (c) stress distribution, and (d) forces on the member	46
Figure 3.7: Idealized diagonal concrete compression strut model.....	47
Figure 3.8: Reduction equations to the concrete compression strength (Mitra and Lowes, 2007).....	48
Figure 3.9: Envelope of the shear stress versus slip response for the interface shear springs (Lowes and Altoontash, 2003).....	49
Figure 4.1: Typical frame model in VecTor5	54
Figure 4.2: Longitudinal and shear strain distributions across sectional depth for a layered analysis (Guner and Vecchio, 2010).....	55
Figure 4.3: Flowchart for the global frame analysis of VecTor5 (Guner and Vecchio, 2010)....	55
Figure 4.4: Joint element implementation in VecTor5	56
Figure 4.5: Flowchart of solution process for the joint element	59
Figure 4.6: Load-displacement response of interface shear spring with different stiffness	64
Figure 4.7: Partitioned joint element stiffness matrix.....	66
Figure 4.8: Joint analysis matrix for frames with multiple interior joints	67
Figure 4.9 Joint panel displacements and rotations	67

Figure 4.10: Flowchart of the solution process for the bar slip springs.....	68
Figure 4.11: Modified bar stress versus slip relationship	69
Figure 4.12: Flowchart of solution process for the shear panel.....	70
Figure 4.13: Stress-strain model for monotonic loading of confined and unconfined concrete (Mander et al., 1988).....	71
Figure 4.14: Effectively confined concrete for rectangular tie reinforcement (Mander et al., 1988).....	72
Figure 4.15: Interior joint information in the common blocks	76
Figure 4.16: Assembling the global stiffness matrix: (a) stiffness of members, (b) stiffness of joints, and (c) stiffness of the structure.....	77
Figure 4.17: Layout of member analysis results for members in joint regions	79
Figure 4.18: Layout of interior joint analysis results in the output files.....	80
Figure 4.19: Definition of layers and faces in joint analysis results	81
Figure 4.20: Sample sketch of a deformed interior joint	82
Figure 5.1: Test setup of Specimens A1 and D1 (adapted from Guner, 2008).....	88
Figure 5.2: Sectional details of Specimens A1 and D1.....	89
Figure 5.3: Analytical model showing dimensions, loading and support restraints of Specimens A1 and D1	90
Figure 5.4: Analytical model showing material types of Specimens A1 and D1	91
Figure 5.5: Comparison of the load-displacement response of Specimen A1	93
Figure 5.6: Cracking pattern of Specimen A1: (a) observed (Shiohara and Kusuhara, 2007) and (b) original VecTor5 simulation	94
Figure 5.7: Load versus joint shear strain relationship of Specimen A1	95
Figure 5.8: Comparison of the load-displacement response of Specimen D1	96
Figure 5.9: Cracking pattern of Specimen D1: (a) observed (Shiohara and Kusuhara, 2008) and (b) original VecTor5 simulation	98
Figure 5.10: Test setup of Specimens Unit 1 (Park and Dai, 1988)	99
Figure 5.11: Test setup of Specimens Unit 2 (Park and Dai, 1988)	100
Figure 5.12: Sectional details of Specimens Unit 1 and Unit 2 (Park and Dai, 1988).....	100
Figure 5.13: Analytical model showing dimensions, loading and support restraints of Specimens Unit 1 and Unit 2.....	102
Figure 5.14: Analytical model showing material types of Specimens Unit 1 and Unit 2.....	103
Figure 5.15: Comparison of the load-displacement response of Specimen Unit 1	105

Figure 5.16: Cracking pattern of Specimen Unit 1: (a) observed (Park and Dai, 1988) and (b) original VecTor5 simulation	107
Figure 5.17: Comparison of the load-displacement response of Specimen Unit 2.....	108
Figure 5.18: Cracking pattern of Specimen Unit 2 predicted by original VecTor5 simulation.	109
Figure 5.19: Test setup of Specimens OKJ2 and OKJ6 (Noguchi and Kashiwazaki, 1992).....	111
Figure 5.20: Sectional details of Specimens OKJ2 and OKJ6: (a) beam section, (b) column section, and (c) detailed joint reinforcement (Noguchi and Kashiwazaki, 1992).....	111
Figure 5.21: Analytical model showing dimensions, loading and support restraints of Specimens OKJ2 and OKJ6	112
Figure 5.22: Analytical model showing material types of Specimens OKJ2 and OKJ6	113
Figure 5.23: Comparison of the load-displacement response of Specimen OKJ2.....	115
Figure 5.24: Cracking pattern of Specimen OKJ1 (Noguchi and Kashiwazaki, 1992).....	116
Figure 5.25: Cracking pattern of Specimen OKJ2 predicted by original VecTor5 simulation .	117
Figure 5.27: Comparison of the load-displacement response of Specimen OKJ6.....	118
Figure 5.28: Cracking pattern of Specimen OKJ6 predicted by original VecTor5 simulation .	119
Figure 5.29: Test setup of Specimens SHC1, SHC2 and SOC3 (Attaalla and Agbabian, 2004)	120
Figure 5.30: Sectional details of Specimens SHC1, SHC2 and SOC3: (a) beam section, (b) column section (Attaalla and Agbabian, 2004), and (c) detailed joint reinforcement (Attaalla, 1997)	121
Figure 5.31: Analytical model showing dimensions, loading and support restraints of Specimens SHC1, SHC2 and SOC3	122
Figure 5.32: Analytical model showing material types of Specimens SHC1, SHC2 and SOC3	122
Figure 5.33: Comparison of the load-displacement response of Specimen SHC1	124
Figure 5.34: Cracking pattern of Specimen SHC1: (a) observed (Attaalla and Agbabian, 2004) and (b) original VecTor5 simulation	126
Figure 5.35: Comparison of the load-displacement response of Specimen SHC2	127
Figure 5.36: Cracking pattern of Specimen SHC2: (a) observed (Attaalla and Agbabian, 2004) and (b) original VecTor5 simulation	128
Figure 5.37: Comparison of the load-displacement response of Specimen SOC3	129
Figure 5.38: Cracking pattern of Specimen SOC3: (a) observed (Attaalla and Agbabian, 2004) and (b) VecTor5 simulation.....	131

Figure 5.39: Envelopes of the load versus the panel shear strain relationships for: (a) Specimen SHC1, (b) Specimen SHC2, and (c) Specimen SOC3.....	131
Figure 5.40: Story shear force versus story drift relationships of Specimen OKJ2 (Noguchi and Kashiwazaki, 1992) subjected to: (a) monotonic and (b) reversed cyclic loading conditions ...	132
Figure 5.41: Comparison of the VecTor5 load-displacement responses of Specimen A1	133
Figure 5.42: Comparison of the load-displacement responses with different confinement effectiveness coefficients	134
Figure 5.43: Comparison of the load-displacement responses without the compression softening effect	135
Figure 5.44: Comparison of the load-displacement responses with bond stresses proposed by Sezen and Moehle (2003)	137
Figure 5.45: Structural details of Specimen HPCF-1 (Xue et al., 2011)	139
Figure 5.46: Applied loads on Specimen HPCF-1 (Xue et al., 2011).....	140
Figure 5.47: Analytical model showing loading and support restraints of Specimens HPCF-1	141
Figure 5.48: Comparison of base shear versus roof drift response of Specimen HPCF-1	142
Figure 5.49: Failures of Specimen HPCF-1 (Xue et al., 2011).....	143
Figure 5.50: Deformed shape and cracking pattern of Specimen HPCF-1	144
Figure 5.51: Structural details of Ghannoum and Moehle Frame (Ghannoum and Moehle, 2012)	145
Figure 5.52: Applied loads on Ghannoum and Moehle Frame (Ghannoum and Moehle, 2012)	146
Figure 5.53: Analytical model showing dimensions, loading and support restraints of Ghannoum and Moehle Frame	147
Figure 5.54: Comparison of base shear versus first floor drift response of Ghannoum and Moehle Frame	148
Figure 5.55: Failures of Ghannoum and Moehle Frame (Ghannoum and Moehle, 2012)	149
Figure 5.56: Damage of interior joints in Ghannoum and Moehle Frame (Ghannoum and Moehle, 2012)	149
Figure 5.57: Deformed shape and cracking pattern of Ghannoum and Moehle Frame.....	150
Figure 5.58: Structural details of Pampanin et al. Frame (Pampanin et al., 2007)	151
Figure 5.59: Applied Loads on Pampanin et al. Frame (Pampanin et al., 2007)	152
Figure 5.60: Analytical model showing dimensions, loading and support restraints of Pampanin et al. Frame.....	153
Figure 5.61: Comparison of base shear versus top drift response of Pampanin et al. Frame	154

Figure 5.62: Failures of Pampanin et al. Frame (Pampanin et al., 2003)	155
Figure 5.63: Damage of interior joints in Pampanin et al. Frame (Pampanin et al., 2007)	155
Figure 5.64: Deformed shape and cracking pattern of Pampanin et al. Frame	156

CHAPTER 1

INTRODUCTION

1.1 Motivations for the Study

According to the U.S. Geological Survey, at least 850,000 people were killed and more than 3 million buildings collapsed or were damaged during the 26 major earthquake events that occurred over the past two decades. Reinforced concrete frame structures were common among those buildings. Common failure modes observed after earthquakes included beam-column joint shear, column shear, beam shear, column axial, reinforcement bond slip, foundation failures and soft story failures, as illustrated in Figure 1.1.

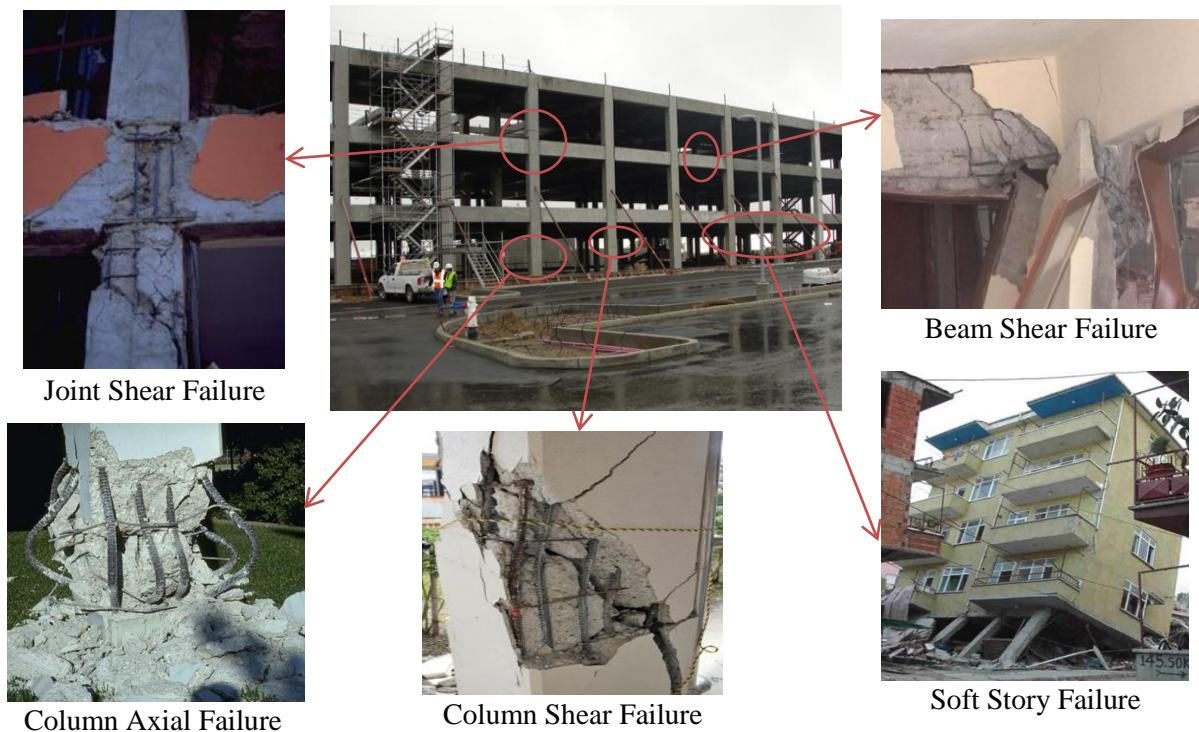


Figure 1.1: Common failure modes of frames subjected to seismic loading (Google Images)

Although the joint shear failure is a local failure mechanism, it often leads to progressive collapse of buildings. Insufficient anchorage lengths of reinforcing bars, unconfined connections, and deterioration of reinforced concrete materials are the main contributors to this type of failure.

Frame joints designed prior to the 1970's according to older design standards, with little or no transverse reinforcement, exhibit non-ductile response and are more vulnerable to joint shear failures. Older design codes did not specify a limit on the joint shear stress or required joint transverse reinforcement prior to the pioneering experiment of Hanson and Connor (1967). As a result, joints in these frames exhibit relatively high joint shear, which contributes to greater story drifts, and higher bond stresses, which may cause bar slippage under seismic loading.

Proper reinforcement detailing in beam-column joints is still a subject of active research. Joints in newer buildings possess better reinforcement detailing with transverse reinforcement as specified in the concrete building design codes such as CSA A23.3-14. Nonetheless, experimental tests have demonstrated that the newer joint types will still exhibit shear cracking under a strong seismic loading, significantly contributing to story drifts of the global structure (Shin and LaFave, 2004).

In the traditional analysis of reinforced concrete frame structures subjected to seismic loading, beam-column joints are assumed rigid. This assumption implies that the joint core remains elastic and deforms as a rigid body throughout an earthquake even if the beams and columns undergo significant deformation and sustain severe damage. On the contrary, experimental studies (e.g., Walker, 2001) have demonstrated that beam-column joint deformations due to shear cracking and bond slip are major contributors to lateral story drifts. One extreme case example including a non-ductile beam-column joint containing no transverse reinforcement is presented in Figure 1.2. Since the pioneering experiment in 1967, there has been an ongoing effort in understanding the behavior of beam-column joints under seismic actions, and creating numerical simulation methods to model and determine joint response under various loading conditions. Researchers have proposed a variety of beam-column joint models. These models can be categorized into three classes: rotational hinge models, component models, and finite element models. Each model has its advantages and limitations, and there is no scientific consensus on a model that is optimal for all applications.

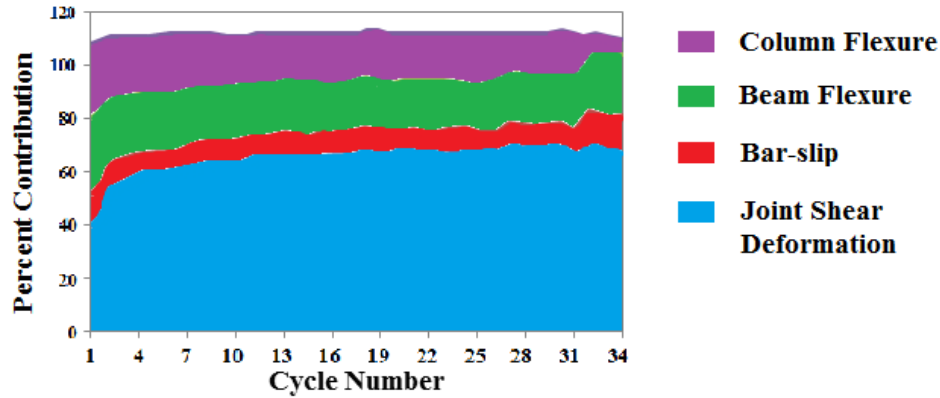


Figure 1.2: Contributions of displacement factors to story drift for an older type joint, Specimen CD15-14, subjected to reversed cyclic loading (Walker, 2001)

In spite of the developments in understanding and quantifying joint behavior, there is a lack of holistic frame analysis procedures simulating the joint behavior in addition to other important global failure modes. One commonly used technique to model joints in frame analysis procedures is known as “semi-rigid end offsets”. Although this approach is employed to account for increased strengths in joint cores by increasing the stiffness of the joints, it may lead to overestimation of joint strength, joint stiffness and energy dissipation, as well as an underestimation of lateral story drifts. These inaccuracies will be more significant for frames with older type joints designed prior to the introduction of modern design codes. On the other hand, while the existing joint models are effective for the investigation of single isolated joints, they do not consider the interactions or coupling effects between the joints and other parts of the structure. Therefore, there is a need to incorporate a suitable joint model in frame analysis procedures. As a step towards this goal, this study aims to capture the impact of local joint deformations on the global frame response by implementing a suitable joint model into a previously-developed global frame analysis procedure, VecTor5.

1.2 Nonlinear Frame Analysis Program, VecTor5

VecTor5 (Guner and Vecchio, 2010) is a nonlinear analysis program for two-dimensional reinforced concrete frame structures. VecTor5 is based on the Disturbed Stress Field Model (DSFM) by Vecchio (2000); it is capable of capturing shear-related effects coupled with flexural and axial behaviors for frame structures subjected to static (monotonic, cyclic and reversed

cyclic) and dynamic (impact, blast, and seismic) loading conditions. Among all alternative global frame analysis procedures (such as *RUAUMOKO*, *ZEUS* and *IDARC2D*), VecTor5 is selected for this study because it is capable of accurately simulating the nonlinear behavior of beams and columns within a short analysis time while providing sufficient output to fully describe the behavior of the structure. The use of this analysis tool is facilitated by the pre-processor FormWorks (Wong et al., 2013) to create the frame models in a graphical environment. The post-processor Janus (Chak, 2013 and Loya et al., 2016) is used to visualize the analysis results in a powerful graphical environment.

The analysis procedure is based on a total load, iterative, secant stiffness formulation. The computation consists of two interrelated analyses: a global frame analysis using a classical stiffness-based finite element method, followed by the nonlinear sectional analysis for which a layered analysis technique is employed. Additional information is given in Chapter 4.2 of this thesis, and further information about this procedure is provided in “User’s Manual of VecTor5” by Guner and Vecchio (2008).

Currently, VecTor5 employs semi-rigid end offsets to account for the increased strengths in beam-column joint regions. This is achieved by doubling the amount of longitudinal and transverse reinforcement of the members inside joint regions. Consequently, it does not fully capture the behavior of joints, and it tends to overestimate the strength, stiffness and energy dissipation of frames that exhibit significant joint damage. One extreme case example is presented in Figure 1.3. It is expected that the implementation of a suitable local joint model in VecTor5 will be able to further improve not only local joint simulation but also the results obtained from the global frame analysis.

Frame joints can be categorized into three classes: interior joints, exterior joints, and knee joints. This study is exclusively focused on the modeling of interior beam-column joints subjected to monotonic loading conditions because they are the most common type and require the most number of nodes and components for modeling. This study is concerned with structures subjected to monotonic loading conditions.

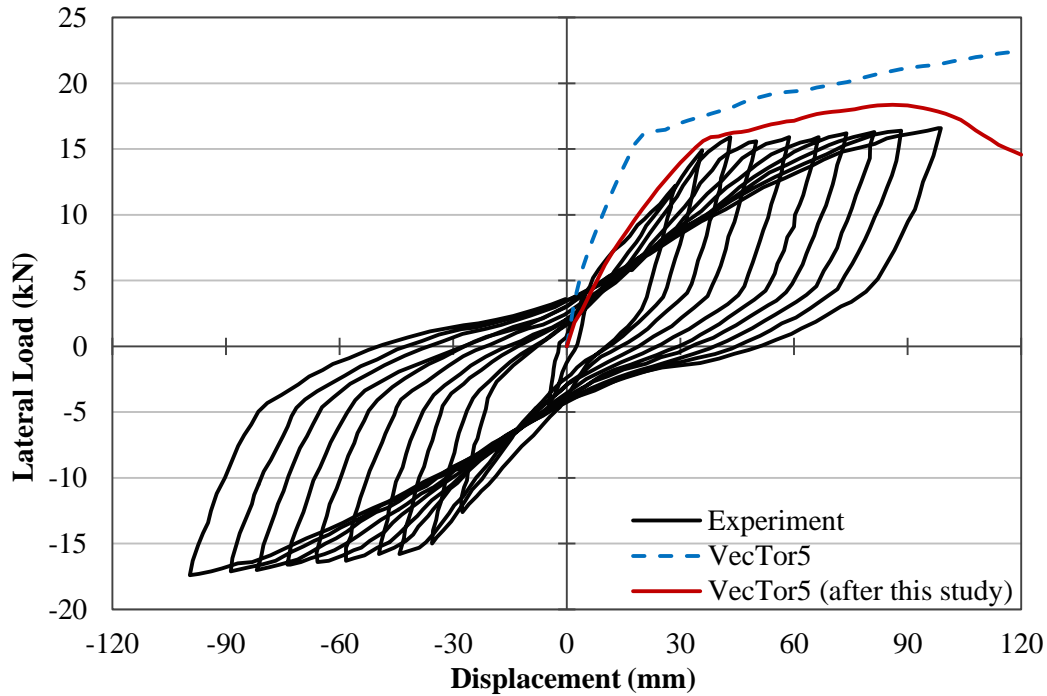


Figure 1.3: Experimental and analytical load-displacement responses of Specimen SHC2 tested by Attaalla and Agbabian (2004)

1.3 Objectives of the Study

The primary focus of this study is to capture the impact of local joint deformations on the global frame response subjected to monotonic loading by implementing a new joint model into the previously-developed global frame analysis procedure VecTor5. VecTor5 is a user-friendly frame analysis procedure that has been validated with over 100 previously-tested structures for simulating the response of frame structures under various loading conditions (e.g. Guner and Vecchio, 2010, 2011, 2012, and Guner 2016). With the implementation of a joint model, this global procedure is expected to provide a better overall load-deflection response including the local joint response. The global procedure will also be able to capture joint failures, which would otherwise not have been detected. The improved analysis procedure will allow for the analysis of new buildings for the performance-based earthquake engineering. It will allow for the analysis of older type buildings to identify the existing buildings which are at the risk of collapse during a future earthquake. The study consists of the following parts: a comprehensive literature review,

identification of a suitable joint model from the literature, simplification of the identified model, implementation of this model into the global analysis procedure, and verification with previously tested specimens.

1.4 Thesis Organization

This thesis focuses on (1) describing the formulations of the new joint element implemented in VecTor5, (2) validating the analysis procedure through the analyses of previously tested beam-column joint subassemblies and frame structures, and (3) providing general guidelines for modeling beam-column joint subassemblies and frame structures with proper modeling of interior beam-column joints.

Chapter 2 provides the literature information for the behavior and modeling of beam-column joints in reinforced concrete frame structures. The fundamental theories and material models are discussed in detail. A selection of nine interior joint models is introduced. All models are capable of capturing joint behavior to some extent, but the decision of which model to implement will be made based on the model accuracy and simplicity.

Chapter 3 discusses the theory and formulations of the selected joint model in detail. This model is capable of capturing joint shear deformations and bond slip effects taking place in interior joints. Models of exterior and knee joints, which are not discussed in this study, require additional considerations. The computational schemes are presented for the joint element formulations.

Chapter 4 describes the implementation of the selected joint model into the nonlinear frame analysis program, VecTor5. The global frame analysis procedure is introduced. The implementation of the joint analysis algorithm is discussed in detail.

Chapter 5 discusses the application and verification of the global frame analysis procedure with the new joint element implementation. Previously tested specimens consisting of nine interior beam-column joint subassemblies and three frame structures were modeled, and the developed formulations are validated through the comparisons of experimental and analytical responses.

The specimens considered cover various material properties, reinforcing ratios, and failure mechanisms.

Chapter 6 includes the summary of the thesis and presents the final conclusions along with recommendations for future research.

CHAPTER 2

MODELING OF BEAM-COLUMN JOINTS

2.1 Chapter Layout

This chapter describes the theoretical principles for modeling reinforced concrete interior beam-column joints subjected to monotonic loading conditions. Throughout this chapter, the existing theories and formulations of joint behavior and models will be described in detail. These models serve as the candidates to be implemented in a nonlinear analysis program for two-dimensional reinforced concrete frame structures.

The chapter starts with a detailed summary of the behavior of interior beam-column joints. Then, a review of previous studies is presented on the Modified Compression Field Theory (MCFT), the strut-and-tie model (STM), and bond stress-slip relationship. These theories and material models are used as the foundation of the joint models proposed by various researchers. The chapter continues with a review of the current state-of-the-art. A selection of nine interior joint models from different studies is introduced. All models are capable of capturing joint behavior to some extent, but the decision of which model to implement will be made based on model accuracy and complexity.

2.2 Beam-Column Joint Behavior

The beam-column joint is a crucial zone in a reinforced concrete moment resisting frame. There are three types of beam-column joints or connections in a frame structure: interior joints, exterior joints, and knee joints (see Figure 2.1). Interior joints refer to the joints with at least two beams framing into a continuous column on the opposite sides. They are also the most common type of joints. Exterior joints are located at the perimeter of the frame with discontinuous beams framing into a continuous column. Knee joints refer to the corner joints at the roof level. They are also the least common type of joints. Earthquake reconnaissance observation indicates that exterior joints are more vulnerable than interior joints due to discontinuous reinforcing bars in the beams.

Failures at the roof level are uncommon. This study is primarily focused on interior joints because they are the most common type and require the most number of nodes and components for modeling. Exterior and knee joints may be modeled by modifying the interior joint formulations and disabling some of the components. However, the behavior and modeling of exterior and knee joints may require additional considerations because of their different nature. The interior beam-column joints will be the main focus of this study.

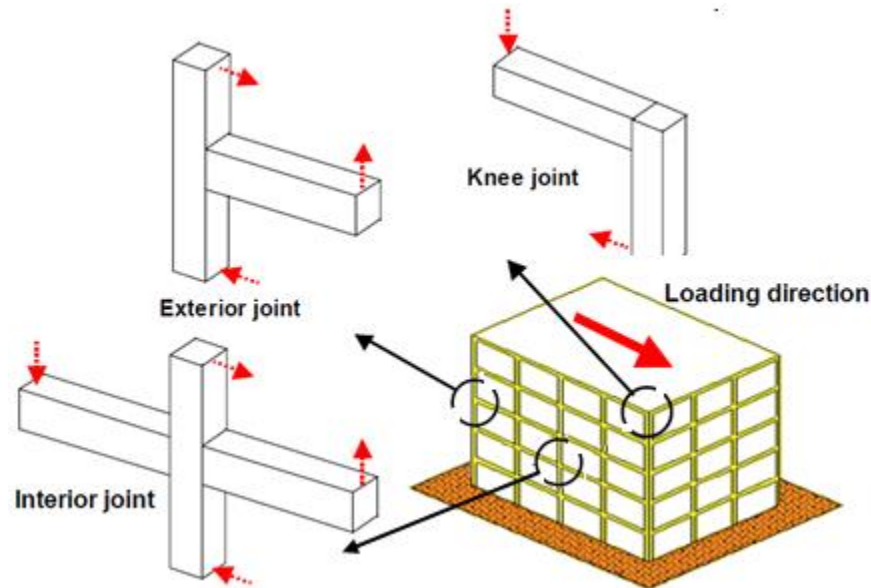


Figure 2.1: Three types of beam-column connections in a reinforced concrete frame (Kim and LaFave, 2009)

In a two-dimensional reinforced concrete frame subjected to seismic loading, beams and columns experience both shear and flexural loading. Figure 2.2 shows the forces that could be expected to develop on the perimeter of an interior joint in a two-dimensional frame subjected to earthquake excitation and gravity loading. The beams are expected to develop shear forces and moments, whereas the columns are expected to carry the gravity load in addition to the shear forces and moments. For frames designed according to modern design codes, the beams are expected to develop flexural strength at the joint interface while the columns are expected to develop moments that approach their flexural strength when the frame is subjected to severe earthquake loading. In older frames, however, shear failure of beams and columns or flexural yielding of columns may occur prior to flexural yielding of beams.

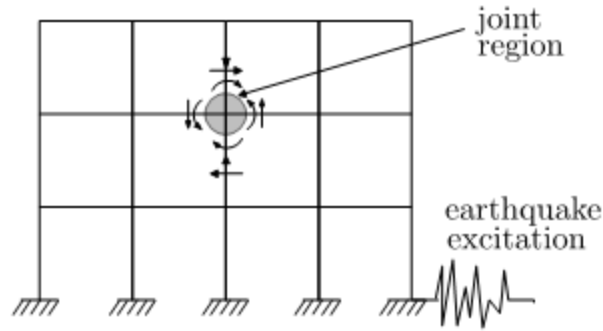


Figure 2.2: Forces expected to develop at the perimeter of an interior joint in a frame under seismic actions (Mitra, 2007)

The load distribution at the joint region is shown in Figure 2.3. The moment on each side of the joint is carried by the tension in the longitudinal reinforcement and the compression in the longitudinal reinforcement and concrete. The joint core also carries shear forces which result from the shear forces developed in the beams and columns framing into the joint. Under severe loading conditions, the moment reversal may create large shear forces within the joint, as well as high bond stresses between the longitudinal reinforcing steel and the surrounding concrete.

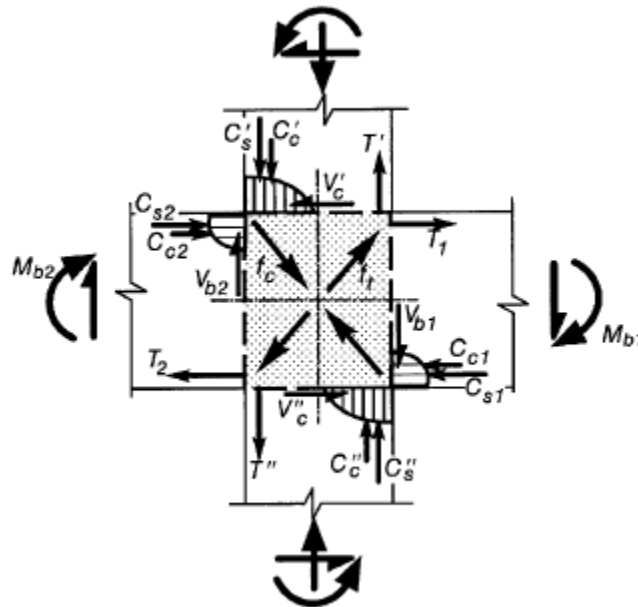


Figure 2.3: Load distribution at the joint region (Hakuto et al., 1999)

Pauley, Park and Priestley (1978) suggested two major shear resisting mechanisms for interior beam-column joints under seismic actions. The first mechanism is the concrete strut mechanism

(see Figure 2.4a). The compression in concrete, the beam and column shear forces and bond forces form a system of equilibrium, in which the joint shear is transmitted via a diagonal concrete strut. The second mechanism is the truss mechanism (see Figure 2.4b). Significant bond forces are applied in the joint as the longitudinal reinforcing steel is subjected to push-pull loading. The effectively anchored horizontal and vertical reinforcing steel in the joint core create a truss system in which the core concrete develops a diagonal compression field that is balanced by the tension in the reinforcement.

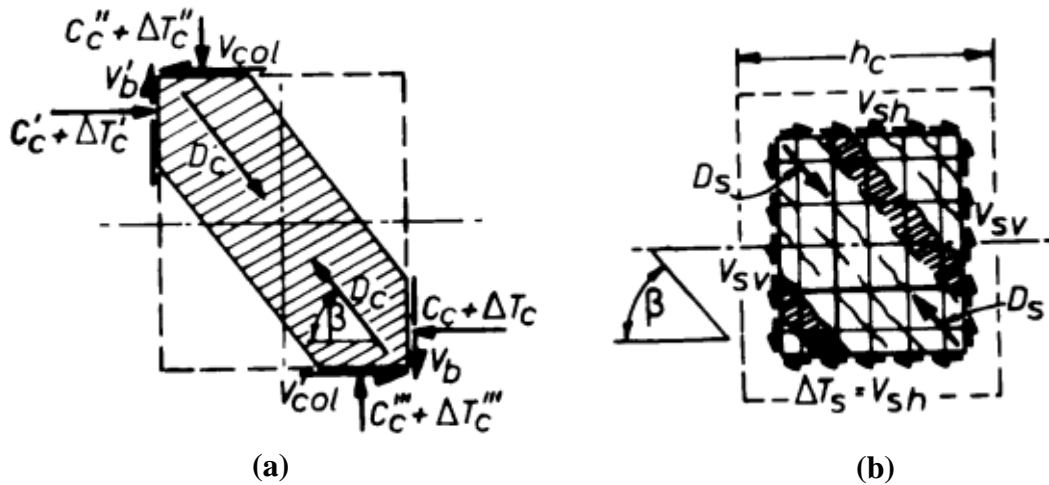


Figure 2.4: Major shear resisting mechanisms: (a) the concrete strut mechanism and (b) the truss mechanism (Pauley et al., 1978)

In addition to the shear behavior, Pauley also considered the bond behavior between the concrete and reinforcing steel in the joint core. Bond slip is joint mechanism which refers to the movement of the longitudinal reinforcing steel with respect to the surrounding concrete due to deterioration of the bond strength between the two (see Figure 2.5). Pauley et al. suggested that the bond in a joint core is mostly affected by the yield penetration of reinforcing bars into the joint from the adjacent plastic hinges, which eventually causes bar pullout, or the separation between the joint element and the adjacent beam and column members. Pauley et al. also suggested that a uniform bond stress distribution along the elastic portion of the longitudinal reinforcement as a probable solution to quantify the bond behavior.

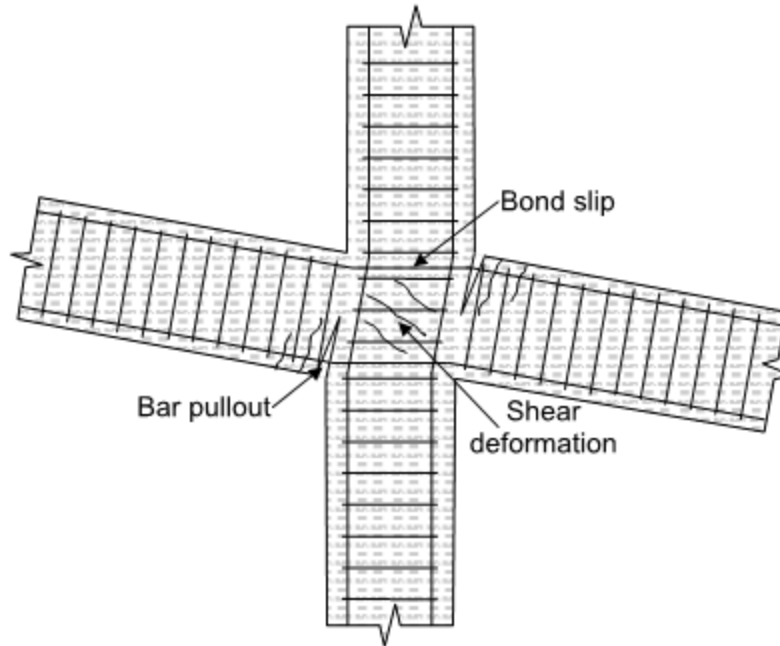


Figure 2.5: Deformed reinforced concrete joint with bond slip and bar pullout (Altoontash, 2004)

There are several factors that may affect the joint shear response and the bond slip response. One of the major factors that affect the joint shear response is the concrete confinement. The truss mechanism will not develop in the joint core in the absence of the transverse reinforcement, which will significantly reduce the joint shear strength for this type of joint compared to the ones with transverse reinforcement. For monotonic loading, experiments have shown that major factors that affect bond slip response include bar diameter, concrete strength, bar clear spacing, restraining reinforcement, and the rate of bar pull-out. Previous studies on testing and rationalizing these two types of responses are discussed below in Section 2.3.

2.3 Review of Existing Behavior Models for Beam-Column Joints

In the last several decades, significant effort has been devoted to laboratory testing and analytical model development for reinforced concrete elements subjected to in-plane shear and normal stresses, including the local bond stress-slip behavior of deformed bars. These studies served as the foundation of the development of local beam-column joint models in the literature.

2.3.1 The Modified Compression Field Theory

The modified compression field theory (MCFT) was formulated by Vecchio and Collins in 1986. It is a smeared, rotating crack model that is capable of predicting the load-deformation response of reinforced concrete elements subjected to in-plane shear and normal stresses. Figure 2.6 shows the loading and the deformation of concrete element subjected to normal and shear stresses. The equilibrium, compatibility and constitutive relationships were derived on the basis of average stresses and average strains. Local stress conditions at crack locations are also considered in this model. The MCFT has been employed by various researchers in developing joint models in order to determine the shear stress-strain response of joint cores, or the relationship between panel shear-equivalent moment and panel shear deformation.

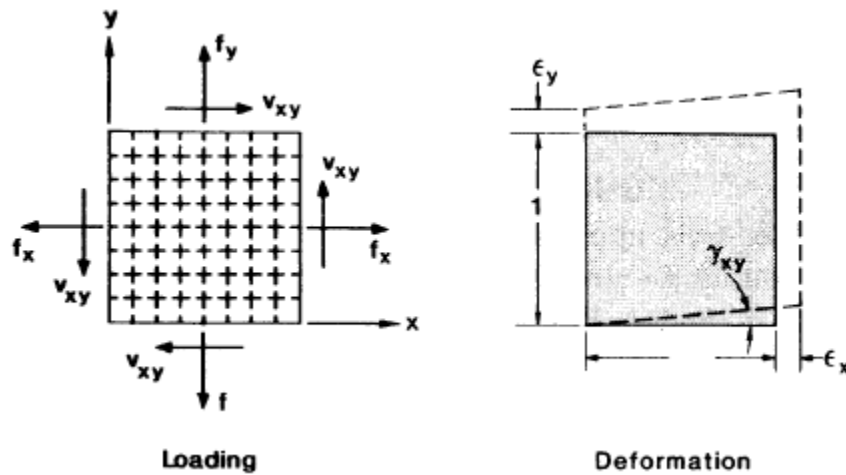


Figure 2.6: Reinforced concrete element subjected to normal and shear stresses (Vecchio and Collins, 1986)

The MCFT is formulated based on four key assumptions. Some of these assumptions may not be suitable for modeling joints. First of all, the reinforcement is assumed to be uniformly distributed within the element. This assumption is usually not true for joints because they are reinforced by horizontal and vertical longitudinal bars in addition to the tie reinforcement along the vertical direction. The spacing between the layers of longitudinal bars may not be uniform. Secondly, loads on the element are assumed to be uniform. This condition may not be valid for interior beam-column joints because the shear stresses from framing beams and columns usually follow a parabolic-like distribution with the peak stress at around the mid-height of the member. The next

assumption is that the bond between the concrete and the reinforcement remains in perfect condition. In fact, the bond between the concrete and the reinforcement in joints usually deteriorates as the frame is subjected to load reversal with large load cycles. Lastly, the MCFT assumes that the principal concrete stress direction coincides with the direction of principal strain, which is generally valid for the interior joints.

The MCFT is formulated based on three conditions: compatibility, equilibrium and stress-strain (i.e., constitutive) relationship. The strain and compatibility requirements are considered in terms of average values over distances crossing several cracks. The compatibility conditions require any deformation experienced by the concrete to be matched with the identical deformation by the reinforcement. Based on the known strains in the x and y directions as well as the shear strain, the strain in any other direction can be found by strain transformation. The equilibrium conditions state that the forces applied to the reinforced concrete element are resisted by stresses in the concrete and the reinforcement. These stresses are also considered in terms of average values. The constitutive relationships link average stresses to average strains for both the concrete and reinforcement. A bilinear stress-strain relationship is adapted for the reinforcement. For concrete in compression, the principal compressive stress is found using a parabolic stress-strain relationship. A reduction factor is applied to the stress to account for the tensile strains in the orthogonal direction that cracks and weakens the concrete. This behavior is known as “compression softening”. For concrete in tension, a linear stress-strain response is used until the cracking strain, where the bond between the concrete and the reinforcement starts to carry the tensile stress, known as “tension stiffening”. Figure 2.7a shows a three-dimensional representation of the compressive constitutive relationship of concrete considering the compression softening effect. Figure 2.7b shows the stress-strain relationship of concrete in tension considering the tension stiffening effect.

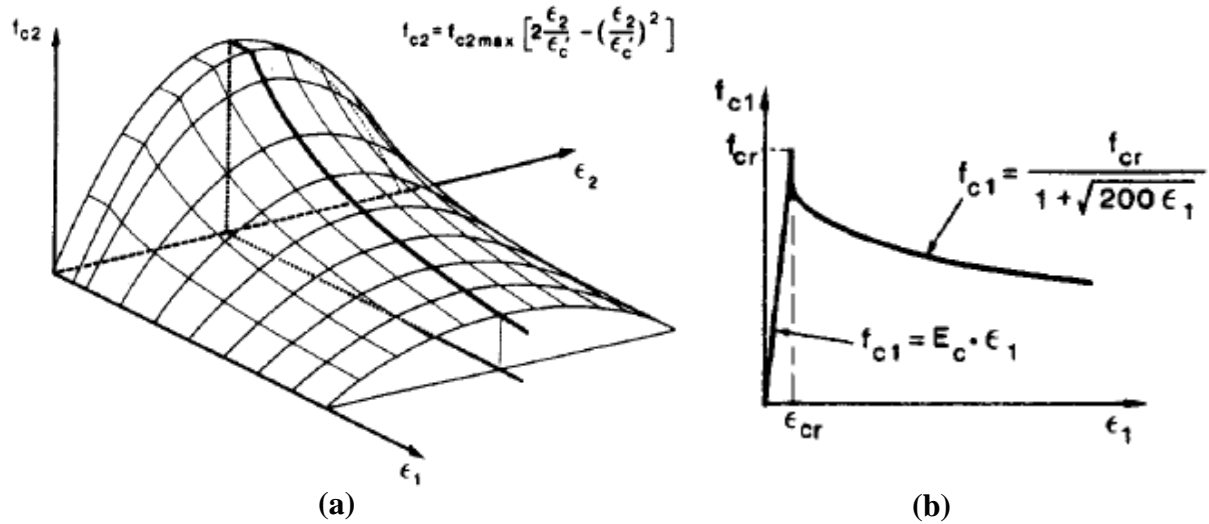


Figure 2.7: Stress-strain relationship for concrete under (a) uniaxial compression and (b) uniaxial tension (Vecchio and Collins, 1986)

The general solution procedure for determining the response of biaxially-loaded elements was presented in Appendix A of the ACI paper by Vecchio and Collins (1986). Determining the shear stress-strain response of the joint core using the MCFT was explained by Altoontash (2004) in his study of reinforced concrete joints. The procedure introduced in this section contains some revisions based on his proposed solution procedure. The input required for determining the shear stress-strain response of the joint core is defined as follows:

- P_v = vertical gravity loading on the joint (kN)
- A_{gv} = gross cross-sectional area of column (mm^2)
- ρ_{sx} = reinforcement ratio for reinforcing steel in the x direction
- ρ_{sy} = reinforcement ratio for reinforcing steel in the y direction
- E_c = modulus of elasticity of concrete (MPa)
- E_s = modulus of elasticity of reinforcement (MPa)
- f_{yx} = yield stress of the x reinforcement (MPa)
- f_{yy} = yield stress of the y reinforcement (MPa)

- f'_c = concrete compressive strength (MPa)
- f'_t = concrete tensile strength (MPa)
- ε'_c = strain in concrete at peak compressive stress
- s_{mx} = mean crack spacing in the x direction (mm)
- s_{my} = mean crack spacing in the y direction (mm)
- a = maximum aggregate size (mm)

The iterative solution procedure to determine the shear stress-strain response of a joint core using the MCFT follows the steps below:

Step 1: Calculate the initial strains in the x and y directions based on the boundary forces. Also, initialize the shear strain.

$$f_x = 0 \quad (2.1)$$

$$f_y = \frac{P_v}{A_{gv}} \quad (2.2)$$

$$\varepsilon_x = 0 \quad (2.3)$$

$$\varepsilon_y = \frac{P_v}{(1-\rho_{sy})E_c + \rho_{sy}E_s} \quad (2.4)$$

$$\gamma_{xy} = 0 \quad (2.5)$$

According to Altoontash, the horizontal strain is assigned a value of zero because it is assumed that the joint does not carry any horizontal forces produced by the beam members framing into the joint. In fact, there is a horizontal component of shear force, and the horizontal strain does not equal to zero. However, for simplicity purposes, the horizontal strain is assumed to be zero.

Step 2: Determine the principal strains and the principal angle.

$$\varepsilon_x = 0 \quad (2.6)$$

$$\varepsilon_1 = \frac{\varepsilon_x + \varepsilon_y}{2} + \sqrt{\left(\frac{\varepsilon_x - \varepsilon_y}{2}\right)^2 + \left(\frac{\gamma_{xy}}{2}\right)^2} \quad (2.7)$$

$$\varepsilon_2 = \frac{\varepsilon_x + \varepsilon_y}{2} - \sqrt{\left(\frac{\varepsilon_x - \varepsilon_y}{2}\right)^2 + \left(\frac{\gamma_{xy}}{2}\right)^2} \quad (2.8)$$

$$\theta_p = \frac{1}{2} \arctan \frac{\gamma_{xy}}{\varepsilon_x - \varepsilon_y} \quad (2.9)$$

Step 3: Determine the stress in the horizontal and the vertical reinforcement.

$$f_{sx} = E_s \varepsilon_{sx} \leq f_{yx} \quad (2.10)$$

$$f_{sy} = E_s \varepsilon_{sy} \leq f_{yy} \quad (2.11)$$

Step 4: Determine the stress in the concrete.

Tensile response:

$$f_{c1} = E_c \varepsilon_1 \quad \text{if } \varepsilon_1 \leq \varepsilon'_t \quad (2.12)$$

$$f_{c1} = \frac{f'_t}{1 + \sqrt{200 \varepsilon_{c1}}} \quad \text{if } \varepsilon_1 > \varepsilon'_t \quad (2.13)$$

Compressive response:

$$f_{c2} = f_{c2max} \left[2 \left(\frac{\varepsilon_2}{\varepsilon'_c} \right) - \left(\frac{\varepsilon_2}{\varepsilon'_c} \right)^2 \right] \quad \text{where } \frac{f_{c2max}}{f'_c} = \frac{1}{0.8 - 0.34 \frac{\varepsilon_1}{\varepsilon'_c}} \leq 1.0 \quad (2.14)$$

Step 5: Determine the concrete stresses in the global coordinate system based on the Mohr's stress transformation equations.

$$f_{cx} = \frac{f_{c1} + f_{c2}}{2} + \frac{f_{c1} - f_{c2}}{2} \cos 2\theta \quad (2.15)$$

$$f_{cy} = \frac{f_{c1} + f_{c2}}{2} - \frac{f_{c1} - f_{c2}}{2} \cos 2\theta \quad (2.16)$$

Step 6: Check the convergence of the horizontal and vertical stresses.

$$f_x^{curr} = f_{cx} + \rho_{sx} f_{sx} \quad (2.17)$$

$$f_y^{curr} = f_{cy} + \rho_{sy} f_{sy} \quad (2.18)$$

Compare the difference between the stress values obtained in this step and the applied stresses calculated in the first step. If the difference is larger than the tolerance, repeat steps 2 to 6 using the following strain values until the convergence criteria are satisfied.

$$\varepsilon_x^{next} = \varepsilon_x^{curr} + \frac{f_x - f_x^{curr}}{(1 - \rho_{sy})E_c + \rho_{sy}E_s} \quad (2.19)$$

$$\varepsilon_y^{next} = \varepsilon_y^{curr} + \frac{f_y - f_y^{curr}}{(1 - \rho_{sy})E_c + \rho_{sy}E_s} \quad (2.20)$$

Step 7: Check probable shear failure modes.

Check reinforcing bar yielding across cracks:

$$f_{c1}^* = \rho_x(f_{yx} - f_{sx})\cos^2\theta_{nx} + \rho_y(f_{yy} - f_{sy})\cos^2\theta_{ny} \quad (2.21)$$

where θ_{nx} is the angle of the principal tensile stress from the x-axis, θ_{ny} is the angle of the principal tensile stress from the y-axis. In order to pass this check, the principal tensile stress, f_{c1} , should be less than f_{c1}^* .

Checking the slip along the crack interface requires the solution of the following five equations to determine the reinforcement stress at the crack interface (i.e. f_{scrx} and f_{scry}):

$$\varepsilon_{scrx} = \varepsilon_{sx} + \Delta\varepsilon_{1cr}\cos^2\theta_{nx} \quad (2.22)$$

$$\varepsilon_{scry} = \varepsilon_{sy} + \Delta\varepsilon_{1cr}\cos^2\theta_{ny} \quad (2.23)$$

$$f_{scrx} = E_s\varepsilon_{scrx} \leq f_{yx} \quad (2.24)$$

$$f_{scry} = E_s\varepsilon_{scry} \leq f_{yy} \quad (2.25)$$

$$f_{c1} = \rho_x(f_{scrx} - f_{sx})\cos^2\theta_{nx} + \rho_y(f_{scry} - f_{sy})\cos^2\theta_{ny} \quad (2.26)$$

The reinforcement stresses at crack interface are used to find the shear stress as follows:

$$v_{ci} = \rho_x(f_{scrx} - f_{sx})\cos\theta_{nx}\sin\theta_{nx} + \rho_y(f_{scry} - f_{sy})\cos\theta_{ny}\sin\theta_{ny} \quad (2.27)$$

The interface shear stress is expected not to exceed the following limit:

$$v_{cimax} = \frac{0.18\sqrt{f'_c}}{0.31 + \frac{24w}{a+16}} \quad \text{where } w = \varepsilon_1 \cdot \frac{1}{\frac{\cos \theta}{s_{mx}} + \frac{\sin \theta}{s_{my}}} \quad (2.28)$$

The solution procedure is repeated for various shear strains to obtain the shear stress-strain response of a joint.

2.3.2 The Strut-and-Tie Model

The strut-and-tie model (STM) is another method for modeling joint shear panels. The concept of the strut-and-tie model was developed in pioneering work by Mörsch (1909). The comprehensive model was presented in detail in a report by Schlaich et al. (1987). The STM is developed to represent the stress fields in reinforced concrete members resulting from the applied loads. Similar to a truss, the STM consists of three elements: compression struts, tension ties, and nodes interconnecting them. An important study in the development of the model is the application to discontinuity regions as proposed by Schlaich et al. (1987). The regions of a structure where the hypothesis of plain strain distribution is valid are usually referred to as “B regions”, or beam regions. The regions of a structure where the strain distribution is significantly nonlinear are usually referred to as “D regions”, or discontinuity regions. These regions are generally located near concentrated loads, supports, corners, joints and openings (see Figure 2.8). The model was originally used to describe the stress fields in beams, but the same model is also applicable to joint regions.

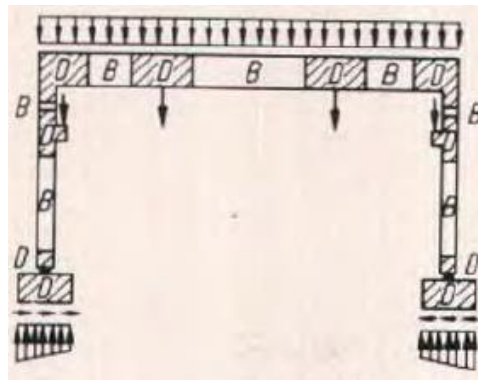


Figure 2.8: B Regions and D Regions in a reinforced concrete frame structure (Schlaich et al., 1987)

Application of the strut-and-tie model to beam-column joints was explained in detail by Mitra (2007) for seismic loading. Each STM was formulated based on four key assumptions. First of all, the development of the model is based on equilibrium conditions and component strengths. Secondly, the joint is subjected to two-dimensional plane stress condition with the out-of-plane depth of the strut taken as the larger dimension of beams' and columns' out-of-plane depths. The third assumption is that the ties representing top and bottom longitudinal reinforcement in the beams and the columns are located at the centroid of the bars. Finally, the strength of the ties representing the longitudinal reinforcement is limited by the ultimate strength of the reinforcing bars, whereas the strength of the ties representing joint transverse reinforcement is limited by the yield strength of the reinforcing bars.

Mitra (2007) introduced three types of strut-and-tie models including a single-strut model, a distributed-truss model, and a combined strut-truss model. In the single-strut model, the compressive load is primarily transferred through a single concrete strut within the joint (see Figure 2.9a). This concept coincides with the load transfer mechanism idealized by Pauley et al. (1978). In addition to the aforementioned assumptions for strut-and-tie models, it was assumed that both joint transverse reinforcement and column longitudinal bars are not modeled explicitly. Strut and node dimensions are defined based on the depth of the compressive stress blocks in the beams and columns framing into the joint at their nominal moments. The strut width is taken as the square root of the summation of the square of the two stress block depths. In the distributed-truss model, the tensile load is transferred through a truss mechanism formed by the mesh of the joint transverse reinforcement and the column longitudinal bars (see Figure 2.9b), similar to the truss mechanism idealized by Pauley et al. (1978). However, the distributed-truss mechanism was not further studied by Mitra because it represents joint load transfer at low load levels prior to the loss of bond strength within the joint region. The last sub-model is the combined strut-truss model, representing the combination of the two models (see Figure 2.9c). The stress in the beam longitudinal reinforcing bars is taken approximately equal to the ultimate strength, and the stress in the joint transverse reinforcement is taken as less than or equal to its yield strength. Mitra suggested using an approach similar to that in the single-strut model to define the width of the strut (see Figure 2.9d). Mitra also concluded that either a single-strut or a combined strut-truss model is suitable for describing the load transfer mechanism within the joint in the peak and post-peak regions, whereas a distributed-truss model is more suitable in the pre-peak region.

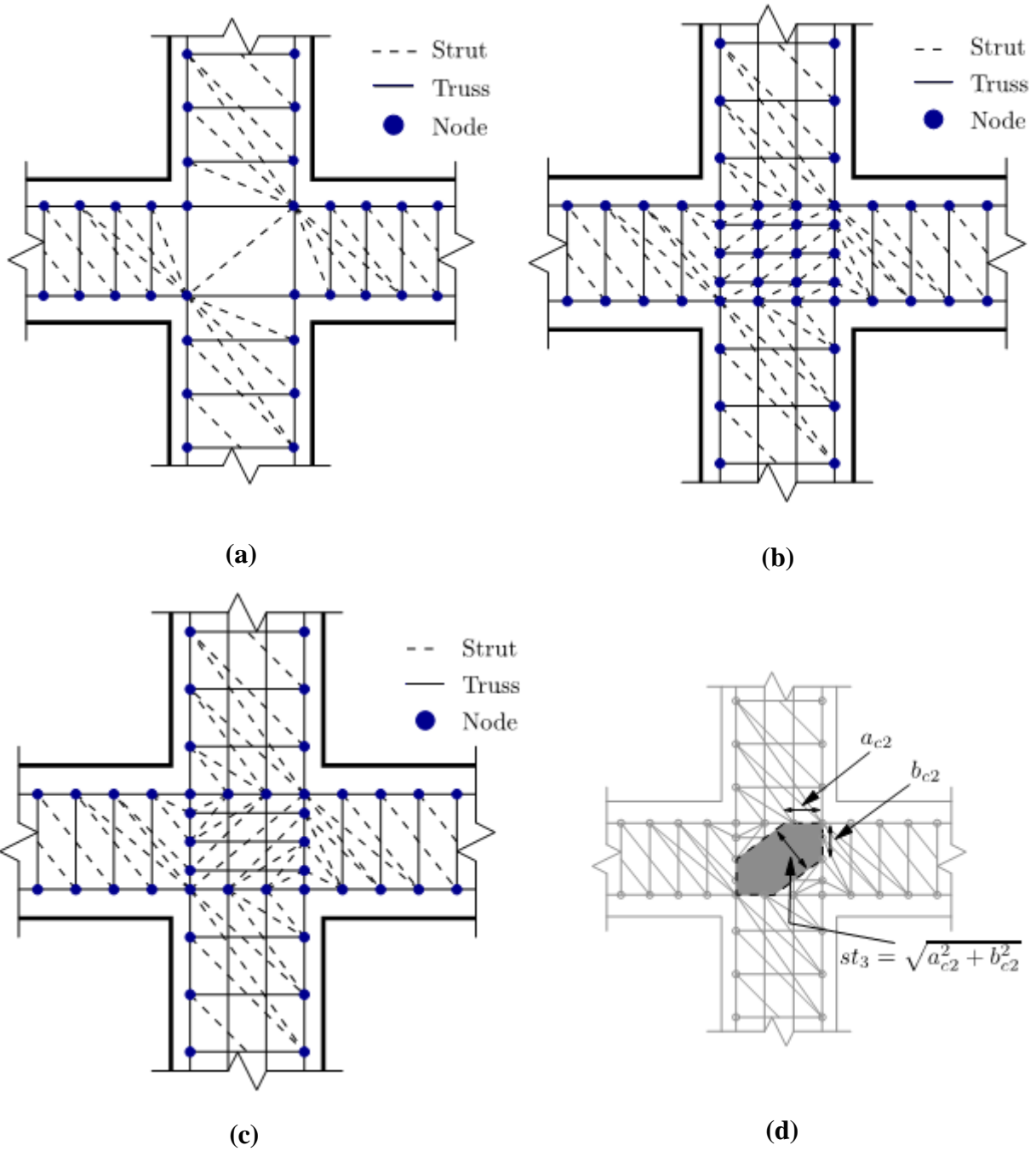


Figure 2.9: The strut-and-tie model: (a) single-strut model, (b) distributed-truss model, (c) combined strut-truss model, and (d) definition of the strut width in combined strut-truss mechanism (Mitra, 2007)

The more complex strut-and-tie models suitable for joint application include the softened strut-and-tie model proposed by Hwang and Lee (2002), and the compatibility strut-and-tie model proposed by Scott et al. (2012).

2.3.3 Bond Stress-Slip Relationship

In traditional analysis of reinforced concrete frame structures subjected to seismic loading, perfect bond between the reinforcement and the concrete is often assumed. Under severe seismic loads, cracks form at the interface of joints and beams framing into the joints (see Figure 2.5). Reinforcing bars at the cracks may be strained beyond their yielding point, while being simultaneously pushed and pulled at the opposite sides of the joint, creating high bond stresses between the longitudinal reinforcing steel and the surrounding concrete. Therefore, modeling of the bond stress-slip relationship becomes a crucial part of effective joint modeling. Two of the earliest studies for characterizing and modeling bond behavior were carried out by Viwathanatepa et al. (1979) and Eligehausen et al. (1983).

Viwathanatepa et al. (1979) tested seventeen specimens of single reinforcing bars embedded in well-confined column stubs subjected to push-pull or pull only loadings. The specimens were made 46 inches (1168 mm) high with the width of the blocks ranging from 15 inches (381 mm) to 25 inches (635 mm) (see Figure 2.10a). A sufficient amount of transverse reinforcement was provided for shear and confinement. The amount of the longitudinal reinforcement was designed to confine crack propagation, limit crack size, and provide strength to resist the applied flexural bending moment. Adequate anchorage length was provided to ensure that the maximum steel stress could be developed. The supports were also designed to minimize the stress concentration developed in the test specimen. The load was applied to the specimens by three hydraulic jacks (see Figure 2.10b). The authors were mainly interested in three aspects of the results: the load-displacement response measured at the protruding end of the bar, the stress and strain distributions along the longitudinal reinforcing bars, and the bond stress distribution along the rebar.

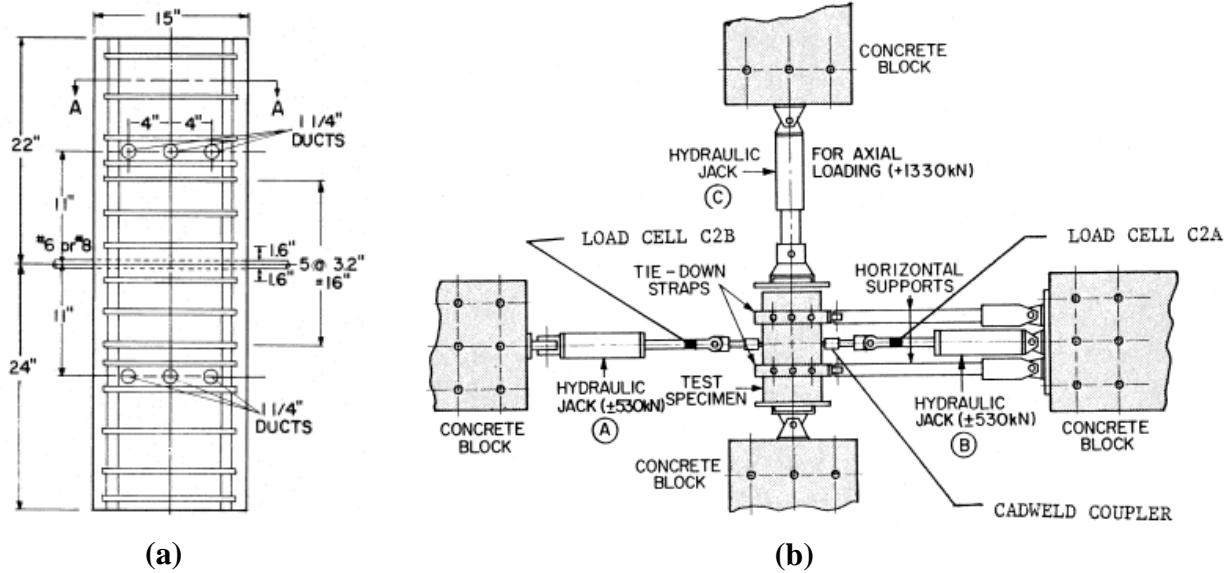


Figure 2.10: Test setup in the bond experiment conducted by Viwathanatapa et al. (1979): **(a)** the elevation view of the specimen and **(b)** the testing apparatus

For the push-pull loading under a monotonic loading history, Viwathanatapa et al. concluded that: (1) the application of a pushing load in addition to a pulling load has little effect from a strength point of view; (2) the application of a pushing load reduces the pull-out ductility; (3) the smaller the bar size, the higher the average bond strength that could be developed; and (4) the bond stress of grooved bars (i.e. bars with reduced effective perimeter and cross-sectional area) may differ by 15% from that of ungrooved bars. Ultimately, Viwathanatapa et al. formulated a bond stress-slip relationship as a step towards determining the load-displacement relationship at the exposed ends of a reinforcing bar embedded in a concrete block subjected to either monotonic or reversed cyclic loading. The actual behavior was idealized as a round bar surrounded by two layers of soft concrete which consisted of an unconfined region near the pull end, a pushed end region and a confined region in the middle. A four-stage monotonic skeleton bond stress-slip curve was constructed based on the response of the three regions (see Figure 2.11a). The curve was further modified using reduction factors and hysteric rules in order to adapt reversed cyclic loading. The soft concrete layers were divided into finite number of elements to be analyzed individually (see Figure 2.11b). The forces and local displacements of the corresponding spring elements are calculated as follows:

$$F = \tau Cl_e \quad (2.29)$$

$$\delta = \gamma t \quad (2.30)$$

where F is the force in the spring element, δ is the local displacement of the spring element, τ is the shear stress of the soft layer element, γ is the shear deformation of the soft layer element, C is the circumference of the rebar, l_e is the length of the soft layer element and t is the thickness of the soft layer. The sum of the results from the individual springs denotes the load-displacement relationship at the exposed ends of a reinforcing bar embedded in concrete (see Figure 2.11c).

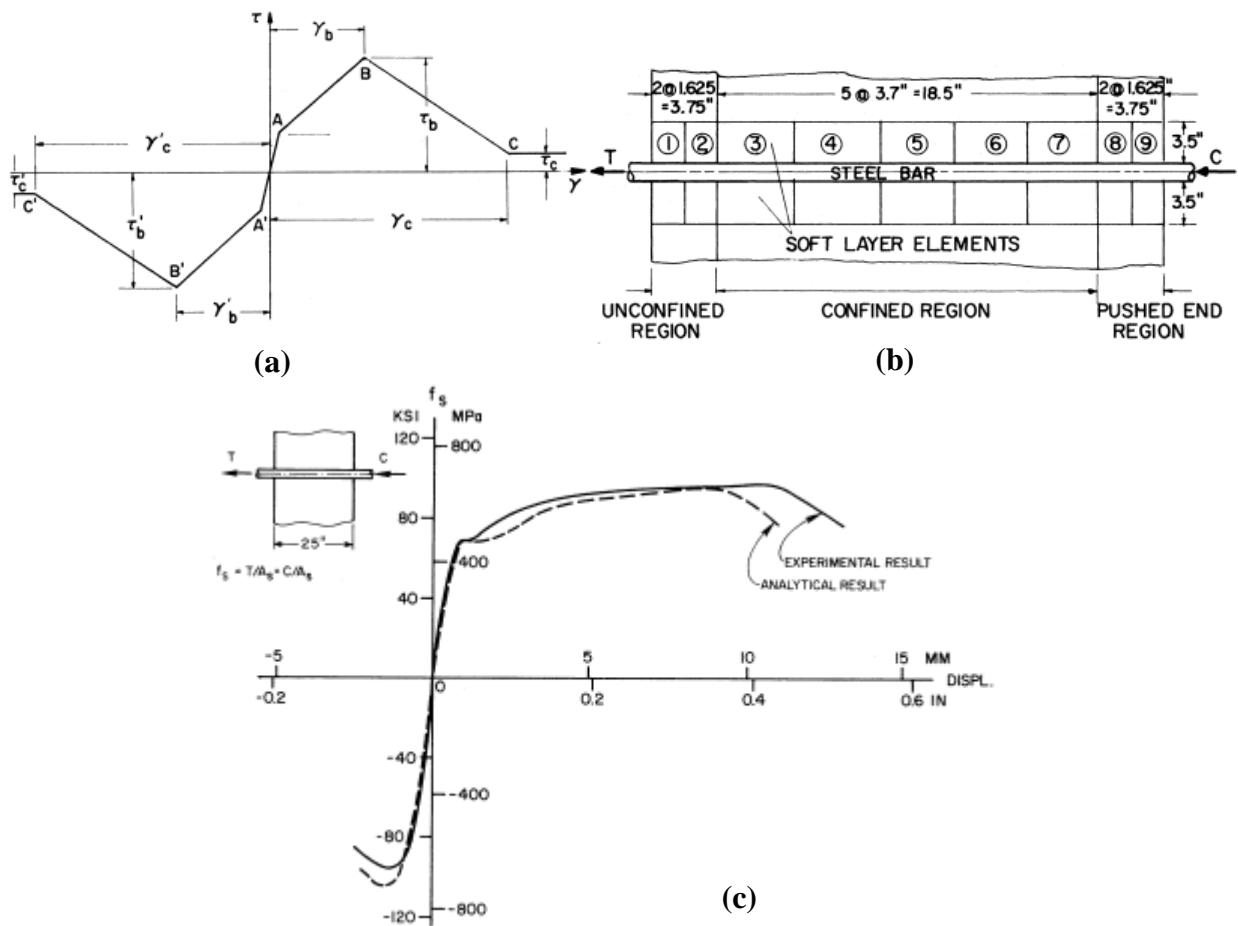


Figure 2.11: Formulation of bond model proposed by Viathanatepa et al. (1979): (a) monotonic skeleton bond stress-slip Curve, (b) finite soft layer elements, and (c) load-displacement relationship of a #8 (25M) bar

Eligenhausen et al. (1983) tested 125 pull-out specimens loaded at one end of the reinforcing bar embedded in concrete blocks. The objective was to study the local bond-stress relationship of deformed bars embedded in confined concrete subjected to monotonic and cyclic loading conditions, and create an analytical model for the bond behavior. The test program was similar to that of Viwathanatepa et al. (1979). Eligenhausen et al. (1983) presented the influence of seven parameters on the bond stress-slip relationship for monotonic loading, as follows:

- (1) Tension or compression loading: The bond stress-slip relationships are approximately equal for bars in tension or compression prior to yielding. After yielding, the bond resistance of bar in tension reduces significantly, whereas the bond resistance of a bar in compression increases.
- (2) Confining reinforcement: The confining reinforcement increases the bond stress required to develop splitting cracks. However, there is an upper limit for effective confining reinforcement beyond which the bond behavior cannot be improved further.
- (3) Bar diameter: The bond resistance for bars with different diameters is slightly different in terms of the initial stiffness and the peak resistance.
- (4) Concrete strength: The initial stiffness and the overall bond resistance increase with increasing concrete strength.
- (5) Bar spacing: The bond behavior improves with increasing bar spacing, but the improvement is relatively small.
- (6) Transverse pressure: Transverse pressure helps develop greater bond resistance while other conditions remain unchanged.
- (7) Rate of pull-out: The bond resistance increases with the increasing rate of bar pull-out.

For cyclic loading, considerations were also given in this study to the behavior in the unloading branch and in the reloading branch. The analysis of the influence of each parameter was also provided in this study.

Eligenhausen et al. (1983) further characterized the mechanism of bond resistance for both monotonic and cyclic loading, and proposed a general analytical model for the local bond stress-slip relationship for confined concrete (see Figure 2.12). In this model, a set of values was provided with the same bond stress-slip relationship assumed regardless of whether the bar was

pulled or pushed. This set of values was further modified according to seven influential parameters to obtain the response for each specific case.

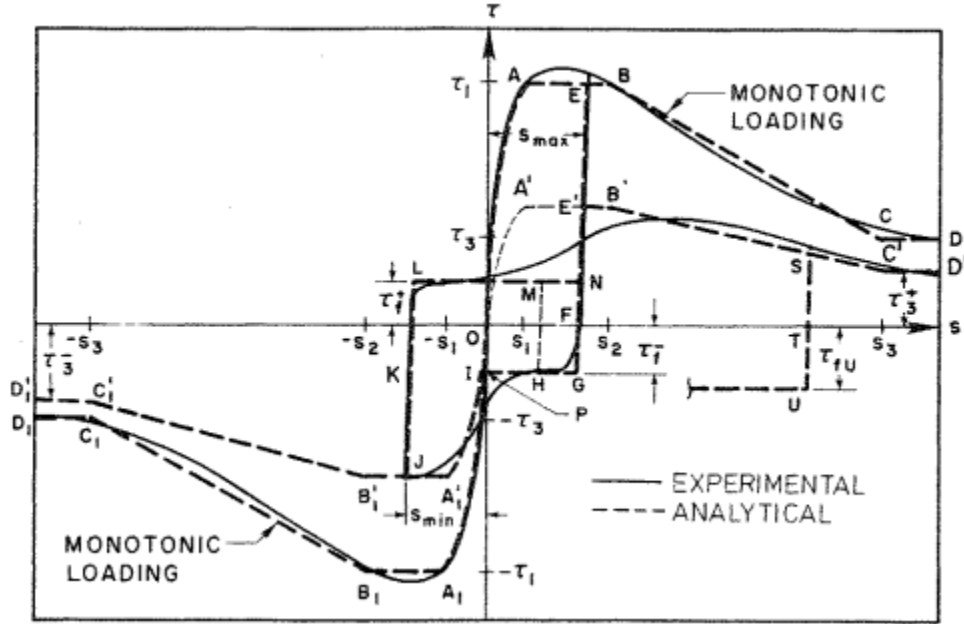


Figure 2.12: Proposed analytical model for local bond stress-slip relationship for confined concrete subjected to monotonic and cyclic loading (Eligenhausen et al., 1983)

For the purpose of joint modeling, however, researchers often prefer to use the assumption of a bi-uniform relationship to model the bond stress distribution along the development length of an anchored reinforcing bar. The relationship between the rebar-end stress and loaded-end slip was obtained from equation derivation and substitution. One of the studies that utilize this technique was done by Sezen and Moehle (2003). The proposed model by Sezen and Moehle is given by:

$$s = \frac{\varepsilon_s f_s d_b}{8\sqrt{f'_c}} \quad f_s \leq f_y \quad (2.31)$$

$$s = \frac{\varepsilon_s f_s d_b}{8\sqrt{f'_c}} + \frac{(\varepsilon_s + \varepsilon_y)(f_s - f_y)d_b}{4\sqrt{f'_c}} \quad f_s > f_y \quad (2.32)$$

where s is the loaded-end slip, ε_s is the reinforcement strain, ε_y is the reinforcement yield strain, f_s is the stress in the reinforcing steel, f_y is the yield stress of the reinforcing steel, d_b is the bar diameter and f'_c is the compressive strength of the concrete. In this model, a uniform bond stress

of $1.0\sqrt{f_c}$ was assumed in the elastic range, whereas a uniform bond stress of $0.5\sqrt{f_c}$ was used in post-yielding range. Another bar stress versus loaded-end slip model, which was based on curve fitting and experimental observations, was proposed by Zhao and Sritharan (2007). The monotonic envelope curve was composed of a straight line for the elastic region and a curvilinear portion for the post-yielding region (see Figure 2.13), as follows:

$$f_s = Ks \quad f_s \leq f_y \quad (2.33)$$

$$f_s = \tilde{\sigma} \cdot (f_u - f_y) + f_y \quad f_s > f_y \quad (2.34)$$

where f_s is the stress in the reinforcing steel, s is the loaded-end slip, f_y is the yield stress of the reinforcing steel, f_u is the ultimate stress of the reinforcing steel, K is the slope of the straight line and $\tilde{\sigma}$ is the normalized bar stress.

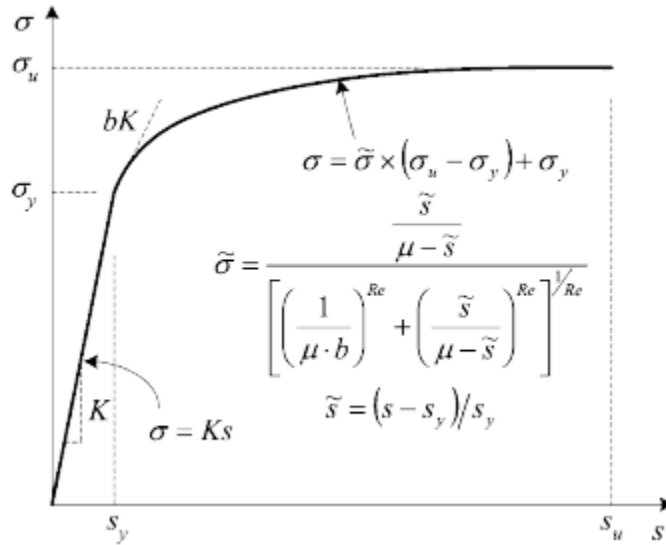


Figure 2.13: Monotonic envelope curve of bar stress versus loaded-end slip relationship (Zhao and Sritharan, 2007)

2.4 Review of Existing Beam-Column Joint Models

Many researchers have proposed various beam-column joint models over the past two decades. These models can be categorized into three types: (1) rotational hinge models such as by Alath and Kunnath (1995), Altoontash (2004) and Shin and LaFave (2004); (2) component models such as by Youssef and Ghobarah (2001), Lowes and Altoontash (2003) and Mitra and Lowes (2007); and (3) finite element models. Rotational hinge models are non-objective and require calibration for each specific type of joint. Finite element models are complex and require significant computational resources; therefore, they are not suitable for holistic frame analysis. Component models provide a good balance between simplicity and accuracy. They are generally objective and suitable for analyzing large frames. They use mechanics-based formulations and generally do not require calibration for each particular joint type.

2.4.1 Rotational Hinge Models

2.4.1.1 Alath and Kunnath (1995)

Alath and Kunnath modeled the joint with four rigid links representing the joint panel geometry, and a zero-length rotational spring with a degrading hysteresis rule representing the joint shear deformations (see Figure 2.14). The joint shear stress-strain relationship was determined empirically, while the cyclic response was captured with a hysteretic model that was calibrated by experiments. The model was validated through a study comparing the analytical and experimental response of an interior beam-column joint subassembly. One disadvantage of this model is that it only considers the joint shear behavior, neglecting the bond slip behavior.

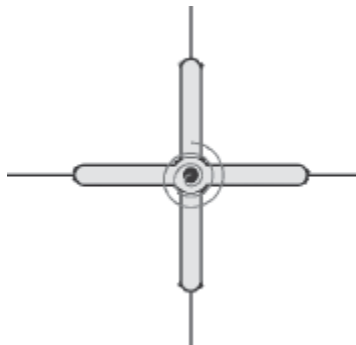


Figure 2.14: Joint model proposed by Alath and Kunnath (Alath and Kunnath, 1995; figure adopted from Celik and Ellingwood, 2008)

2.4.1.2 Altoontash (2004)

Altoontash simplified Lowes and Altoontash's model by introducing four external bar-slip rotational springs at the nodes located at the joint interface, and a central panel rotational spring utilizing the MCFT to represent the shear response (see Figure 2.15). The shear panel maintains its parallelogram shape as it deforms. Altoontash also suggested using fiber sections instead of uniaxial materials to link the joint and the adjacent frame elements in order to obtain more accurate calibration. This model was verified with five non-ductile beam-column subassemblies and a 0.7-scale two-story frame. Due to the use of the calibrated rotational springs, the accuracy of this model depends on the similarity between the joint being modeled and the dataset used in the calibration.

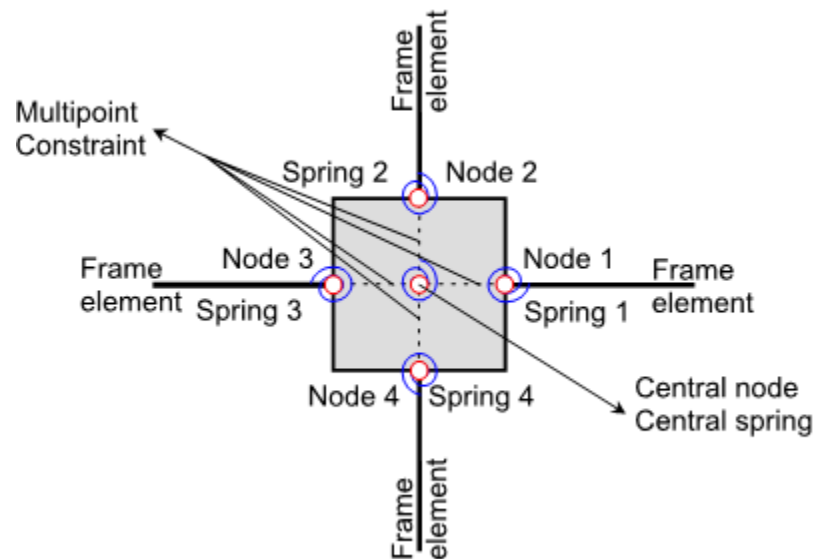


Figure 2.15: Joint model proposed by Altoontash (Altoontash, 2004)

2.4.1.3 Shin and LaFave (2004)

Shin and LaFave proposed a joint model with four rigid links along the edge of the joint panel connected by four hinges at the corners (see Figure 2.16). Three parallel nonlinear rotational springs were embedded into one of the hinges to simulate the joint shear behavior. The MCFT was utilized to determine the moment-curvature relationship of the three springs to capture the joint shear response. In order to model the plastic hinge in beams and bar-slip effects, a rotational plastic hinge spring and a rotational bar-slip spring were attached at the interface between the

beam and the joint on both sides. The model was verified with 26 interior connections containing transverse reinforcement. This model is also a calibrated model. It is only applicable for joints with transverse reinforcement, and cannot model older-type, non-ductile joints.

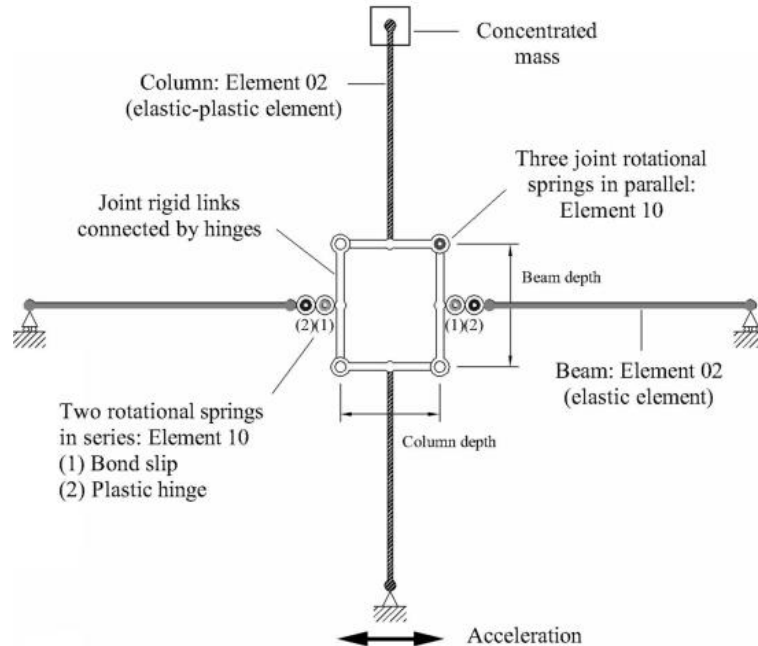


Figure 2.16: Joint model proposed by Shin and LaFave (Shin and LaFave, 2004)

2.4.2 Component Models

2.4.2.1 Lowes and Altoontash (2003) and Mitra and Lowes (2007)

Lowes and Altoontash proposed a joint element with four nodes and thirteen degrees of freedom including eight bar-slip springs, four interface shear springs and a shear panel (see Figure 2.17). The MCFT was employed to model the shear panel. A bond slip relationship was proposed based on the experimental data from Eligenhausen et al. (1983). A relatively stiff interface-shear spring response was assumed. The joint model was verified against four joint subassemblies. Mitra and Lowes evaluated and improved this model subsequently. The MCFT-based model was found to underestimate the strength of joints with low transverse reinforcement ratios and overestimate the strength of joints with high transverse reinforcement ratios. In this improved model, shear is transferred primarily through a concrete compressive strut. It was demonstrated that this approach provided a more accurate prediction for the shear panel response. Mitra and Lowes model was implemented in OpenSees. The model was evaluated by comparing the simulated and

observed responses of 57 previous experimental specimens of interior joints. Although this model is capable of predicting the response of joints under monotonic and cyclic loading, it has three drawbacks: complicated definition of the model parameters, intra-element solution procedure, and potential numerical convergence problems under cyclic loading.

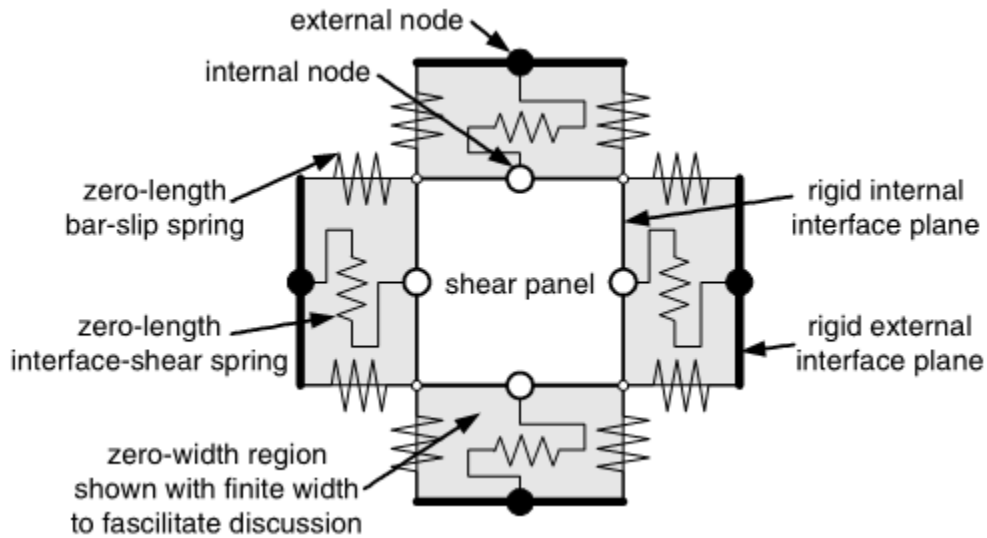


Figure 2.17: Joint model proposed by Lowes and Altoontash (Lowes and Altoontash, 2003)

2.4.2.2 Ghobarah and Youssef (2001)

Ghobarah and Youssef proposed a joint element with two diagonal springs linking the opposite corners of the joint element (see Figure 2.18). The MCFT was employed to simulate the shear deformations in the joint panel zone. Three sets of concrete and steel springs were used at each side of the joint perimeter to account for the bond-slip effects. The joint model, along with a proposed structural wall model, was incorporated in a structural analysis program and verified with a three-story non-ductile frame. This model requires a large amount of springs with separate constitutive models, which may limit its applicability.

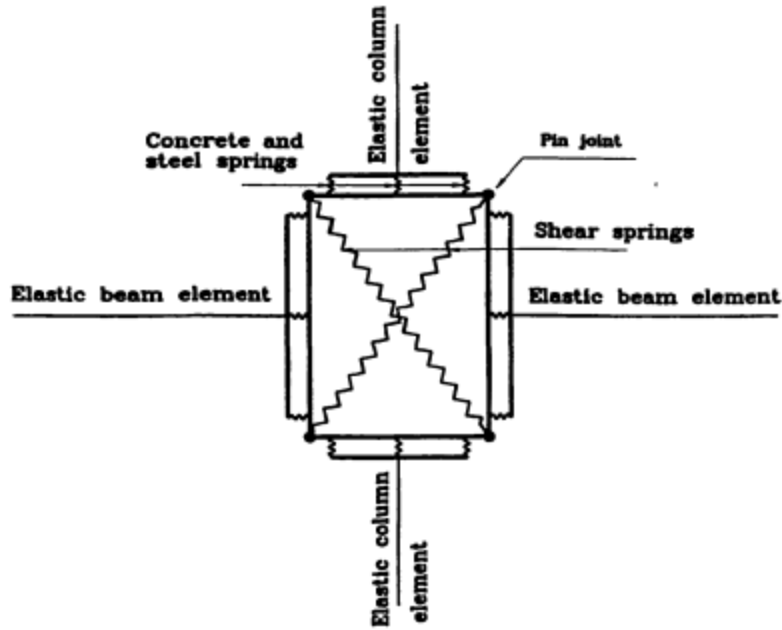


Figure 2.18: Joint model proposed by Ghobarah and Youssef (Ghobarah and Youssef, 2001)

2.4.2.3 Fleury et al. (2000)

Fleury et al. proposed a multi-component model for the simulation of multiple components consisting of a single joint element and the surrounding components (see Figure 2.19). The joint core behavior was described by a concrete element and a transverse reinforcement element. A series of elements was used to describe the longitudinal reinforcing steel in the beam members and its bond throughout the joint. The longitudinal reinforcing steel was represented by two-node bar elements. The connections of the beams to the joint were also represented by two elements. All these elements were connected by an imposed relationship between degrees of freedom. This model was applied to an interior beam-column connection containing transverse reinforcement. The consideration of bond slip helps the model obtain satisfactory estimation of the dissipated energy. This joint model is also overly complex for the implementation in this study because it involves the simulation of various types of elements and the relationships among all these elements.

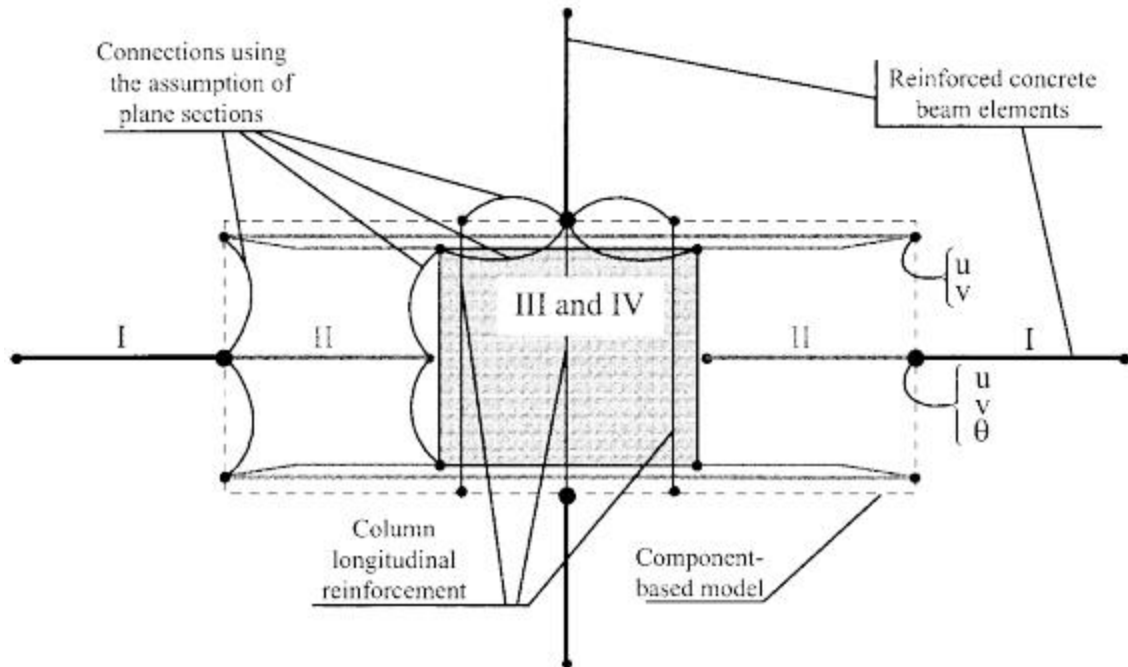


Figure 2.19: Joint model proposed by Fleury et al. (Fleury et al., 2000)

2.4.2.4 Elmersi et al. (2000)

Elmersi et al. proposed a 12-node multi-component model to represent the beam-column joint response (see Figure 2.20a). The joint element employs a fixed, smeared-crack concrete constitutive model for the normal stress function and the shear stress function. This joint element is connected to beams and columns with ten transitional nodes representing the plastic hinge regions in the beams and the columns. The beams and columns were modeled with elastic beam line elements, and the flexural reinforcement was modeled with inelastic truss elements. Contact elements connecting the joint nodes and the transition nodes were used to model the bond slip effects (see Figure 2.20b). The bond slip material model was a modified version based on the Eligenhausen et al. (1983) model. This analytical model was verified against the experimental data from Viwathanatepa et al. (1979). The joint element demonstrated good correlation between the predictions and experimental data of two interior beam-column subassemblies in terms of strength and bond slip deformations. However, this model is relatively complex and may require significant analysis time for large frames.

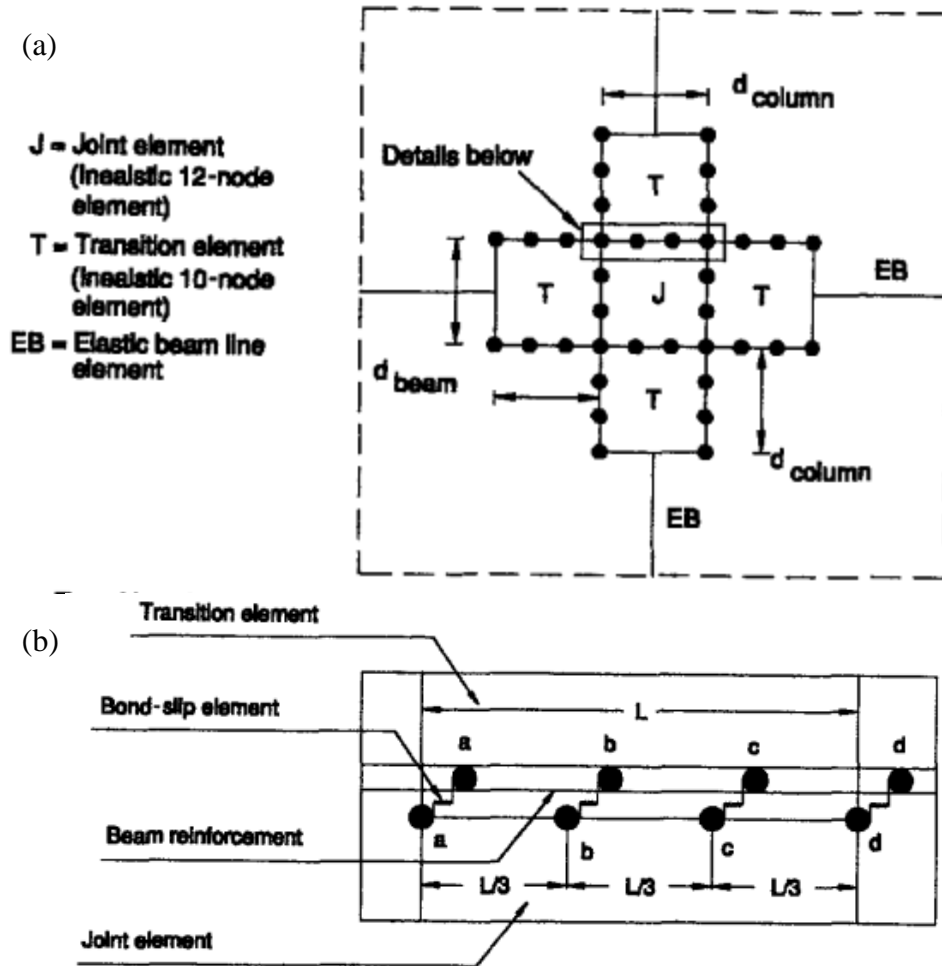


Figure 2.20: Joint model proposed by Elmorsi et al.: (a) proposed element and (b) details of the bond slip element (Elmorsi et al., 2000)

2.4.2.5 Shiohara (2004)

Shiohara presented the concept of quadruple flexural resistance in beam-column joints (see Figure 2.21). He proposed that shear deformation in the connection was not uniformly distributed and it involved the rotation of four triangular concrete segments because of crack opening and closing. The segments also provided moment resistance and shear resistance in the joint. There are two sets of critical deformation modes in this model. The “B-Mode” considers failure at the interface between the joint and the members framing into the joint, while the “J-Mode” considers joint failure with critical sections on the two diagonal lines. Shiohara’s theory provided a different way of idealizing joint behavior. However, this model is more suitable for

hand calculations rather than software implementation. In addition, verification studies are not available for this model.

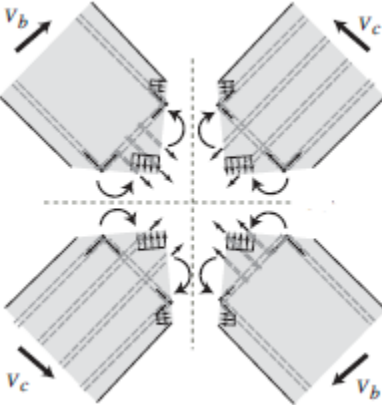


Figure 2.21: Joint model proposed by Shiohara (Shiohara, 2004)

CHAPTER 3

IMPLEMENTED JOINT ELEMENT MODEL

3.1 Chapter Layout

After review of the current state-of-the-art for the modeling of interior beam-column joints of reinforced concrete frame structures, the model proposed by Mitra and Lowes (2007) was selected to be implemented in a previously-developed global frame analysis procedure. This chapter will introduce the theoretical principles and mathematical formulation of the joint element model implemented.

Mitra and Lowes modified and improved the model proposed by Lowes and Altoontash (2003). This component model is capable of capturing bond slip response and joint shear actions in the joint region. Although the model is applicable to frames subjected to reversed cyclic loading, this chapter, and this study, focuses on the monotonic response as a foundation to understand the performance of the implementation of this model. The chapter starts with an introduction to the joint element formulation, and continues with the modeling of three types of components including bar slip springs, a shear panel component and the interface shear springs. Finally, a summary of the computation schemes to simulate the joint response under monotonic loading is provided at the end of the chapter.

3.2 Joint Element Formulation

The implemented beam-column joint model adopts the model proposed by Mitra and Lowes (2007), which was modified and improved based on the model proposed by Lowes and Altoontash (2003). This is a four node, thirteen degree-of-freedom component model that consists of eight zero-length bar slip springs which simulate the strength and stiffness loss of bond between concrete and reinforcing bars, four interface shear springs which simulate the shear transfer from beams and columns to the joint, and a panel element which simulate shear deformation in the joint region (see Figure 3.1). This model represents the inelastic actions

taking place in joints including mechanisms of joint core shear resistance and bond slip response. Although the joint element represents actions in an interior joint, the formulation is also applicable to exterior joints and knee joints with some modifications, which are not discussed in detail in the original study. Mitra and Lowes evaluated this model by comparing simulated and observed responses over 57 previous experimental investigations of interior joints consisting of 52 specimens with transverse reinforcement and 5 specimens without transverse reinforcement. They concluded that the model provided good results in terms of the failure mechanism, stiffness of the overall structure, maximum strength, drift at maximum strength and the pinching ratio. This model was found suitable for the implementation into the global frame analysis procedure of VecTor5 given that the required input for the local joint element is already calculated by the global procedure.

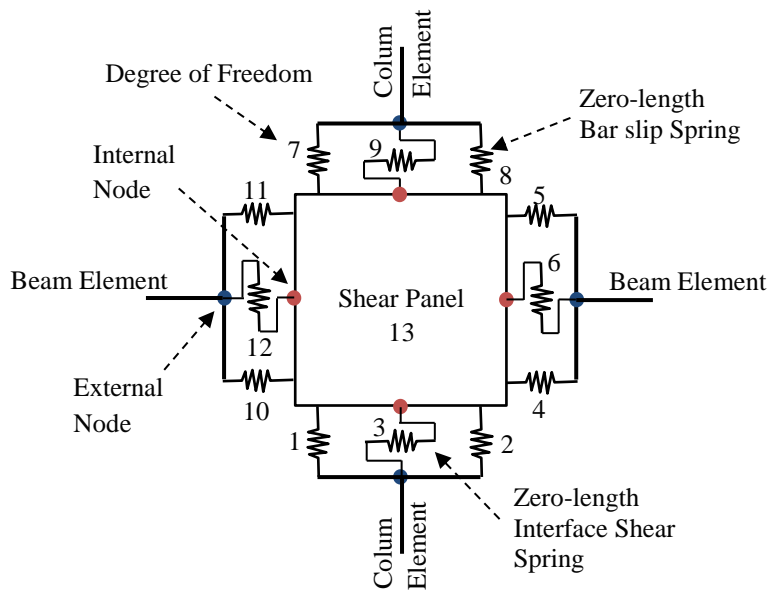


Figure 3.1: Implemented interior beam-column joint model (Mitra and Lowes, 2007)

The solution of this model requires finding component deformations and the corresponding material state of the joint element. The joint element is formulated based on compatibility, equilibrium and constitutive relationships. Compatibility of the element requires the four external nodal displacements to be compatible with the thirteen component deformations. Equilibrium of the element needs to be satisfied at four external and four internal nodes. Constitutive relationships, which consist of a bond slip response and a joint shear response, relate the

component deformations to the component forces. A representation of the displacement, deformation and force variables is illustrated in Figure 3.2.

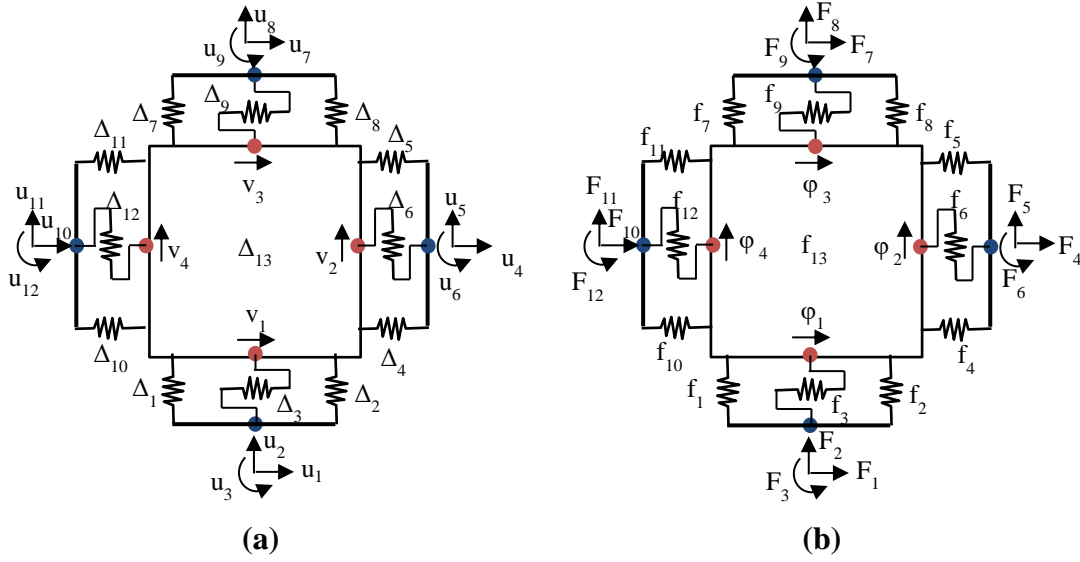


Figure 3.2: Definition of displacements, deformations and forces in the model: **(a)** external displacements and component deformations and **(b)** external forces and component forces

Deformation of the joint element components is defined by the external nodal displacements. A positive deformation of the bar slip component is associated with a tensile force applied to the bars. A positive shear deformation of the panel component is associated with the positive shear forces at the internal nodes in the joint core. A positive deformation of the interface shear component is associated with the positive external shear displacement. The twelve external displacements and rotations, u_i , are converted to thirteen component deformations, Δ_i , using the following equations proposed by Mitra and Lowes:

$$\Delta_1 = -u_2 + \frac{\hat{w}}{2}u_3 + \frac{\hat{w}}{2}\left(\frac{v_4 - v_2}{w}\right) + \frac{v_4 + v_2}{2} \quad (3.1a)$$

$$\Delta_2 = -u_2 - \frac{\hat{w}}{2}u_3 + \frac{\hat{w}}{2}\left(\frac{v_2 - v_4}{w}\right) + \frac{v_4 + v_2}{2} \quad (3.1b)$$

$$\Delta_3 = u_1 - v_1 \quad (3.1c)$$

$$\Delta_4 = u_4 + \frac{\hat{h}}{2}u_6 - \frac{\hat{h}}{2}\left(\frac{v_1 - v_3}{h}\right) - \frac{v_1 + v_3}{2} \quad (3.1d)$$

$$\Delta_5 = u_4 - \frac{\hat{h}}{2} u_6 - \frac{\hat{h}}{2} \left(\frac{v_3 - v_1}{h} \right) - \frac{v_1 + v_3}{2} \quad (3.1e)$$

$$\Delta_6 = u_5 - v_2 \quad (3.1f)$$

$$\Delta_7 = u_8 - \frac{\hat{w}}{2} u_9 + \frac{\hat{w}}{2} \left(\frac{v_2 - v_4}{w} \right) - \frac{v_2 + v_4}{2} \quad (3.1g)$$

$$\Delta_8 = u_8 + \frac{\hat{w}}{2} u_9 - \frac{\hat{w}}{2} \left(\frac{v_2 - v_4}{w} \right) - \frac{v_2 + v_4}{2} \quad (3.1h)$$

$$\Delta_9 = u_7 - v_3 \quad (3.1i)$$

$$\Delta_{10} = -u_{10} - \frac{\hat{h}}{2} u_{12} + \frac{\hat{h}}{2} \left(\frac{v_1 - v_3}{h} \right) + \frac{v_1 + v_3}{2} \quad (3.1j)$$

$$\Delta_{11} = -u_{10} + \frac{\hat{h}}{2} u_{12} - \frac{\hat{h}}{2} \left(\frac{v_1 - v_3}{h} \right) + \frac{v_1 + v_3}{2} \quad (3.1k)$$

$$\Delta_{12} = u_{11} - v_4 \quad (3.1l)$$

$$\Delta_{13} = -\frac{v_1}{h} + \frac{v_2}{w} + \frac{v_3}{h} - \frac{v_4}{w} \quad (3.1m)$$

where v is the internal nodal displacement, h is the height of the joint, w is the width of the joint, \hat{h} is the distance between the bar slip springs on the beam side, and \hat{w} is the distance between the bar slip springs on the column side. In the Lowes and Altoontash model, the width and the height are used instead of the distances between the bar slip springs. This modification is made in the Mitra and Lowes model to improve the simulation of the bar slip spring force demands. The thirteen equations can also be written in a matrix representation as follows:

$$[\Delta_{13 \times 1}] = [A_{13 \times 16}] \begin{bmatrix} u_{12 \times 1} \\ v_{4 \times 1} \end{bmatrix} \quad (3.2)$$

where A is the transformation matrix that converts the nodal displacements to component deformations. Figure 3.3 illustrates the expanded matrix formulation of this equation.

Similarly, the external and internal nodal resultants are computed from the component forces by imposing the equilibrium conditions on the four external and four internal nodes. The material state of the shear panel component, which is assumed to deform only in shear, implies that the internal nodal resultants equal to zero. The equilibrium equations proposed by Mitra and Lowes are listed as follows:

$$\begin{bmatrix} \Delta_1 \\ \Delta_2 \\ \Delta_3 \\ \Delta_4 \\ \Delta_5 \\ \Delta_6 \\ \Delta_7 \\ \Delta_8 \\ \Delta_9 \\ \Delta_{10} \\ \Delta_{11} \\ \Delta_{12} \\ \Delta_{13} \end{bmatrix} = \begin{bmatrix} 0 & -1 & \frac{\hat{w}}{2} & 0 & 0 & 0 & 0 & 0 & 0 & 0 & 0 & 0 & 0 & \frac{(w-\hat{w})}{2w} & 0 & \frac{(w+\hat{w})}{2w} \\ 0 & -1 & -\frac{\hat{w}}{2} & 0 & 0 & 0 & 0 & 0 & 0 & 0 & 0 & 0 & 0 & \frac{(w+\hat{w})}{2w} & 0 & \frac{(w-\hat{w})}{2w} \\ 1 & 0 & 0 & 0 & 0 & 0 & 0 & 0 & 0 & 0 & 0 & 0 & -1 & 0 & 0 & 0 \\ 0 & 0 & 0 & 1 & 0 & \frac{\hat{h}}{2} & 0 & 0 & 0 & 0 & 0 & 0 & -\frac{(h+\hat{h})}{2h} & 0 & -\frac{(h-\hat{h})}{2h} & 0 \\ 0 & 0 & 0 & 1 & 0 & -\frac{\hat{h}}{2} & 0 & 0 & 0 & 0 & 0 & 0 & -\frac{(h-\hat{h})}{2h} & 0 & -\frac{(h+\hat{h})}{2h} & 0 \\ 0 & 0 & 0 & 0 & 1 & 0 & 0 & 0 & 0 & 0 & 0 & 0 & 0 & -1 & 0 & 0 \\ 0 & 0 & 0 & 0 & 0 & 0 & 0 & 1 & -\frac{\hat{w}}{2} & 0 & 0 & 0 & 0 & -\frac{(w-\hat{w})}{2w} & 0 & -\frac{(w+\hat{w})}{2w} \\ 0 & 0 & 0 & 0 & 0 & 0 & 0 & 1 & \frac{\hat{w}}{2} & 0 & 0 & 0 & 0 & -\frac{(w+\hat{w})}{2w} & 0 & -\frac{(w-\hat{w})}{2w} \\ 0 & 0 & 0 & 0 & 0 & 0 & 1 & 0 & 0 & 0 & 0 & 0 & 0 & 0 & -1 & 0 \\ 0 & 0 & 0 & 0 & 0 & 0 & 0 & 0 & 0 & -1 & 0 & -\frac{\hat{h}}{2} & \frac{(h+\hat{h})}{2h} & 0 & \frac{(h-\hat{h})}{2h} & 0 \\ 0 & 0 & 0 & 0 & 0 & 0 & 0 & 0 & 0 & -1 & 0 & \frac{\hat{h}}{2} & \frac{(h-\hat{h})}{2h} & 0 & \frac{(h+\hat{h})}{2h} & 0 \\ 0 & 0 & 0 & 0 & 0 & 0 & 0 & 0 & 0 & 1 & 0 & 0 & 0 & 0 & 0 & -1 \\ 0 & 0 & 0 & 0 & 0 & 0 & 0 & 0 & 0 & 0 & 0 & 0 & -\frac{1}{h} & \frac{1}{w} & \frac{1}{h} & -\frac{1}{w} \end{bmatrix} \cdot \begin{bmatrix} u_1 \\ u_2 \\ u_3 \\ u_4 \\ u_5 \\ u_6 \\ u_7 \\ u_8 \\ u_9 \\ u_{10} \\ u_{11} \\ u_{12} \\ v_1 \\ v_2 \\ v_3 \\ v_4 \end{bmatrix}$$

Figure 3.3: Compatibility equations of the implemented joint model (Mitra and Lowes, 2007)

$$F_1 = f_3 \quad (3.3a)$$

$$F_2 = -f_1 - f_2 \quad (3.3b)$$

$$F_3 = \frac{\hat{w}}{2}(f_2 - f_1) \quad (3.3c)$$

$$F_4 = f_4 + f_5 \quad (3.3d)$$

$$F_5 = f_6 \quad (3.3e)$$

$$F_6 = \frac{\hat{h}}{2}(f_4 - f_5) \quad (3.3f)$$

$$F_7 = f_9 \quad (3.3g)$$

$$F_8 = f_7 + f_8 \quad (3.3h)$$

$$F_9 = \frac{\hat{w}}{2}(f_8 - f_7) \quad (3.3i)$$

$$F_{10} = -f_{10} - f_{11} \quad (3.3j)$$

$$F_{11} = f_{12} \quad (3.3k)$$

$$F_{12} = \frac{\hat{h}}{2}(f_{11} - f_{10}) \quad (3.3l)$$

$$\varphi_1 = -f_3 - \frac{1}{2}\left(1 + \frac{\hat{h}}{h}\right)(f_4 - f_{10}) - \frac{1}{2}\left(1 - \frac{\hat{h}}{h}\right)(f_5 - f_{11}) - \frac{f_{13}}{h} \quad (3.3m)$$

$$\varphi_2 = -f_6 - \frac{1}{2}\left(1 + \frac{\hat{w}}{w}\right)(f_8 - f_2) - \frac{1}{2}\left(1 - \frac{\hat{w}}{w}\right)(f_7 - f_1) + \frac{f_{13}}{w} \quad (3.3n)$$

$$\varphi_3 = -f_9 - \frac{1}{2}\left(1 + \frac{\hat{h}}{h}\right)(f_5 - f_{11}) - \frac{1}{2}\left(1 - \frac{\hat{h}}{h}\right)(f_4 - f_{10}) + \frac{f_{13}}{h} \quad (3.3o)$$

$$\varphi_4 = -f_{12} - \frac{1}{2}\left(1 + \frac{\hat{w}}{w}\right)(f_7 - f_1) - \frac{1}{2}\left(1 - \frac{\hat{w}}{w}\right)(f_8 - f_2) - \frac{f_{13}}{w} \quad (3.3p)$$

where F_i is the external nodal resultant, f_i is the component force and φ_i is the interior nodal resultant which equals to zero at the equilibrium state. The sixteen equations can also be written in a matrix representation as follows:

$$\begin{bmatrix} F_{12 \times 1} \\ \varphi_{4 \times 1} \end{bmatrix} = [A^T_{16 \times 13}] [f_{13 \times 1}] \quad (3.4)$$

where A^T is the transposed transformation matrix that converts the component forces to nodal resultants. A vector of external nodal resultants is obtained in this process. The derivative of the resultants with respect to the external nodal displacements, also known as the element tangent matrix, is calculated as follows:

$$[K_{elem\ 16 \times 16}] = [A^T_{16 \times 13}] [k_{13 \times 13}] [A_{13 \times 16}] \text{ where } k_i = \frac{df_i}{d\Delta_i}, i = 1, 2, \dots, 13 \quad (3.5)$$

In this equation, K_{elem} is the element tangent matrix, A is the transformation matrix and k is a diagonal matrix of thirteen component tangents.

3.3 Modeling Bond Slip Response

Modeling of bond slip effect is crucial for the simulation of inelastic beam-column joint response. During an earthquake event, tensile stress at one end of a reinforcing bar may penetrate into the joint region. This causes significant elongation of the reinforcement. Furthermore, the bond

between the reinforcing steel and concrete may deteriorate and cause additional deformation. The combination of these two effects is referred to as “strain penetration”. The bar slip springs in the joint element are utilized to represent this action.

The bond slip model developed by Mitra and Lowes was based on the experimental data of Elighausen et al. (1983) and four assumptions about the bond stress distribution (see Figure 3.4) including: (1) bond slip is defined as the relative movement of the reinforcing steel with respect to the interface of the joint; (2) the model only considers the contribution from the elongation of the reinforcement; (3) the reinforcing bar is assumed to have zero slip at zero bar stress; and (4) the bond stress is assumed to be uniform prior to yielding of the reinforcing steel and piecewise uniform after yielding.

The bar stress and slip model was derived based on the equilibrium condition of the force transferred from the concrete to the reinforcing steel and the force carried by the reinforcing steel, as follows:

$$F_s = f_s \cdot \frac{\pi d_b^2}{4} = \mu \pi d_b l_d \quad (3.6)$$

where F_s is the force carried by the reinforcing steel, f_s is the stress in the reinforcing steel, d_b is the diameter of the bar, μ is the bond stress, and l_d is the development length of the bar to transfer the force through bond stress. The reinforcing steel material model is assumed to be plastic with elastic hardening. By writing the equilibrium equation in terms of strain in the reinforcing steel and integrating the strain from the anchorage point to the joint interface, the relationship between the bar stress and slip is obtained. The model proposed by Mitra and Lowes is summarized below.

$$\Delta_{slip} = 2 \frac{\tau_E}{E} \frac{l_s^2}{d_b} \quad \text{for } f_s < f_y \quad (3.7a)$$

$$\Delta_{slip} = 2 \frac{\tau_E}{E} \frac{l_e^2}{d_b} + \frac{f_y l_y}{E} + 2 \frac{\tau_Y}{E_{sh}} \frac{l_y^2}{d_b} \quad \text{for } f_s \geq f_y \quad (3.7b)$$

$$\text{where } l_{fs} = \frac{f_s A_b}{\tau_{ET} \pi d_b} \quad (3.7c)$$

$$l_e = \frac{f_y A_b}{\tau_{ET} \pi d_b} \quad (3.7d)$$

$$l_y = \frac{f_s - f_y A_b}{\tau_{YT} \pi d_b} \quad (3.7e)$$

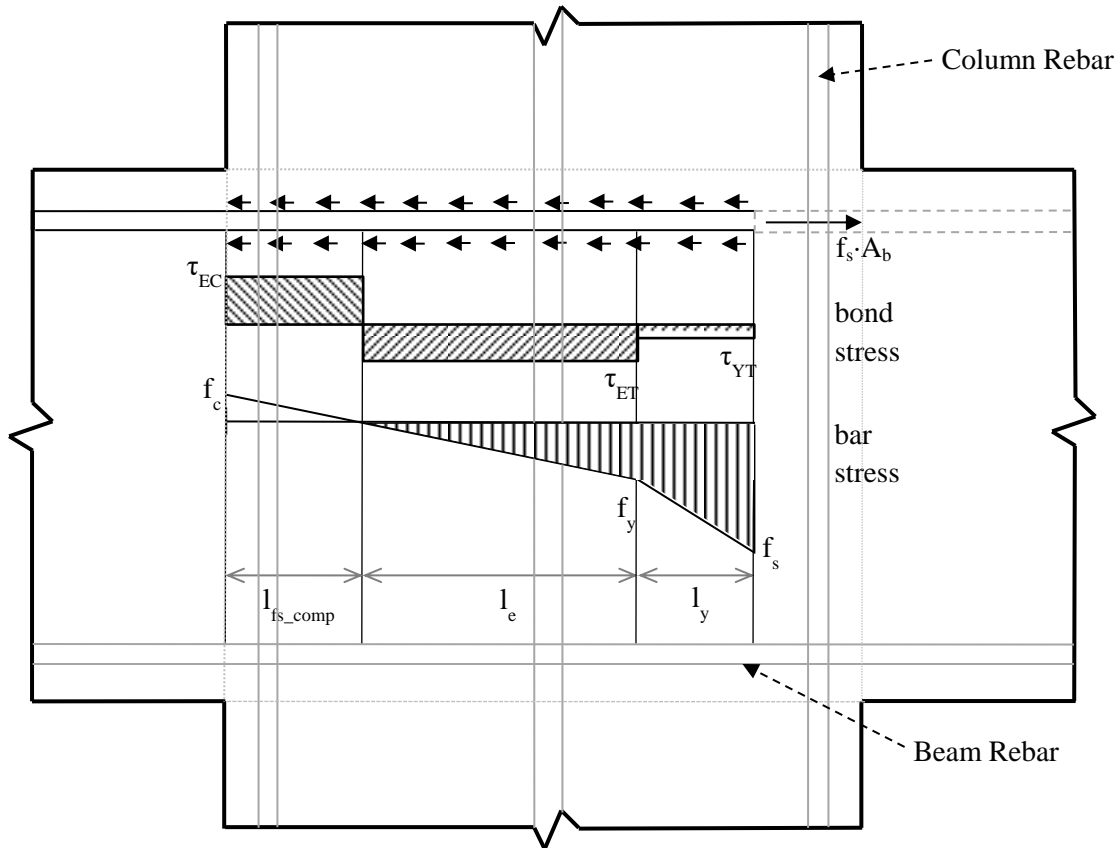


Figure 3.4: Bond stress and bar stress distribution along a reinforcing bar anchored in a joint

In this set of equations, Δ_{slip} is the slip of the reinforcing steel at the joint interface, f_s is the stress in the reinforcing steel at the interface of the joint, f_y is the yield stress of steel, E is the modulus of elasticity of steel, E_{sh} is the hardening modulus of steel, d_b is the nominal bar diameter, A_b is the nominal bar area, τ_E is the bond stress of elastic steel, and τ_Y is the bond stress of post-yielding steel. Average bond stress values for various rebar conditions are listed in Table 3.1. Figure 3.5 shows the proposed bar stress versus slip model, the model from Sezen and Moehle (2003), and the experimental data provided by Viwathanatepa et al. (1979).

Table 3.1: Average bond stress for various rebar conditions

Rebar Condition	Average Bond Stress in MPa (f_c in MPa)
Tension, Elastic Rebar	$\tau_{ET} = 1.8\sqrt{f_c}$
Tension, Post-Yielding Rebar	$\tau_{YT} = 0.4\sqrt{f_c}$ to $0.05\sqrt{f_c}$
Compression, Elastic Rebar	$\tau_{EC} = 2.2\sqrt{f_c}$
Compression, Post-Yielding Rebar	$\tau_{YC} = 3.6\sqrt{f_c}$

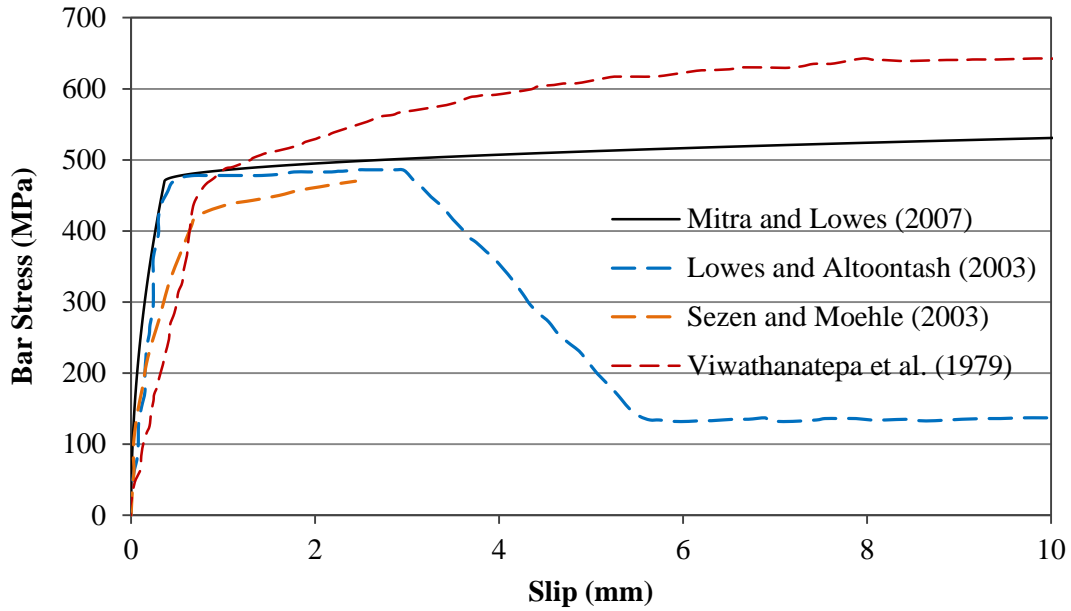


Figure 3.5: Bar stress versus slip relationship from various studies and experiments

The bar stress versus slip model for monotonic loading presented in Mitra and Lowes is similar to that presented in Lowes and Altoontash. The only difference is the initiation of the strength loss in the response. The Lowes and Altoontash model used a slip limit of 3.0 mm, which was found to be too conservative. The Mitra and Lowes delayed the initiation of the strength loss until the reinforcing steel reaches its ultimate strength. On the other hand, this model also improved the reversed cyclic response of the bar slip springs. Mitra and Lowes defined the unloading and reloading path and a damage model to represent the influence of load history on the response. These parameters are crucial for successful modeling of the reversed cyclic response.

The bar stress is finally related to the force in bar slip springs to complete the calculation. Determination of the magnitude and location of the bar slip springs requires sectional analysis of the beam and column members framing into the joint at nominal flexural strength. The computation of nominal flexural strength follows the criteria of ACI Committee 318 (2008). The ACI code was employed over the CSA code because the study was conducted in the United States. It is expected that the CSA criteria will produce similar results because the CSA criteria are similar to the ACI criteria. According to the criteria, a linear strain distribution is assumed across the section of a member with the top concrete strain set at -0.003. The compressive stress block approach is employed to determine the compressive force carried by the concrete, and tension stiffening is neglected for simplicity. Using the ACI criteria, the concrete and steel compression resultants are defined as follows:

$$C_c = 0.85f'_c\beta cw \quad (3.8)$$

$$C'_s = f'_s A'_s = 0.003 \frac{c-d'}{c} E_s A'_s \quad (3.9)$$

where C_c is the total compressive force carried by the concrete, C'_s is the total compressive force carried by the reinforcing steel, f'_c is the concrete compressive strength, c is the depth of neutral axis, d' is the depth of the reinforcing steel carrying compression, E_s is the modulus of elasticity of steel, and A'_s is the area of the reinforcing steel carrying compression. The compressive and tensile resultants, or bar slip spring forces, are defined as a function of the bar stress, given by:

$$C_{resultant} = C'_s + C_c = f'_s A'_s \left\{ 1 + \frac{0.85f'_c dw}{E_s A'_s} \frac{2(1-j)}{0.003\beta \left[1 - \frac{d'}{d} \frac{\beta}{2(1-j)} \right]} \right\} \quad (3.10)$$

$$T_{resultant} = f_s A_s \quad (3.11)$$

where j is a constant taken as 0.85 for beams and 0.75 for columns, β is the depth coefficient of the stress block, f'_s is the bar stress of the reinforcing steel carrying compression, f_s is the bar stress of the reinforcing steel carrying tension, and A_s is the area of the reinforcing steel carrying tension. The location of bar slip springs is identical to the location of the compression and tension resultants. Figure 3.6 illustrates the strain distribution, stress distribution and forces acting on a frame member at the nominal flexural strength.

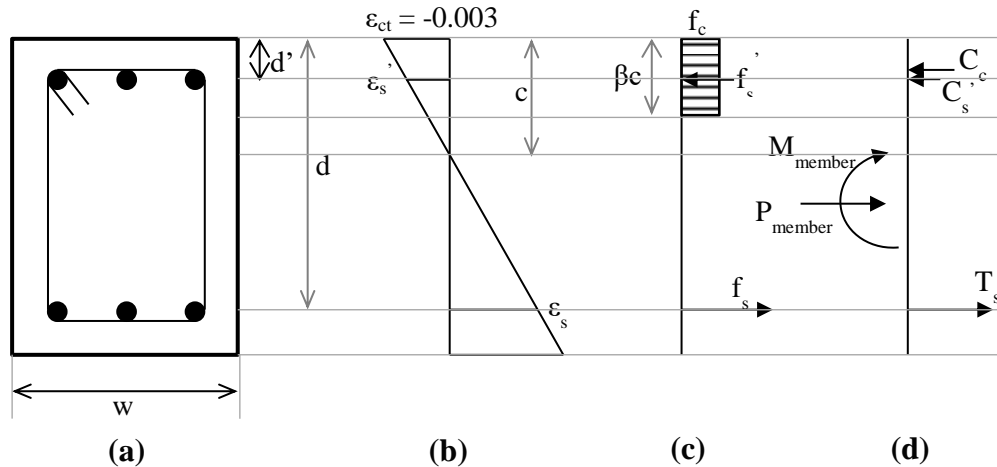


Figure 3.6: Sectional analysis of a frame member at the nominal flexural strength: (a) member cross-section, (b) strain distribution, (c) stress distribution, and (d) forces on the member

3.4 Modeling Joint Shear Response

Determination of the shear panel response requires the relationship between the shear-equivalent moment (i.e. moment due to shear force couple acting on the joint panel) and panel shear deformation. In the Lowes and Altoontash model, the Modified Compression Field Theory was employed to calibrate the joint shear response model as a function of the concrete material properties, the reinforcing steel material properties, and the reinforcing ratio in the vertical and horizontal directions. The subsequent study by Mitra and Lowes suggested that the MCFT-based joint shear models underestimate the strength of joints with low transverse reinforcement ratios and overestimate the strength of joints with high transverse reinforcement ratios. In the Mitra and Lowes model, joint shear is transferred via a concrete compression strut as shown in Figure 3.7. The concrete strut is confined by the longitudinal reinforcing steel in the joint due to the beam and column members framing into the joint, and the transverse reinforcement in the joint region. The stress-strain model proposed by Mander et al. (1988) for the uniaxially confined concrete is employed to determine the stress in the strut. Because of the confinement, the stress obtained using the model is generally greater than that obtained from the classic parabolic stress-strain model for joints with transverse reinforcement. Mitra and Lowes' study does not provide the details of the application of this stress-strain model.

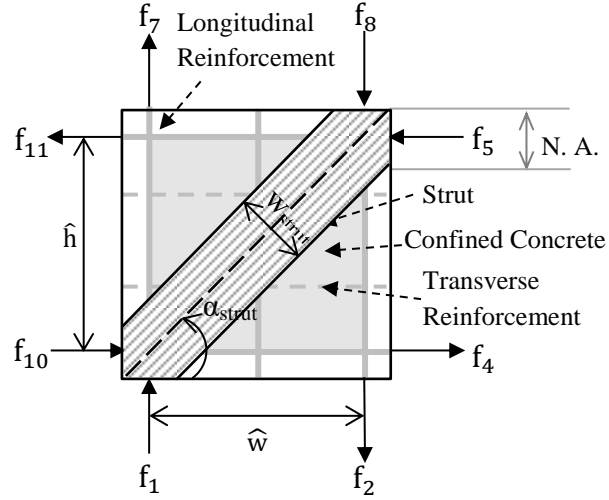


Figure 3.7: Idealized diagonal concrete compression strut model

The compressive stress in the strut obtained from the stress-strain model is then adjusted to account for cracking due to the tensile straining in the orthogonal direction of the strut, or the “compression softening” effect. Mitra and Lowes compared five different compression softening models. The Mitra and Lowes model was found to provide a better fit than others for joints with and without transverse reinforcement. The reduction factor for joints with transverse reinforcement was defined by Mitra and Lowes as:

$$\frac{f_{cstrut}}{f_{cMander}} = 3.62 \left| \frac{\varepsilon_t}{\varepsilon_{cc}} \right|^2 - 2.82 \left| \frac{\varepsilon_t}{\varepsilon_{cc}} \right| + 1 \quad \text{for} \quad \left| \frac{\varepsilon_t}{\varepsilon_{cc}} \right| < 0.39 \quad (3.12a)$$

$$\frac{f_{cstrut}}{f_{cMander}} = 0.45 \quad \text{for} \quad \left| \frac{\varepsilon_t}{\varepsilon_{cc}} \right| \geq 0.39 \quad (3.12b)$$

For joints without transverse reinforcement, the reduction factor was defined as follows:

$$\frac{f_{cstrut}}{f_{cMander}} = 0.36 \left| \frac{\varepsilon_t}{\varepsilon_{cc}} \right|^2 - 0.60 \left| \frac{\varepsilon_t}{\varepsilon_{cc}} \right| + 1 \quad \text{for} \quad \left| \frac{\varepsilon_t}{\varepsilon_{cc}} \right| < 0.83 \quad (3.13a)$$

$$\frac{f_{cstrut}}{f_{cMander}} = 0.75 \quad \text{for} \quad \left| \frac{\varepsilon_t}{\varepsilon_{cc}} \right| \geq 0.83 \quad (3.13b)$$

where f_{cstrut} is the compressive stress in the strut after the reduction, $f_{cMander}$ is the compressive stress in the strut considering the concrete confinement; ε_t is the principal tensile strain of concrete in the shear panel; and ε_{cc} is the strain of the confined concrete at the peak stress.

Figure 3.8 presents the reduction functions for the concrete compression strength according to the five compression softening models. For joints with transverse reinforcement, the reduction factor obtained from the proposed softening model at low principal tensile strain is significantly lower than that given by other models.

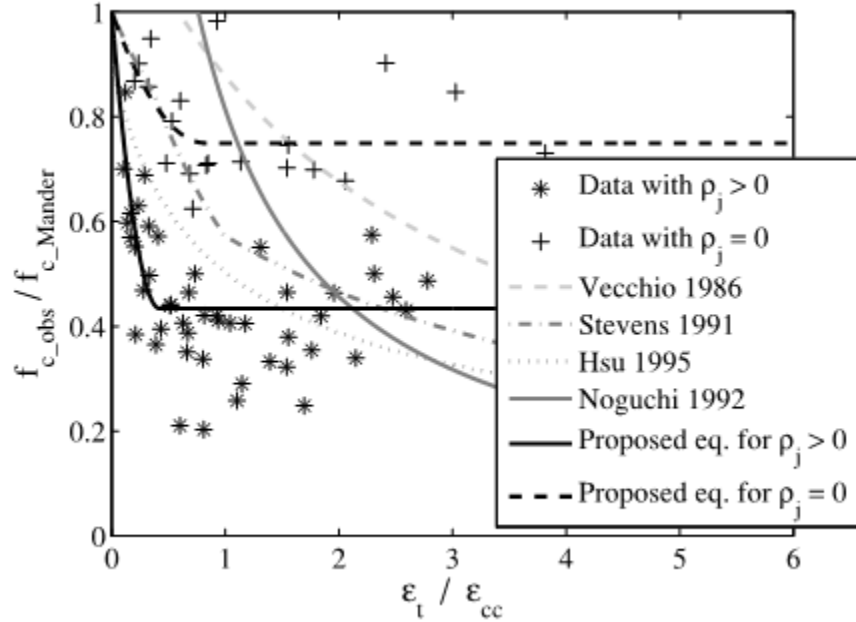


Figure 3.8: Reduction equations to the concrete compression strength (Mitra and Lowes, 2007)

After the strut stress is obtained, the panel shear stress is the horizontal (or vertical) component of the strut stress, obtained according to the following equation:

$$\tau_{strut} = f_{c_strut} \frac{w_{strut} \cos \alpha_{strut}}{w} = f_{c_strut} \frac{w_{strut} \sin \alpha_{strut}}{h} \quad (3.14)$$

where τ_{strut} is the shear stress acting on the panel, w_{strut} is the in-plane width of the strut, α_{strut} is the angle of inclination of the strut, and w and h are the in-plane width and height of the shear panel, respectively. Finally, the obtained strut stress is multiplied by the volume of the shear panel to complete the calculation for the shear-equivalent moment (f_{13}) acting on the panel component.

3.5 Modeling of Interface Shear Response

Under severe earthquake loading, flexural cracks may form at the perimeter of the joint cores and they may widen with subsequent load cycles. These cracks open and close with load cycles. As cracks widen, the shear force that can be transferred across the crack surface also decreases. Despite the use of interface shear springs in the implemented model, they are not very effective for capturing interface shear response due to lack of experimental data for the simulation of this response. The Lowes and Altoontash study used a calibrated model for interface shear components based on the results of research by Walraven (1981, 1994). In this model, the interface shear stress is a function of the bond slip and crack width on the interface of the joint as presented in Figure 3.9. The implementation of this component is complex because it involves consideration of many factors and parameters, especially for the joints subjected to reversed cyclic loading. As a result, interface shear springs were defined to be stiff and elastic in the Mitra and Lowes model. The simplification of modeling of interface shear response was not further elaborated in their study.

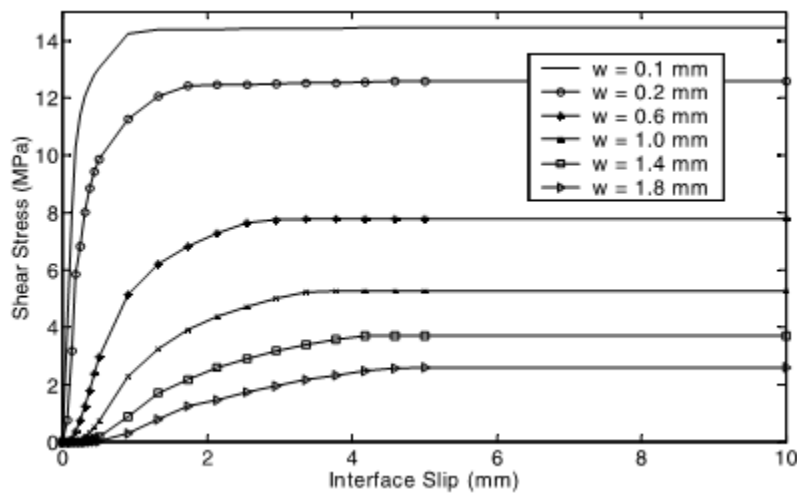


Figure 3.9: Envelope of the shear stress versus slip response for the interface shear springs (Lowes and Altoontash, 2003)

3.6 Computation Schemes

The computation schemes to simulate joint response under monotonic loading are explained in Section 4.8 of Mitra (2008). The following discussion is a summary of the procedure with the modifications aimed to fit it into the global frame analysis procedure of VecTor5. Given the concrete and reinforcement properties, the load application details, and the geometry of an interior joint, the following general procedure is carried out to determine the local response of an interior beam-column joint:

1. From the output of the global analysis procedure, determine the coordinates of four external nodes and the magnitudes of the four external shear forces at the perimeter of the joint. These force and displacement parameters are input for the local joint element calculation.
2. Complete the sectional analysis at the nominal flexural strength for beam and column elements that frame into the joint. It is assumed that beams carry zero axial loads while columns carry axial load associated with gravity loading.
3. From the sectional analysis at the nominal flexural strength, determine: (1) the distance between the compression and tension resultants, (2) the neutral axis depth, and (3) the ratio of the compressive force carried by the longitudinal reinforcing steel to the total compressive force carried by the section. This ratio is assumed to be constant for all load stages.
4. From the geometry of the joint core, determine (1) joint element transformation matrix, $[A_{13 \times 16}]$, (2) the width of the concrete compression strut, w_{strut} , and (3) the angle of inclination of the concrete compression strut, α_{strut} .
5. Interface shear springs are assumed to remain stiff and elastic.
6. Determine the bar slip spring response using the bar stress versus slip model proposed by Mitra and Lowes.
7. Determine the concrete compression strut response using the Mander et al. model for the confined concrete and the concrete strength reduction factor considering compression softening.
8. Check whether the local convergence criteria are satisfied (i.e. the four interior nodal resultants are equal to zero). If not, repeat steps 5 to 7 with a new set of internal nodal

displacements until the convergence criteria are satisfied. The calculations carried out to determine the new internal nodal displacements will be discussed in detail in Section 4.3.1.

This procedure will be carried out for local analysis of interior beam-column joints subjected to monotonic loading conditions in this study. For joints subjected to reversed cyclic loading, the damage models proposed by Mitra and Lowes must be applied to account for strength and stiffness reductions, which are not performed in this study.

CHAPTER 4

JOINT ELEMENT IMPLEMENTATION IN VECTOR5

4.1 Chapter Layout

The selected interior joint model was implemented in VecTor5, a nonlinear analysis program for two-dimensional reinforced concrete frame structures. The program currently uses semi-rigid end offsets to model joints. This method is not ideal for modeling damage or failure modes involving excessive deformations of joint cores. The essence of the joint element implementation is to replace all members and nodes inside the joint region with a single joint element. It is expected that the implementation will improve the modeling of both local joint response and global frame response.

The chapter starts with a discussion of global frame modeling including an introduction to the global frame analysis procedure. The joint analysis algorithm is then presented along with modifications of the global frame analysis procedure to facilitate the joint implementation. The chapter continues with new guidelines for modeling joints to accommodate the implementation. Finally, the content and interpretation of the joint analysis results in the output files are provided at the end of the chapter.

4.2 Global Frame Modeling

Using semi-rigid end offsets is a common technique of modeling beam-column joints in frame analysis. It is employed to account for increased strengths in joint cores by increasing the stiffness of the joints. This approach may lead to overestimation of joint strength, stiffness and energy dissipation, as well as an underestimation of lateral story drifts. Pinching behavior, which is the loss of stiffness due to damage and interaction of structural components under a large deformation, is also not captured. These inaccuracies will be more severe for frames with older-type joints designed prior to the introduction of modern design codes. An inelastic joint model is needed for analyzing new buildings for performance-based earthquake engineering, and for

analyzing older buildings to identify the existing buildings which are at the risk of collapse during a future earthquake.

Lumped-plasticity and distributed-plasticity models are the two popular methods for the simulation of frame elements. Lumped-plasticity models consider the use of zero-length plastic hinges at the critical locations connected by linear elastic elements. Examples of computer programs that employ this method include *OpenSees*, *RUAUMOKO*, *SAP2000*, and *ZEUS*. Distributed-plasticity models consider material nonlinearity at any element section. Element response is obtained by the numerical integration of the sectional response. This method is more sophisticated and generally more accurate than the lumped-plasticity models. Examples of computer programs that employ this method include *VecTor5*, *IDARC2D* and *Perform3D*.

The Mitra and Lowes joint model has been implemented in OpenSees. OpenSees uses either a lumped-plasticity or a distributed-plasticity model; it is also capable of modeling joints. However, it requires the user to write a code for modeling, and does not provide a graphical user interface or visual representation of the results. As a result, it is mainly used by researchers for special investigations.

An example of a structural analysis program that employs the distributed-plasticity model is *VecTor5*. *VecTor5* (Guner, 2008) is a nonlinear analysis program for two-dimensional reinforced concrete frame structures developed at the University of Toronto. The program was developed based on a predecessor program, *TEMPEST* (Vecchio 1987; Vecchio and Collins 1988) with the ability to capture shear effects and significant second-order mechanisms. *VecTor5* includes a graphical pre-processor (*FormWorks* by Wong et al., 2013) for users to create frame models, and a post-processor (*Janus* by Loya et al., 2016) to visualize analysis results. Previous studies verified this procedure with over 100 experimental specimens and demonstrated that the program was able to accurately simulate the nonlinear behavior of frames. One limitation of *VecTor5* is that it employs semi-rigid end offsets to account for increased strengths in beam-column joint regions (see Figure 4.1). Guner and Vecchio (2010) suggested that the procedure is not suitable for the consideration of damage or failure modes involving excessive deformations of beam-column joint cores. Consequently, the procedure does not capture the joint behavior. As such, it may overestimate the strength, stiffness and energy

dissipation of frames that exhibit significant joint damage (see Figure 1.3). Improvements must be made to enhance the modeling of frames to capture the joint damage.

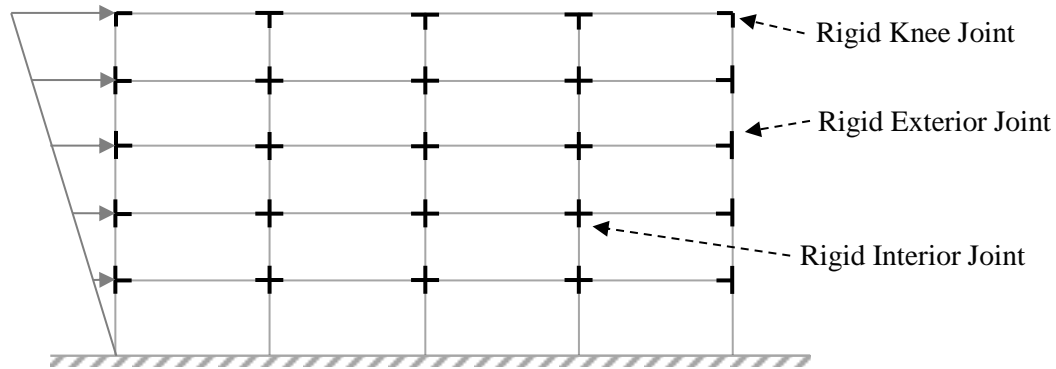


Figure 4.1: Typical frame model in VecTor5

As a step towards the goal of capturing the impact of local joint deformations on the global frame response, the Mitra and Lowes model is implemented in VecTor5 for the consideration of the response of interior joints subjected to monotonic loading. The first step is to understand the basic analysis steps of the global frame analysis procedure. The program divides a frame model into a finite number of members. For each member, a layered (fiber) analysis technique is employed for the nonlinear sectional analysis, as shown in Figure 4.2. Each concrete and steel layer is analyzed individually based on the Disturbed Stress Field Model (DSFM). Figure 4.3 shows a flowchart for global frame analysis of VecTor5 proposed by Guner and Vecchio. Figure 4.4 illustrates the joint element implementation in VecTor5.

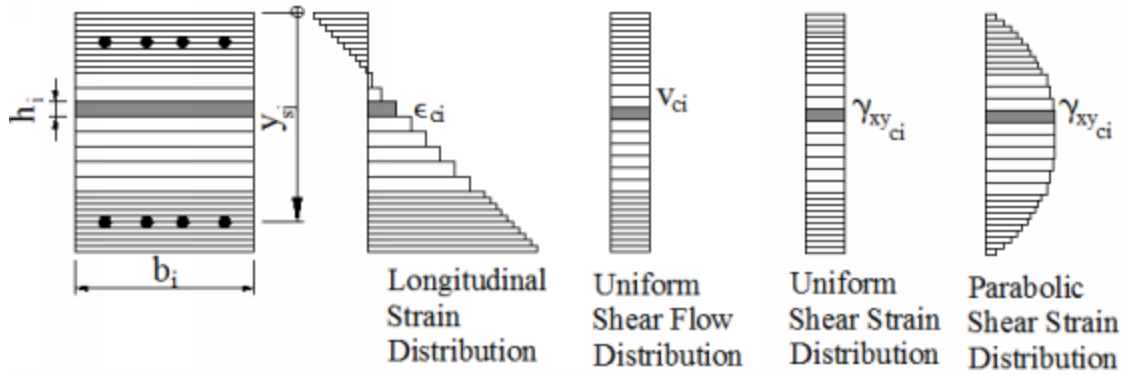


Figure 4.2: Longitudinal and shear strain distributions across sectional depth for a layered analysis (Guner and Vecchio, 2010)

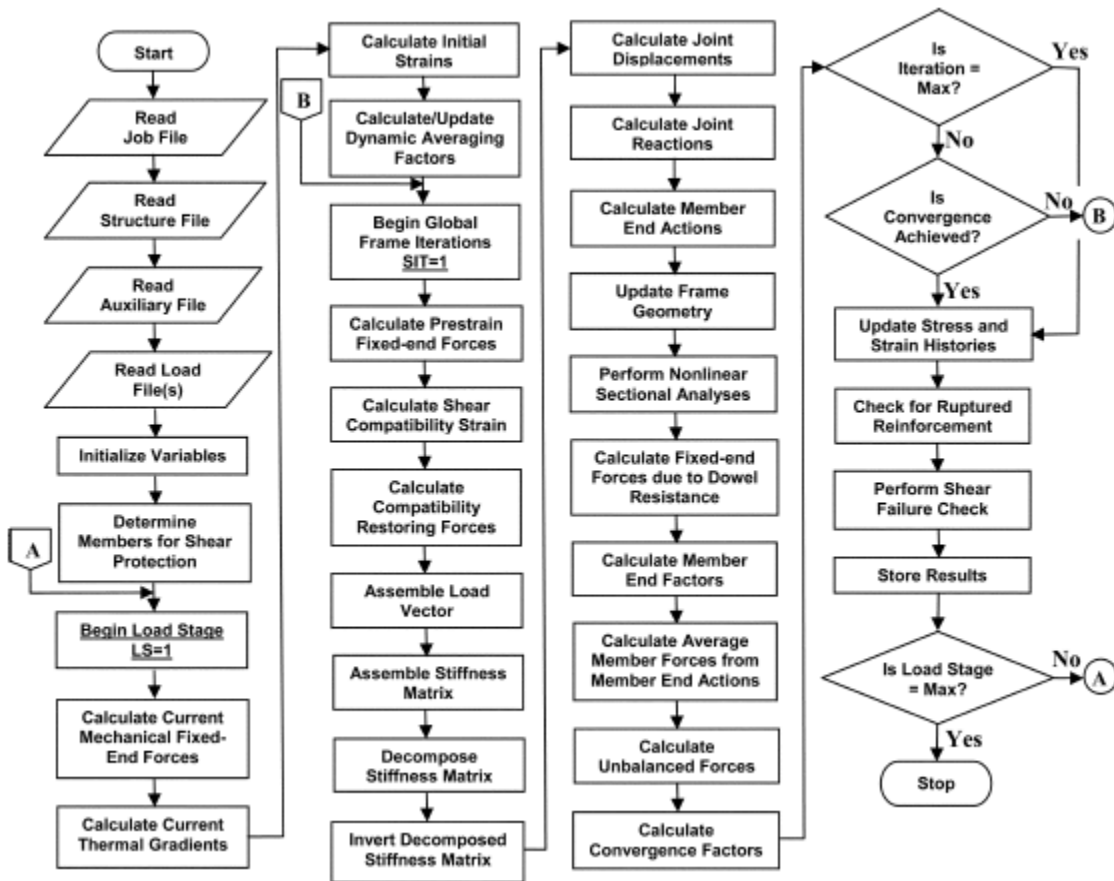


Figure 4.3: Flowchart for the global frame analysis of VecTor5 (Guner and Vecchio, 2010)

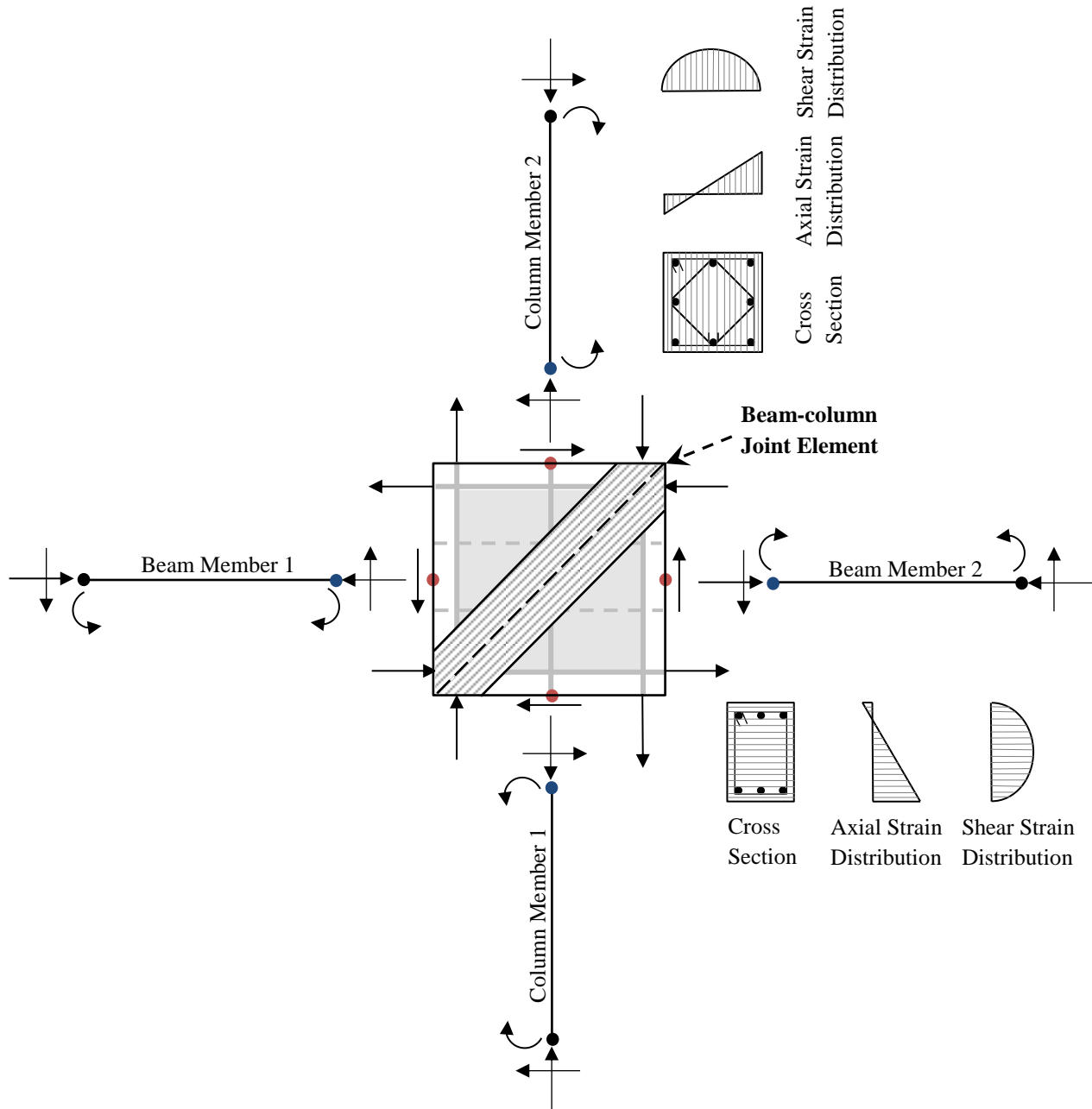


Figure 4.4: Joint element implementation in VecTor5

The global analysis procedure starts with reading four input text files consisting of structure, load, job and auxiliary files. These files define the geometry of the structure, material properties, loading data, analysis parameters, material behavior models and other general parameters required by the program. Then, the load vector and the stiffness matrix are assembled. A linear elastic analysis of the structure is performed to determine nodal displacements, nodal reactions

and member end actions. The geometry of the frame is updated based on the computed nodal displacements. The program continues to determine the axial and shear strain distributions through the depth of each member and performs nonlinear sectional analysis iterations to calculate sectional forces. The unbalanced forces, or the difference between the global and sectional forces, are calculated for each member, and added to the compatibility restoring forces to be applied to the structure in the next iteration. The calculations for the nonlinear sectional analysis are repeated until all unbalanced forces become zero or the number of maximum iteration is reached. Finally, the results obtained for the current load stage are stored in an output text file before proceeding to the next load stage. The implementation of the joint element does not change these basic analysis steps of the global procedure. However, the implementation requires new subroutines for the local joint analysis, as well as modifications of the global analysis procedure.

4.3 Joint Analysis Algorithm

The joint analysis algorithm follows the general solution provided in Lowes and Altoontash (2003). Implementation of the joint element required the addition of three new subroutines into the source files. The local joint element subroutine is the main subroutine that contains the full joint analysis algorithm. This subroutine is called in the main function. The bar slip spring subroutine and the shear panel subroutine are implemented to determine the bond slip response and the joint shear response, respectively. They are called in the local joint element subroutine.

4.3.1 Subroutine: Local Joint Element

The local joint element subroutine was constructed based on the component model proposed by Mitra and Lowes (2007). Details of the model were presented in Chapter 3. Some changes were made to better integrate the joint model into the global algorithm, and several assumptions were made for information that was not provided in detail in Mitra and Lowes (2007).

The algorithm of the subroutine follows the computation schemes suggested in Section 3.6. This iterative solution process includes: (1) obtaining input material properties, geometric properties and other relevant parameters from the global procedure; (2) performing sectional analysis at nominal flexural strength for the beam and column elements that frame into the joint; (3)

determining the transformation matrix and component deformations; (4) determining the resultants or loads on all 13 components; and (5) checking whether the convergence criteria are satisfied or not. Figure 4.5 shows a flowchart of the solution process for the joint element.

Input variables for the joint element subroutine includes: concrete material properties, reinforcing steel material properties, joint geometric properties and other parameters obtained from the global procedure. Table 4.1 provides a list of input variables required by the subroutine. These variables and symbols will be referenced and explained in the following sections.

The input variables categorized as “other parameters” store relevant properties that are required by the joint subroutine. Array *DLIST* stores the translations and rotation of each node for a given load stage, *LS*. External nodal displacements are taken from this array. The member end forces are stored in the *FORCE* matrix. The shear forces acting on the joint and axial load on the joint core in the vertical direction are obtained from this matrix. Integer *JINT* indicates the total number of interior joints in the structure. Matrix *JNTINT* contains node numbers that define an interior joint in the counter-clockwise direction starting from the bottom node. Matrix *JMINT* contains the member numbers of members framing into the joint in the counter-clockwise direction starting from the bottom member, whereas matrix *JNTINTT* contains the member numbers of members in the joint region in the counter-clockwise direction starting from the bottom member. These node and member numbers are used as indices to identify the location and properties of interior joints in the structure. The first member number (i.e. the bottom column member in the joint region) and the second member number (i.e. the beam member on the right side of the joint region) in matrices *JMINT* and *JNTINTT* are used to access the properties of the column members and the beam members, respectively.

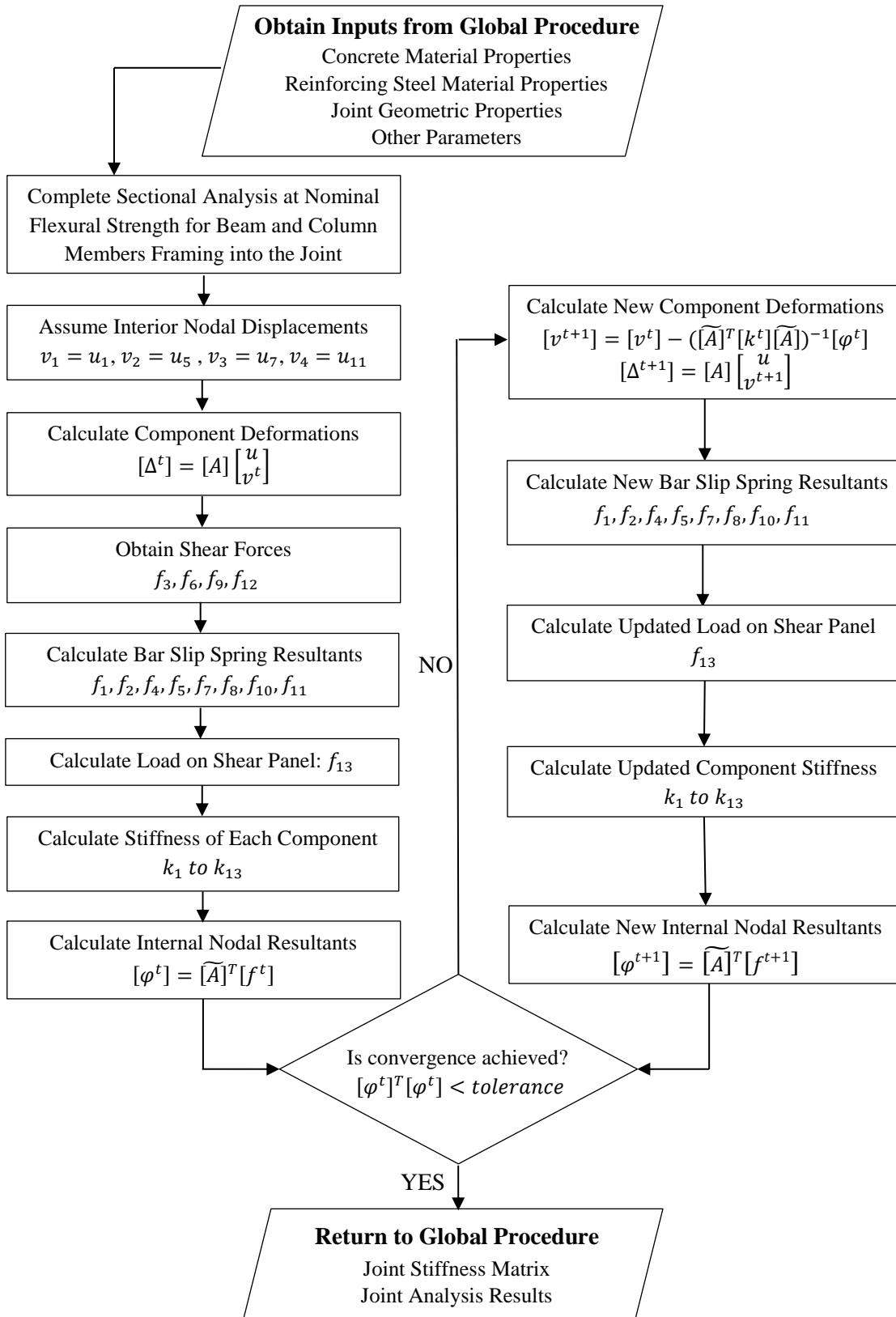


Figure 4.5: Flowchart of solution process for the joint element

Table 4.1: List of input variables required by local joint element subroutine

Type of Input Variables	Input Variables
Concrete Material Properties	$f'_c, f_t, \epsilon'_c, E_c, S_{mx}, S_{my}$
Reinforcing Steel Material Properties	$NSC, NSB, DLC, DLB, ALC, ALB$ $f_{yc}, f_{yb}, f_{uc}, f_{ub}, d_{bc}, d_{bb}, A_{bc}, A_{bb}, E_{sc}, E_{sb}, E_{shc}, E_{shb}$ $f_{yt}, d_{bt}, A_{bt}, E_{st}, \rho_x, \rho_y, \rho_z$
Joint Geometric Properties	w_c, w_b, w, h, t, s, cc
Other Parameters	$LS, DLIST, FORCE, JINT, JNTINT, JMINT, JNTINTT$

The solution process starts with sectional analyses of the beam and column members framing into the joint at nominal flexural strength. Details of the calculations are given in Section 3.3. For this strength calculation, it is assumed that the beams carry zero axial load while the columns carry axial load. A linear axial strain distribution is assumed through the height of the section with the strain at extreme compression fiber taken as -0.003. The strain, stress and force associated with the reinforcing steel are usually computed for individual layers. In this case, however, all longitudinal reinforcing steel carrying compression is lumped at one point while all longitudinal reinforcing steel carrying tension is lumped at another point. This is because the compressive resultant is written as a function of the bar stress of the reinforcing steel carrying compression according to Equation 3.10, and the tensile resultant is written as a function of the bar stress of the reinforcing steel carrying tension according to Equation 3.11.

$$C_{resultant} = C'_s + C_c = f'_s A'_s \left\{ 1 + \frac{0.85 f'_c dw}{E_s A'_s} \frac{2(1-j)}{0.003 \beta \left[1 - \frac{d'}{d} \frac{\beta}{2(1-j)} \right]} \right\} \quad (3.10)$$

$$T_{resultant} = f_s A_s \quad (3.11)$$

In this implementation, the longitudinal reinforcing bars within 50% depth of the beam section and 45% depth of the column section are assumed to carry compression, while the remaining rebars are assumed to carry tension. The top of the section is defined as the location of the extreme compression fiber. The centroid and the area of lumped bars are determined using the following equations:

$$A'_s = \sum A'_{s,i} \quad \text{where } d'_i < 0.50h \text{ for beams, or } d'_i < 0.45h \text{ for columns} \quad (4.1)$$

$$d' = \frac{\sum A'_{s,i} \cdot d'_i}{\sum A'_{s,i}} \quad (4.2)$$

$$A_s = \sum A_{s,i} \quad \text{where } d_i \geq 0.50h \text{ for beams, or } d_i \geq 0.45h \text{ for columns} \quad (4.3)$$

$$d = \frac{\sum A_{s,i} \cdot d_i}{\sum A_{s,i}} \quad (4.4)$$

where i denotes individual longitudinal bar layers from the top layer to the bottom layer and all other variables are as previously defined. The required input for this calculation [i.e., total number of rebar layers in the beams (NSB) and columns (NSC), depth of rebar layers in the beams (DLB) and columns (DLC), and area of rebar layers in the beams (ALB) and columns (ALC)] are provided by the global procedure. In the sectional analysis, it is assumed that all of the tensile force is carried by the reinforcing steel, and that the total compressive force is carried by the concrete and the reinforcing steel. Therefore, the ratio of the resultant force over the force carried by the reinforcing steel is given by:

$$r_{ten} = \frac{T_{resultant}}{f_s A_s} = 1.0 \quad (4.5)$$

$$r_{comp} = \frac{C_{resultant}}{f'_s A'_s} = 1 + \frac{0.85 f'_c d w}{E_s A'_s} \frac{2(1-j)}{0.003 \beta \left[1 - \frac{d'}{d} \frac{\beta}{2(1-j)} \right]} \quad (4.6)$$

All variables were defined in Section 3.3. The last part of the sectional analysis is to determine the location of the bar slip springs, as follows:

$$loc_{ten} = d \quad (4.7)$$

$$loc_{comp} = \frac{d' \cdot (1.0) + 0.5 \beta c \cdot (r_{comp} - 1)}{r_{comp}} \quad (4.8)$$

where d is the depth of the reinforcing steel carrying tension, d' is the depth of the reinforcing steel carrying compression, c is the depth of the neutral axis, β is the depth coefficient of the stress block, and r_{comp} is the ratio of the compressive resultant force over the force carried by the compressive reinforcing steel. Finally, the distance between the bar slip springs, which is used to construct the transformation matrix, is calculated as:

$$\widehat{w} = loc_{ten_column} - loc_{comp_column} \quad (4.9)$$

$$\widehat{h} = loc_{ten_beam} - loc_{comp_beam} \quad (4.10)$$

where \widehat{w} is the distance between the bar slip springs in the columns and \widehat{h} is the distance between the bar slip springs in the beams.

The next step of the solution process is to calculate component deformations using Equation 3.1 or 3.2:

$$\Delta_1 = -u_2 + \frac{\widehat{w}}{2}u_3 + \frac{\widehat{w}}{2}\left(\frac{v_4-v_2}{w}\right) + \frac{v_4+v_2}{2} \quad (3.1a)$$

$$\Delta_2 = -u_2 - \frac{\widehat{w}}{2}u_3 + \frac{\widehat{w}}{2}\left(\frac{v_2-v_4}{w}\right) + \frac{v_4+v_2}{2} \quad (3.1b)$$

$$\Delta_3 = u_1 - v_1 \quad (3.1c)$$

$$\Delta_4 = u_4 + \frac{\widehat{h}}{2}u_6 - \frac{\widehat{h}}{2}\left(\frac{v_1-v_3}{h}\right) - \frac{v_1+v_3}{2} \quad (3.1d)$$

$$\Delta_5 = u_4 - \frac{\widehat{h}}{2}u_6 - \frac{\widehat{h}}{2}\left(\frac{v_3-v_1}{h}\right) - \frac{v_1+v_3}{2} \quad (3.1e)$$

$$\Delta_6 = u_5 - v_2 \quad (3.1f)$$

$$\Delta_7 = u_8 - \frac{\widehat{w}}{2}u_9 + \frac{\widehat{w}}{2}\left(\frac{v_2-v_4}{w}\right) - \frac{v_2+v_4}{2} \quad (3.1g)$$

$$\Delta_8 = u_8 + \frac{\widehat{w}}{2}u_9 - \frac{\widehat{w}}{2}\left(\frac{v_2-v_4}{w}\right) - \frac{v_2+v_4}{2} \quad (3.1h)$$

$$\Delta_9 = u_7 - v_3 \quad (3.1i)$$

$$\Delta_{10} = -u_{10} - \frac{\widehat{h}}{2}u_{12} + \frac{\widehat{h}}{2}\left(\frac{v_1-v_3}{h}\right) + \frac{v_1+v_3}{2} \quad (3.1j)$$

$$\Delta_{11} = -u_{10} + \frac{\widehat{h}}{2}u_{12} - \frac{\widehat{h}}{2}\left(\frac{v_1-v_3}{h}\right) + \frac{v_1+v_3}{2} \quad (3.1k)$$

$$\Delta_{12} = u_{11} - v_4 \quad (3.1l)$$

$$\Delta_{13} = -\frac{v_1}{h} + \frac{v_2}{w} + \frac{v_3}{h} - \frac{v_4}{w} \quad (3.1m)$$

$$[\Delta_{13 \times 1}] = [A_{13 \times 16}] \begin{bmatrix} u_{12 \times 1} \\ v_{4 \times 1} \end{bmatrix} \quad (3.2)$$

The external nodal displacements and joint geometric properties required to complete the calculation are provided as input by the global procedure. The internal nodal displacements are also unknown. In the first iteration, the internal nodal displacements are assumed to be the same as the nearest external nodal displacements parallel to the face of the joint panel, as follows:

$$v_1 = u_1 \quad (4.11a)$$

$$v_2 = u_5 \quad (4.11b)$$

$$v_3 = u_7 \quad (4.11c)$$

$$v_4 = u_{11} \quad (4.11d)$$

After the component deformations are determined, the algorithm proceeds to calculate corresponding force resultants, shear equivalent moment and component stiffness. The force resultant and stiffness of the bar slip springs are computed in the bar slip spring subroutine. The shear equivalent moment and stiffness of joint panel are computed in the shear panel subroutine. The interface shear springs are assumed to remain stiff and elastic. Forces in the springs are assumed to be the same as the shear forces acting on the joint according to Equation 3.3:

$$F_1 = f_3 \quad (3.3a)$$

$$F_5 = f_6 \quad (3.3e)$$

$$F_7 = f_9 \quad (3.3g)$$

$$F_{11} = f_{12} \quad (3.3k)$$

Different stiffness values for the interface shear springs were tested in the program to see how they affect the global load-displacement response, as well as the number of iterations needed for the solution to achieve the convergence. Three stiffness values were tested and it was found that the global load-displacement responses obtained were very similar (see Figure 4.6). Furthermore, the lower the stiffness value, the lesser the iterations needed for the solution to converge (see Table 4.2). However, convergence was not achieved for very low stiffness values. The stiffness value of 100,000 kN/mm was found to be effective for the implementation in terms of accuracy,

efficiency and reliability. Therefore, this value was selected as the stiffness of interface shear springs. The stiffness value of 10,000 kN/mm was found to produce unstable global load-deflection response (e.g. spikes) in some cases. The stiffness value of 1,000,000 kN/mm was found to produce the identical response as the selected value, but about ten times the number of iterations were needed to achieve convergence.

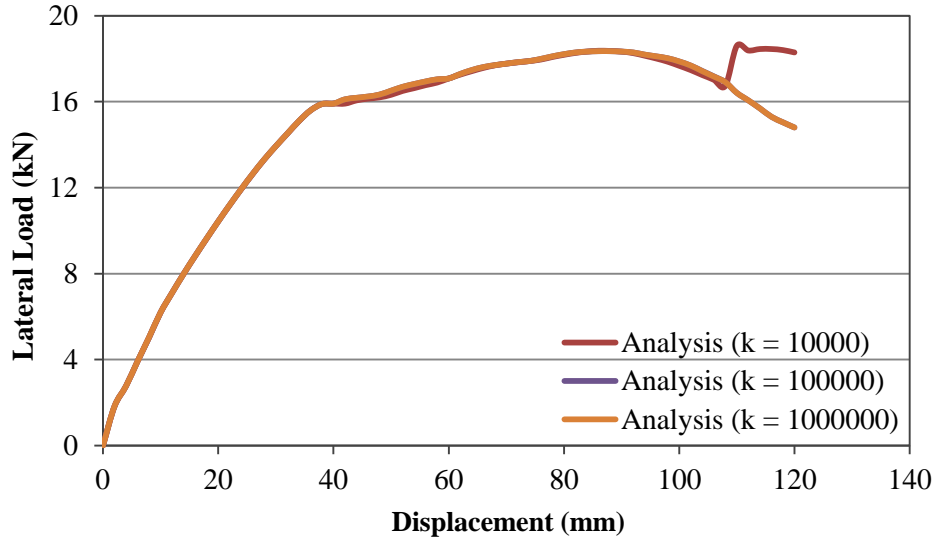


Figure 4.6: Load-displacement response of interface shear spring with different stiffness

Table 4.2: Iterations to convergence for selected stiffness values

Stiffness (kN/mm)	10,000	100,000	1,000,000
Load Stage	# of Iterations to Converge		
10	12	82	789
20	14	97	933
30	15	107	1030
40	15	107	1033

The algorithm continues to calculate the four internal nodal resultants using Equation 3.3:

$$\varphi_1 = -f_3 - \frac{1}{2} \left(1 + \frac{\hat{h}}{h}\right) (f_4 - f_{10}) - \frac{1}{2} \left(1 - \frac{\hat{h}}{h}\right) (f_5 - f_{11}) - \frac{f_{13}}{h} \quad (3.3m)$$

$$\varphi_2 = -f_6 - \frac{1}{2} \left(1 + \frac{\hat{w}}{w}\right) (f_8 - f_2) - \frac{1}{2} \left(1 - \frac{\hat{w}}{w}\right) (f_7 - f_1) + \frac{f_{13}}{w} \quad (3.3n)$$

$$\varphi_3 = -f_9 - \frac{1}{2}\left(1 + \frac{\hat{h}}{h}\right)(f_5 - f_{11}) - \frac{1}{2}\left(1 - \frac{\hat{h}}{h}\right)(f_4 - f_{10}) + \frac{f_{13}}{h} \quad (3.3o)$$

$$\varphi_4 = -f_{12} - \frac{1}{2}\left(1 + \frac{\hat{w}}{w}\right)(f_7 - f_1) - \frac{1}{2}\left(1 - \frac{\hat{w}}{w}\right)(f_8 - f_2) - \frac{f_{13}}{w} \quad (3.3p)$$

In order to achieve the state of convergence, the square of each resultant must be less than the tolerance. The tolerance was set as 1 kN² in the algorithm. If convergence is not achieved, new component deformations are calculated using the following equations:

$$[v^{t+1}] = [v^t] - (\widetilde{[A]}^T [k] \widetilde{[A]})^{-1} [\varphi^t] \quad (4.12)$$

$$[\Delta^{t+1}] = [A] \begin{bmatrix} u \\ v^{t+1} \end{bmatrix} \quad (4.13)$$

where k is a diagonal matrix of the 13 component stiffness values, $\widetilde{[A]}$ refers to columns 10 to 13 of the transformation matrix, superscript t indicates variables from the current iteration, superscript $t + 1$ indicates variables for the next iteration, and all other variables are the same as previously defined. The updated component deformations are used to determine the corresponding component resultants and stiffness. The same calculations are repeated until the convergence criteria are satisfied. There are times when the criteria cannot be satisfied, or when a large number of iteration is required to achieve convergence. One such case occurs at the early load stages when compression in the column dictates the response of the shear panel. Therefore, the maximum number of iteration is set to 1,000 to facilitate the solution process.

The joint element subroutine returns a joint analysis matrix (SJA) to the global procedure, and stores the joint analysis results for the user to inspect. The stiffness matrix of the joint element with the size of 16 by 16, is calculated based on the component stiffness according to Equation 3.5:

$$[K_{elem\ 16 \times 16}] = [A^T_{16 \times 13}] [k_{13 \times 13}] [A_{13 \times 16}] \text{ where } k_i = \frac{df_i}{d\Delta_i}, i = 1, 2, \dots, 13 \quad (3.5)$$

Instead of using the tangent stiffness, the component secant stiffness is used to avoid getting extremely large stiffness values at low component deformations. The stiffness matrix is condensed with respect to the four exterior nodes (i.e. the first 12 degree-of-freedom) using the partitioned matrix and static condensation (see Figure 4.7), given by:

$$[K_{12 \times 12}] = [K_{AA}] - [K_{AB}][K_{BB}]^{-1}[K_{BA}] \quad (4.14)$$

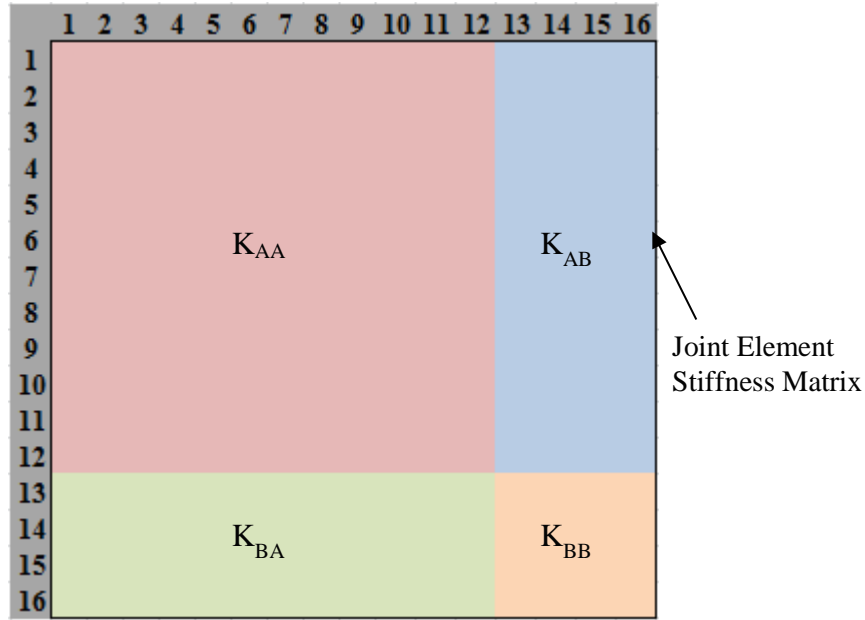


Figure 4.7: Partitioned joint element stiffness matrix

The condensed matrix, with the dimension of 12 by 12, is then projected to a joint analysis matrix, which has the same size as the global stiffness matrix (see Figure 4.8). For frames with multiple interior joints, condensed stiffness matrices are determined for individual joints which are translated into a large joint analysis matrix. Meanwhile, joint analysis results are stored in the common blocks and printed in the output file at the end of every global iteration. The results include cracking parameters, joint core parameters, reinforcing steel parameters and joint panel coordinates. All parameters are computed in the bar slip spring subroutine and the shear panel subroutine. Joint panel displacements and rotations (see Figure 4.9) are calculated using the following equations:

$$X_{left} = X_{right} = 0.5 * (v_1 + v_3) \quad (4.15a)$$

$$Y_{left} = v_4 \quad (4.15b)$$

$$Y_{right} = v_2 \quad (4.15c)$$

$$Z_{left} = Z_{right} = \frac{v_1 - v_3}{h} \quad (4.15d)$$

$$X_{top} = v_3 \tag{4.15e}$$

$$X_{bottom} = v_1 \tag{4.15f}$$

$$Y_{top} = Y_{bottom} = 0.5 * (v_2 + v_4) \tag{4.15g}$$

$$Z_{top} = Z_{bottom} = \frac{v_2 - v_4}{w} \tag{4.15h}$$

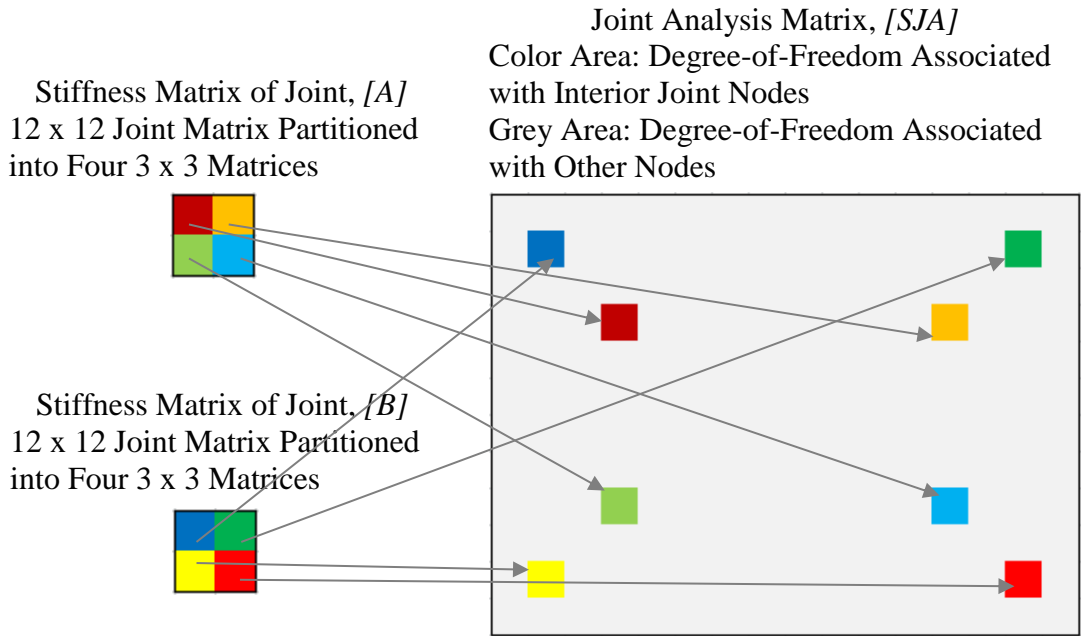


Figure 4.8: Joint analysis matrix for frames with multiple interior joints

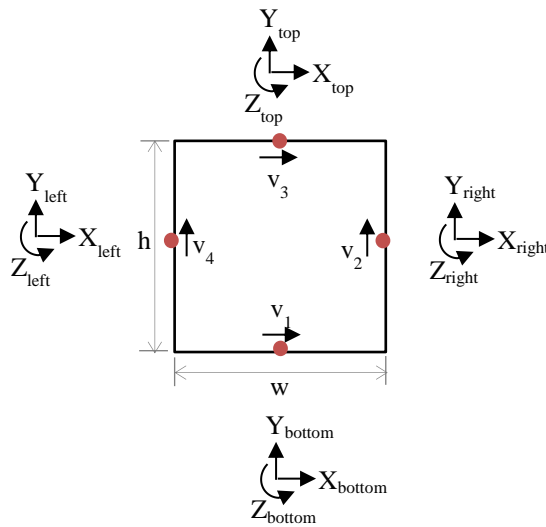


Figure 4.9 Joint panel displacements and rotations

where X is the horizontal translation of the node, Y is the vertical translation of the node, Z is the rotation of the shear panel face, and the subscripts indicate the faces of the joint core, with respect to which the calculations are performed. All other variables are as previously defined.

4.3.2 Subroutine: Bar Slip Spring

The bar slip spring subroutine was constructed based on the bar stress versus slip relationship presented in Section 3.3. Properties of the longitudinal reinforcement and the surrounding concrete are supplied to this subroutine. The algorithm takes the input spring deformation and calculates the corresponding spring force and secant stiffness. A flowchart of the implemented algorithm to determine the bar slip spring response is presented in Figure 4.10.

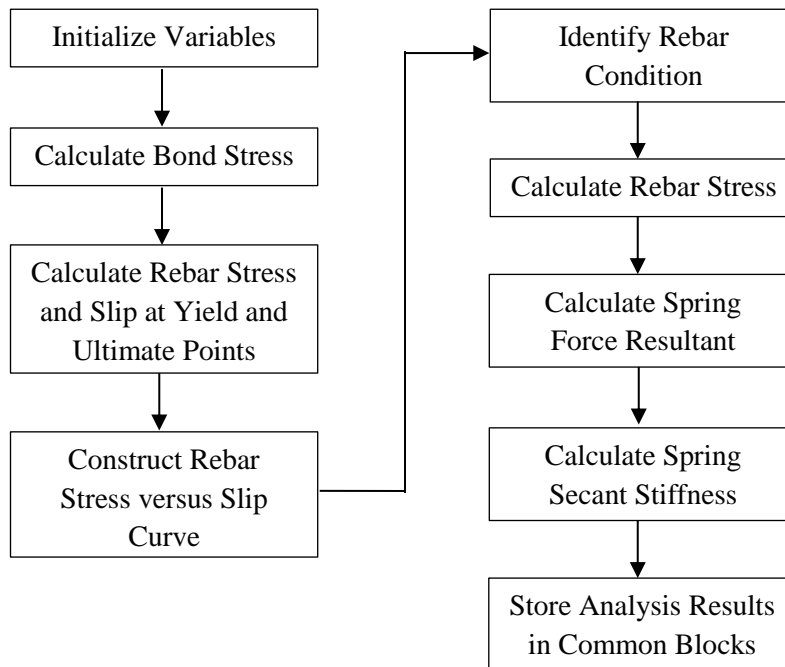


Figure 4.10: Flowchart of the solution process for the bar slip springs

The bar stress versus slip curve is divided into four segments: elastic tension, post-yielding tension, elastic compression and post-yielding compression. Equation 3.7 and Table 3.1 were employed to construct the curve.

$$\Delta_{slip} = 2 \frac{\tau_E l_{fs}^2}{E d_b} \quad \text{for } f_s < f_y \quad (3.7a)$$

$$\Delta_{slip} = 2 \frac{\tau_E l_e^2}{E d_b} + \frac{f_y l_y}{E} + 2 \frac{\tau_Y l_y^2}{E_{sh} d_b} \quad \text{for } f_s \geq f_y \quad (3.7b)$$

The average bond stress for post-yielding tension rebar, ranging from $0.4\sqrt{f_c}$ to $0.05\sqrt{f_c}$, was taken as $0.2\sqrt{f_c}$. The slope of the curve, or the stiffness of bar slip spring, is large at low slip. It greatly contributes to the overall stiffness of the joint element, making it significantly stiffer. Therefore, a linear relationship is used in the elastic tension and compression regions. Figure 4.11 shows a typical bar stress versus slip curve for reinforcing steel. The bar stress is used to calculate the spring force resultant and stiffness. The resultant was defined as a function of the bar stress in Equation 3.10 and 3.11:

$$C_{resultant} = C'_s + C_c = f'_s A'_s \left\{ 1 + \frac{0.85 f'_c d w}{E_s A'_s} \frac{2(1-j)}{0.003 \beta \left[1 - \frac{d'}{d} \frac{\beta}{2(1-j)} \right]} \right\} \quad (3.10)$$

$$T_{resultant} = f_s A_s \quad (3.11)$$

The secant stiffness is defined as the force resultant divided by the spring deformation. Rebar end stress and slip are provided as a part of the joint analysis results in the output files for users.

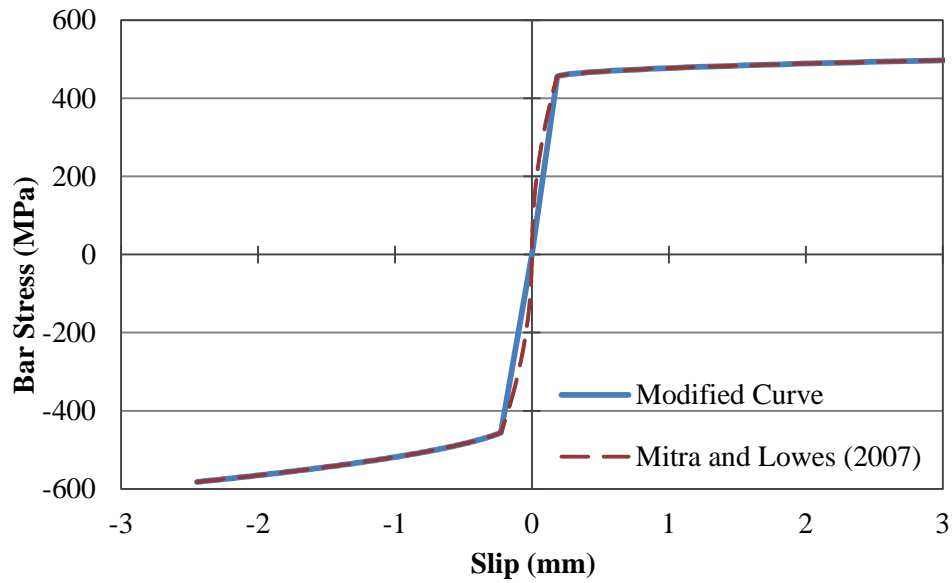


Figure 4.11: Modified bar stress versus slip relationship

4.3.3 Subroutine: Shear Panel

The shear panel subroutine was constructed based on the Mander et al. (1988) model for uniaxial confined concrete with a reduction factor proposed by Mitra and Lowes. The related information on the modeling of joint shear response was presented in Section 3.4. The properties of the concrete and layout of the longitudinal and transverse reinforcing steel are supplied to the subroutine. The algorithm takes the input panel shear deformation and calculates the corresponding shear equivalent moment and secant stiffness values. A flowchart of the implemented algorithm to determine the shear panel response is presented in Figure 4.12.

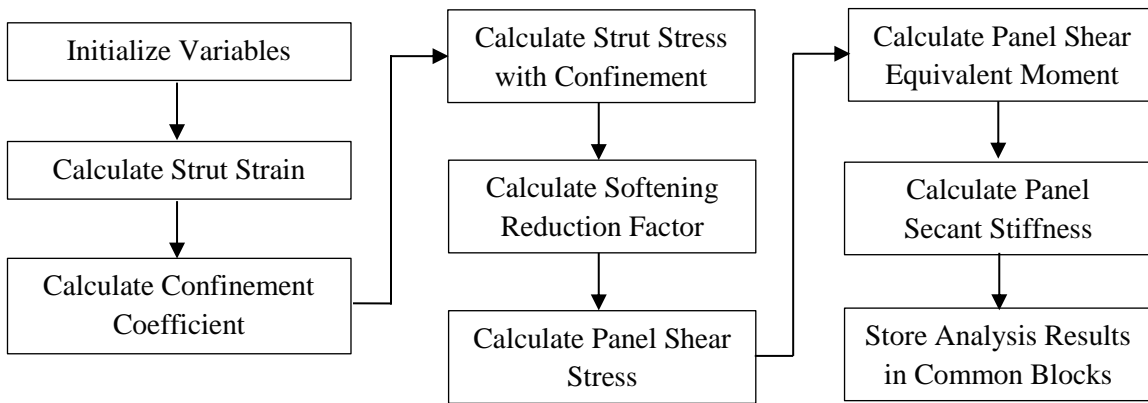


Figure 4.12: Flowchart of solution process for the shear panel

The strain of the diagonal concrete strut is not directly given as an input. Therefore, the compressive strain in the diagonal strut is calculated using the following strain transformation equations:

$$\varepsilon_{strut} = \varepsilon_x \cos^2(\alpha_{strut}) + \varepsilon_y \sin^2(\alpha_{strut}) + \left(\frac{\Delta_{13}}{2}\right) \sin(\alpha_{strut}) \cos(\alpha_{strut}) \quad (4.16)$$

$$\varepsilon_x = 0 \quad (2.3)$$

$$\varepsilon_y = \frac{P_v}{(1-\rho_{sy})E_c + \rho_{sy}E_s} \quad (2.4)$$

In this equation, ε_x is taken as zero by Equation 2.3, ε_y is the compressive strain in the vertical direction by Equation 2.4, Δ_{13} is the input panel shear deformation, and α_{strut} is the angle of inclination of the diagonal strut. The angle of inclination aligns with the shorter diagonal of the shear panel. For the first five load stages, the compressive strain in the vertical direction is taken

as zero because the domination of column compression in the early load stages may produce the undesired result of the stiffness matrix not being positive definite at early load stages.

Mander et al. proposed a theoretical stress-strain model for confined concrete. Figure 4.13 illustrates the stress-strain model for the monotonic loading of confined and unconfined concrete. It also suggests that the confined concrete fails at the first hoop fracture. This model considers the fraction of concrete that is confined by the transverse reinforcing steel, and enhances the strength and ductility of the concrete according to the confinement effectiveness coefficient. The confined concrete compressive stress f_{cc} is given by

$$f_{cc} = \frac{f'_{cc} x r}{r - 1 + x^r} \quad (4.17)$$

$$\text{where } x = \frac{\varepsilon_{strut}}{\varepsilon'_{cc}} \quad (4.18)$$

$$\text{and } r = \frac{E_c}{E_c - E_{sec}} \quad (4.19)$$

where f'_{cc} is the compressive strength of confined concrete, parameter x is a function of the strut strain, and parameter r is a function of the tangent modulus of elasticity of concrete E_c and the secant modulus of elasticity of concrete E_{sec} . The tangent modulus is given as an input to the subroutine. The secant modulus is given by

$$E_{sec} = \frac{f'_{cc}}{\varepsilon'_{cc}} \quad (4.20)$$

where ε'_{cc} is the strain at the compressive strength of confined concrete.

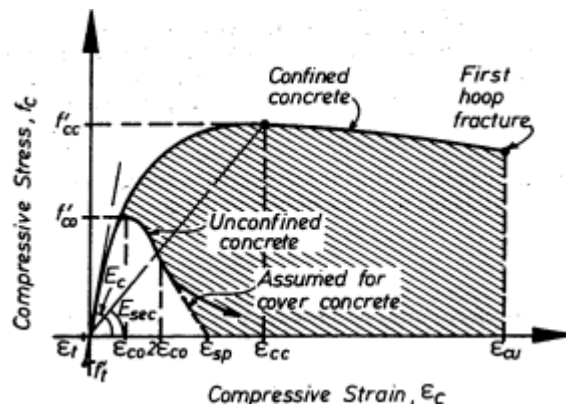


Figure 4.13: Stress-strain model for monotonic loading of confined and unconfined concrete (Mander et al., 1988)

Determination of the confined concrete strength and strain requires the consideration of the effective confinement. Figure 4.14 shows effectively confined concrete in section and elevation views.

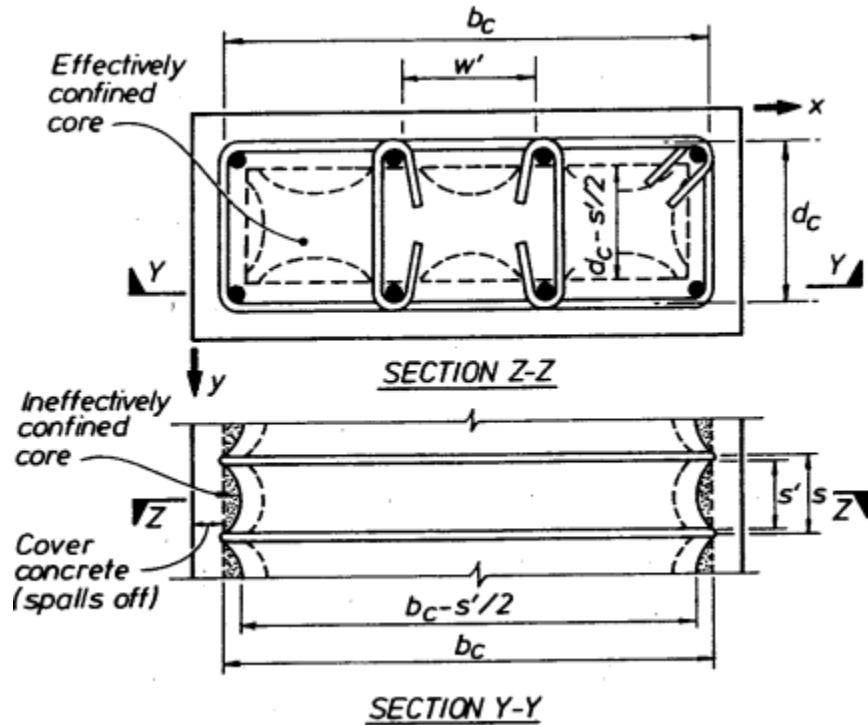


Figure 4.14: Effectively confined concrete for rectangular tie reinforcement (Mander et al., 1988)

The concrete is confined by rectangular ties in the out-of-plane direction, creating a lateral pressure to stiffen the concrete core. It is assumed that the effective confinement in concrete diagonal strut equals to the effective confinement of a column segment associated with the interior joint. The confinement effectiveness coefficient k_e is given by

$$k_e = \frac{(1 - \sum_{i=1}^n \frac{(w'_i)^2}{16b_c d_c}) (1 - \frac{s'}{2b_c}) (1 - \frac{s'}{2d_c})}{1 - \rho_{cc}} \quad (4.21)$$

where n represents the number of longitudinal bars in the column, ρ_{cc} is the ratio of the longitudinal reinforcement to area of the confined core section, w' is the clear distance between the longitudinal rebars in the column, s' is the clear spacing of transverse tie reinforcement, b_c and d_c are dimensions to the centerline of the perimeter tie reinforcement in the x and y directions of the column section, respectively. For joints with no transverse reinforcement or

with ineffective transverse reinforcement (i.e. k_e less than zero), a value of zero is assigned to the coefficient. Most of the dimensions are determined based on the input geometric parameters. Because the distance between the longitudinal bars of the same layer is not a required input by the user, it is assumed to be the inner circumference of the tie divided by the number of longitudinal bars. Then, the lateral confining stresses in the x and y directions are calculated as

$$f_{lx} = k_e \rho_x f_{yt} \quad (4.22)$$

$$f_{ly} = k_e \rho_y f_{yt} \quad (4.23)$$

where f_{yt} is the yield stress of transverse reinforcement, and ρ_x and ρ_y are the transverse reinforcing ratios in the x and y directions of the column section, respectively.

The last step to construct the stress-strain model is to determine the confined concrete strength f'_{cc} and corresponding strain ϵ'_{cc} using the following equations:

$$f'_{cc} = f'_c \left(-1.254 + 2.254 \sqrt{1 + \frac{7.94 f_l}{f'_c} + 2 \frac{f_l}{f'_c}} \right) \quad (4.24)$$

$$\epsilon'_{cc} = \epsilon'_c \left[1 + 5 \left(\frac{f'_{cc}}{f'_c} - 1 \right) \right] \quad (4.25)$$

where f'_c is the compressive strength of unconfined concrete, ϵ'_c is the strain at compressive strength, and f_l is the average confining pressure taken as the average of confining pressure in the x and y directions of the column section. The confined concrete strength and strain are substituted into Equations 4.17 and 4.18 to determine the stress of the confined concrete for a given strut strain.

The strut stress obtained from the stress-strain model for the confined concrete is multiplied by a reduction factor accounting for the compression softening effect. The principal tensile and compressive strains were given by Equation 2.7 and 2.8, respectively.

$$\epsilon_1 = \frac{\epsilon_x + \epsilon_y}{2} + \sqrt{\left(\frac{\epsilon_x - \epsilon_y}{2} \right)^2 + \left(\frac{\gamma_{xy}}{2} \right)^2} \quad (2.7)$$

$$\epsilon_2 = \frac{\epsilon_x + \epsilon_y}{2} - \sqrt{\left(\frac{\epsilon_x - \epsilon_y}{2} \right)^2 + \left(\frac{\gamma_{xy}}{2} \right)^2} \quad (2.8)$$

The reduction factor was given by Equation 3.12 for joints with transverse reinforcement and Equation 3.13 for joints without transverse reinforcement.

$$\frac{f_{cstrut}}{f_{cMander}} = 3.62 \left| \frac{\varepsilon_t}{\varepsilon_{cc}} \right|^2 - 2.82 \left| \frac{\varepsilon_t}{\varepsilon_{cc}} \right| + 1 \quad \text{for} \quad \left| \frac{\varepsilon_t}{\varepsilon_{cc}} \right| < 0.39 \quad (3.12a)$$

$$\frac{f_{cstrut}}{f_{cMander}} = 0.45 \quad \text{for} \quad \left| \frac{\varepsilon_t}{\varepsilon_{cc}} \right| \geq 0.39 \quad (3.12b)$$

$$\frac{f_{cstrut}}{f_{cMander}} = 0.36 \left| \frac{\varepsilon_t}{\varepsilon_{cc}} \right|^2 - 0.60 \left| \frac{\varepsilon_t}{\varepsilon_{cc}} \right| + 1 \quad \text{for} \quad \left| \frac{\varepsilon_t}{\varepsilon_{cc}} \right| < 0.83 \quad (3.13a)$$

$$\frac{f_{cstrut}}{f_{cMander}} = 0.75 \quad \text{for} \quad \left| \frac{\varepsilon_t}{\varepsilon_{cc}} \right| \geq 0.83 \quad (3.13b)$$

Then, the panel shear stress was determined using the obtained strut stress and Equation 3.14.

$$\tau_{strut} = f_{c_strut} \frac{w_{strut} \cos \alpha_{strut}}{w} = f_{c_strut} \frac{w_{strut} \sin \alpha_{strut}}{h} \quad (3.14)$$

Finally, the shear equivalent moment acting on the joint panel component is calculated as

$$f_{13} = \tau_{strut} \cdot w \cdot h \cdot t \quad (4.26)$$

where w , h and t are the width, height and thickness of the joint panel, respectively. The secant stiffness is defined as the shear equivalent moment divided by the panel shear deformation.

At the end of the subroutine, the cracking angle θ_{cr} , the mean crack spacing s_{cr} , the mean crack width w_{cr} , the tie strain ε_{sz} and the tie stress f_{sz} are calculated as a part of the joint analysis results in the output files using the following equations:

$$\theta_{cr} = \left| 90^\circ + \frac{1}{2} \arctan \frac{2\Delta_{13}}{\varepsilon_x - \varepsilon_y} \right| \quad (4.27)$$

$$s_{cr} = \frac{1}{\frac{\cos \theta}{s_{mx}} + \frac{\sin \theta}{s_{my}}} \quad (4.28)$$

$$w_{cr} = \varepsilon_1 \cdot s_{cr} \quad (4.29)$$

$$\varepsilon_{sz} = \frac{E_c}{E_c + \rho_z E_{sz}} \left(-0.15 \frac{f_2}{\varepsilon_2} \right) \quad (4.30)$$

$$f_{sz} = E_s \cdot \varepsilon_{sz} \leq f_{yz} \quad (4.31)$$

where s_{mx} and s_{my} are the mean crack spacing in the x and y directions of the shear panel, ρ_z is the out-of-plane reinforcing ratio, E_{sz} is the modulus of elasticity of the transverse reinforcement, f_{yz} is the yield stress of the transverse reinforcement, and all other variables are previously defined.

4.4 Modifications of the Global Frame Analysis Procedure

In order to integrate the local joint element into the global frame analysis procedure, proper modifications of the global frame analysis procedure are necessary. There are three components of the global procedure that requires modifications. The first component is the detection of the interior joints. Interior joints are detected in the shear protection subroutine, and the relevant information is stored in the common blocks. The next part is the assembly of the global stiffness matrix. A revised method is proposed to fit the replacement of the existing beam and column members in the joint region for the joint elements. Finally, two minor modifications are made in the main program to facilitate the joint implementation.

4.4.1 Detection of Interior Joints

Detection of interior joints is performed in the shear protection subroutine. The obtained joint information is also stored in the form of arrays and matrices in the common blocks. The relevant variables are introduced in Section 4.3.1. In this algorithm, an interior joint node is labelled if the node is associated with four members. Similarly, an exterior joint node has three members framing into it, whereas a knee joint node has two members framing into it. The total numbers of interior, exterior and knee joints are also noted. The joint element algorithm requires input such as the node numbers that define an interior joint, the member numbers of in-framing members, and the members in the joint region. The input is sorted into arrays or matrices in the counter-clockwise direction starting from the bottom. Figure 4.15 shows an example of the interior joint information stored in the common blocks. The node numbers, for example, are sorted based on their coordinates. The node with the lowest y coordinate among the four external nodes is defined as the bottom node. The node with the highest x coordinate is defined as the second node in the list. The node with the highest y coordinate appears as the third node in the list. The last

node is the one with the lowest x coordinate. The member information is also identified and stored in a similar way.

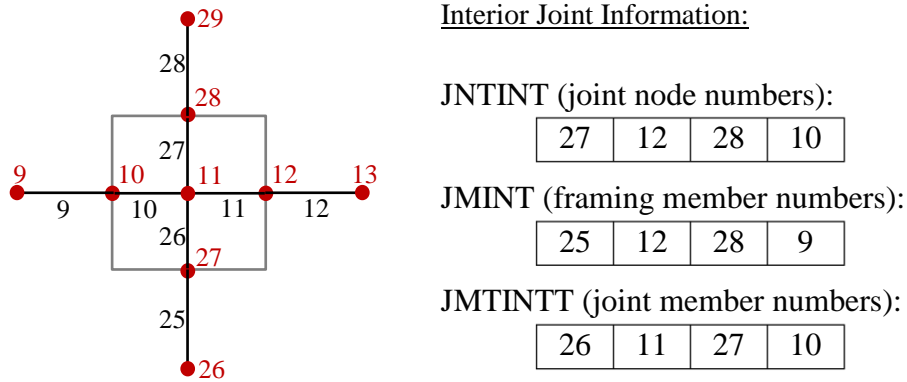


Figure 4.15: Interior joint information in the common blocks

4.4.2 Assembly of the Global Stiffness Matrix

The method to assemble the global stiffness matrix is modified for the joint element implementation. In the original algorithm, stiffness matrices for individual members are assembled into a global stiffness matrix as shown in Figure 4.16a. The implementation omits the joint nodes and replaces four members in the joint regions with joint elements. The element stiffness matrices of all interior joints in the structure are stored into a joint analysis matrix with the same size as the global matrix as shown in Figure 4.16b. Eventually, the joint analysis matrix is added to the member stiffness matrix for the assembly of the global stiffness as shown in Figure 4.16c. Because of the omission of the interior joint nodes, the size of the global stiffness matrix is reduced by a degree of three for each interior joint detected. The size of the load and the displacement vectors is also adjusted to reflect the removal of the joint nodes.

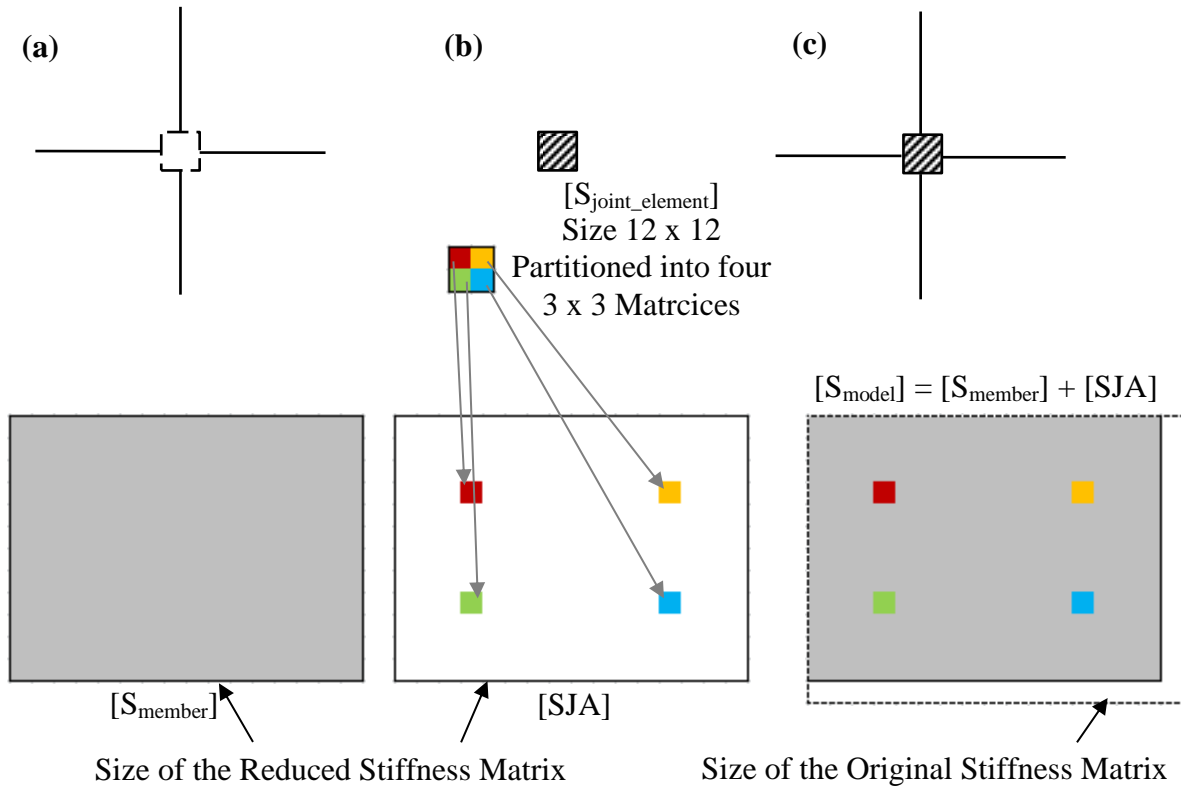


Figure 4.16: Assembling the global stiffness matrix: (a) stiffness of members, (b) stiffness of joints, and (c) stiffness of the structure

4.4.3 Solution to the Global Frame Analysis

The basic analysis steps of the global procedure presented in Section 4.2 remain unchanged. However, there are two minor modifications made in the main program. The first modification was the inclusion of a mechanism to turn on and off the interior joint analysis. Interger *JAMODE* was created for this purpose. This check takes place at the beginning of the global frame iterations. If there is at least one interior joint presented, the joint analysis mode is turned on from the second sectional iteration of the first load stage and beyond. In this case, the node numbers are revised to accompany the size reduction of the global stiffness matrix. Then, the joint analysis subroutine is called for each interior joint detected just prior to the assembly of the global stiffness matrix. However, the subroutine is only called for the first three sectional iterations of each load stage in order to provide a more stable environment for the subsequent iterations of the nonlinear sectional analysis. Calling the subroutine for all sectional iterations

may result in a constant convergence factor throughout the iterations of a load stage. The second minor change concerned the unbalanced force. The unbalanced force approach is not applicable to the joint element because the layered analysis is not performed. The unbalanced forces and the compatibility restoring forces are set to zero for members in the joint region. This eliminates the possibility of getting unrealistic convergence factors for those members in the sectional iterations.

4.5 Guidelines for Modeling Beam-Column Joints

The implementation of the joint element requires new guidelines for modeling beam-column joints in VecTor5. Originally, VecTor5 employed semi-rigid end offsets to model beam-column joints in a frame structure. This technique requires doubling the amount of longitudinal and transverse reinforcing steel for members inside the joint region. The concrete properties remain unchanged. For the updated VecTor5 considering joint behavior, the interior joints should be modeled without semi-rigid end offsets, whereas exterior and knee joints should still be modeled with semi-rigid end offsets. The user should follow the following general guidelines and assumptions during the process of model creation:

- An interior joint should be modeled with two identical beam members and two identical column members.
- The beam members account for the longitudinal reinforcing bars in the x direction in the joint region.
- The column members account for the longitudinal reinforcing bars in the y direction and the transverse reinforcement in the joint region.
- The longitudinal reinforcing bars with different diameters may be used to construct the joint model. However, the average diameter of the compression or tension bars is calculated and used for bar slip spring calculations.
- For joints with no transverse reinforcement, the spacing and the reinforcing ratio of transverse reinforcement should be input as zero.
- For joints reinforced with a single set of tie reinforcement, the spacing of transverse reinforcement is assumed to be half of the joint height.

- For joints reinforced with multiple sets of tie reinforcement, the spacing provided in the design is used.
- For joints reinforced with a combination of square and diamond orientation of ties, the area of the transverse reinforcement is assumed to be the sum of the two.
- Steel plates and fiber-reinforced polymer composites used as transverse reinforcement are not considered in the joint analysis.

Members outside the joint regions are modeled using the same technique as before. Additional information on modeling reinforced concrete frame structures in VecTor5 is available in “User’s Manual of VecTor5” by Guner and Vecchio (2008).

4.6 Interpretation of Results

Results from the joint analysis are printed in the output files for users to review. This following section will discuss the layout and content of joint analysis results. This information will be used to develop a graphical representation in the post-processing program Janus by subsequent students.

4.6.1 Output Files

VecTor5 stores the analysis results of individual load stages in output files (*.A5E). The results from interior joint analysis are printed at the end of the output file. The member and joint analysis results for the members associated with the interior joints are shown in Figure 4.17 and Figure 4.18, respectively.

```

MEMBER SECTION STRESSES AND STRAINS
*****
AVERAGE VALUES

MEMBER : 10

SEE JOINT : 3

```

Figure 4.17: Layout of member analysis results for members in joint regions

```

INTERIOR JOINT ANALYSIS RESULTS
*****
AVERAGE VALUES

JOINT :      3

CRACK WIDTH :    0.610 mm    SOFTENING COEFFICIENT :    0.450    STRUT STRAIN :    -1.490 me
CRACK SPACING : 212.132 mm  CONFINEMENT COEFFICIENT :    0.725    STRUT STRESS :    -12.579 MPa
CRACK ANGLE :   45.176 deg  PANEL SHEAR STRAIN :    -5.819 me    TIE STRAIN :    0.841 me
                                PANEL SHEAR STRESS :    -2.881 MPa    TIE STRESS :    127.056 MPa

FACE          REBAR STRESS          SLIP          PANEL COORDINATES
              LAYER 1    LAYER 2    LAYER 1    LAYER 2    X          Y          Z
              (MPa)      (MPa)      (mm)      (mm)      (mm)      (mm)      (rad)
LEFT          206.25    -17.37    0.0831    -0.0086    5.000     1.022    -0.00141
RIGHT         -19.04     213.73    -0.0094    0.0861    5.000     -1.148    -0.00141
TOP           109.02     -92.54    0.0367    -0.0381    5.213     -0.063    -0.00723
BOTTOM        -92.37     109.52    -0.0380    0.0369    4.788     -0.063    -0.00723

```

Figure 4.18: Layout of interior joint analysis results in the output files

In Figure 4.18, the first parameter presented is the node number of an interior joint. Then, the crack parameters including crack widths, spacing and direction are given in the first column. Joint panel parameters are presented in the second and the third columns. The softening parameter is the reduction factor due to the compression softening effect. This factor is calculated according to Equation 3.12 and 3.13. The confinement coefficient indicates how well the joint is confined. This coefficient is calculated according to Equation 4.21. A value of 1.0 indicates that the joint is fully confined and a value of zero indicates that the joint contains ineffective or no transverse reinforcement. Other joint panel parameters listed include panel shear stress and strain in the concrete strut, and stress and strain in the tie reinforcement. These parameters are calculated in the joint shear subroutine, as described in Section 4.3.3.

The second part of the analysis results presents rebar stress at the interface of the joint, the bond slip values, and the nodal displacements and rotations of the joint panel. Rebar stress and bond slip are listed in terms of “layer 1” and “layer 2” as shown in Figure 4.19. For the left and right faces of the joint, “layer 1” coincides with the location of the bar slip springs on the top, and “layer 2” coincides with the location of the bar slip springs at the bottom. For the top and bottom faces of the joint, “layer 1” coincides with the location of the bar slip springs on the left side, and “layer 2” coincides with the location of the bar slip springs on the right side. The definition of these terms is irrelevant to the definition of the orientation of the members framing into the joint because all joint elements are defined and analyzed in the same and consistent manner.

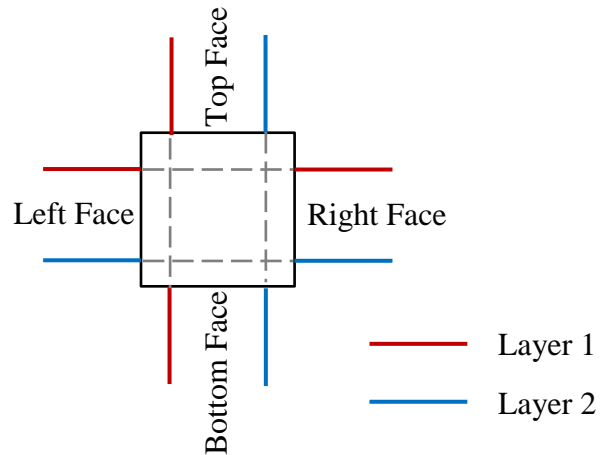


Figure 4.19: Definition of layers and faces in joint analysis results

4.6.2 Graphical Representation

Janus, the post-processor of VecTor5, reads the data from the output files and creates a graphical representation of the analysis results. Detailed information about the program is given in “User's Manual of Janus for VecTor5” developed by Chak (2013) and subsequently improved by Loya et al. (2016). The joint analysis results are currently not read by Janus because the joint response is a new addition to VecTor5. However, there is a need to create a visual representation based on the data from the joint analysis results so that users can understand the results in a more convenient and intuitive way.

The basic procedure to sketch the deformed joint using the data obtained in the output files should follow these four steps:

1. Delete the four members in the interior joint region from the current Janus graphical representation of the structure. The rest of the structure should be kept as it is.
2. Draw the perimeter of the interior joint. The four nodal coordinates (i.e., x and y panel coordinates) defines the location of the deformed joint. The shape of the joint is defined by the rotation (i.e. z panel coordinate) of each face of the joint.
3. Draw the cracks in the joint panel. The cracks are drawn using the crack width, crack spacing and crack angle provided in the interior joint analysis results
4. Label the bond slip values and the crack widths. These values may be displayed when they exceed a certain value (e.g. 0.5 mm).

- The reinforcing bar at the interface of the interior joint may be displayed in a green color if the yielding stress is reached.

Figure 4.20 illustrates the concept of sketching the deformed interior joint using some sample values. Components with negative slip are not important for the graphical representation; they are only used to construct the material model. Meanwhile, for the components with significant positive slip, an opening at the interface of the joint should be displayed, as it represents cracking between the interior joint and the members framing into the joint.

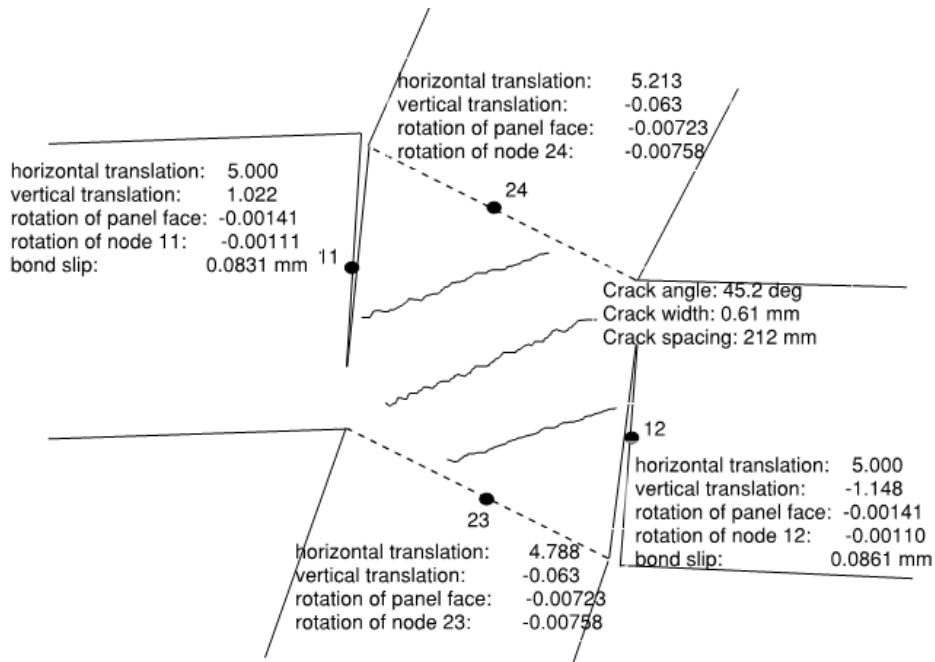


Figure 4.20: Sample sketch of a deformed interior joint

CHAPTER 5

MODEL EVALUATION AND VERIFICATION

5.1 Chapter Layout

In this chapter, the modified frame analysis procedure VecTor5 with the new joint element is evaluated and validated with experimental tests of beam-column joint subassemblies and large reinforced concrete frame structures. Examples and important considerations in modeling the joint subassemblies and frames are also discussed. The structures considered include: two joint subassemblies tested by Shiohara and Kusuhara (2007), two joint assemblies tested by Park and Dai (1988), two joint assemblies tested by Noguchi and Kashiwazaki (1992), three joint assemblies tested by Attaalla and Agbabian (2004), and three frame structures tested by Xue et al. (2011), Ghannoum and Moehle (2012), and Pampanin et al. (2007).

The chapter starts with a summary of nine interior beam-column subassemblies modeled using the analysis procedure with the new joint element. It is then followed by detailed discussions of each specimen including the experimental setup, analytical modeling, and comparisons of the experimental and analytical responses. The chapter continues with a parametric study to investigate the impact of four parameters on the analytical load-displacement response of the test specimens. The parameters include: loading type, confinement, compression softening, and bond stress. Finally, three large-scale frame structures from the literature were analyzed. The results are presented and discussed at the end of this chapter.

5.2 Beam-Column Subassemblies

5.2.1 Summary

In order to assess the performance of VecTor5 with the new joint element, nine interior beam-column subassemblies from four different tests were selected for evaluation and verification. In

this chapter, analyses performed using VecTor5 with the new joint element are referred to with the name of the joint element subroutine, V5FBCA.

The inputs used for the analyses with V5FBCA and VecTor5 were almost identical. The only difference was that the semi-rigid end offsets were not used for interior joints in the analysis with V5FBCA. The analyses with V5FBCA and VecTor5 employed common modeling options. The V5FBCA and VecTor5 analyses were performed using only the default or typical material behavior models to assess the capabilities without using special program modifications. Table 5.1 lists the default material behavior models and analysis parameters used in V5FBCA and VecTor5. One exception of the material behavior model was the concrete compression base curve. For high strength concrete with compressive strength greater than 42 MPa, Popovics (HSC) model was employed instead of the default Hognestad parabola model.

Table 5.1: Material behavior models and analysis parameters used in VecTor5

Material Property	Model
Concrete Compression Base Curve	Popovics – NSC
Concrete Compression Post-Peak	Modified Park-Kent
Concrete Compression Softening	Vecchio 1992-A
Concrete Tension Stiffening	Modified Bentz
Concrete Tension Softening	Linear
Concrete Tension Splitting	Not Considered
Concrete Confined Strength	Kupfer / Richart
Concrete Dilation	Variable - Kupfer
Concrete Cracking Criterion	Mohr-Coulomb (Stress)
Concrete Crack Width Check	Crack Limit (Agg/5)
Concrete Hysteresis	NL (Vecchio)
Concrete Slip Distortion	Vecchio-Lai
Reinforcement Hysteresis	Seckin with Bauschinger
Reinforcement Dowel Action	Tassios (Crack Slip)
Reinforcement Buckling	Malvar and Crawford
Geometric Nonlinearity	Considered
Shear Analysis Mode	Parabolic Shear Strain
Shear Protection	On
Convergence Limit	1.00001
Maximum Number of Iterations	100

In addition, the response parameters not explicitly calculated in the programs were approximated based on the following assumptions:

- In analyses with the original VecTor5 program, bar stresses at the joint interface were assumed to equal to the bar stresses in the members framing into the joint. Beam and column members in the joint region were not used because the method of semi-rigid end offsets significantly reduced the reinforcement stresses in those members.
- For joints with multiple layers of longitudinal reinforcing bars, the stresses in the two extreme layers of steel were used for the comparison.

In the experimental studies, eight subassemblies were subjected to reversed cyclic loading conditions, and one subassembly was tested under monotonic loading. The analytical study is focused on the interior beam-column joints subjected to monotonic loading. Therefore, the specimens were modeled under monotonic loading conditions. Table 5.2 summarizes the geometric properties and analytical results of nine specimens. These experimental joint subassemblies exhibited one of the following three failure mechanisms: beam yielding with no joint failure (BY), joint failure prior to beam yielding (JF), and beam yielding followed by joint failure (BYJF).

Table 5.2: Summary of the specimen properties and analytical results of interior beam-column subassemblies

Specimen	Shiohara and Kusahara (2007)		Park and Dai (1988)		
	A1	D1	U1	U2	
(a) Beam Properties					
Top Reinforcement	8-D13	6-D13	5-D16	2-D28	
Bottom Reinforcement	8-D13	6-D13	2-D16	2-D20	
Transverse Reinforcement	D6 @ 50 mm	D6 @ 50 mm	various	various	
(b) Column Properties					
Longitudinal Reinforcement	16-D13	14-D13	8-D16	8-D20	
Transverse Reinforcement	D6 @ 50 mm	D6 @ 50 mm	various	various	
(c) Joint Properties					
Concrete Strength (MPa)	28.3	30.4	45.9	36.0	
Height (mm)	300	300	457	457	
Width (mm)	300	300	406	406	
Thickness (mm)	300	300	305	305	
Trans. Reinforcement	5-D6	5-D6	5-D12/D8	5-D12	
Confinement Coefficient	0.725	0.702	0.560	0.570	
(d) Results (“Analysis” refers to the results from V5FBCA analysis)					
Failure Mechanism	Analysis	JF	JF	BY	BY
	Experiment	BYJF	BYJF	BY	BY

Peak Load (kN)	Analysis	94.0	112.7	94.7	132.7	
	Experiment	126.6	133.9	80.0	111.0	
	Analysis/Exp.	0.74	0.84	1.18	1.20	
	VT5/Exp.	1.24	1.22	1.18	1.29	
Max. Panel Shear Stress (MPa)	Analysis	3.70	4.40	3.70	4.91	
	Experiment	N/A	N/A	N/A	N/A	
	Analysis/Exp.	N/A	N/A	N/A	N/A	
Load at First Beam Yielding (kN)	Analysis	N/A	N/A	67.6	50.6	
	Experiment	118.6	89.7	54.2	78.9	
	Analysis/Exp.	N/A	N/A	1.25	0.64	
	VT5/Exp.	1.19	1.49	1.32	1.29	
Specimen	Noguchi and Kashiwazaki (1992)		Attaalla and Agbabian (2004)			
	OKJ-2	OKJ-6	SHC-1	SHC-2	SOC-3	
(a) Beam Properties						
Top Reinforcement	9-D13	8-D13	3-D10	3-D10	3-D10	
Bottom Reinforcement	7-D13	7-D13	3-D10	3-D10	3-D10	
Transverse Reinforcement	D6 @ 50 mm	D6 @ 50 mm	D6 @ 72 mm	D6 @ 72 mm	D6 @ 72 mm	
(b) Column Properties						
Longitudinal Reinforcement	20-D13	20-D13	4-D13	4-D13	4-D13	
Transverse Reinforcement	D6 @ 40 mm	D6 @ 40 mm	D6 @ 51 mm	D6 @ 51 mm	D6 @ 51 mm	
(c) Joint Properties						
Concrete Strength (MPa)	70.0	53.5	56.5	59.5	47.2	
Height (mm)	300	300	203	203	203	
Width (mm)	300	300	178	178	178	
Thickness (mm)	300	300	127	127	127	
Transverse Reinforcement	6-D6	6-D6	1-D6	2-D6	2-D6	
Confinement Coefficient	0.786	0.786	0.102	0.189	0.187	
(d) Results (“Analysis” refers to the results from V5FBCA analysis)						
Failure Mechanism	Analysis	BY	BY	BYJF	BYJF	BYJF
	Experiment	BYJF	JF	BYJF	BYJF	BYJF
Peak Load (kN)	Analysis	265.6	264.2	16.38	18.36	15.65
	Experiment	237.0	214.0	16.02	16.73	16.02
	Analysis/Exp	1.12	1.23	1.02	1.10	0.94
	VT5/Exp.	1.16	1.25	1.34	1.29	1.26
Max. Panel Shear Stress (MPa)	Analysis	12.81	11.53	5.21	5.80	4.87
	Experiment	14.16	13.11	6.88	7.24	7.20
	Analysis/Exp	0.90	0.88	0.76	0.80	0.68
Load at First Beam Yielding (kN)	Analysis	245.9	248.2	15.91	15.59	15.47
	Experiment	237	N/A	11.90	12.20	13.40
	Analysis/Exp	1.04	N/A	1.34	1.30	1.15
	VT5/Exp.	1.02	N/A	1.30	1.32	1.20
Mean (Analysis/Exp)	Peak Load		1.05 (9 specimens)			
	Max. Panel Shear Stress		0.80 (5 specimens)			
	Load at First Beam Yielding		1.12 (6 specimens)			
Coefficient of Variation (%)	Peak Load		16.3 (9 specimens)			
	Max. Panel Shear Stress		11.2 (5 specimens)			
	Load at First Beam Yielding		23.1 (6 specimens)			

Mean (VT5/Exp)	Peak Load	1.25 (9 specimens)
	Load at First Beam Yielding	1.27 (8 specimens)
VT5 Coefficient of Variation (%)	Peak Load	4.5 (9 specimens)
	Load at First Beam Yielding	10.7 (8 specimens)

With the new joint element, VecTor5 was able to provide better predictions in terms of failure mechanism and peak loads. For the nine interior joint subassemblies modeled, the ratio of predicted and observed peak load had a mean of 1.06 and a coefficient of variation of 18.3%. For the six specimens that exhibit beam yielding, the ratio of predicted and observed load at first beam yielding had a mean of 1.09 and a coefficient of variation of 21.5%.

5.2.2 Shiohara and Kusuhara (2007)

The first set of subassemblies modeled was from a benchmark test conducted by Shiohara and Kusuhara at the University of Tokyo in Japan. Six half-scaled reinforced concrete beam-column joint subassemblies isolated from moment resisting frames were tested. These specimens were seismically designed according to the AIJ Guidelines (1999). Specimen A1 was selected for this verification study. Other specimens were excluded because they were either exterior or knee joints. Shiohara and Kusuhara presented the test results of four additional specimens with similar experimental setup in their subsequent study (Shiohara and Kusuhara, 2008). Specimen D1 was selected as the second specimen for the verification.

5.2.2.1 Test Specimens

Specimens A1 and D1 had identical overall dimensions, loading setup and support restraints, but the sectional and material properties were slightly different. Figure 5.1 shows the test setup, and Figure 5.2 shows the sectional details of Specimens A1 and D1. All beam and column sections were 300 by 300 mm. The joint panel was reinforced with three transverse hoops. To measure the post-yielding stress and strain in the longitudinal reinforcing bar in the specimens, a box shape groove was made on two sides of each bar for the installation of strain gauges. The location of the grooved longitudinal bars in the beam sections is indicated by solid dots in Figure 5.2. The cross-sectional area of grooved bars was 75% of the original cross-sectional area. These bars were used inside the joint panel as well as in the beam at the locations within 450 mm from

the face of the column. The material properties of the concrete and the reinforcement are listed in Table 5.3. The subassemblies were loaded by a displacement-based horizontal reversed cyclic load, and a constant axial load of 216 kN was applied at the top of the column. A pin support was provided at the bottom of the column, and a roller was provided at both ends of the beam. This test setup was used to simulate a typical boundary condition of an interior joint.

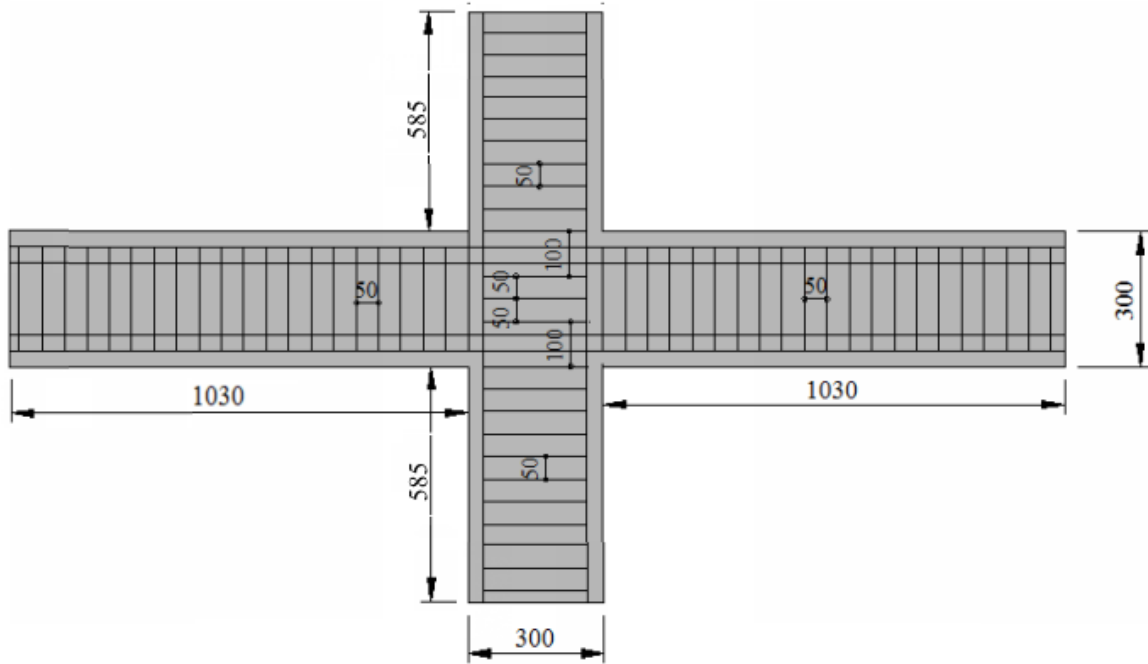


Figure 5.1: Test setup of Specimens A1 and D1 (adapted from Guner, 2008)

Table 5.3: Material properties of Specimens A1 and D1

Bar Type	Reinforcement Properties							Concrete Properties				
	d_b (mm)	F_y (MPa)	F_u (MPa)	E_s (MPa)	E_{sh} (MPa)	ϵ_{sh} ($\times 10^{-3}$)	ϵ_u ($\times 10^{-3}$)	Spec.	f'_c (MPa)	f'_t (MPa)	E_c (MPa)	ϵ'_c ($\times 10^{-3}$)
D13B ¹	12.7	456	582	176000	952	27.6	160	A1	28.3	1.76	25900	1.87
D13C ¹	12.7	357	493	176000	1032	28.2	160	D1	30.4	1.82	30000	2.03
D6 ¹	6.4	326	388	151000	5391	4.2	15.7					
D16B ²	16.0	379	558	187000	1352	27.6	160					
D13C ²	12.7	375	538	187000	1237	28.2	160					
D6 ²	6.4	366	504	191000	12000	4.2	15.7					

1: Used in Specimen A1
2: Used in Specimen D1

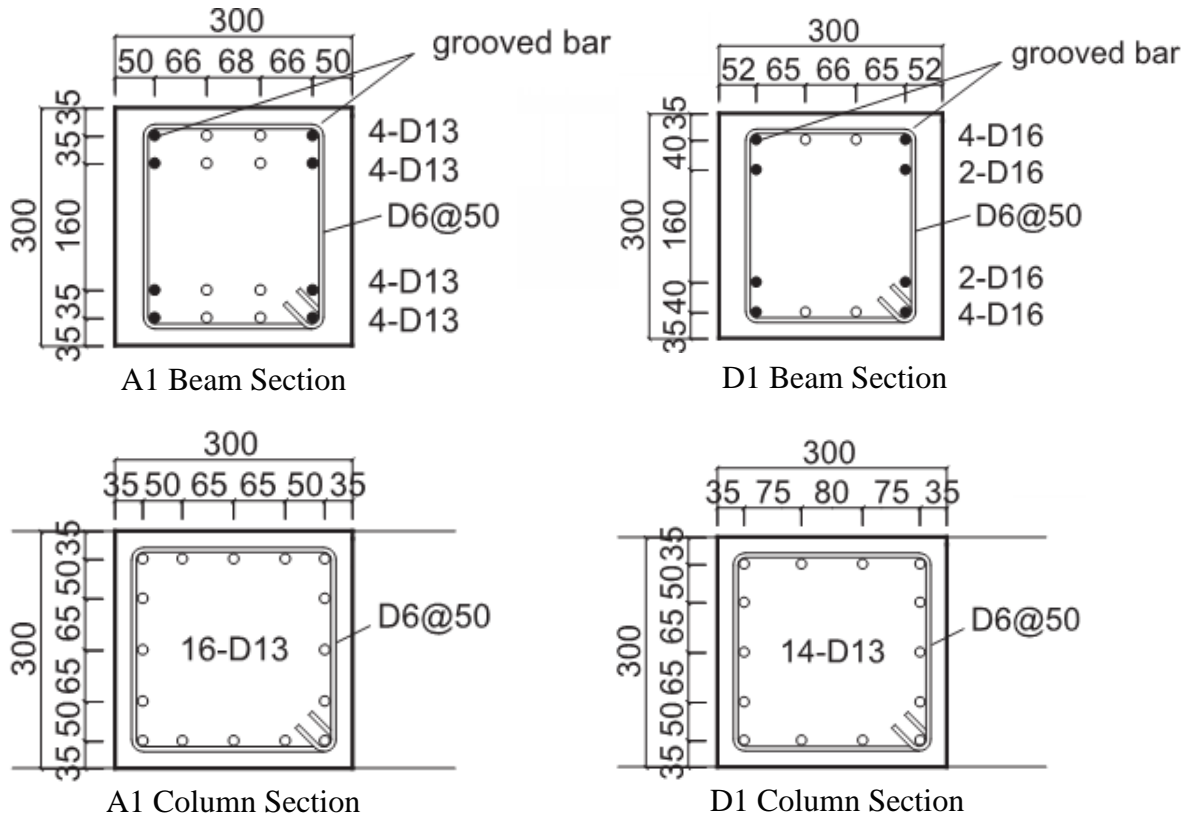


Figure 5.2: Sectional details of Specimens A1 and D1

5.2.2.2 Analytical Modeling

The two subassemblies were modeled using the same structural model, loading type and boundary conditions. The details and material properties of members were slightly different. Figure 5.3 shows the analytical model with dimensions, loading and support restraints. There were 37 nodes, 36 members and 4 support restraints in the model. The support conditions included restraints of the horizontal and vertical translations at Node 26 and restraint of the vertical translation at Node 1 and Node 25. An axial compressive load of 216 kN was applied at Node 37. A positive displacement at Node 37 was applied in 81 load stages with an increment of 1 mm starting from a zero displacement.

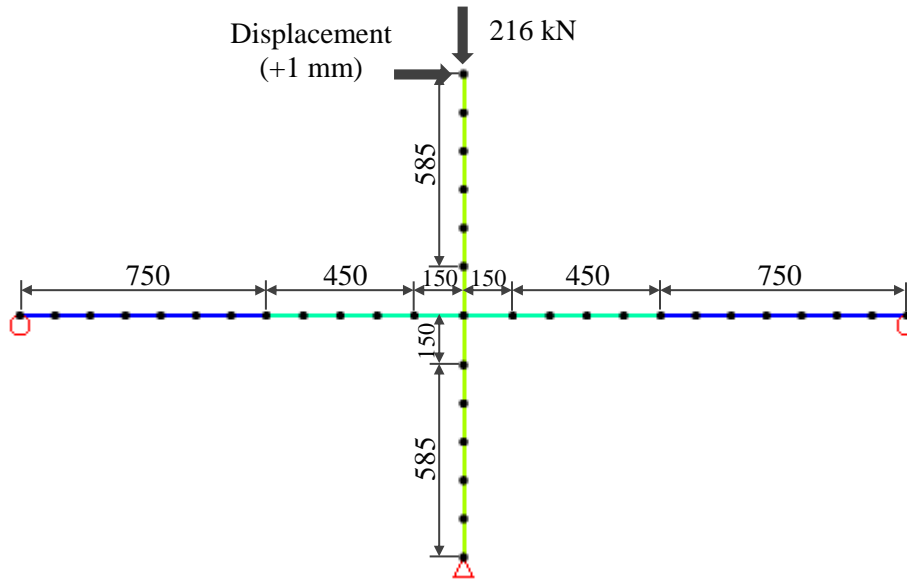


Figure 5.3: Analytical model showing dimensions, loading and support restraints of Specimens A1 and D1

Five member types were created to build the model (see Figure 5.4). The beam sections near the roller supports were represented by Member Type 1 (MT1) whereas the beam sections near the column were represented by MT2 accounting for the grooved bars. The column sections were represented by MT3. The interior joint was modeled by MT2 in the horizontal direction and MT3 in the vertical direction. MT4 and MT5 were created by doubling the reinforcing ratios of MT2 and MT3, respectively, to simulate the relatively stiffer response of the joint panel. MT4 and MT5 were only used in the analysis with the original VecTor5 program for the purpose of comparing the responses obtained prior and after the joint implementation. Each member was divided into 18 concrete layers to perform the sectional fiber analysis. Detailed general and sectional material properties of Specimen A1 are presented in Tables 5.4, 5.5 and 5.6. Specimen D1 was modeled using a similar approach.

For VecTor5 modeling of beam-column joint subassemblies, it is recommended to use at least 30 layers for the concrete sections. Layers at the top and bottom of the section should be finer than the ones at the centroid and the neutral axis. This refinement, which is valid for all the specimens modeled in this study, may further improve the analytical results.

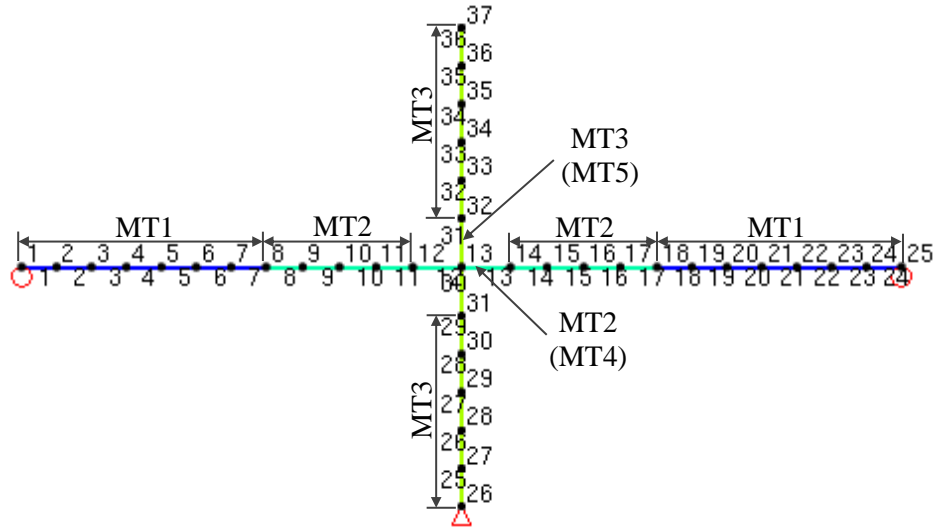


Figure 5.4: Analytical model showing material types of Specimens A1 and D1

Table 5.4: General material specifications of Specimen A1

MT	Concrete Properties					Transverse Reinforcement Properties						
	f'_c (MPa)	f'_t (MPa)	E_c (MPa)	ϵ'_c ($\times 10^{-3}$)	Other	s_t (mm)	d_{bt} (mm)	F_{yt} (MPa)	F_{ut} (MPa)	E_{st} (MPa)	ϵ_{sht} ($\times 10^{-3}$)	ϵ_{ut} ($\times 10^{-3}$)
1-5	28.3	1.76	25900	1.87	default	50.0	6.4	326	388	151000	4.2	15.7

Table 5.5: Reinforced concrete material specifications of Specimen A1

MT	D_c (mm)	W_c (mm)	ρ_t (%)	ρ_z (%)	N_x	MT	D_c (mm)	W_c (mm)	ρ_t (%)	ρ_z (%)	N_x
1	22.00	300	0.000	0.876	1	4	22.00	300	0.000	1.752	1
	17.02		0.427	0.876	3		17.02		0.854	1.752	3
	15.39		0.427	0.000	5		15.39		0.854	0.000	5
	15.39		0.427	0.000	5		15.39		0.854	0.000	5
	17.02		0.427	0.876	3		17.02		0.854	1.752	3
	22.00		0.000	0.876	1		22.00		0.000	1.752	1
2	22.00	300	0.000	0.876	1	5	22.00	300	0.000	1.752	1
	17.02		0.427	0.876	3		17.02		0.854	1.752	3
	15.39		0.427	0.000	5		15.39		0.854	0.000	5
	15.39		0.427	0.000	5		15.39		0.854	0.000	5
	17.02		0.427	0.876	3		17.02		0.854	1.752	3
	22.00		0.000	0.876	1		22.00		0.000	1.752	1
3	22.00	300	0.000	0.876	1	5	22.00	300	0.000	1.752	1
	17.02		0.427	0.876	3		17.02		0.854	1.752	3
	15.39		0.427	0.000	5		15.39		0.854	0.000	5
	15.39		0.427	0.000	5		15.39		0.854	0.000	5
	17.02		0.427	0.876	3		17.02		0.854	1.752	3
	22.00		0.000	0.876	1		22.00		0.000	1.752	1

MT: Member Type
 D_c : Layer Depth
 W_c : Width of the Section
 ρ_t : Transverse Reinforcing Ratio
 ρ_z : Out-of-Plane Reinforcing Ratio
 N_x : Number of Layers

Table 5.6: Longitudinal reinforcement material specifications of Specimen A1

MT	N	Y_s (mm)	A_s (mm ²)	D_b (mm)	F_y (MPa)	F_u (MPa)	E_s (MPa)	ϵ_{sh} ($\times 10^{-3}$)	ϵ_u ($\times 10^{-3}$)
1	1	35	508	12.7	456	582	176000	27.6	160
	2	70	508						
	3	230	508						
	4	265	508						
2	1	35	446	11.9	456	582	176000	27.6	160
	2	70	446						
	3	230	446						
	4	265	446						
3	1	35	635	12.7	357	493	176000	28.2	160
	2	85	254						
	3	150	254						
	4	215	254						
	5	265	635						
4	1	35	892	11.9	456	582	176000	27.6	160
	2	70	892						
	3	230	892						
	4	265	892						
5	1	35	1270	12.7	357	493	176000	28.2	160
	2	85	508						
	3	150	508						
	4	215	508						
	5	265	1270						

5.2.2.3 Comparison of the Analytical and Experimental Responses

Specimen A1

Specimens A1 and D1 were analyzed with V5FBCA and VecTor5. A comparison of the lateral load-deflection responses at the column tip is given in Figure 5.5. Detailed comparisons of the response parameters are reported in Table 5.7.

Table 5.7: Comparison of experimental and analytical results of Specimen A1

	Experiment	V5FBCA	VecTor5
Failure Mechanism	BYJF	JF	BY
Peak Load (kN) (Ratio = Analysis/Experiment)	126.6	94.0 (0.74)	157.6 (1.24)
Max. Panel Shear Stress (MPa) (Ratio = Analysis/Experiment)	N/A	3.70 (N/A)	N/A (N/A)
Load at First Beam Yielding (kN) (Ratio = Analysis/Experiment)	118.6	N/A (N/A)	140.7 (1.19)

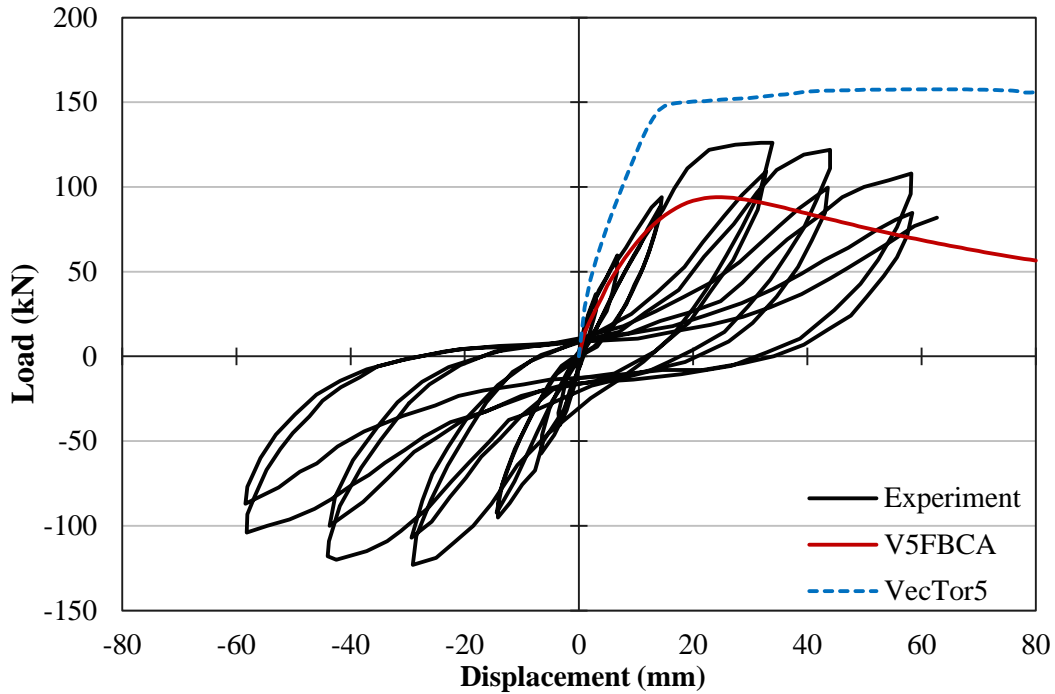


Figure 5.5: Comparison of the load-displacement response of Specimen A1

In the experiment, the beam yielded at a displacement of 21 mm, where the face rotation of the joint panel suddenly increased, greatly contributing to the overall displacement of the subassembly. At a displacement of 29 mm, the concrete crushed at the beam-joint interface, and the concrete cover started spalling off from the joint panel. At a displacement of 44 mm, the concrete cover spalled off thoroughly, which exposed the ties. Figure 5.6a shows the joint panel condition at a displacement of 60 mm.

As observed from Figure 5.5, VecTor5 overestimated the stiffness and strength of the subassembly by 24%. V5FBCA, on the other hand, underestimated the strength of the subassembly by 26%, but the stiffness and the shape of the response curve were predicted better. V5FBCA predicted a joint failure without yielding of the beam reinforcement, whereas the specimen exhibited a failure mechanism of beam yielding followed by joint failure in the experiment. The shear panel reached its peak stress of 3.70 MPa at a displacement of 26 mm, when the subassembly reached its peak load of 93.2 kN. The average crack width in the joint panel at a displacement of 60 mm was determined as 5.5 mm.

On the contrary, VecTor5 predicted failure due to beam yielding. VecTor5 predicted beam yielding at the joint interface at a displacement of 13 mm. Flexural cracks initiated in Members 11 and 14 propagated with increasing applied displacement. Cracking in the joint panel was relatively insignificant (see Figure 5.6b).

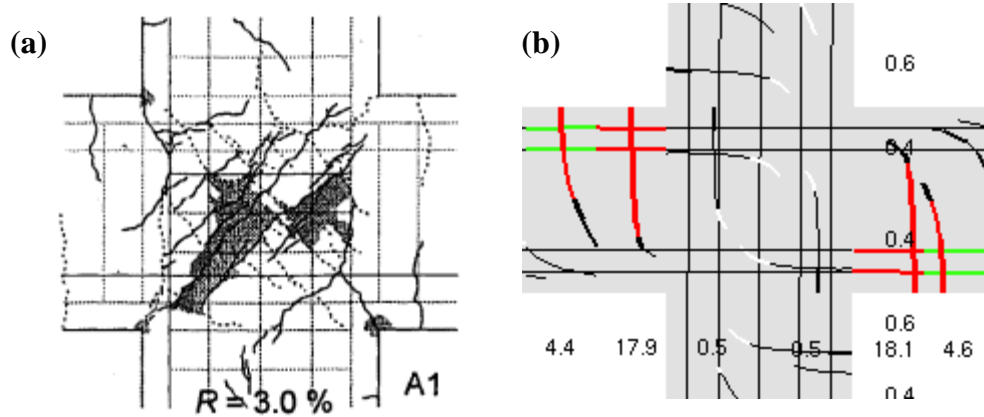


Figure 5.6: Cracking pattern of Specimen A1: (a) observed (Shiohara and Kusuhara, 2007) and (b) original VecTor5 simulation

Overall, neither of the predictions was a good match with the experimental response. V5FBCA provided a slightly better prediction by identifying the joint failure and the subsequent loss of stiffness. V5FBCA also provided a good prediction on the concrete response of the joint core.

Two relationships obtained from the analysis were compared to the experimental results. Lateral load versus shear strain of the joint panel was the first relationship for the evaluation. Figure 5.7 shows the relationship from the experimental response envelope and the monotonic analysis. The analytical response presented a lower shear strain of 26.4×10^{-3} than the experimental shear strain of 31.8×10^{-3} at a displacement of 60 mm. The load from the analysis was lower than that from the experiment because of the underestimation of the strength of the subassembly.

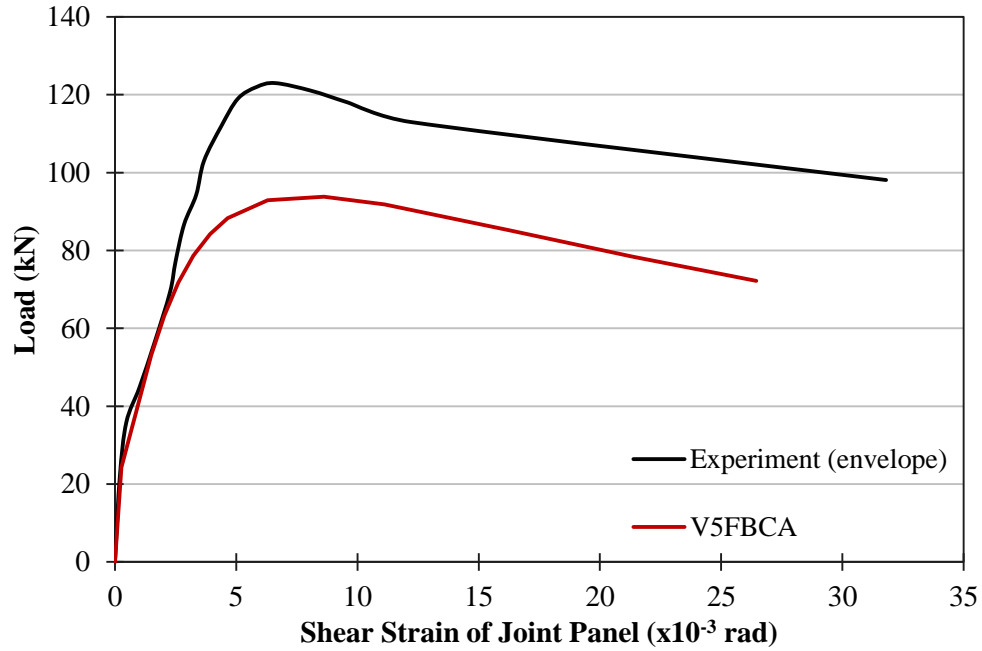


Figure 5.7: Load versus joint shear strain relationship of Specimen A1

The second parameter for evaluation was the stress in the longitudinal reinforcement. The stresses obtained from the analysis were compared to those obtained from VecTor5 (see Table 5.8). The stresses in the extreme layer of bars of the beam and column sections were selected for this comparison because they represented the extreme values of reinforcement stress in the section. V5FBCA was capable of predicting both tensile and compressive stresses reasonably well. The stress prediction followed a monotonic trend up to the peak load. One exception was that yielding of the beam bars was not captured by V5FBCA because of the low global prediction of the load-displacement response.

Table 5.8: Stress in the longitudinal bars at the joint panel interface of Specimen A1

Disp.	Rebar Stress (MPa)							
	Bottom Face Compression Side		Bottom Face Tension Side		Right Face Tension Side		Right Face Compression Side	
	V5FBCA	VT5	V5FBCA	VT5	V5FBCA	VT5	V5FBCA	VT5
2	-43	-39	-48	2	55	61	-6	-27
4	-57	-58	-3	24	100	135	-10	-40
6	-72	-77	43	57	145	198	-13	-50
8	-81	-95	73	93	176	250	-16	-60
10	-89	-111	99	130	202	260	-18	-70
12	-95	-127	119	166	224	380	-19	-79
14	-100	-140	136	198	241	456	-21	-83
16	-104	-145	148	214	255	456	-22	-80
20	-108	-147	164	218	272	456	-23	-60
25	-110	-148	170	221	280	456	-24	-39
30	-108	-150	168	226	282	456	-25	-28
40	-104	-153	157	235	283	457	-27	-16
50	-98	-167	145	298	285	476	-30	-12
60	-93	-178	135	353	293	496	-34	-2

Specimen D1

A comparison of the lateral load-deflection responses at the column tip is given in Figure 5.8.

The detailed comparisons of the response parameters are reported in Table 5.9.

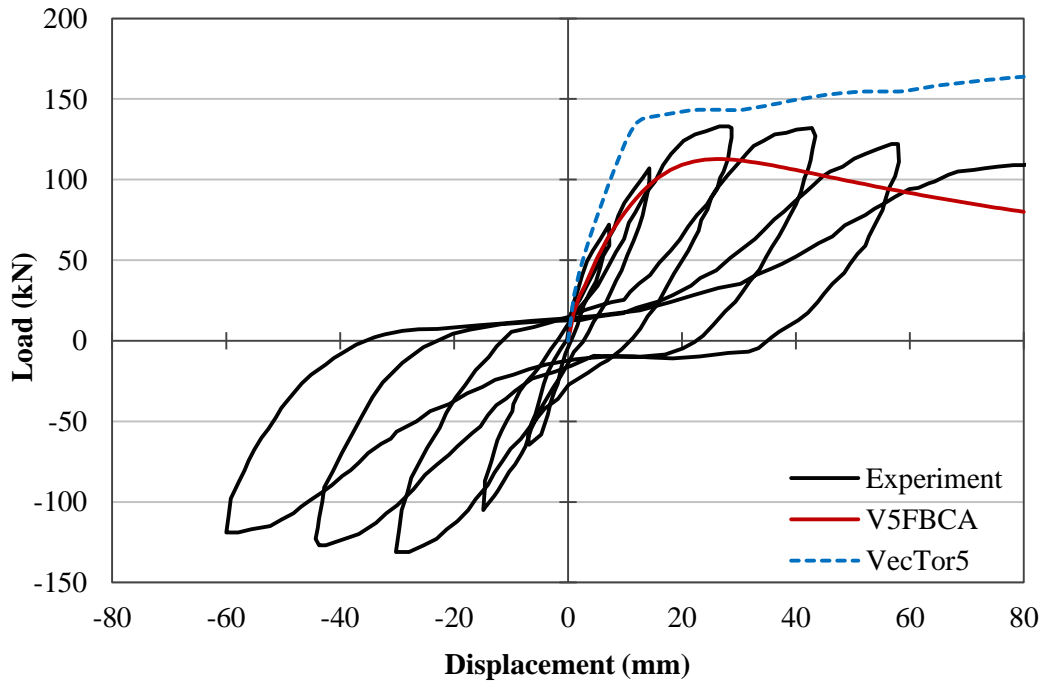


Figure 5.8: Comparison of the load-displacement response of Specimen D1

Table 5.9: Comparison of experimental and analytical results of Specimen D1

	Experiment	V5FBCA	VecTor5
Failure Mechanism	BYJF	JF	BY
Peak Load (kN) <i>(Ratio = Analysis/Experiment)</i>	133.9	112.7 <i>(0.84)</i>	163.2 <i>(1.22)</i>
Max. Panel Shear Stress (MPa) <i>(Ratio = Analysis/Experiment)</i>	N/A	4.40 <i>(N/A)</i>	N/A <i>(N/A)</i>
Load at First Beam Yielding (kN) <i>(Ratio = Analysis/Experiment)</i>	89.7	N/A <i>(N/A)</i>	134.1 <i>(1.49)</i>

Specimen D1 had a higher concrete strength than Specimen A1 with a smaller reinforcing steel ratio and reduced yield strength for the reinforcing bars. This coincided with the observation of greater peak load due to the stiffer joint core. Load and the corresponding displacement of the first beam yielding were less than those observed for Specimen A1. In the experiment, the first beam yielding occurred at a displacement of 12 mm, and yielding of the joint hoop was found at a displacement of 24 mm. The concrete cover started spalling off at a displacement of 44 mm (see Figure 5.9a). The failure of the subassembly was initiated by beam yielding followed by concrete crushing and spalling in the joint panel.

The load-displacement response predicted by V5FBCA and VecTor5 followed the same trends as before. VecTor5 overestimated the strength of the subassembly by 22%, whereas V5FBCA underestimated the strength by 16%. V5FBCA predicted joint failure without yielding of the beam reinforcement whereas the specimen exhibited a failure mechanism of beam yielding followed by joint failure in the experiment. Yielding of the joint hoop was found at a displacement of 24 mm. The shear panel reached its peak stress of 4.40 MPa at a displacement of 26 mm, where the subassembly reached the peak load of 112.7 kN. The average crack width in the joint panel at a displacement of 60 mm was 5.5 mm.

On the other hand, VecTor5 predicted failure due to beam yielding. VecTor5 predicted beam yielding at a displacement of 11 mm. Flexural cracking initiated at the beam-column interface and propagated with increasing applied displacement. Shear cracking on the joint panel was relatively insignificant compared to the beam flexural cracks (see Figure 5.9b).

Overall, the prediction of the load-displacement response of Specimen D1 was better than that of Specimen A1. V5FBCA provided a slightly better prediction than VecTor5 by identifying the joint failure and the subsequent loss of stiffness.

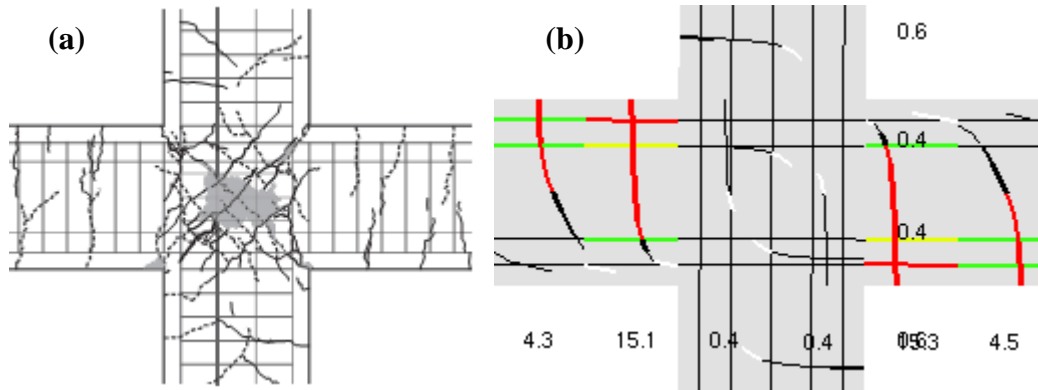


Figure 5.9: Cracking pattern of Specimen D1: (a) observed (Shiohara and Kusuhara, 2008) and (b) original VecTor5 simulation

5.2.3 Park and Dai (1988)

The second set of subassemblies modeled was from tests conducted by Park and Dai. Four interior beam-column subassemblies were tested under reversed cyclic and gravity loading. These specimens were designed following the requirements of the New Zealand concrete design code, NZS 3101. Plastic hinging was designed to take place in the beams. Two out of the four interior joint subassemblies, Unit 1 and Unit 2, were selected for verification. The other two specimens were excluded because they presented only slightly different concrete strength and reinforcing details from the selected specimens.

5.2.3.1 Test Specimens

Specimens Unit 1 and Unit 2 had identical dimensions, loading setup and support restraints, but the magnitudes of the applied gravity loads were different. The two subassemblies used different sectional designs with different concrete and reinforcing steel material properties. Figure 5.10 and Figure 5.11 shows the test setup. Figure 5.12 shows sectional details of Unit 1 and Unit 2. The beams were 457 by 229 mm, and the columns were 406 by 305 mm. Note that the part of the

column section was reinforced using ties with a combination of square and diamond orientation. The spacing and type of transverse reinforcement varied along the length of the beams and columns. The joint was reinforced with five transverse ties in both subassemblies. The material properties of the concrete and the reinforcement are listed in Table 5.10. The subassemblies were loaded in a displacement-controlled mode. A pair of gravity loads of 55 kN and 67 kN were applied at 848 mm away from the column centerlines of Specimens Unit 1 and Unit 2, respectively. The displacement-based horizontal reversed cyclic load was applied at the top of the column. The subassemblies were supported by a pin at the bottom of the column. The supports at both ends of the beam restricted movement in the vertical direction. This setup was used to simulate a typical boundary condition of an interior joint.

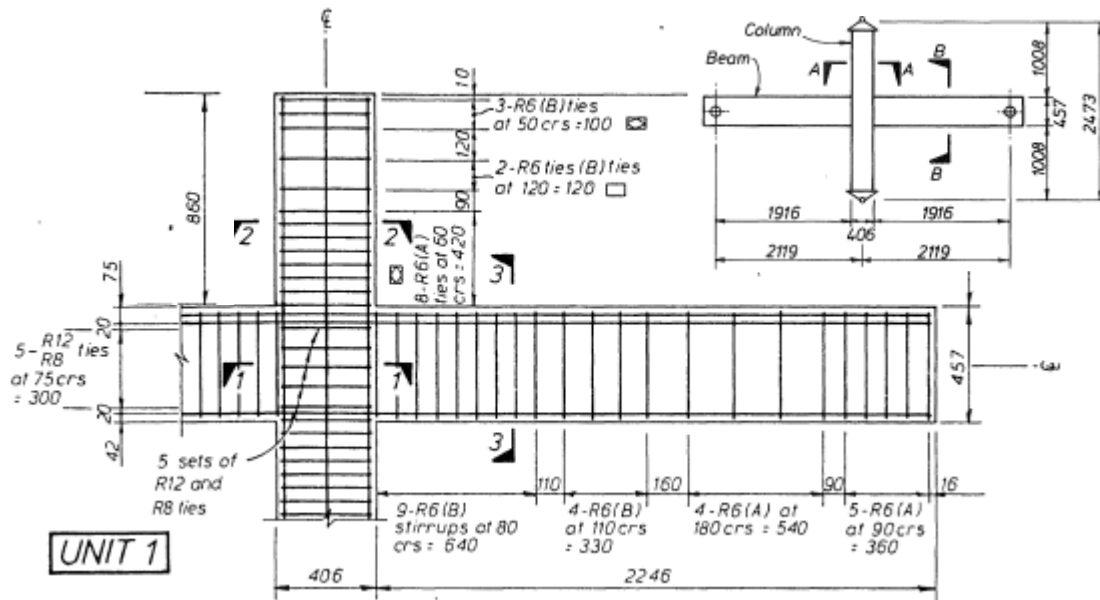


Figure 5.10: Test setup of Specimen Unit 1 (Park and Dai, 1988)

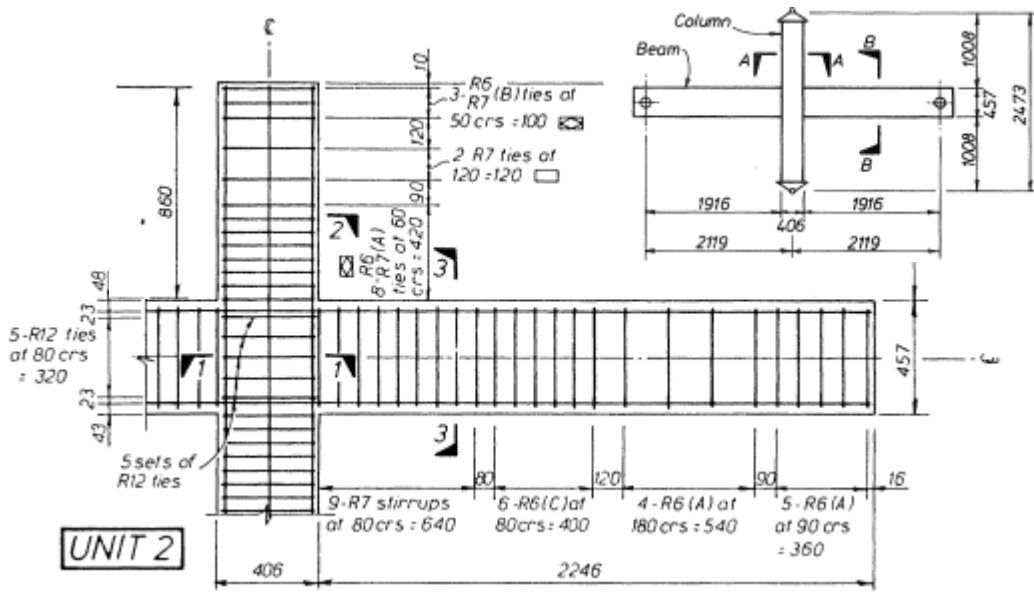
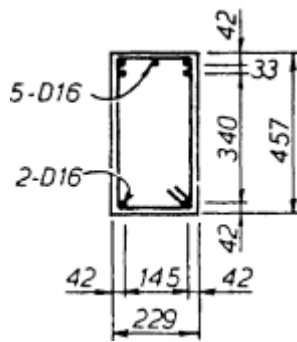
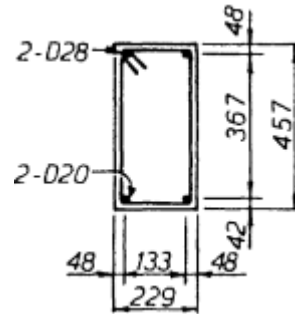


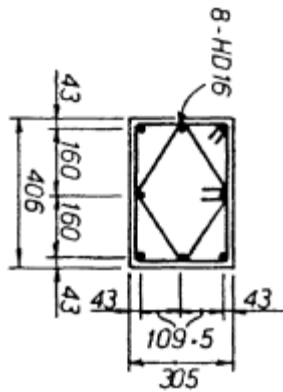
Figure 5.11: Test setup of Specimen Unit 2 (Park and Dai, 1988)



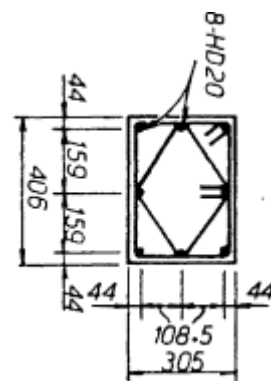
Unit 1 Beam Section



Unit 2 Beam Section



Unit 1 Column Section



Unit 2 Column Section

Figure 5.12: Sectional details of Specimens Unit 1 and Unit 2 (Park and Dai, 1988)

Table 5.10: Material properties of Specimens Unit 1 and Unit 2

Bar Type	Reinforcement Properties							Spec.	Concrete Properties			
	d_b (mm)	F_y (MPa)	F_u (MPa)	E_s (MPa)	E_{sh} (MPa)	ϵ_{sh} ($\times 10^{-3}$)	ϵ_u ($\times 10^{-3}$)		f'_c (MPa)	f'_t^* (MPa)	E_c^* (MPa)	ϵ'_c^* ($\times 10^{-3}$)
D16B ¹	16.0	294	434	210400	3580	25.5	64.6	Unit 1	45.9	2.24	29400	2.14
HD16C ¹	16.0	498	660	196600	3051	18.0	71.1	Unit 2	36.0	1.98	26820	2.07
D28B ²	28.0	314	482	200700	4260	19.3	58.7					
D20B ²	20.0	300	447	210300	3522	23.8	65.5					
HD20C ²	20.0	476	644	197100	2800	18.0	78.0					
R6(A) ^{1,2}	6.0	282	403	205800	1453	5.0	88.3					
R6(B) ¹	6.0	366	466	203400	1541	5.0	69.9					
R6(C) ²	6.0	360	445	202400	1123	5.0	80.7					
R7 ²	7.0	364	521	201100	2133	5.0	78.6					
R8 ²	8.0	360	492	189300	1760	5.0	80.0					
R12 ^{1,2}	12.0	283	420	202700	1930	5.0	76.0					

1: Used in Specimen Unit 1
 2: Used in Specimen Unit 2
 *: estimated

5.2.3.2 Analytical Modeling

The subassemblies were modeled using the same structural model and boundary conditions, but with different loading and sectional properties. Figure 5.13 shows the analytical model with dimensions, loading, and support restraints. There were 37 nodes, 36 members, and 4 support restraints in the model. Node 26 was restrained in both the horizontal and vertical directions for a pin support, while Nodes 1 and 25 were restrained in the vertical direction for roller supports. Gravity loads of 55 kN were applied at Nodes 8 and 18 of Unit 1. Gravity loads of 67 kN were applied at the same nodes for Unit 2. A positive horizontal displacement at Node 37 was applied in 81 load stages with an increment of 2 mm starting from a zero displacement.

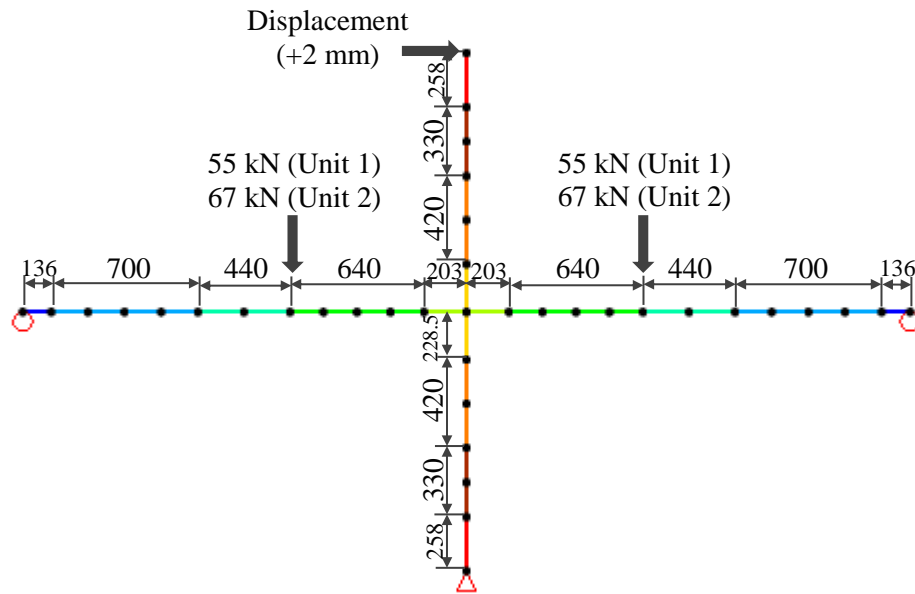


Figure 5.13: Analytical model showing dimensions, loading and support restraints of Specimens Unit 1 and Unit 2

Eleven member types were created to build the model (see Figure 5.14). Member Types 1 through 5 were used to model the beam. Member Types 6 through 9 were used to model the column. Multiple member types were needed for the beam and column sections because of the varying transverse reinforcement along the length of the members. Based on the cross-sectional area of the ties, a weighted average of the transverse reinforcement properties was used for the column sections reinforced with a combination of R8 and R12 ties. The interior joint was modeled by MT5 in the horizontal direction and MT6 in the vertical direction. MT10 and MT11 were created by doubling the reinforcement ratios of MT5 and MT6, respectively, to simulate the relatively stiffer behavior of the joint panel. MT10 and MT11 were used as semi-rigid end offsets in the analysis with the original VecTor5 program. Each member was divided into 18 to 22 concrete layers to perform the fiber analysis. More detailed properties of Specimen Unit 1 are presented in Table 5.11, 5.12 and 5.13. Specimen Unit 2 was modeled using a similar approach.

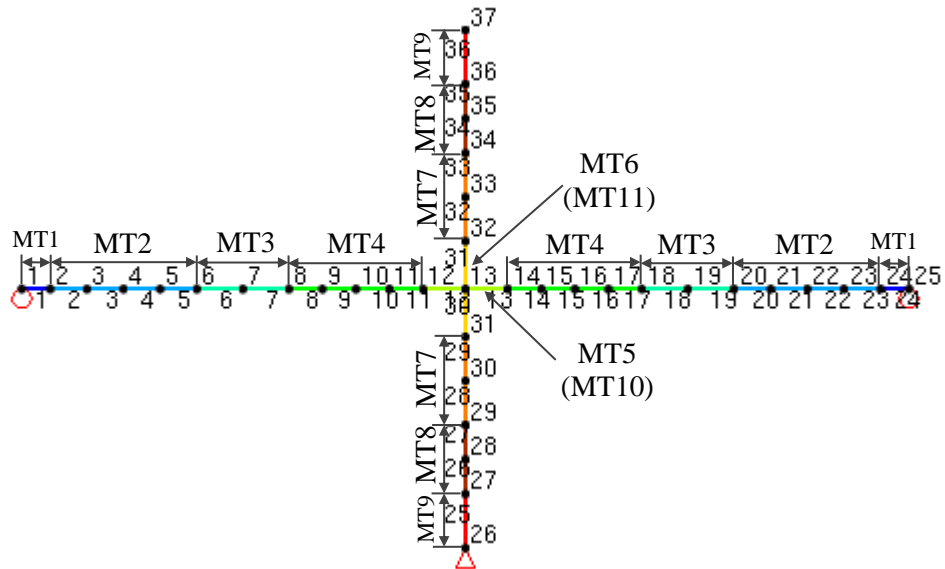


Figure 5.14: Analytical model showing material types of Specimens Unit 1 and Unit 2

Table 5.11: General material specifications of Specimen Unit 1

MT	Concrete Properties					Transverse Reinforcement Properties						
	f'_c (MPa)	f'_t (MPa)	E_c (MPa)	ϵ'_c ($\times 10^{-3}$)	Other	s_t (mm)	d_{bt} (mm)	F_{yt} (MPa)	F_{ut} (MPa)	E_{st} (MPa)	ϵ_{sht} ($\times 10^{-3}$)	ϵ_{ut} ($\times 10^{-3}$)
1	45.9	2.24	29400	2.14	default	90	6.0	282	403	205800	5.0	88.3
2						180	6.0	282	403	205800	5.0	88.3
3						110	6.0	366	466	203400	5.0	69.9
4						80	6.0	366	466	203400	5.0	69.9
5						0	0	0	--	--	--	--
6						75	14.4	283	420	202700	5.0	76.0
7						60	8.5	282	403	205800	5.0	88.3
8						120	6.0	366	466	203400	5.0	69.9
9						50	8.5	366	466	203400	5.0	69.9
10						0	0	0	--	--	--	--
11						75	14.4	283	420	202700	5.0	76.0

Table 5.12: Reinforced concrete material specifications of Specimen Unit 1

MT	D_c (mm)	W_c (mm)	ρ_t (%)	ρ_z (%)	N_x	MT	D_c (mm)	W_c (mm)	ρ_t (%)	ρ_z (%)	N_x
1	28.00	229	0.000	0.414	1	7	27.00	305	0.000	0.990	1
	24.01		0.275	0.414	2		20.41		0.610	0.990	3
	19.06		0.275	0.000	8		19.13		0.610	0.000	6
	19.06		0.275	0.000	8		19.13		0.610	0.000	6
	24.01		0.275	0.414	2		20.41		0.610	0.990	3
	28.00		0.000	0.414	1		27.00		0.000	0.990	1

2	28.00	229	0.000	0.213	1	8	27.00	305	0.000	0.310	1
	24.01		0.141	0.213	2		24.01		0.160	0.310	2
	19.06		0.141	0.000	8		21.33		0.160	0.000	6
	19.06		0.141	0.000	8		21.33		0.160	0.000	6
	24.01		0.141	0.213	2		24.01		0.160	0.310	2
	28.00		0.000	0.213	1		27.00		0.000	0.310	1
3	28.00	229	0.000	0.338	1	9	27.00	305	0.000	1.190	1
	24.01		0.225	0.338	2		20.41		0.730	1.190	3
	19.06		0.225	0.000	8		19.13		0.730	0.000	6
	19.06		0.225	0.000	8		19.13		0.730	0.000	6
	24.01		0.225	0.338	2		20.41		0.730	1.190	3
	28.00		0.000	0.338	1		27.00		0.000	1.190	1
4	28.00	229	0.000	0.465	1	10	28.00	229	0.000	0.000	1
	24.01		0.309	0.465	2		20.05		0.000	0.000	10
	19.06		0.309	0.000	8		20.05		0.000	0.000	10
	19.06		0.309	0.000	8		28.00		0.000	0.000	1
	24.01		0.309	0.465	2		19.50		0.000	3.240	1
	28.00		0.000	0.465	1		21.74		2.860	3.240	5
5	28.00	229	0.000	0.000	1	11	18.70	305	2.860	0.000	4
	20.05		0.000	0.000	10		18.70		2.860	0.000	4
	20.05		0.000	0.000	10		21.74		2.860	3.240	5
	28.00		0.000	0.000	1		19.50		0.000	3.240	1
6	19.50	305	0.000	1.620	1						
	21.74		1.430	1.620	5						
	18.70		1.430	0.000	4						
	18.70		1.430	0.000	4						
	21.74		1.430	1.620	5						
	19.50		0.000	1.620	1						

Table 5.13: Longitudinal reinforcement material specifications of Specimen Unit 1

MT	N	Y_s (mm)	A_s (mm ²)	D_b (mm)	F_y (MPa)	F_u (MPa)	E_s (MPa)	ϵ_{sh} ($\times 10^{-3}$)	ϵ_u ($\times 10^{-3}$)
1-5	1	42	600	16.0	294	434	210400	25.5	64.6
	2	75	400						
	3	415	400						
6-9	1	43	600	16.0	498	660	196600	18.0	71.1
	2	203	400						
	3	363	600						
10	1	42	1200	16.0	294	434	210400	25.5	64.6
	2	75	800						
	3	415	800						
11	1	43	1200	16.0	498	660	196600	18.0	71.1
	2	203	800						
	3	363	1200						

5.2.3.3 Comparison of the Analytical and Experimental Responses

Specimen Unit 1

Specimen Unit 1 was analyzed with V5FBCA and VecTor5. A comparison of the lateral load-deflection responses at the column tip is given in Figure 5.15. Detailed comparisons of the response parameters are reported in Table 5.14.

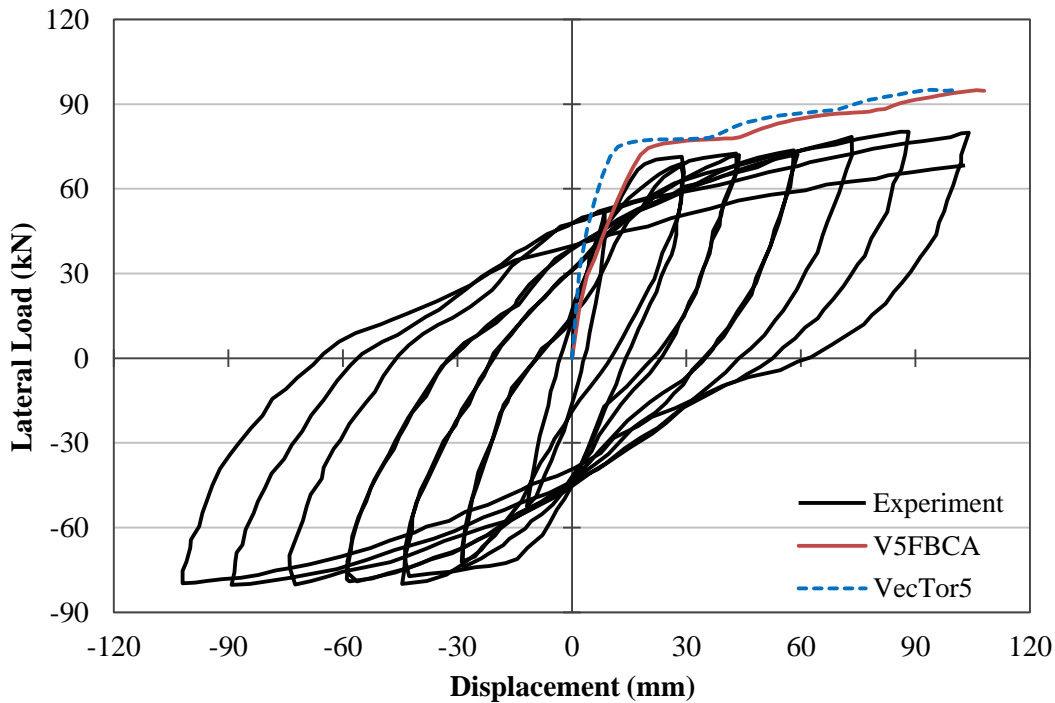


Figure 5.15: Comparison of the load-displacement response of Specimen Unit 1

Table 5.14: Comparison of experimental and analytical results of Specimen Unit 1

	Experiment	V5FBCA	VecTor5
Failure Mechanism	BY	BY	BY
Peak Load (kN) <i>(Ratio = Analysis/Experiment)</i>	80.2	94.7 <i>(1.18)</i>	95.0 <i>(1.18)</i>
Max. Panel Shear Stress (MPa) <i>(Ratio = Analysis/Experiment)</i>	N/A	3.73 <i>(N/A)</i>	N/A <i>(N/A)</i>
Load at First Beam Yielding (kN) <i>(Ratio = Analysis/Experiment)</i>	54.2	67.6 <i>(1.25)</i>	71.4 <i>(1.32)</i>

The subassembly was designed for plastic hinging to take place in the beams. The joint panel was designed with sufficient transverse reinforcement to avoid excessive joint damage. In the experiment, the subassembly failed due to excessive flexural cracking in the region adjacent to the column faces. The subassembly sustained its strength and stiffness throughout the test. The first plastic hinge was formed when the lateral load was 54.2 kN. At a displacement of 30 mm, the maximum crack width measured was 1.8 mm in the beam, and 0.2 mm in the joint core. The first cover concrete spalling, occurring on the beam, was observed at a displacement of 45 mm, when the maximum crack width on the joint panel was found to be 0.6 mm. The hoops in the joint core reached the yielding stress at the end of the test. Figure 5.16a shows the joint panel condition at a displacement of 102 mm.

The failure mode predicted by the analysis procedures was flexural failure due to beam yielding. This prediction matched well with the observed failure mechanism. The analysis results from V5FBCA were found to be similar to the results from VecTor5 because the response was governed by yielding of the beam, and the joint was heavily reinforced. V5FBCA predicted the first yielding of the beam longitudinal bar at the left face of the joint panel at a displacement of 16 mm. With increasing applied displacement, the flexural cracks propagated through the depth of the beam section. At a displacement of 30 mm, the maximum crack width in the beam was 2.7 mm, while the average crack width in the joint panel was 0.65 mm. The average crack width in the joint core was 0.67 mm at a displacement of 46 mm. However, the transverse reinforcement only reached 45% of the yielding stress at the end of the simulation, which disagreed with the experimental observations. The joint core had not reached its shear capacity by the time the failure took place.

VecTor5 predicted the first beam yielding at a displacement of 10 mm. Flexural failure of Member 9 took place at a displacement of 100 mm. The joint core was undamaged because of the semi-rigid end offsets in addition to the sufficient transverse reinforcement. Figure 5.16b shows the simulated joint panel conditions by VecTor5 at a displacement of 100 mm.

In conclusion, V5FBCA provided an acceptable prediction in terms of the maximum load. The analytical results presented good conditions of the joint panel throughout the simulation, matching the experimental observations. The failure mechanism of beam yielding was also captured successfully. However, there was a discrepancy of the initial stiffness between

V5FBCA and VT5. The stiffness values were expected to be similar because the failure mechanism was beam yielding.

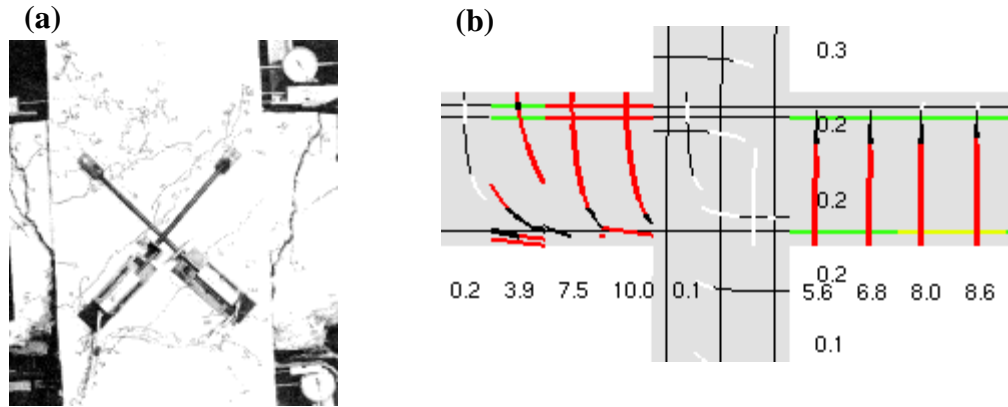


Figure 5.16: Cracking pattern of Specimen Unit 1: (a) observed (Park and Dai, 1988) and (b) original VecTor5 simulation

The stresses obtained from the analysis were compared to those obtained from VecTor5 (see Table 5.15). The stresses on the top and left faces of the joint panel were selected for the comparison. V5FBCA was capable of predicting both tensile and compressive stresses reasonably well. The stress prediction followed a monotonic trend. One exception was that yielding of the columns bars was predicted by V5FBCA, which did not match with the experimental observations.

Table 5.15: Stress in the longitudinal bars at the joint panel interface of Specimen Unit 1

Disp.	Rebar Stress (MPa)							
	Top Face Tension Side		Top Face Compression Side		Left Face Compression Side		Left Face Tension Side	
	V5FBCA	VT5	V5FBCA	VT5	V5FBCA	VT5	V5FBCA	VT5
2	137	11	-9	-16	-14	-28	147	52
8	330	115	-20	-45	-21	-63	301	212
20	506	202	-34	-59	-38	-59	325	294
60	532	252	-39	-67	-46	-20	328	378
80	533	279	-40	-72	-48	-58	329	404
100	535	352	-43	-65	-52	-126	331	421

Specimen Unit 2

A comparison of the lateral load-deflection responses at the column tip is given in Figure 5.17. Detailed comparisons of the response parameters are reported in Table 5.16.

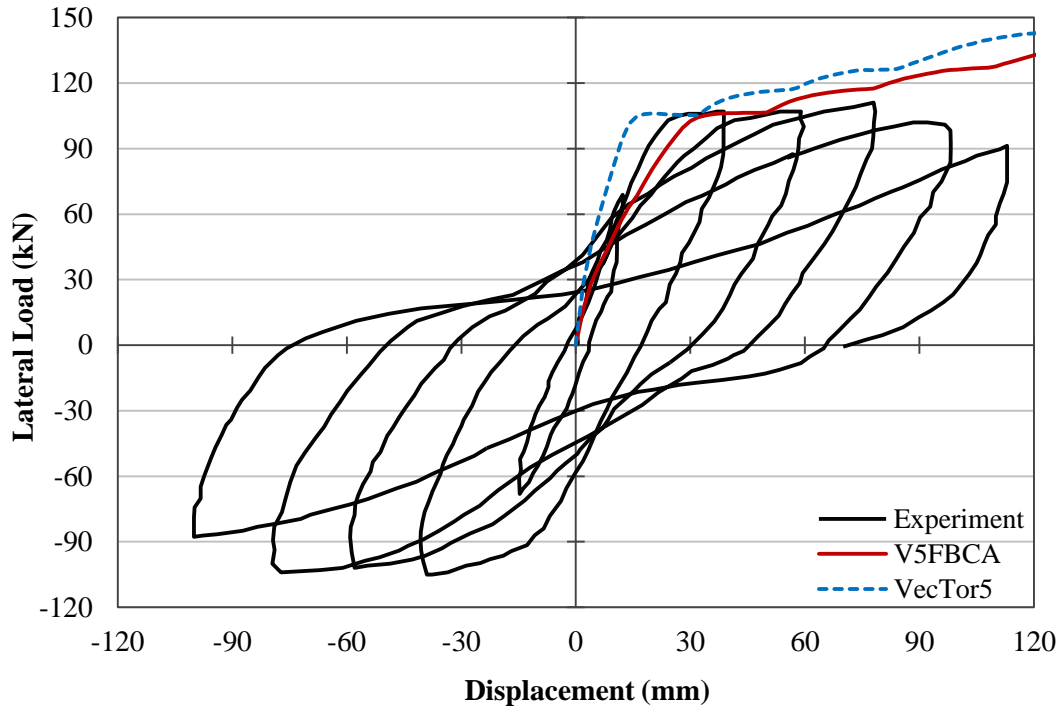


Figure 5.17: Comparison of the load-displacement response of Specimen Unit 2

Table 5.16: Comparison of experimental and analytical results of Specimen Unit 2

	Experiment	V5FBCA	VecTor5
Failure Mechanism	BY	BY	BY
Peak Load (kN) (Ratio = Analysis/Experiment)	111.0	132.7 (1.20)	142.8 (1.29)
Max. Panel Shear Stress (MPa) (Ratio = Analysis/Experiment)	N/A	4.91 (N/A)	N/A (N/A)
Load at First Beam Yielding (kN) (Ratio = Analysis/Experiment)	78.9	50.6 (0.64)	101.4 (1.29)

The experimental load-displacement response of Unit 2 was similar to Unit 1. The subassembly exhibited a flexural failure at the beam-column panel zone interface. A greater peak load was observed because of the higher longitudinal reinforcing ratio in the critical beam sections. The first spalling of cover concrete in the beam was observed at a displacement of 45 mm, where the

maximum crack width on the joint core was found to be 0.4 mm. The hoop stress in the joint core was close to its yielding stress at the end of the test. Pictures of the condition of Unit 2 at the end of the test were not provided in the original paper.

V5FBCA and VecTor5 both predicted the failure mechanism well as beam yielding. V5FBCA predicted the first yielding at a displacement of 10 mm. At a displacement of 45 mm, the flexural cracks propagated through the beam section. At this time, the maximum crack width in the beam was 3.0 mm, while the average crack width in the joint panel was 0.66 mm. Member 9 eventually failed in flexure.

VecTor5 predicted the first beam yielding at a displacement of 14 mm. Flexural failure of Member 9 took place at a displacement of 128 mm. Shear cracking in the joint panel was minimal. Figure 5.18 shows the predicted joint panel conditions by VecTor5 at failure.

In conclusion, V5FBCA provided a satisfactory prediction on the behavior of the joint panel. The joint panel was in good condition throughout the simulation, matching the experimental observations. The failure mechanism of beam yielding was also captured successfully.

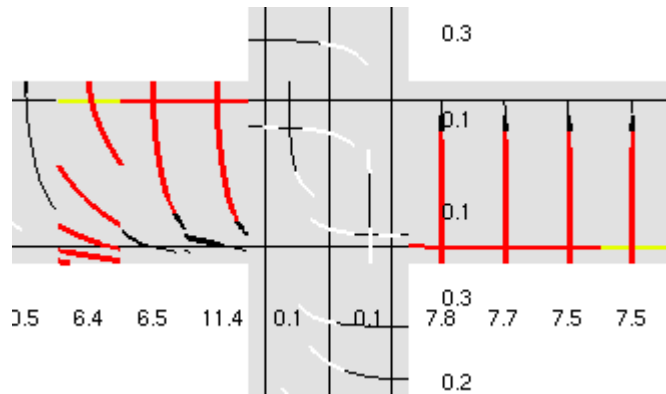


Figure 5.18: Cracking pattern of Specimen Unit 2 predicted by original VecTor5 simulation

5.2.4 Noguchi and Kashiwazaki (1992)

The third set of subassemblies modeled was from a test conducted by Noguchi and Kashiwazaki at Chiba University in Japan. Six one-third scaled interior beam-column joints with high-strength concrete and reinforcement were tested. These subassemblies were designed according to the AIJ

Guidelines (1988). One of the objectives was to study whether the provisions were applicable to joints with high-strength materials and to establish a universal design method regardless of the material strengths. Two of the six subassemblies, OKJ2 and OKJ6, were selected for verification. Specimen OKJ2 was selected because the subassembly was tested under monotonic loading conditions. Specimen OKJ6 was selected as a comparison companion because it had a lower concrete strength than Specimen OKJ2. The other four specimens were excluded because they presented only slightly different concrete strength and reinforcing details from the selected specimens.

5.2.4.1 Test Specimens

Specimens OKJ2 and OKJ6 had identical overall dimensions, loading setup, and support restrains, but the magnitudes of the column axial load were different. The subassemblies were designed with different concrete strength and section properties. Figures 5.19 and 5.20 show the test setup and sectional details, respectively. The dimensions of the beams were 300 by 200 mm, and the dimensions of the columns were 300 by 300 mm. The longitudinal reinforcement in the columns was designed to remain elastic. The joint panel was reinforced with three sets of transverse tie reinforcement. Each set of reinforcement contained two ties. The material properties of the concrete and the reinforcement are listed in Table 5.17. The subassemblies were loaded by a displacement-controlled actuator. Constant compressive loads of 756 kN and 578 kN were applied along the centerline of the column of Specimens OKJ2 and OKJ6, respectively. Both ends of the beam were supported in the vertical direction. The bottom of the subassembly was supported while the horizontal loading point was at the top of the column.

Table 5.17: Material properties of Specimens OKJ2 and OKJ6

Bar Type	Reinforcement Properties							Spec.	Concrete Properties			
	d_b (mm)	F_y (MPa)	F_u (MPa)	E_s (MPa)	E_{sh}^* (MPa)	ϵ_{sh}^* ($\times 10^{-3}$)	ϵ_u^* ($\times 10^{-3}$)		f'_c (MPa)	f'_t (MPa)	E_c (MPa)	ϵ'_c ($\times 10^{-3}$)
D13	13.0	718	767	186000	408	4.0	40.0	OKJ2	70.0	2.76	35100	2.96
D6	6.0	955	1140	182000	5324	5.3	40.0	OKJ6	53.5	2.41	36800	2.23

*: estimated

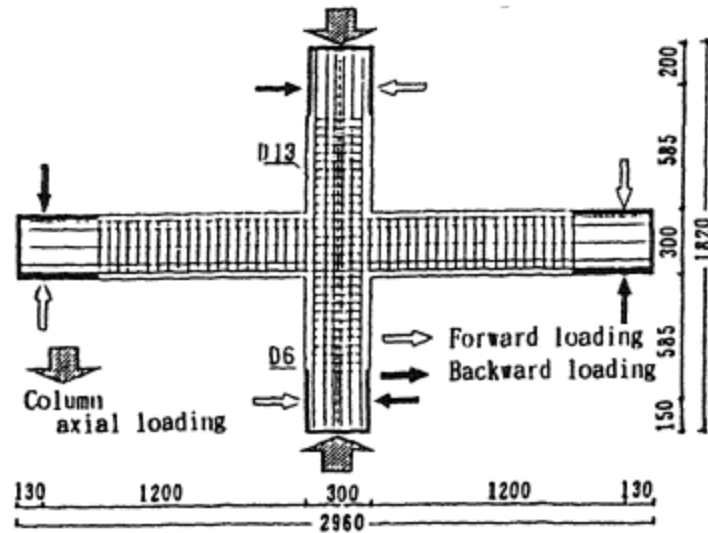


Figure 5.19: Test setup of Specimens OKJ2 and OKJ6 (Noguchi and Kashiwazaki, 1992)

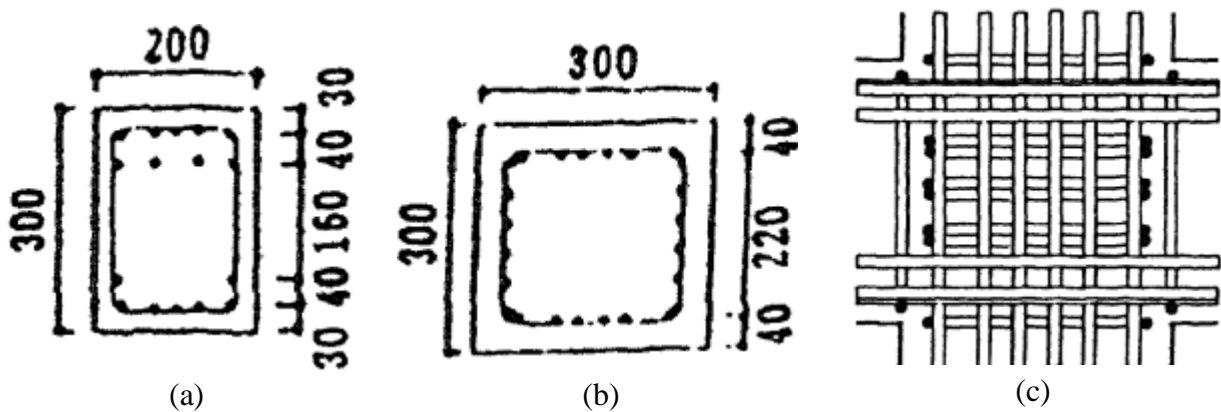


Figure 5.20: Sectional details of Specimens OKJ2 and OKJ6: (a) beam section, (b) column section, and (c) detailed joint reinforcement (Noguchi and Kashiwazaki, 1992)

5.4.3.2 Analytical Modeling

The subassemblies were modeled using the same structural model and boundary conditions, but the loading and sectional properties were changed. Figure 5.21 shows the analytical model with dimensions, loading, and support restraints. There were 33 nodes, 32 members, and 4 support restraints in the model. Both Node 2 and Node 20 were restrained in the vertical direction. Node 22 was restrained in the horizontal and vertical directions. Column compressive loads of 756 kN and 577.8 kN were applied at Node 33 of Specimens OKJ2 and OKJ6, respectively. In addition,

a positive horizontal displacement was applied at Node 33 in 161 load stages with an increment of 1 mm starting from a zero displacement.

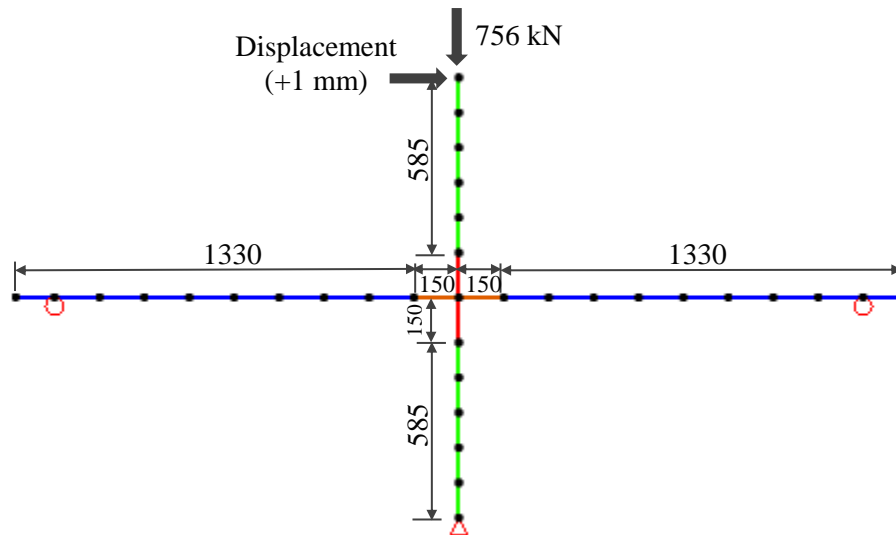


Figure 5.21: Analytical model showing dimensions, loading and support restraints of Specimens OKJ2 and OKJ6

Six member types were created to build the model (see Figure 5.22). Member Types 1 and 2 were used to model the beam sections. Member Types 3 and 4 were used to model the column sections. The interior joint was modeled by MT2 in the horizontal direction and MT4 in the vertical direction. MT5 and MT6 were created by doubling the reinforcement ratios of MT2 and MT4, respectively, to account for semi-rigid end offsets in the joint region. Each member was divided into 20 to 22 concrete layers to perform the layered sectional analysis. Detailed general and sectional material properties of Specimen OKJ2 are presented in Table 5.18, 5.19 and 5.20. Specimen OKJ6 was modeled using a similar approach.

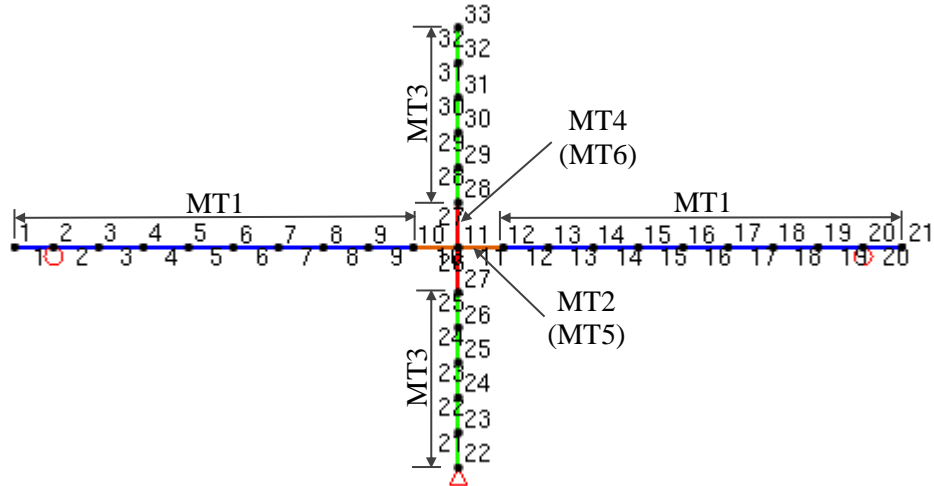


Figure 5.22: Analytical model showing material types of Specimens OKJ2 and OKJ6

Table 5.18: General material specifications of Specimen OKJ2

MT	Concrete Properties					Transverse Reinforcement Properties						
	f'_c (MPa)	f'_t (MPa)	E_c (MPa)	ϵ'_c ($\times 10^{-3}$)	Other	s_t (mm)	d_{bt} (mm)	F_{yt} (MPa)	F_{ut} (MPa)	E_{st} (MPa)	ϵ_{sht} ($\times 10^{-3}$)	ϵ_{ut} ($\times 10^{-3}$)
1	70.0	2.76	35100	2.96	default	50	6.0	995	1140	182000	5	40
2						0	0	995	1140	182000	5	40
3						40	6	995	1140	182000	5	40
4						50	8.4	995	1140	182000	5	40
5						0	0	995	1140	182000	5	40
6						50	8.4	995	1140	182000	5	40

Table 5.19: Reinforced concrete material specifications of Specimen OKJ2

MT	D_c (mm)	W_c (mm)	ρ_t (%)	ρ_z (%)	N_x	MT	D_c (mm)	W_c (mm)	ρ_t (%)	ρ_z (%)	N_x
1	18.00	200	0.000	0.851	1	4	14.00	300	0.000	1.172	2
	15.92		0.560	0.851	3		13.51		0.747	1.172	5
	14.04		0.560	0.000	6		13.61		0.747	0.000	4
	14.04		0.560	0.000	6		13.61		0.747	0.000	4
	15.92		0.560	0.851	3		13.51		0.747	1.172	5
	18.00		0.000	0.851	1		14.00		0.000	1.172	2
2	18.00	200	0.000	0.000	1	5	18.00	200	0.000	0.000	1
	14.67		0.000	0.000	9		14.67		0.000	0.000	9
	14.67		0.000	0.000	9		14.67		0.000	0.000	9
	18.00		0.000	0.000	1		18.00		0.000	0.000	1
3	14.00	300	0.000	0.924	2	6	14.00	300	0.000	2.344	2
	15.92		0.467	0.924	3		13.51		1.494	2.344	5
	14.84		0.467	0.000	5		13.61		1.494	0.000	4
	14.84		0.467	0.000	5		13.61		1.494	0.000	4
	15.92		0.467	0.924	3		13.51		1.494	2.344	5
	14.00		0.000	0.924	2		14.00		0.000	2.344	2

Table 5.20: Longitudinal reinforcement material specifications of Specimen OKJ2

MT	N	Y_s (mm)	A_s (mm ²)	D_b (mm)	F_y (MPa)	F_u (MPa)	E_s (MPa)	ϵ_{sh} ($\times 10^{-3}$)	ϵ_u ($\times 10^{-3}$)
1-2	1	30	660	13.0	718	767	186000	40	160
	2	70	528						
	3	230	264						
	4	270	660						
3-4	1	40	792	13.0	718	767	186000	40	160
	2	84	264						
	3	128	264						
	4	172	264						
	5	216	264						
	6	260	792						
5	1	30	1320	13.0	718	767	186000	40	160
	2	70	1056						
	3	230	528						
	4	270	1320						
6	1	40	1584	13.0	718	767	186000	40	160
	2	84	528						
	3	128	528						
	4	172	528						
	5	216	528						
	6	260	1584						

5.2.4.3 Comparison of the Analytical and Experimental Responses

Specimen OKJ2

Specimens OKJ2 and OKJ6 were analyzed with V5FBCA and VecTor5. A comparison of the load-deflection responses at the column tip is given in Figure 5.23. Note that the positive displacement was obtained from the backward loading condition in the experiment. Detailed comparisons of the response parameters are reported in Table 5.21.

Table 5.21: Comparison of experimental and analytical results of Specimen OKJ2

	Experiment	V5FBCA	VecTor5
Failure Mechanism	BYJF	BY	BY
Peak Load (kN) (Ratio = Analysis/Experiment)	237.0	265.6 (1.12)	274.7 (1.16)
Max. Panel Shear Stress (MPa) (Ratio = Analysis/Experiment)	14.16	12.81 (0.90)	N/A (N/A)
Load at First Beam Yielding (kN) (Ratio = Analysis/Experiment)	237.0	245.9 (1.04)	241.4 (1.02)

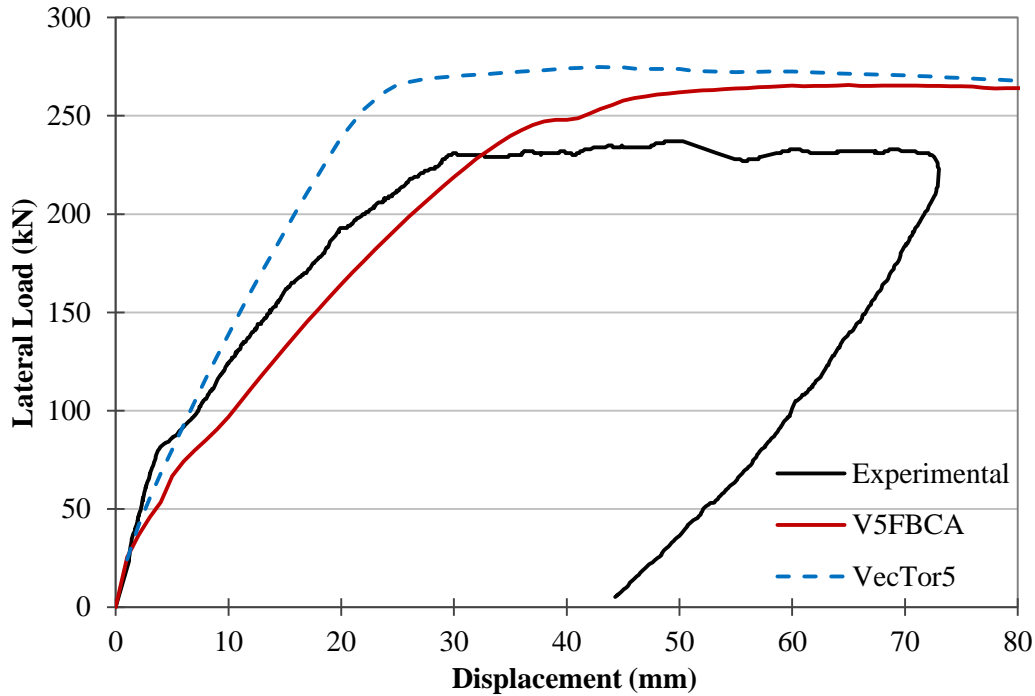


Figure 5.23: Comparison of the load-displacement response of Specimen OKJ2

The subassembly exhibited the response mechanism of beam yielding followed by joint failure. The joint shear cracks and splitting cracks along the column longitudinal bars were noticeable. The beam bars yielded at the same time as the joint core reached its maximum shear strength. The specimen attained a load of 230 kN at a displacement of 36 mm, and sustained this load up to a displacement of 72 mm, where the subassembly lost its strength. At this time, the joint shear distortion contributed to approximately 43% of the story drift. At a displacement of 36 mm, the compressive strain in the concrete strut was measured to be approximately 4.5×10^{-3} . The maximum shear strength of 14.2 MPa was reached at a displacement of 55 mm. The joint shear distortion at the maximum shear strength was 26.0×10^{-3} . The maximum joint distortion was 40.0×10^{-3} at the failure of the structure. The bond of the beam longitudinal bars inside the joint was in good condition. Figure 5.24 shows the cracking pattern of Specimen OKJ1, which had the identical structural properties as Specimen OKJ2 with reversed cyclic loading applied to the structure, at a displacement of 36 mm.

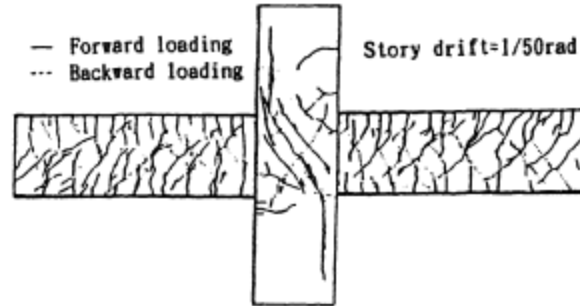


Figure 5.24: Cracking pattern of Specimen OKJ1 (Noguchi and Kashiwazaki, 1992)

The peak loads obtained from V5FBCA and VecTor5 were 12% and 16% higher than the observed peak load, and they predicted the same failure mechanism due to beam yielding. V5FBCA predicted a peak load of 265 kN at a displacement of 67 mm. The beam reinforcing bars yielded on the left face of the joint panel at a displacement of 36 mm. With the increasing applied displacement, the predicted average panel crack widths were 1.6 mm at a displacement of 80 mm and 1.8 mm at a displacement of 100 mm. The joint core reached its maximum shear stress of 12.8 MPa at a displacement of 158 mm, when the average crack width was 2.1 mm.

VecTor5 predicted a peak load of 274 kN at a displacement of 41 mm. The top longitudinal reinforcement in Member 9 and the bottom longitudinal reinforcement in Member 12 reached the yielding stress at a displacement of 19 mm. Flexural cracks with widths over 13 mm were found in Members 9 and 12 at a displacement of 100 mm. The joint panel was calculated to be in good condition throughout the simulation (see Figure 5.25a).

Overall, the analytical load-displacement response predicted by V5FBCA was better than VecTor5 prediction in terms of the peak load, the maximum shear panel stress, and the load at first beam yielding. However, the ductility of the subassembly was overestimated by 122% compared to the observed ductility, resulting an inaccurate prediction of the failure mechanism of the specimen.

The stresses obtained from the analysis were compared to those obtained from VecTor5 (see Table 5.22). Bar stresses on the bottom and right faces were selected for the comparison. The tensile stress predictions seemed to follow the VecTor5 results. However, the compressive stresses on the right face predicted by V5FBCA were significantly different from the results obtained from VecTor5.

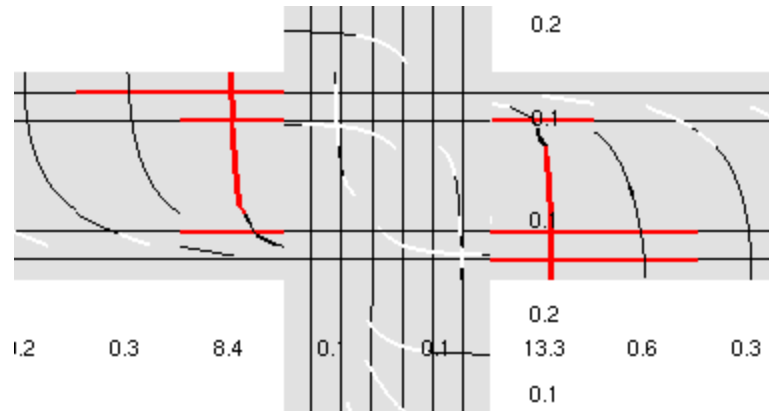


Figure 5.25: Cracking pattern of Specimen OKJ2 predicted by original VecTor5 simulation

Table 5.22: Stress in the longitudinal bars at the joint panel interface of Specimen OKJ2

Disp.	Rebar Stress (MPa)							
	Bottom Face Compression Side		Bottom Face Tension Side		Right Face Tension Side		Right Face Compression Side	
	V5FBCA	VT5	V5FBCA	VT5	V5FBCA	VT5	V5FBCA	VT5
2	-46	-65	-219	-24	95	62	-9	-45
3	-51	-72	-188	-17	128	107	-11	-61
5	-57	-85	-140	-5	174	195	-12	-88
10	-71	-120	-48	36	267	387	-16	-145
20	-95	-195	123	214	448	718	-26	-245
30	-114	-215	265	270	596	718	-34	-345
40	-126	-220	354	289	702	718	-40	-485
50	-133	-223	394	299	692	718	-50	-629
60	-135	-225	413	310	712	729	-54	-718
70	-138	-228	429	318	720	741	-57	-718
80	-138	-229	432	323	738	750	-58	-718

Specimen OKJ6

A comparison of the load-deflection responses at the column tip is given in Figure 5.27. Detailed comparisons of the response parameters are reported in Table 5.23.

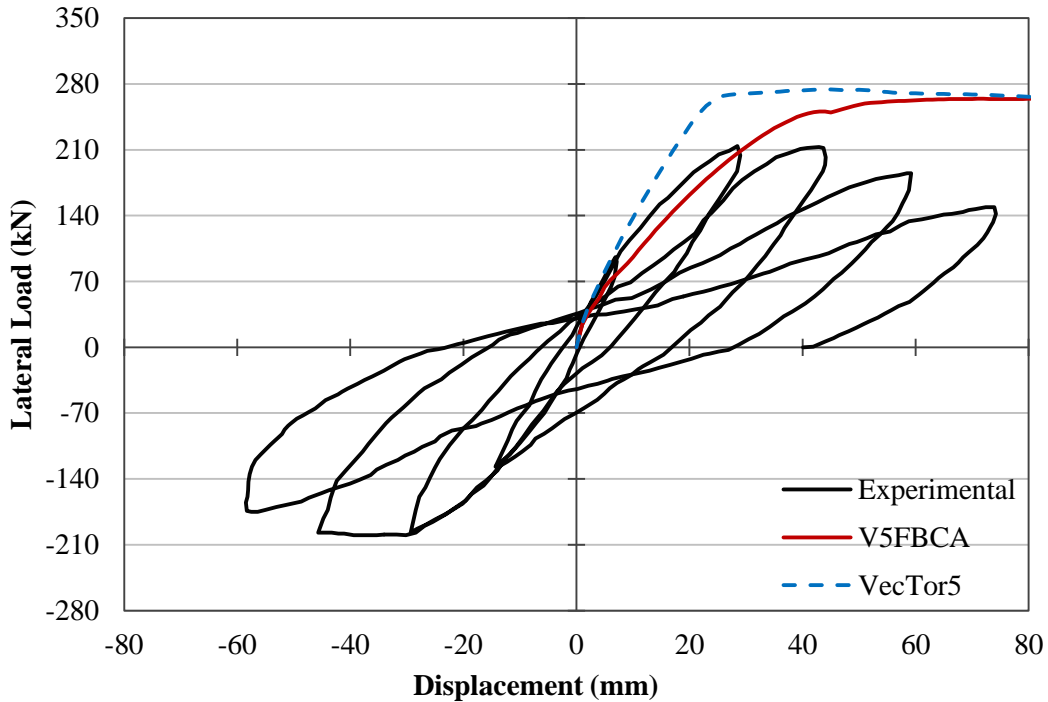


Figure 5.27: Comparison of the load-displacement response of Specimen OKJ6

Table 5.23: Comparison of experimental and analytical results of Specimen OKJ6

	Experiment	V5FBCA	VecTor5
Failure Mechanism	JF	BY	BY
Peak Load (kN) (Ratio = Analysis/Experiment)	214.0	264.2 (1.23)	273.8 (1.28)
Max. Panel Shear Stress (MPa) (Ratio = Analysis/Experiment)	13.11	11.53 (0.88)	N/A (N/A)
Load at First Beam Yielding (kN) (Ratio = Analysis/Experiment)	N/A	248.2 (N/A)	248.9 (N/A)

Specimen OKJ6 had a lower peak load and maximum panel shear stress than Specimen OKJ2 due to the lower concrete strength. The subassembly failed in joint shear with noticeable joint shear cracking. The maximum shear stress of 13.1 MPa was reached at a displacement of 55 mm, and the corresponding shear distortion was 15.5×10^{-3} . The tensile reinforcement at the critical section reached its yielding stress at a displacement of 55 mm, where the strain penetration was also observed in the beam longitudinal reinforcement inside the joint. The maximum shear distortion of the subassembly was 19.3×10^{-3} at a displacement of 91 mm.

V5FBCA suggested a failure mechanism due to beam yielding. The predicted peak load was 263 kN at a displacement of 71 mm. Beam reinforcing bars yielded on the left face of the joint panel at a displacement of 39 mm, and the transverse reinforcement yielded in the joint core at a displacement of 100 mm, when the average crack width of the joint panel was found to be 2.4 mm. The maximum shear stress of 11.5 MPa was reached at a displacement of 103 mm, and the corresponding shear distortion was 19.2×10^{-3} .

VecTor5 predicted failure initiated by beam yielding, with a peak load of 268 kN at a displacement of 42 mm. The beam longitudinal reinforcement reached the yielding stress at a displacement of 20 mm. Flexural cracks with widths over 12 mm were found in Members 9 and 12 at a displacement of 100 mm (see Figure 5.28a). The joint panel was in a good condition throughout the analysis.

The analytical response predicted by V5FBCA was a good match for the experimental results in terms of the peak load and the maximum shear panel stress. However, both three programs were not capable of capturing the joint failure which had been observed in the experiment.

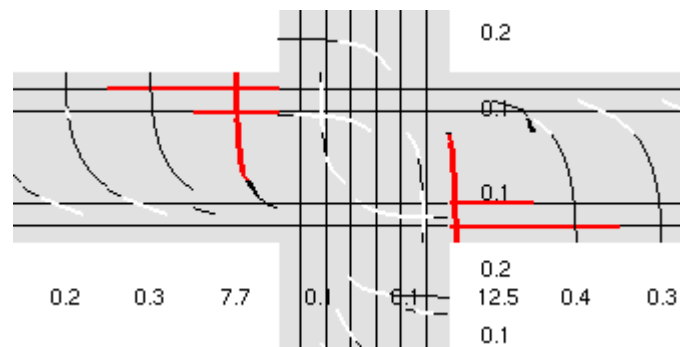


Figure 5.28: Cracking pattern of Specimen OKJ6 predicted by original VecTor5 simulation

5.2.5 Attaalla and Agbabian (2004)

The last set of subassemblies modeled was from tests conducted by Attaalla (1997). The journal paper was published by Attaalla and Agbabian in 2004. Four one-third scaled specimens of interior beam-column joints with high strength concrete were presented. The subassemblies were designed according to the recommendations of the ACI 318-89 (1989). One of the objectives was

to understand whether the definition of the joint shear strength as a function of the square root of the concrete compressive strength was applicable to high strength concrete. Three joint subassemblies, SHC1, SHC2 and SOC3 were selected for verification. Specimen SHC3 was excluded because the joint core was reinforced with steel fibers.

5.2.5.1 Test Specimens

The subassemblies had identical overall dimensions, loading setup, and support restraints, but the joint reinforcement and concrete properties were different. Figures 5.29 and 5.30 show the test setup and the sectional details, respectively. The beam was 203 by 127 mm, and the column was 178 by 127 mm. The subassemblies were designed to exhibit joint shear damage mechanisms under earthquake loading. The joint panel of Specimen SHC1 was reinforced by one transverse tie, whereas the joint panel of Specimens SHC2 and SOC3 were reinforced by two transverse ties. The material properties of the high strength concrete and the reinforcement are listed in Table 5.24. The subassemblies were loaded in a displacement-controlled mode. A constant compressive load of 58 kN was applied along the centerline of the column. The subassemblies were supported by a hinged support at the right end of the beam and two roller supports at the top and bottom of the column. The displacement was applied in the vertical direction at the left end of the beam.

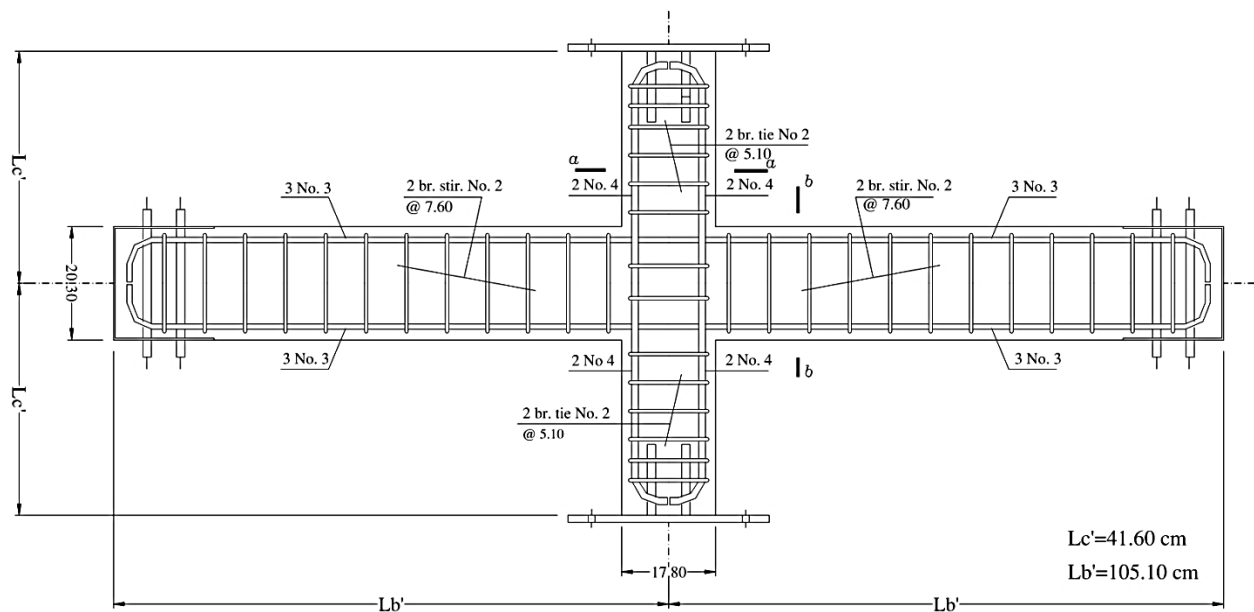


Figure 5.29: Test setup of Specimens SHC1, SHC2 and SOC3 (Attaalla and Agbabian, 2004)

Table 5.24: Material properties of Specimens SHC1, SHC2 and SOC3

Bar Type	Reinforcement Properties							Spec.	Concrete Properties			
	d_b (mm)	F_y (MPa)	F_u (MPa)	E_s (MPa)	E_{sh}^* (MPa)	ϵ_{sh}^* ($\times 10^{-3}$)	ϵ_u^* ($\times 10^{-3}$)		f'_c (MPa)	f'_t^* (MPa)	E_c^* (MPa)	ϵ'_c ($\times 10^{-3}$)
#4	12.7	414	620	200000	2289	10.0	100.0	SHC1	56.6	2.48	30165	3.75
#3	9.53	414	620	200000	2289	10.0	100.0	SHC2	59.6	2.55	29790	4.00
#2	6.35	552	650	200000	1089	10.0	100.0	SOC3	47.2	2.27	31453	3.50

*: estimated

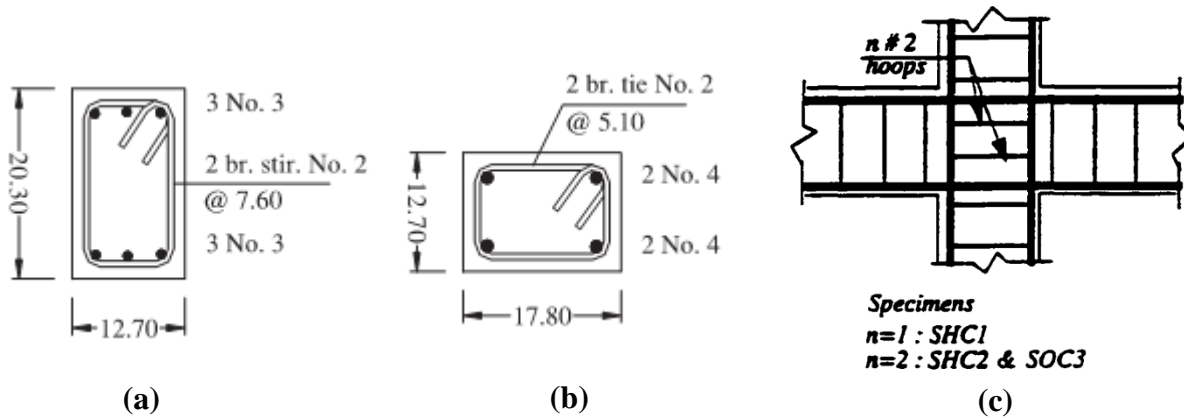


Figure 5.30: Sectional details of Specimens SHC1, SHC2 and SOC3: (a) beam section, (b) column section (Attaalla and Agbabian, 2004), and (c) detailed joint reinforcement (Attaalla, 1997)

5.2.5.2 Analytical Modeling

The two subassemblies were modeled using the same structural model, applied loading, and boundary conditions, but with differing concrete properties. Figure 5.31 shows the analytical model with dimensions, loading, and support restraints. There were 33 nodes, 32 members, and 4 support restraints in the model. Node 23 was restrained in the horizontal and vertical directions for a hinge support, and Nodes 24 and 33 were restrained in the horizontal direction for roller supports. A column compressive load of 58 kN was modeled by applying compressive nodal forces at Nodes 24 and 33. In addition, a negative vertical displacement was applied at the left end of the beam in 61 load stages with an increment of 2 mm starting from a zero displacement.

Six member types were created to build the model (Figure 5.32). Member Types 1 and 2 were used to model the beam sections. Member Types 3 and 4 were used to model the column sections. The interior joint was modeled by MT2 in the horizontal direction and MT4 in the vertical direction. MT5 and MT6 were created by doubling the reinforcement ratios of MT2 and MT4, respectively, to account for increased joint stiffness in the VecTor5 analysis. Each member was divided into 20 to 24 concrete layers to perform the fiber analysis. Detailed general and sectional material properties of Specimen SHC1 are presented in Table 5.25, 5.26 and 5.27. Specimens SHC2 and SOC3 were modeled using a similar approach.

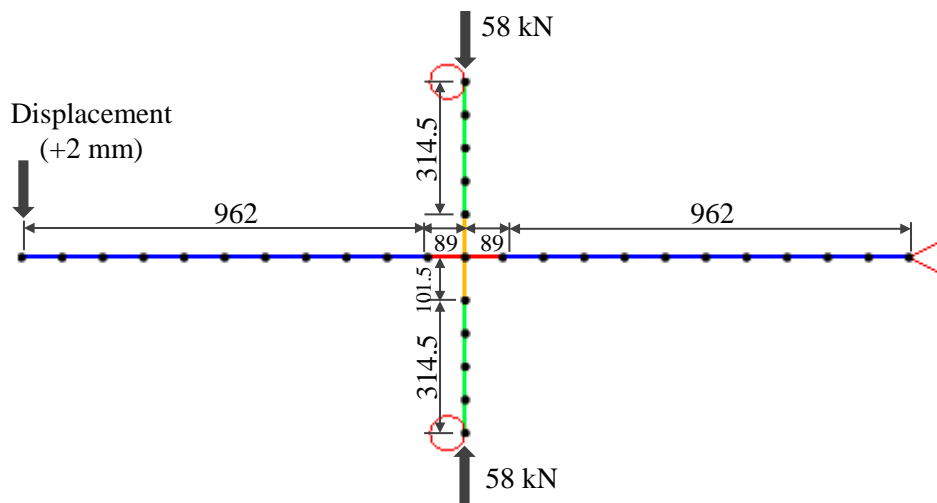


Figure 5.31: Analytical model showing dimensions, loading and support restraints of Specimens SHC1, SHC2 and SOC3

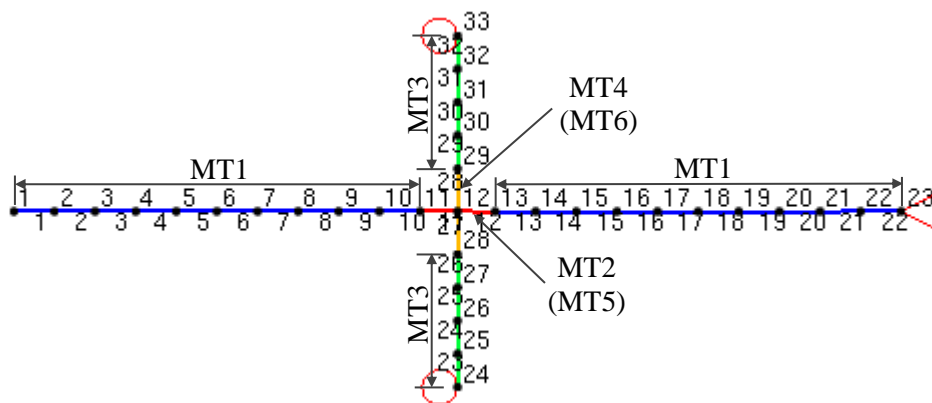


Figure 5.32: Analytical model showing material types of Specimens SHC1, SHC2 and SOC3

Table 5.25: General material specifications of Specimen SHC1

MT	Concrete Properties					Transverse Reinforcement Properties						
	f'_c (MPa)	f'_t (MPa)	E_c (MPa)	ε'_c ($\times 10^{-3}$)	Other	s_t (mm)	d_{bt} (mm)	F_{yt} (MPa)	F_{ut} (MPa)	E_{st} (MPa)	ε_{sh} ($\times 10^{-3}$)	ε_{ut} ($\times 10^{-3}$)
1	56.6	2.48	30165	3.75	default	76	6.4	552	650	200000	10	100
2						0	0	--	--	--	--	
3						51	6.4	552	650	200000	10	100
4						101.5	6.4	552	650	200000	10	100
5						0	0	--	--	--	--	--
6						101.5	6.4	552	650	200000	10	100

Table 5.26: Reinforced concrete material specifications of Specimen SHC1

MT	D_c (mm)	W_c (mm)	ρ_t (%)	ρ_z (%)	N_x	MT	D_c (mm)	W_c (mm)	ρ_t (%)	ρ_z (%)	N_x
1	10.0	127	0.000	0.592	2	4	10.0	127	0.000	0.444	2
	8.51		0.663	0.592	6		8.51		0.496	0.444	6
	7.61		0.663	0.000	4		8.97		0.496	0.000	2
	7.61		0.663	0.000	4		8.97		0.496	0.000	2
	8.51		0.663	0.592	6		8.51		0.496	0.444	6
	10.0		0.000	0.592	2		10.0		0.000	0.444	2
2	10.0	127	0.000	0.000	2	5	10.0	127	0.000	0.000	2
	10.19		0.000	0.000	8		10.19		0.000	0.000	8
	10.19		0.000	0.000	8		10.19		0.000	0.000	8
	10.0		0.000	0.000	2		10.0		0.000	0.000	2
3	10.0	127	0.000	0.883	2	6	10.0	127	0.000	0.888	2
	8.51		0.988	0.883	6		8.51		0.992	0.888	6
	8.97		0.988	0.000	2		8.97		0.992	0.000	2
	8.97		0.988	0.000	2		8.97		0.992	0.000	2
	8.51		0.988	0.883	6		8.51		0.992	0.888	6
	10.0		0.000	0.883	2		10.0		0.000	0.888	2

Table 5.27: Longitudinal reinforcement material specifications of Specimen SHC1

MT	N	Y_s (mm)	A_s (mm^2)	D_b (mm)	F_y (MPa)	F_u (MPa)	E_s (MPa)	ε_{sh} ($\times 10^{-3}$)	ε_u ($\times 10^{-3}$)
1-2	1	32	213	9.5	414	620	200000	10	100
	2	171	213						
3-4	1	32	258	12.8	414	620	200000	10	100
	2	171	258						
5	1	33	426	9.5	414	620	200000	10	100
	2	145	426						
6	1	33	516	12.8	414	620	200000	10	100
	2	145	516						

5.2.5.3 Comparison of the Analytical and Experimental Responses

Specimen SHC1

The three subassemblies were analyzed with V5FBCA and VecTor5. A comparison of the vertical load-deflection responses at Node 1 is shown in Figure 5.33. Detailed comparisons of the response parameters are reported in Table 5.28.

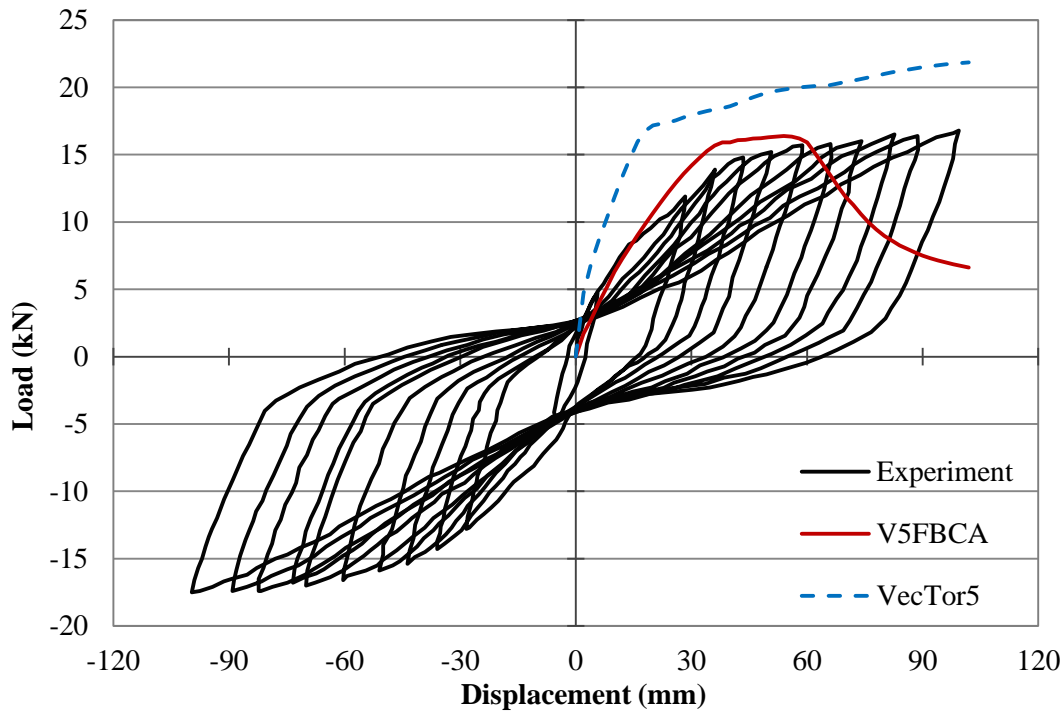


Figure 5.33: Comparison of the load-displacement response of Specimen SHC1

Table 5.28: Comparison of experimental and analytical results of Specimen SHC1

	Experiment	V5FBCA	VecTor5
Failure Mechanism	BYJF	BYJF	BY
Peak Load (kN) <i>(Ratio = Analysis/Experiment)</i>	16.02	16.38 <i>(1.02)</i>	21.47 <i>(1.34)</i>
Max. Panel Shear Stress (MPa) <i>(Ratio = Analysis/Experiment)</i>	6.88	5.21 <i>(0.76)</i>	N/A <i>(N/A)</i>
Load at First Beam Yielding (kN) <i>(Ratio = Analysis/Experiment)</i>	11.90	15.91 <i>(1.34)</i>	15.42 <i>(1.30)</i>

The failure of the subassembly was mainly due to the shear mechanism in the joint core, but damage in beams close to the column faces was noticeable. Figure 5.34a shows the cracking pattern of Specimen SHC1 at the end of the test. The peak load was 16.02 kN at a displacement of 100 mm. The longitudinal reinforcement of the beams yielded at the joint interface at a displacement of 28 mm. The maximum shear stress of the joint panel was 6.88 MPa with the corresponding maximum shear distortion of 12.7×10^{-3} .

V5FBCA predicted the failure mechanism as beam yielding followed by joint failure, matching well with the experimental observations. The original VecTor5, on the other hand, predicted the failure mechanism due to beam yielding. V5FBCA predicted a peak load of 16.4 kN at a displacement of 54 mm. The longitudinal reinforcement of the beam yielded at both sides of the column interface at a displacement of 36 mm. The column steel did not yield throughout the simulation. The maximum shear stress of 5.2 MPa was reached at a displacement of 50 mm with the corresponding shear strain of 9.0×10^{-3} . The average crack width was 1.1 mm. The joint transverse reinforcement yielded at a displacement of 54 mm, at which point the structure started losing its strength and the load gradually declined.

VecTor5 predicted a load of 21.5 kN at a displacement of 100 mm. The longitudinal reinforcement of the beam yielded at a displacement of 18 mm. The column steel yielded at a displacement of 42 mm. Flexural cracking in the beams close to the joint panel was noticeable at a displacement of 100 mm (see Figure 5.34b).

Overall, the analytical response predicted by V5FBCA was a good match for the experimental results in terms of the peak load and the stiffness of the subassembly. V5FBCA successfully captured the failure mechanism as beam yielding followed by joint failure.

The stresses obtained from the analysis were compared to those obtained from VecTor5 and (see Table 5.29). The stresses on the top and left faces of the joint panel were selected for the comparison because cracking was expected to form near these interfaces. The tensile stresses in the longitudinal steel predicted by V5FBCA were slightly lower than the values from VecTor5. On the other hand, the compressive stresses in the beam bars predicted by V5FBCA showed some disagreement with the values from VecTor5.

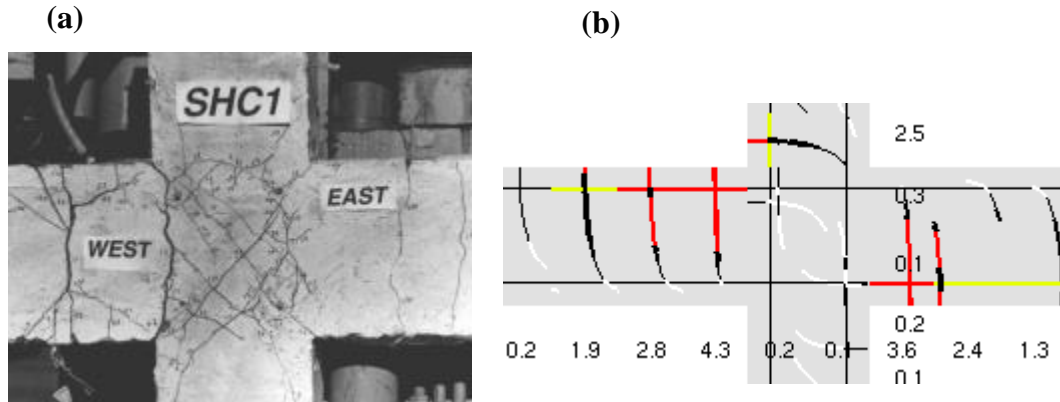


Figure 5.34: Cracking pattern of Specimen SHC1: (a) observed (Attaalla and Agbabian, 2004) and (b) original VecTor5 simulation

Table 5.29: Stress in the longitudinal bars at the joint panel interface of Specimen SHC1

Disp.	Rebar Stress (MPa)							
	Top Face Tension Side		Top Face Compression Side		Left Face Compression Side		Left Face Tension Side	
	V5FBCA	VT5	V5FBCA	VT5	V5FBCA	VT5	V5FBCA	VT5
2	-23	-3	-69	-39	-6	-21	8	22
3	-28	12	-43	-54	-10	-40	14	68
5	17	65	-37	-80	-3	-63	132	166
10	148	238	-57	-127	-6	-102	252	414
15	243	304	-72	-142	-8	12	343	435
20	300	339	-80	-159	-8	60	403	470
25	326	414	-84	-156	-6	84	437	490
30	286	414	-78	-122	-2	110	428	507

Specimen SHC2

A comparison of the vertical load-deflection responses at Node 1 is presented in Figure 5.35. Detailed comparisons of the response parameters are reported in Table 5.30.

Table 5.30: Comparison of experimental and analytical results of Specimen SHC2

	Experiment	V5FBCA	VecTor5
Failure Mechanism	BYJF	BYJF	BY
Peak Load (kN) (Ratio = Analysis/Experiment)	16.73	18.36 (1.10)	21.55 (1.29)
Max. Panel Shear Stress (MPa) (Ratio = Analysis/Experiment)	7.24	5.80 (0.80)	N/A (N/A)
Load at First Beam Yielding (kN) (Ratio = Analysis/Experiment)	12.20	15.92 (1.30)	16.08 (1.32)

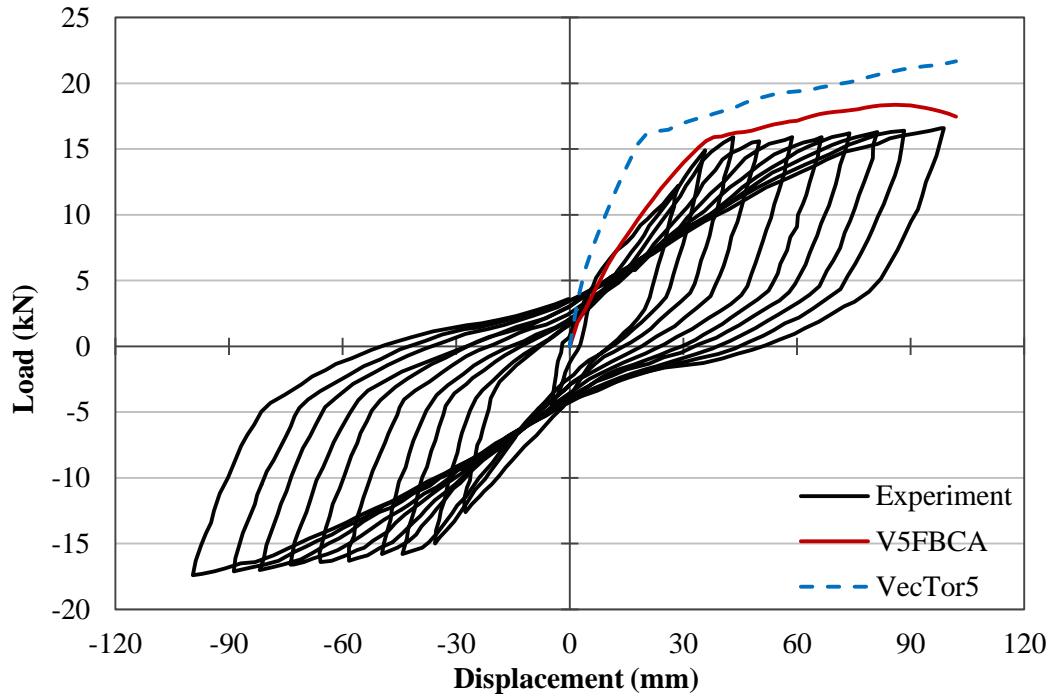


Figure 5.35: Comparison of the load-displacement response of Specimen SHC2

Specimen SHC2 had two transverse ties in the joint core as opposed of one transverse tie in Specimen SHC1. It was expected that the addition of the transverse reinforcement would delay the formation of joint shear cracks, but two major diagonal cracks formed early at a displacement of 28 mm, which was the same as the case for Specimen SHC1. The failure of the subassembly was mainly due to the shear mechanism in the joint core, but damage in the beams close to the column faces was noticeable. Figure 5.36a shows the cracking pattern of Specimen SHC2 at the end of the test. The peak load was 16.7 kN at a displacement of 100 mm. The longitudinal reinforcement of the beams yielded at the joint interface at a displacement of 28 mm. The maximum shear stress of the joint panel was 7.24 MPa with the corresponding maximum shear distortion of 8.7×10^{-3} . The additional transverse reinforcement increased the joint shear strength by only 5%, but it significantly reduced the joint shear deformation by 45%.

V5FBCA predicted the failure mechanism as beam yielding followed by joint failure, matching well with the experimental observations. The original VecTor5, on the other hand, predicted the failure mechanism due to beam yielding. V5FBCA predicted a peak load of 18.4 kN at a displacement of 86 mm. The longitudinal reinforcement of the beam yielded at the left column

interface at a displacement of 38 mm. The transverse reinforcement yielded at a displacement of 66 mm, when the structure started losing its strength and the load slowly declined. The maximum shear stress of 5.8 MPa was reached at a displacement of 82 mm with the corresponding shear strain of 12.2×10^{-3} . The average crack width was 1.4 mm at this time.

VecTor5 predicted a load capacity of 21.6 kN at a displacement of 100 mm. The longitudinal reinforcement of the beam yielded at a displacement of 20 mm. The column steel yielded at a displacement of 44 mm. Flexural cracking in the beams close to the joint panel was noticeable at a displacement of 100 mm. The joint was in good condition without noticeable shear cracking (see Figure 5.36b).

In conclusion, the analytical response predicted by V5FBCA was a good match for the experimental results in terms of the peak load and the stiffness of the subassembly. V5FBCA successfully captured the failure mechanism as beam yielding followed by joint failure. The response of the joint shear panel was predicted reasonably well.

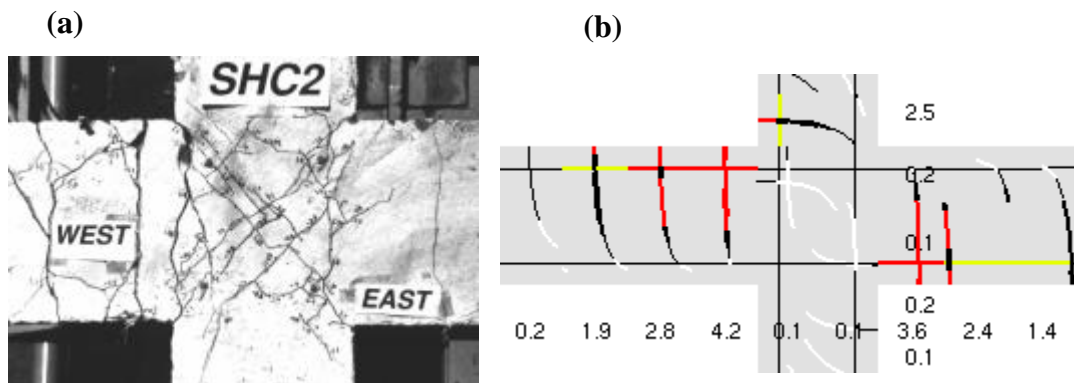


Figure 5.36: Cracking pattern of Specimen SHC2: (a) observed (Attaalla and Agbabian, 2004) and (b) original VecTor5 simulation

Specimen SOC3

A comparison of the vertical load-deflection responses at Node 1 is given in Figure 5.37. Detailed comparisons of the response parameters are reported in Table 5.31.

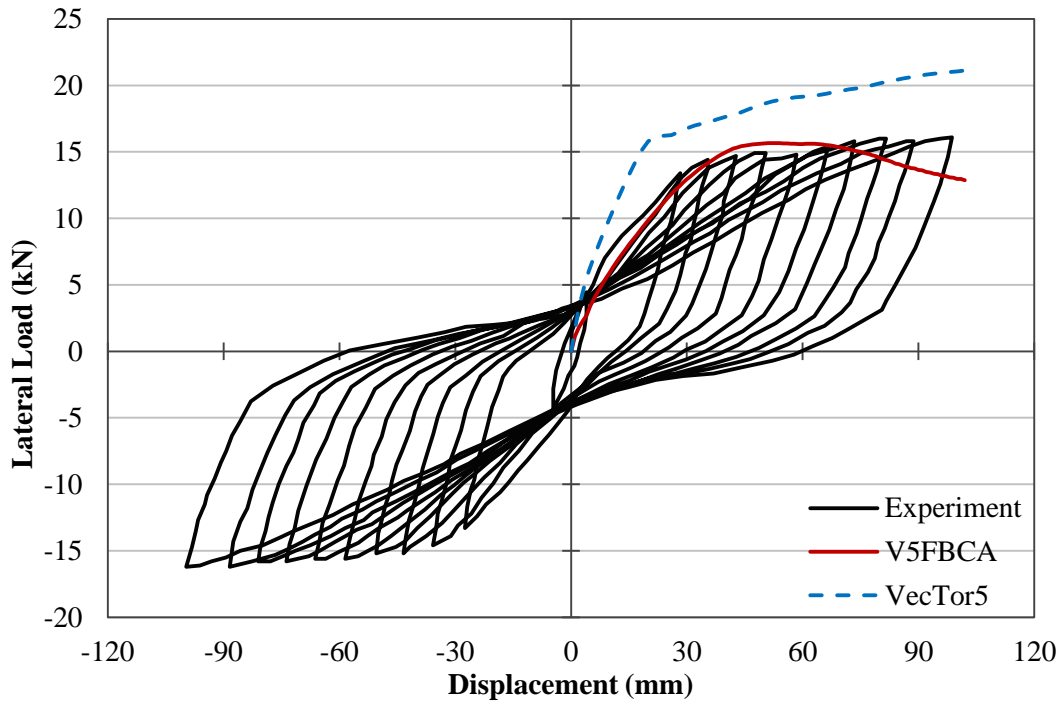


Figure 5.37: Comparison of the load-displacement response of Specimen SOC3

Table 5.31: Comparison of experimental and analytical results of Specimen SOC3

	Experiment	V5FBCA	VecTor5
Failure Mechanism	BYJF	BYJF	BY
Peak Load (kN) <i>(Ratio = Analysis/Experiment)</i>	16.69	15.65 <i>(0.94)</i>	21.05 <i>(1.26)</i>
Max. Panel Shear Stress (MPa) <i>(Ratio = Analysis/Experiment)</i>	7.20	4.87 <i>(0.68)</i>	N/A <i>(N/A)</i>
Load at First Beam Yielding (kN) <i>(Ratio = Analysis/Experiment)</i>	13.40	15.47 <i>(1.15)</i>	16.12 <i>(1.20)</i>

Specimen SOC3 had two transverse ties in the joint core. The subassembly failed due to joint shear failure. Two major diagonal cracks formed at a displacement of 28 mm. The peak load was 16.7 kN at a displacement of 100 mm. Figure 5.38a shows the cracking pattern of Specimen SOC3 at the end of the test. Despite the 26% increase in concrete strength used in Specimen SHC2, the maximum shear stress in Specimen SOC3 and SHC2 were close to each other. The shear distortion of Specimen SHC2 was 14% less than that of Specimen SOC3 due to higher concrete strength of the joint core. The longitudinal reinforcement of the beams yielded adjacent

to the joint interface at a displacement of approximately 28 mm. The maximum shear stress of the joint panel was 7.2 MPa with the corresponding maximum shear distortion of 10.2×10^{-3} .

V5FBCA predicted the failure mechanism as beam yielding followed by joint failure, matching well with the experimental observations. Once again, the original VecTor5 predicted the failure mechanism as beam yielding. V5FBCA predicted a peak load of 15.7 kN at a displacement of 100 mm. The longitudinal reinforcement of the beam yielded at the left column interface at a displacement of 43 mm. The transverse reinforcement yielded at a displacement of 45 mm, where the structure started losing its strength and the load slowly started to decline. The maximum shear stress of 4.9 MPa was also reached at a displacement of 54 mm with the corresponding shear strain of 11.9×10^{-3} . At this time, the average crack width was 1.4 mm.

VecTor5 predicted a load of 21.1 kN at a displacement of 100 mm. The longitudinal reinforcement of the beam yielded at a displacement of 22 mm. The column steel yielded at a displacement of 44 mm. Flexural cracking in beams close to the joint panel was noticeable at a displacement of 100 mm. The joint was in good condition without noticeable shear cracking (see Figure 5.38b).

Overall, the analytical response predicted by V5FBCA was a good match for the experimental results in terms of the peak load and the stiffness of the subassembly. V5FBCA successfully captured the failure mechanism as beam yielding followed by joint failure.

A comparison of the envelopes of the beam shear force versus the panel shear strain is given in Figure 5.39. Attaalla and Agbabian concluded that increasing the amount of joint ties in Specimens SHC2 and SOC3 did not affect the shear stiffness of the joint. The change in slope of the curve was due to the formation of the main diagonal cracks at a displacement of 28 mm. The analytical response was plotted up to the shear strain at the maximum panel shear stress. The analytical responses showed good correlation with the experimental results in terms of the maximum load. However, the stiffness of the joint panel prior to the formation of the main diagonal cracks did not match well with the observed results. The analysis also predicted greater maximum panel shear strain of Specimens SHC2 and SOC3 than that of Specimen SHC1 due to the increasing amount of transverse reinforcement in the joint core.

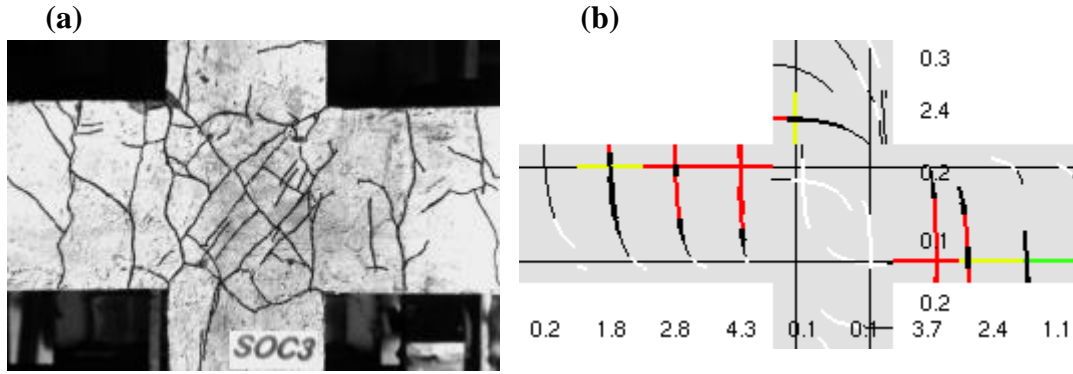


Figure 5.38: Cracking pattern of Specimen SOC3: (a) observed (Attaalla and Agbabian, 2004) and (b) VecTor5 simulation

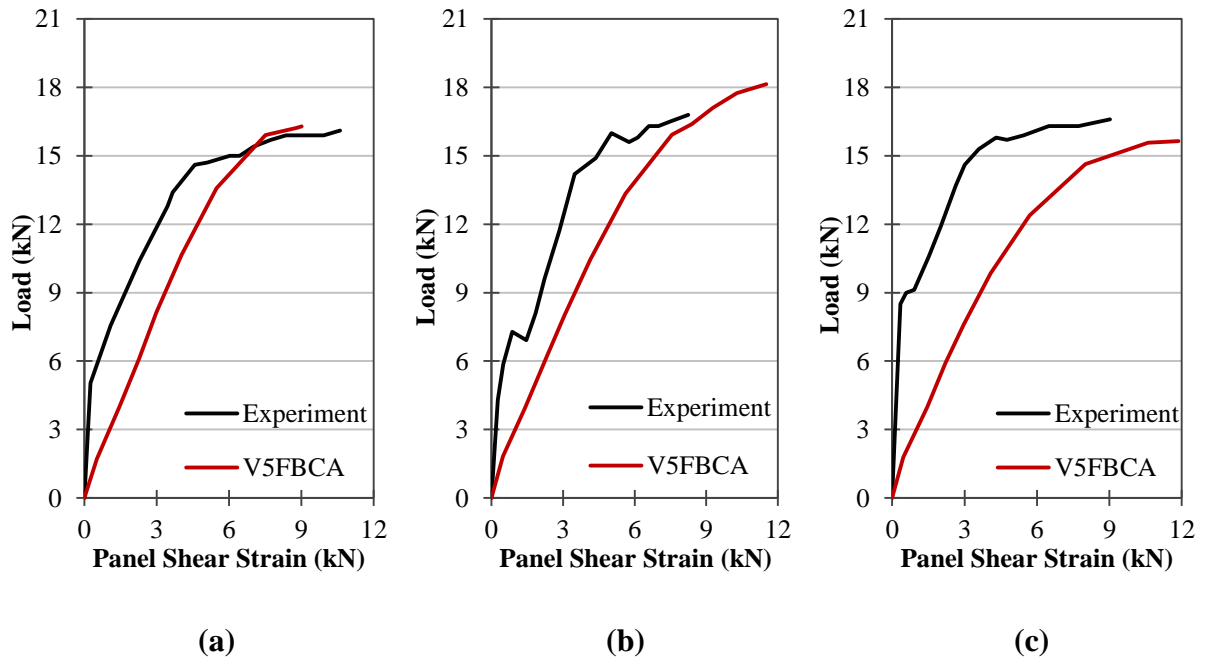


Figure 5.39: Envelopes of the load versus the panel shear strain relationships for: (a) Specimen SHC1, (b) Specimen SHC2, and (c) Specimen SOC3

5.3 Parametric Study of Beam-Column Joint Subassemblies

Parametric studies were carried out to investigate the impact of four parameters on the load-displacement response of the subassemblies. The parameters include: loading type, confinement, compression softening, and bond stress. The impact of the loading type was studied in order to understand whether the backbone curve of the reversed cyclic response was a good representation of the monotonic response. To assess the impact of the loading type on the load-displacement response, a comparison involving the response of Specimen OKJ2 tested under the monotonic and reversed cyclic loading conditions is presented in Figure 5.40. In this example, the stiffness of the subassembly prior to 30 mm story drift and the peak load for both loading conditions were similar. However, the monotonic response was able to sustain the peak load, but the reversed cyclic response showed the loss of stiffness. In addition, the analytical responses under monotonic and reversed cyclic loading conditions were compared. Figure 5.41 shows a comparison of the VecTor5 analytical load-displacement responses of Specimen A1. In this example, the monotonic response curve was capable of capturing the initial and post-yielding stiffness of the reversed cyclic response. The peak loads and the load at first beam yielding simulated under the monotonic and reversed cyclic loading conditions were also comparable. In conclusion, the backbone curve of the reversed cyclic response was a good representation of the monotonic response in terms of the peak load and the initial stiffness of the structure. However, the loss of stiffness due to the hysteretic response may not be captured by the monotonic response.

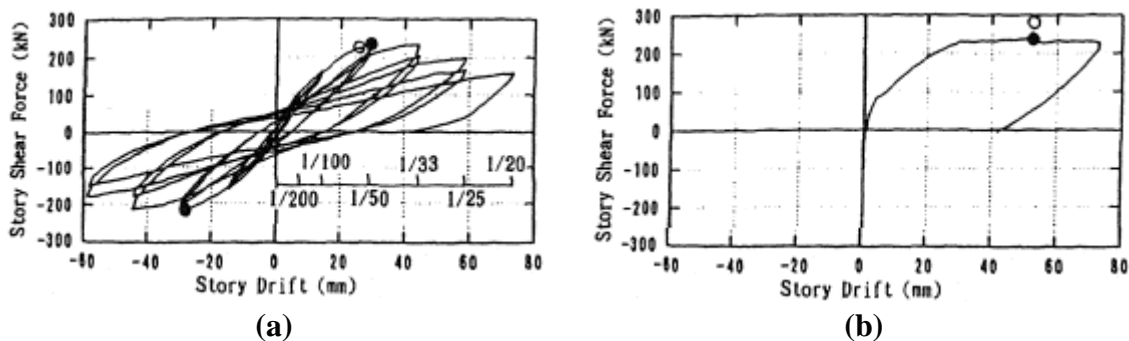


Figure 5.40: Story shear force versus story drift relationships of Specimen OKJ2 (Noguchi and Kashiwazaki, 1992) subjected to: (a) monotonic and (b) reversed cyclic loading conditions

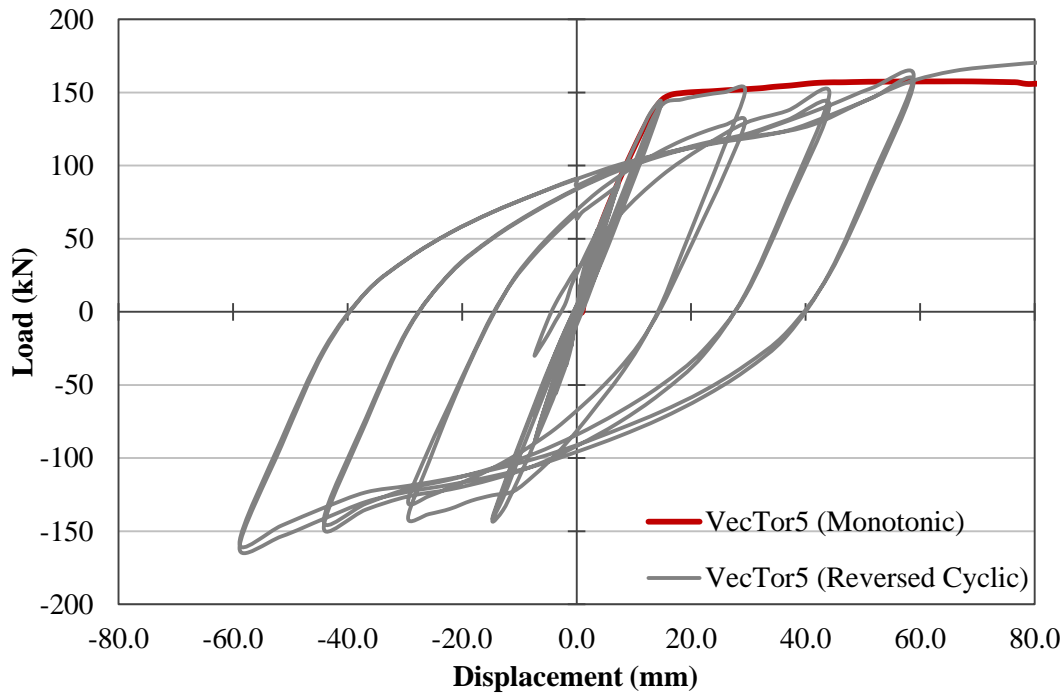


Figure 5.41: Comparison of the VecTor5 load-displacement responses of Specimen A1

The second parameter was the impact of the confinement effectiveness coefficient, which considers the confinement in the column section as well as the confinement contributed by the transverse reinforcement in the joint core. The formulation details were provided in Section 4.3.3. The value of 1.0 represents a fully confined joint core, whereas the value of 0 represents joints with no or ineffective transverse reinforcement. The subassemblies were tested under these two conditions and the load-displacement responses were compared to the original analytical response (see Figure 5.42). It was observed that confinement from the transverse reinforcement delayed concrete crushing of the joint core, providing greater strength for subassemblies that exhibited significant joint damage.

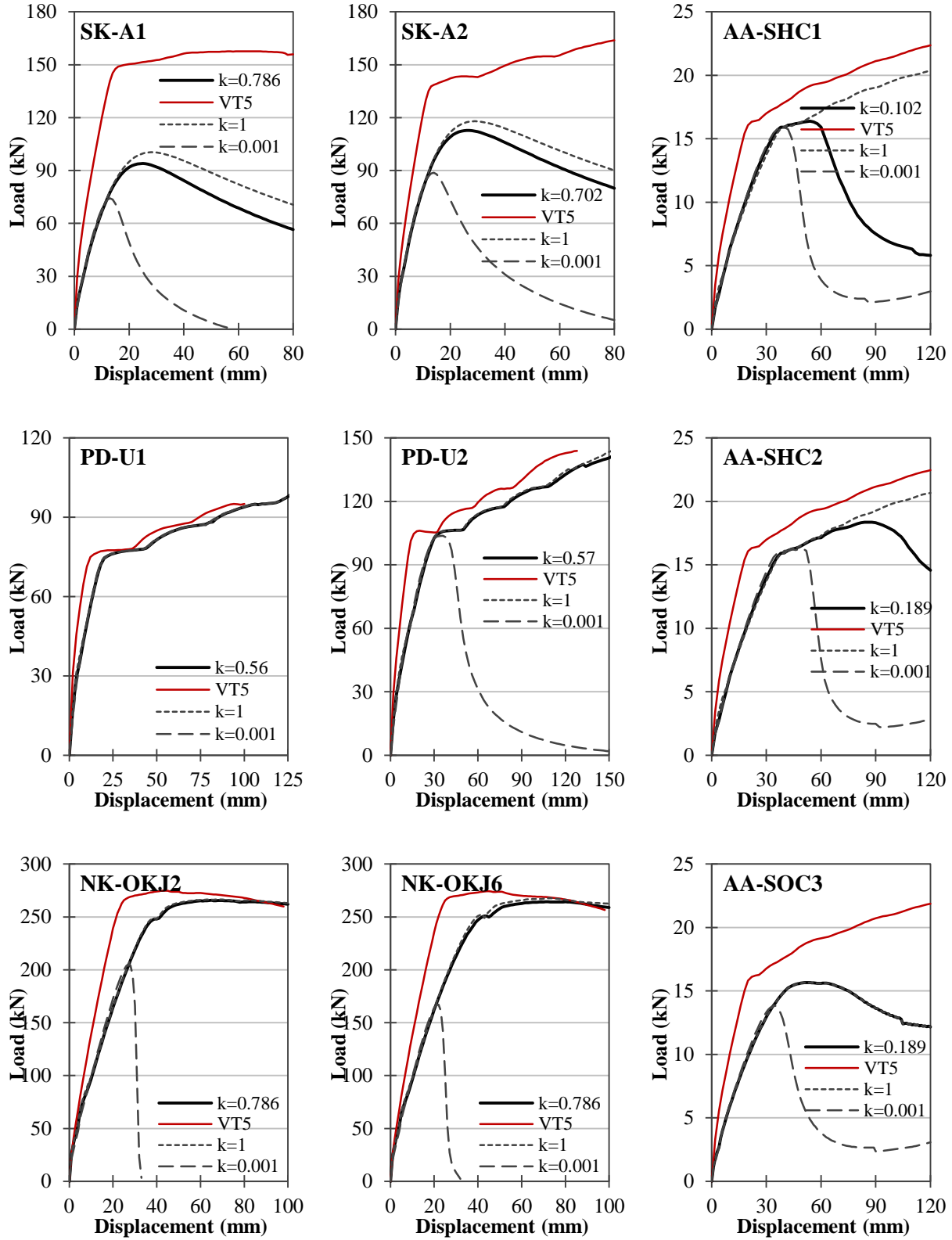
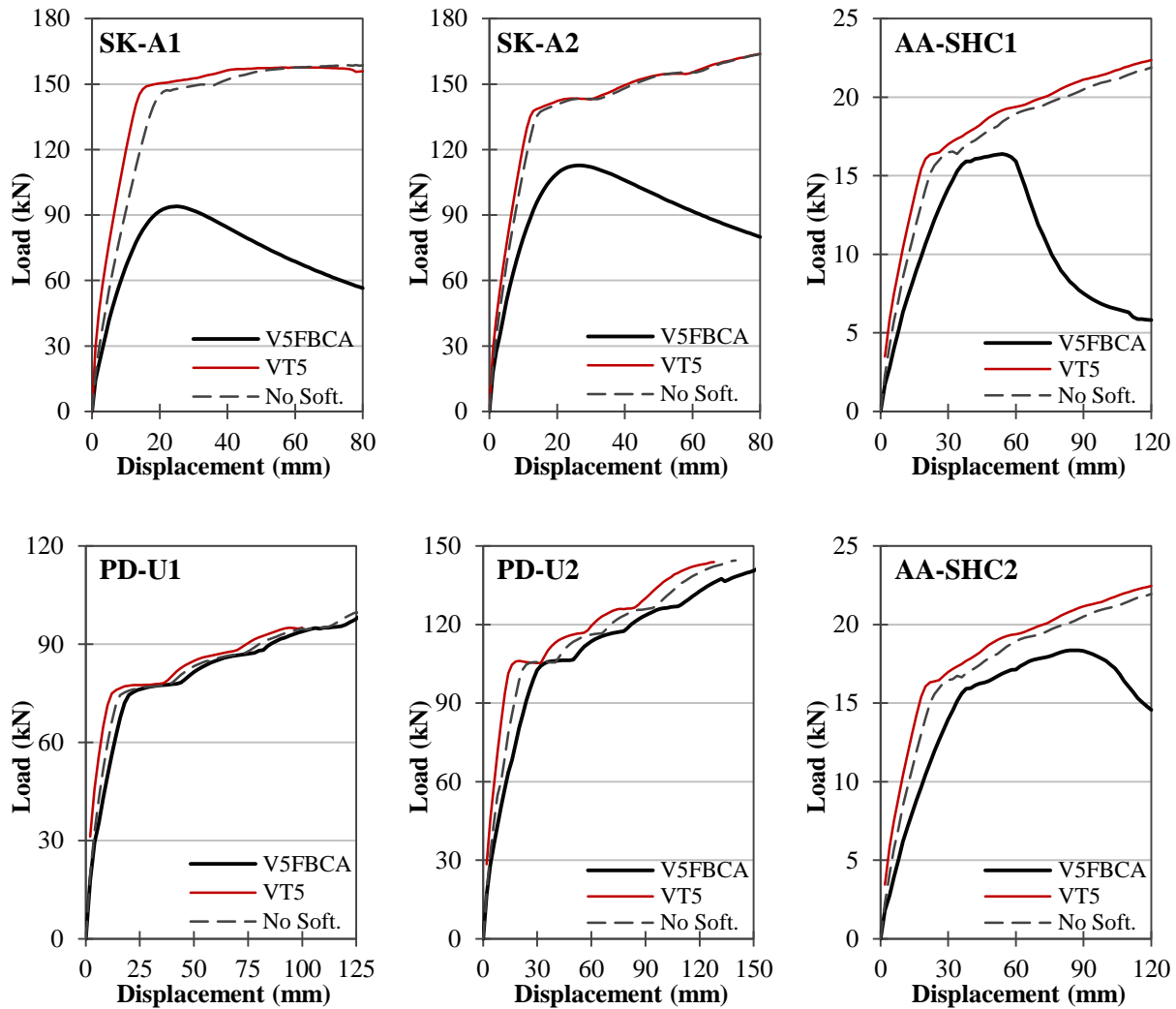


Figure 5.42: Comparison of the load-displacement responses with different confinement effectiveness coefficients

The next parameter investigated was the impact of the reduction factor due to the compression softening effect. The formulation details were provided in Section 3.4. The reduction factor of 1.0 was selected to represent no strength reduction due to joint cracking. It was anticipated that the obtained load-displacement response would be close to the response from the original VecTor5 with semi-rigid end offsets. This was verified by a comparison of the responses as shown in Figure 5.43. The investigation concluded that the response predicted by V5FBCA was similar to the original VecTor5 prediction with the consideration of the joint response.



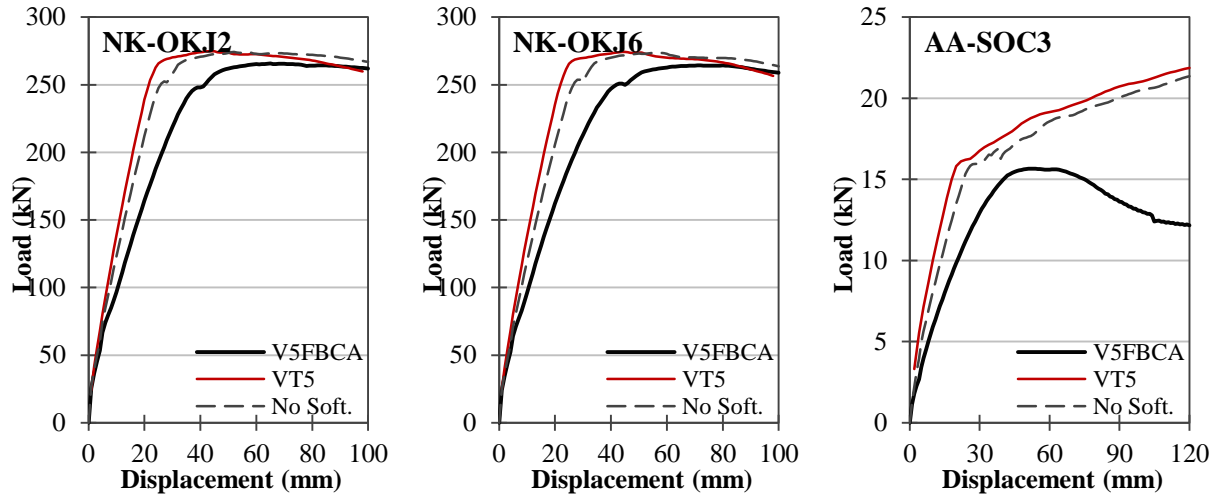
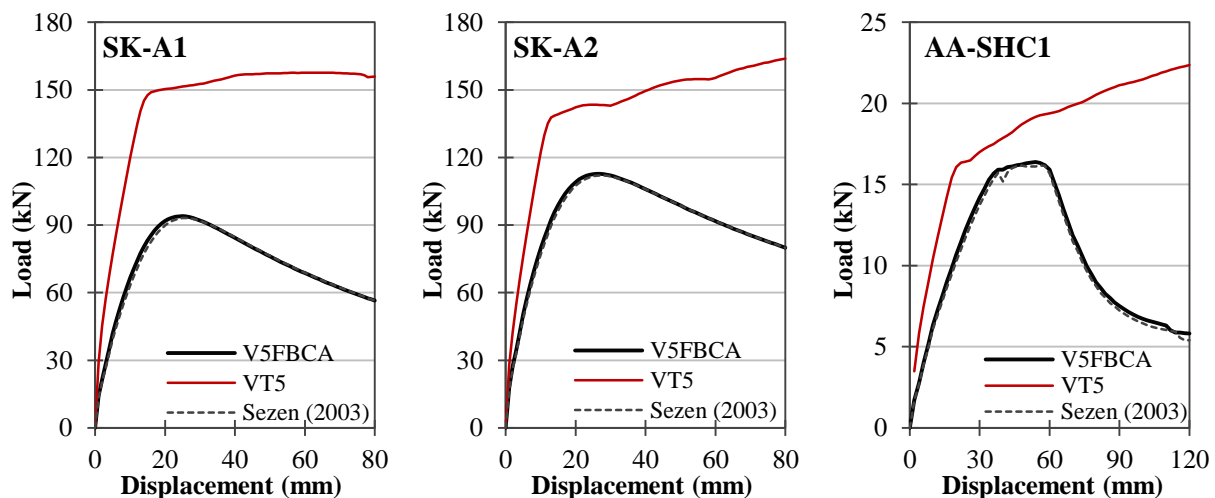


Figure 5.43: Comparison of the load-displacement responses without the compression softening effect

The last parameter examined was the bond stress. Uniform bond stresses were assumed along the longitudinal bars in the joint core depending on the rebar conditions as presented in Table 3.1. In order to assess the impact of the assumed bond stress on the load-displacement response, bi-uniform bond stresses proposed by Sezen and Moehle (2003) were employed and tested. Formulation details of the bond model were presented in Section 2.3.3. A comparison of the responses shown in Figure 5.44 concluded that the assumption of the bond stresses did not have a significant impact on the global load-displacement response for the subassemblies. This may be explained by the observation that the subassemblies did not exhibit major bond damage or failure during the tests.



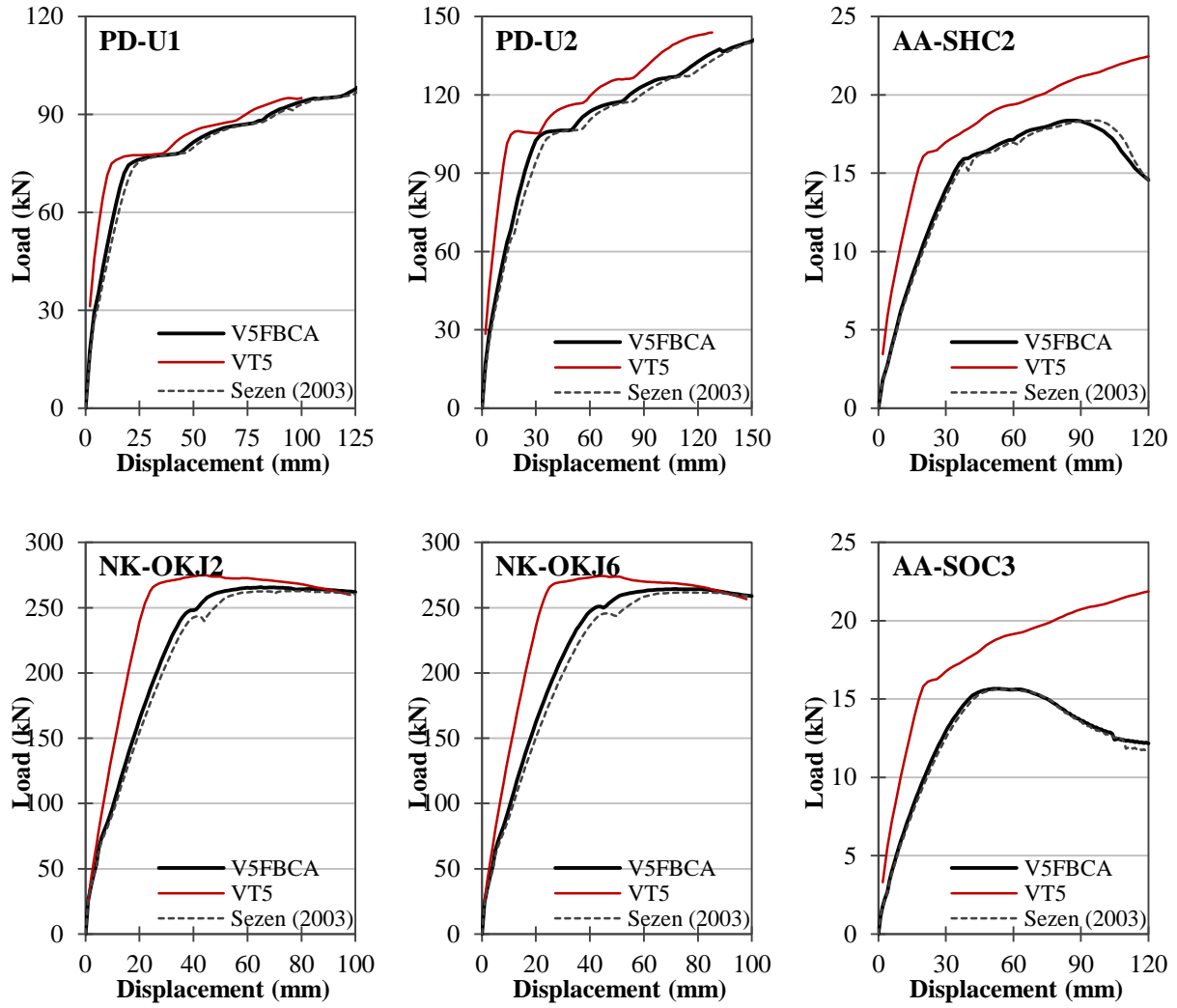


Figure 5.44: Comparison of the load-displacement responses with bond stresses proposed by Sezen and Moehle (2003)

5.4 Frame Structures

5.4.1 Summary

In order to assess the performance of VecTor5 with the new joint element, three large-scale frame structures with different joint reinforcement ratios were selected for evaluation and verification. The frame structures were analyzed with V5FBCA and the original VecTor5.

The inputs used for the analyses with V5FBCA and VecTor5 were almost identical. The only difference was that the semi-rigid end offsets were not used for interior joints in the analysis with V5FBCA. The external and knee joints, on the other hand, were modeled with the semi-rigid end offsets in both analyses. Once again, the default or typical material behavior models to assess the capabilities without using special program modifications.

The analytical load-deflection responses from V5FBCA and VecTor5 were compared with the experimental responses. The failure mechanisms and the cracking patterns of the frame structures were also compared in the study. The analytical responses, failure mechanism, and response from V5FBCA showed good correlation with the experimental results.

5.4.2 Xue et al. Frame (2011)

An experimental program was conducted to investigate the seismic performance of high-performance concrete frames under low reversed cyclic loading (Xue et al., 2011). The experiment involved testing two specimens of a one-fifth scale, two-story, two-bay high-performance concrete frames under constant vertical loads and applied reversed cyclic loads. The frame specimens were detailed in conformity with the requirements of ACI 318-08 (2008). One of the frames, HPCF-1, was selected for evaluation and verification. The other specimen was excluded because it involved prestressing.

The test frame was constructed with a center-to-center span of 2700 mm, a story height of 1000 mm and an overall height of 2610 mm (see Figure 5.45). All beams were 220 mm deep and 150 mm wide, and all columns were 200 mm deep and 200 mm wide. The frame was built integral with a heavily reinforced base which was 300 mm deep and 300 mm wide. The base was bolted

to the strong floor, essentially creating a fixed base. The material properties of the concrete and the reinforcement are listed in Table 5.32.

Testing of the frame involved applying constant gravity loads and a reversed cyclic lateral load as shown in Figure 5.46. The vertical loads were applied at the top of the three columns. The middle column had an axial load of 804 kN, while the other two columns each had an axial load of 402 kN. The lateral load was applied in two stages. The first stage was the load-controlled stage in which a cyclic load reversal was applied until the cracking load. The corresponding roof lateral drift was defined as Δ . In the second stage, the frame was tested under displacement control. Three cyclic load reversals were applied at displacement levels of multiples of Δ (e.g. Δ , 2Δ , 3Δ), and terminated after the first cyclic load reversal of 5Δ . This lateral load was provided by a hydraulic actuator and applied through a steel beam to the second story at the left column.

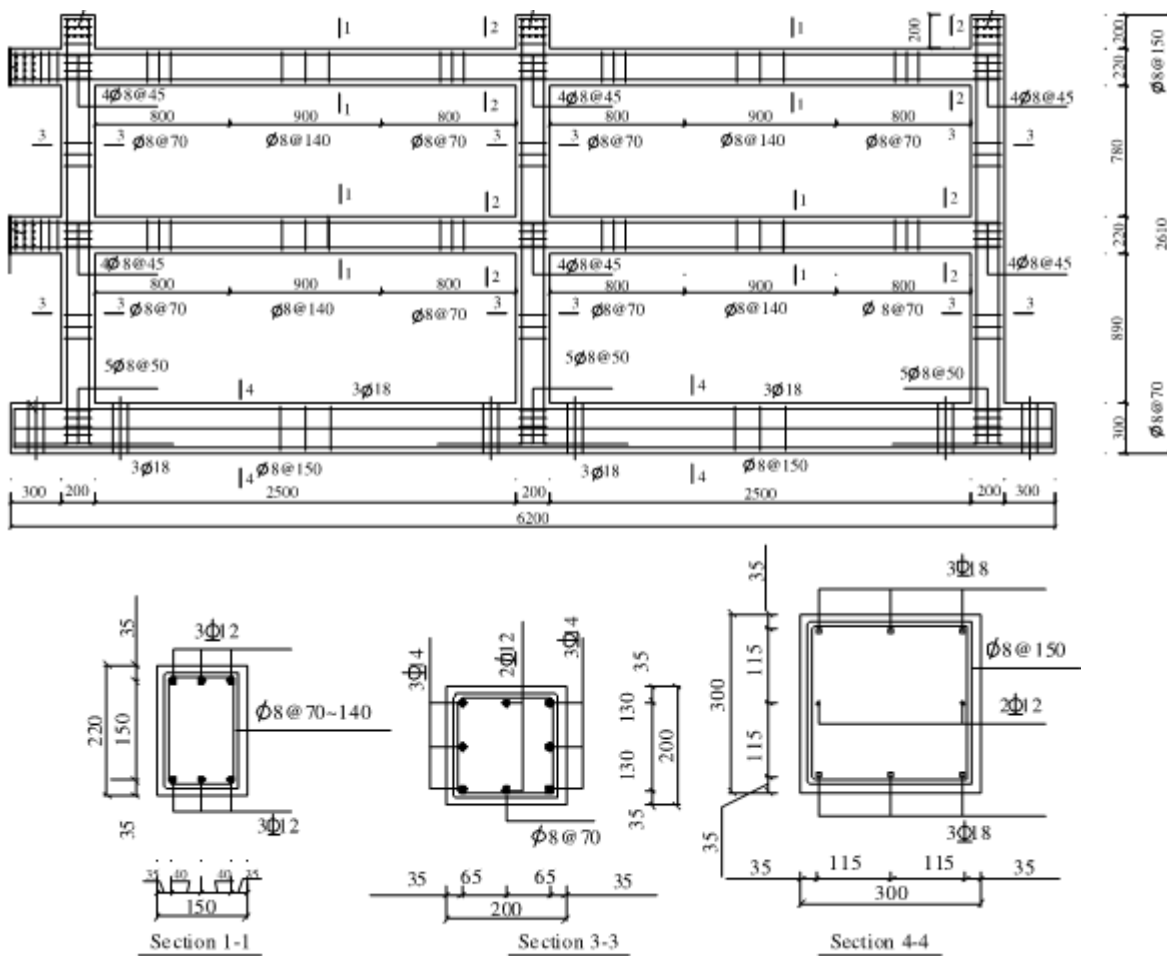


Figure 5.45: Structural details of Specimen HPCF-1 (Xue et al., 2011)

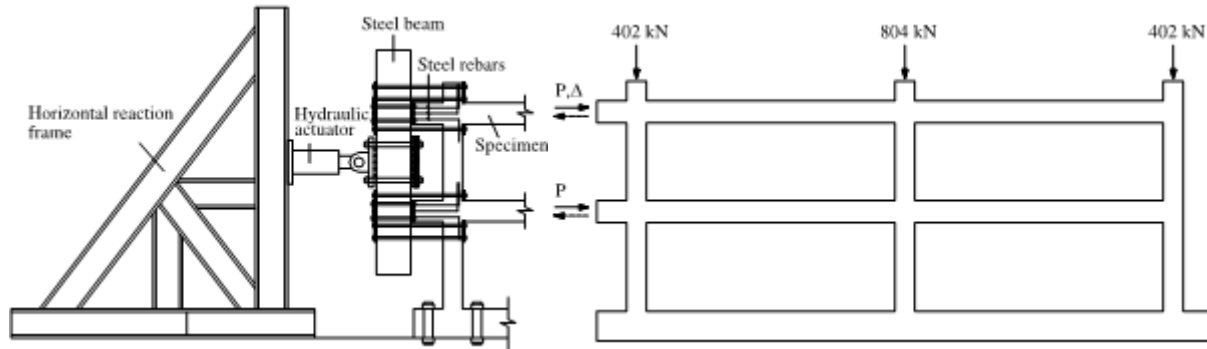


Figure 5.46: Applied loads on Specimen HPCF-1 (Xue et al., 2011)

Table 5.32: Material properties of Specimen HPCF-1

Bar Type	Reinforcement Properties							Spec.	Concrete Properties		
	d_b (mm)	F_y (MPa)	F_u (MPa)	E_s (MPa)	E_{sh}^* (MPa)	ϵ_{sh}^* ($\times 10^{-3}$)	ϵ_u^* ($\times 10^{-3}$)		f'_c (MPa)	E_c (MPa)	ϵ'_c ($\times 10^{-3}$)
D14	14.0	268.3	373.3	144000	533	10	207	HPCF-1	46.9	36100	2.40
D12	12.0	362.6	506.0	143000	829	10	183				
D8	8.0	534.6	594.0	201000	261	10	238				

*: estimated

5.4.2.1 Analytical Modeling

The beams and columns were divided into a number of segments to create the frame model of the structure. Segment lengths were approximately 100 mm, which was half of the cross-sectional depth of the column. Figure 5.47 shows the analytical model with loading and support restraints. There were 171 nodes, 170 members, 9 support restraints and 1 interior joint in the model. The base of the frame was not modeled explicitly in this model. Instead, Nodes 1, 27 and 53 at the bottom of the columns were restrained in the horizontal, vertical and rotational directions. The constant gravity loads were modeled with an axial load of 804 kN applied at Node 52, and axial loads of 402 kN applied at Nodes 26 and 78. A monotonically increasing displacement was applied at Node 20 in the horizontal direction. The displacement was applied in 41 load stages with an increment of 1 mm starting from zero displacement. The extension of the beams and columns were not modeled because otherwise the program would have identified Node 52 as an interior joint, providing inaccurate predictions.

Eleven member types were created to build the model. Member Types 1 through 4 were used to model the columns. Member Types 5 through 8 were used to model the beams. Member Types 9 and 10 were created with half of the longitudinal and transverse reinforcement of MT2 and MT8, respectively, to simulate the properties of the interior joint in the horizontal and vertical directions. It is important to note that the exterior and knee joints in this frame model were still modeled with semi-rigid end offsets since the implemented joint model is valid for the interior joints only (i.e. MT2 and MT8). Member Type 11 was used to represent the steel beam for the load application. MT11 was given relatively high reinforcing steel ratios in order to avoid local failure of the left column. Each member was divided into 20 to 22 concrete layers to perform the layered sectional analysis.

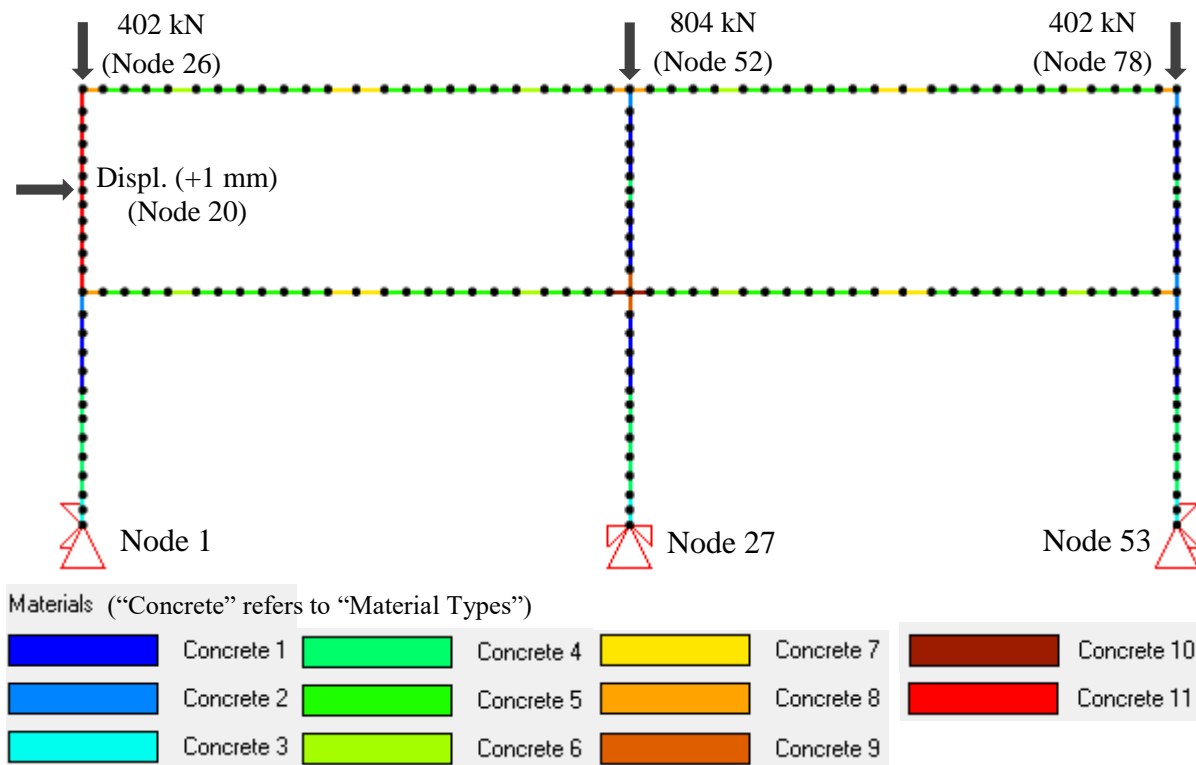


Figure 5.47: Analytical model showing loading and support restraints of Specimens HPCF-1

5.4.2.2 Comparison of the Analytical and Experimental Responses

The experimental and analytical responses are compared in Figure 5.48. Detailed comparisons of the response parameters are reported in Table 5.33.

The load-displacement response predicted by V5FBCA had greater strength but lesser ductility than the observed response. The predicted maximum lateral load was 15% higher than that from the experiment. In the experiment, the test frame showed good seismic performance and failed in partial beam sideway mechanism, which involved the formation of plastic hinges at the beam ends. The initiation of the cracks took place at the column base and mid-span of the beams before the full vertical loads were achieved. With increasing lateral drifts, cracks formed at the beam ends and gradually penetrated through the depth of the section. Meanwhile, shear cracks started forming at the base of the middle column. Vertical cracks due to relatively high axial load also became visible. The frame structure eventually failed due to the formation of plastic hinges at column bases. Figure 5.49 shows the flexural failure of the beam end and the shear failure of the column base.

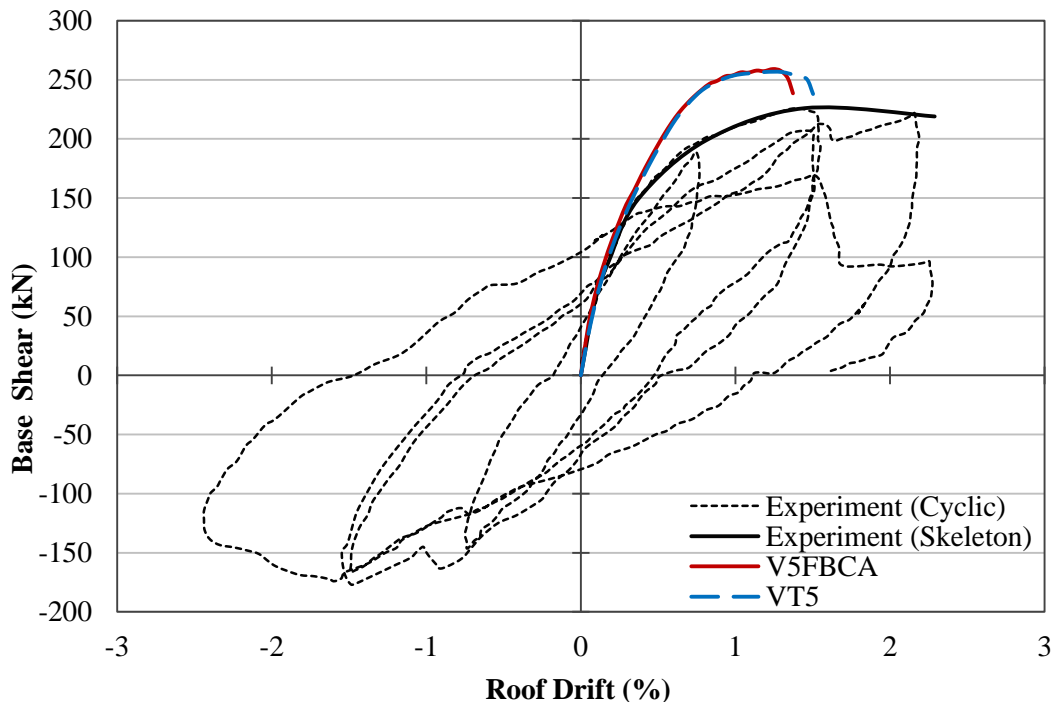


Figure 5.48: Comparison of base shear versus roof drift response of Specimen HPCF-1



Figure 5.49: Failures of Specimen HPCF-1 (Xue et al., 2011)

Table 5.33: Comparison of experimental and analytical results of Specimen HPCF-1

Event	First Yielding of Reinforcement			Maximum Lateral Load		
	Analysis	Experiment	Ratio	Analysis	Experiment	Ratio
Lateral Load (kN)	213.3	195.8	1.09	259.1	225.0	1.15
Roof Drift (mm)	13.2	19.9	0.66	28.0	37.8	0.74
Global Stiffness (kN/mm)	16.16	9.85	1.64	9.25	5.95	1.56

The analytical results suggested a similar failure mechanism. Yielding of the column reinforcement took place at the base of the right column at a roof drift of 0.6%. Meanwhile, flexural cracks started forming at the beam ends near the column faces on the first story. With increasing applied lateral loads, the flexural cracks became longer and wider. The frame eventually failed due to the shear failure at the first story of the east column. Figure 5.50 shows the deformed shape and cracking pattern of the frame at the end of the simulation. Shear cracks at the base of the columns were noticeable before the failure of the frame took place. The compression softening coefficient of the interior joint core was 0.865 at the end of the simulation, meaning that the interior joint was in a good condition throughout the analysis.

The experimental study did not provide detailed information about the joint core during the test because the joint failure was not the governing failure mode of the specimen. Damages on the beam ends and the base of the columns were more severe than the damage in the interior joint. Therefore, the load-displacement responses predicted by V5FBCA and VecTor5 are nearly identical. This was because only one of the six joints was modeled using the new joint element. Even if there had been widespread joint damage, the responses would have been the same due to the five semi-rigid joints. The observation confirmed that the joint model implementation does not change the response of frames with minimal joint damage. This study also verified that the

program is capable of capturing other failure mechanisms while considering the response of interior joints.

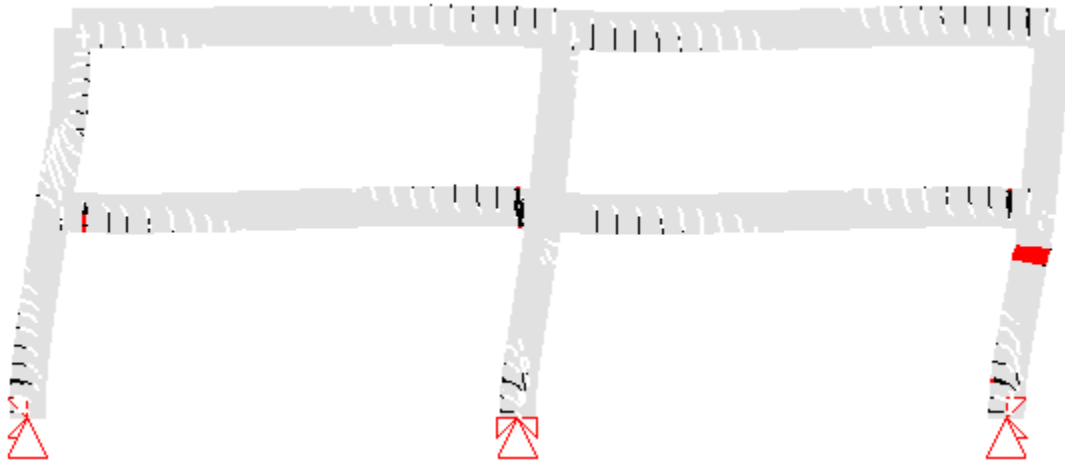


Figure 5.50: Deformed shape and cracking pattern of Specimen HPCF-1

5.4.3 Ghannoum and Moehle (2012)

An experimental program was conducted to investigate the dynamic collapse of older-type construction (Ghannoum and Moehle, 2012). The experiment involved testing a one-third scale, three-story, three-bay frame structure on a shake table. The test frame was constructed with a center-to-center span of 1780 mm, a story height of 1220 mm and an overall height of 3960 mm (see Figure 5.51). All beams were 230 mm deep and 150 mm wide, and all columns were 150 mm deep and 150 mm wide. The frame was built integral with four reinforced concrete footings on top of the shake table. Two of the four columns were designed to represent the older-type building construction. They had the identical configurations with widely spaced ties with 90-degree hooks. The other two identical ductile columns were designed in accordance with the ACI318-08 (2008) requirements for special moment-resisting frames. The purpose of this mixed-type construction was to delay the collapse of the frame due to the failure of older-type columns. The design of the frame created a strong-beam, weak-column mechanism. Beam-column joints were also designed in accordance with ACI318-08 (2008) requirements for special moment-resisting frames. Therefore, a joint failure was not expected. The material properties of the concrete and the reinforcement are listed in Table 5.34.

The testing of the frame involved the application of gravity loads and ground acceleration (see Figure 5.52). Four packets of lead were bolted to each beam span, producing dead loads in a typical office building. Each packet weighted 6.67 kN. Additional information regarding this experiment can be found in Ghannoum (2007).

Table 5.34: Material properties of Ghannoum and Moehle Frame

Bar Type	Reinforcement Properties							Spec.	Concrete Properties		
	d_b (mm)	F_y (MPa)	F_u (MPa)	E_s (MPa)	E_{sh}^* (MPa)	ϵ_{sh}^* ($\times 10^{-3}$)	ϵ_u ($\times 10^{-3}$)		f'_c (MPa)	E_c (MPa)	ϵ'_c ($\times 10^{-3}$)
#3	9.5	441	584	188227	1241	10.0	125.0	Ghannoum	24.6	19000	2.90
#2	6.3	483	623	182711	1632	10.0	96.2				
3/16 in.	4.8	556	557	187365	27397	3.6	3.7				
1/8 in.	3.2	655	680	181332	10200	10.0	12.5				

*: estimated

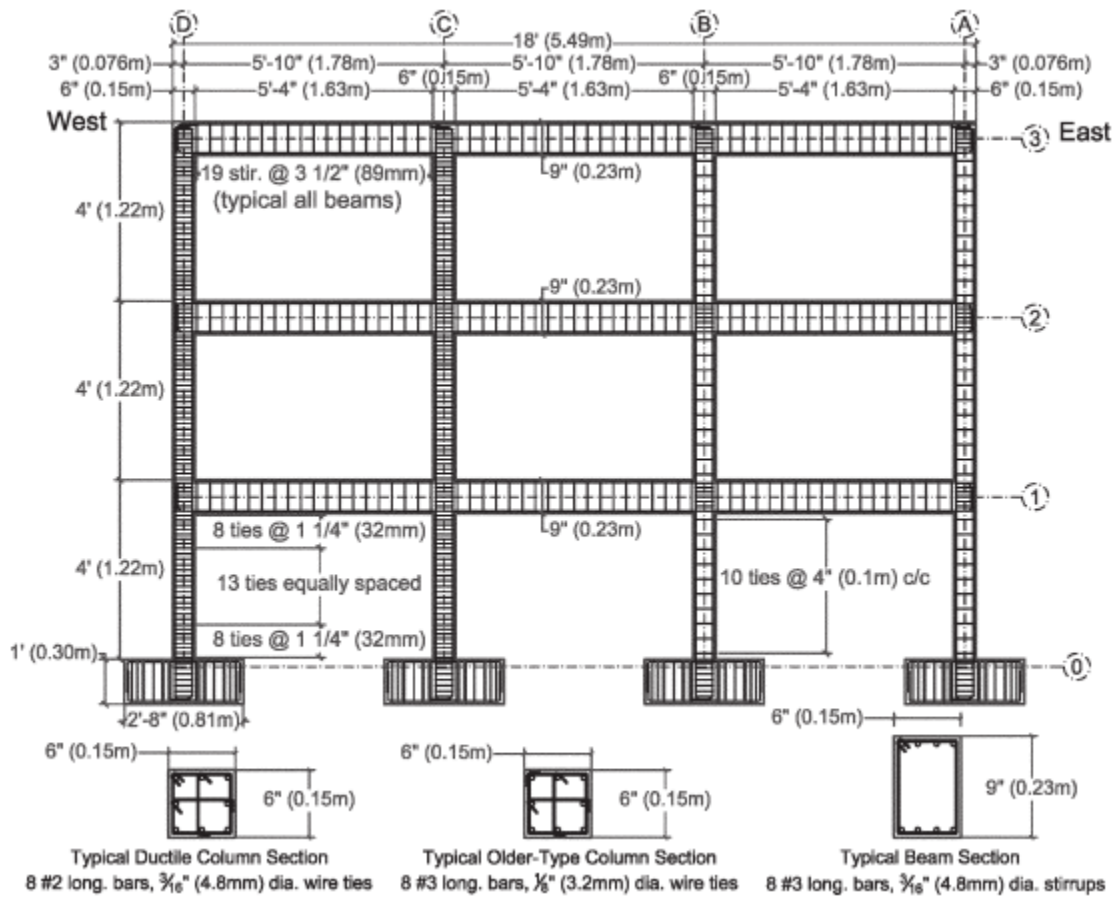


Figure 5.51: Structural details of Ghannoum and Moehle frame (Ghannoum and Moehle, 2012)

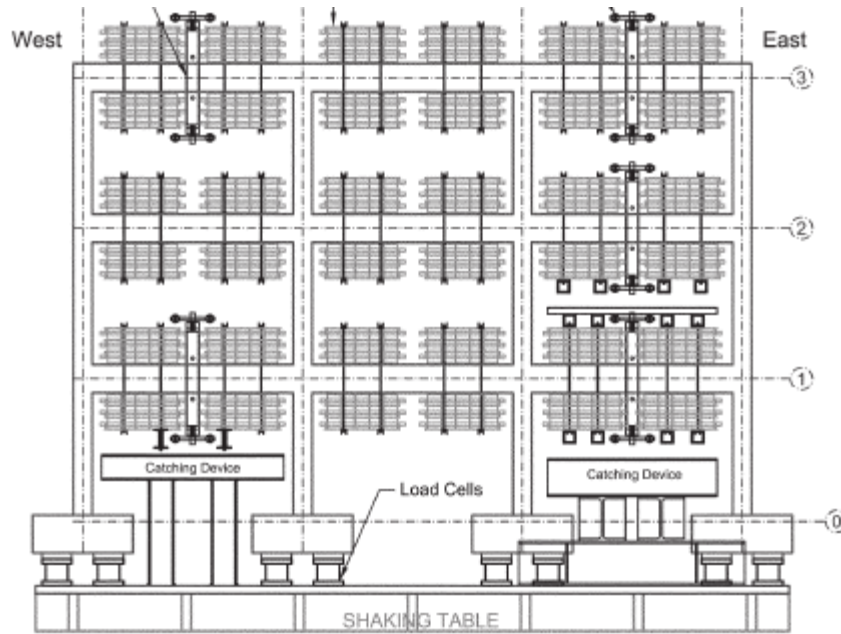


Figure 5.52: Applied loads on Ghannoum and Moehle frame (Ghannoum and Moehle, 2012)

5.4.3.1 Analytical Modeling

The beams and columns were divided into a number of segments to create the frame model of the structure. Segment lengths were approximately 75 mm, which was half of the cross-sectional depth of the column. Figure 5.53 shows the analytical model with loading and support restraints. There were 349 nodes, 344 members, 12 support restraints, and 4 interior joint in the model. The footings were not modeled explicitly in this model. Instead, Nodes 1, 51, 101 and 151 at the bottom of the columns were restrained in the horizontal, vertical and rotational directions. The gravity loads provided by four lead packets on each beam span were modeled with two point loads of 13.34 kN. These loads were applied at 435 mm away from the face of the columns. Rather than the ground acceleration, a displacement-controlled pushover analysis was employed, in which a horizontal displacement was applied at the west end of the roof with an increment of 10 mm starting from a zero displacement. Displacements were also applied at the west end of the first and the second floors with the magnitudes proportional to the height of the floor.

Eight member types were created to build the model. Member Types 1 through 4 were used to model the columns. Member Type 5 was used to model the beams. Member Types 6 and 7 were created with doubling the longitudinal and transverse reinforcement amounts of MT1 and MT3,

respectively, to employ semi-rigid end offsets of column members. Member Type 8 was created with doubling the longitudinal and transverse reinforcement amounts of MT5 to employ semi-rigid end offsets of beam members. Note that the semi-rigid end offsets only applied to exterior and knee joints, whereas interior joints were modeled with MT1, MT3 and MT5. Each member was divided into 16 to 24 concrete layers to perform the sectional analysis.

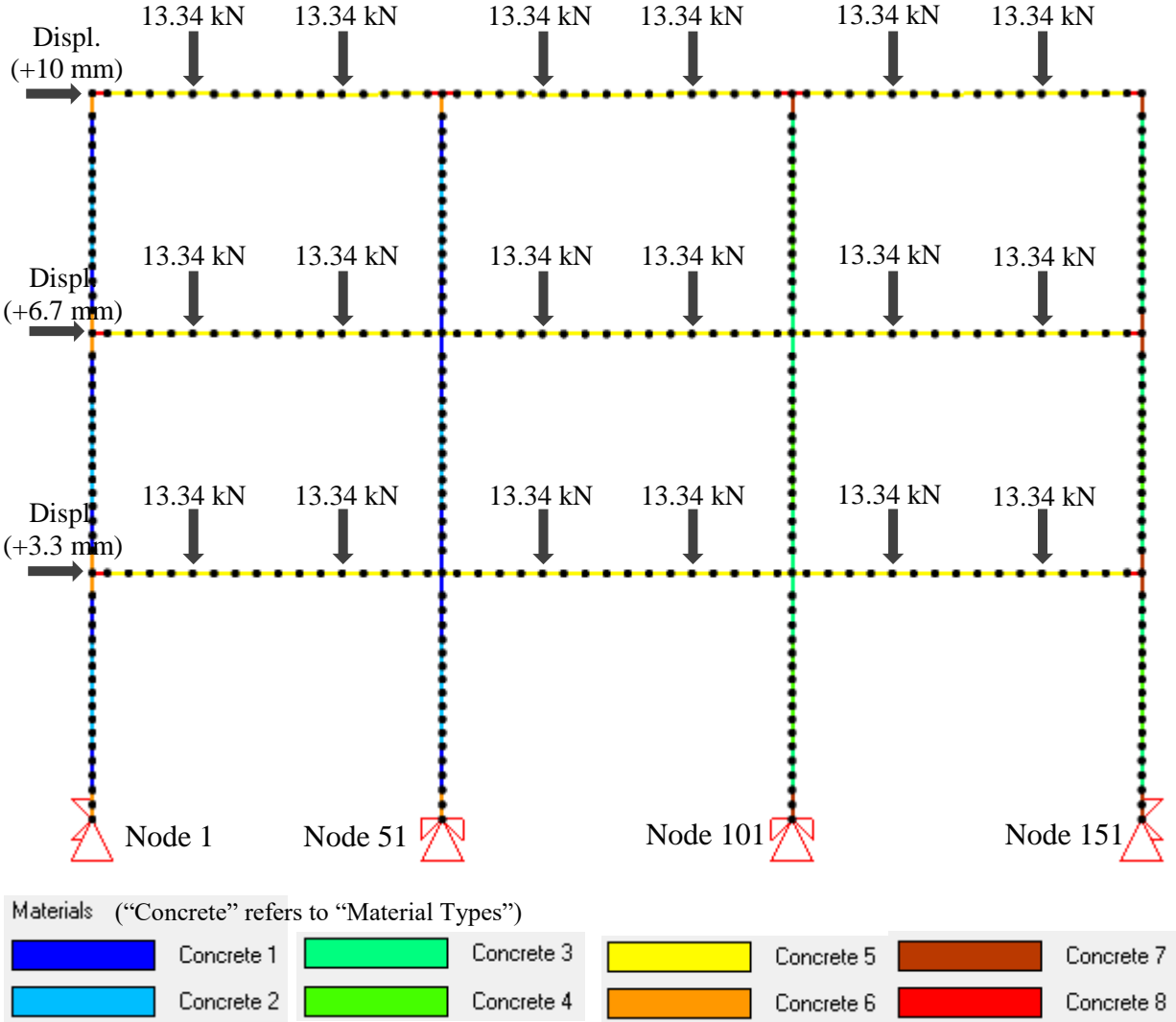


Figure 5.53: Analytical model showing dimensions, loading and support restraints of Ghannoum and Moehle frame

5.4.3.2 Comparison of the Analytical and Experimental Responses

The experimental and analytical responses of base shear versus first floor drift are compared in Figure 5.54. The experimental results from Dynamic Test 1 were selected for the comparison because the subsequent dynamic tests were performed on the damaged structure resulted from this test. The cyclic plot of the experimental load-deflection response was digitized from the original paper.

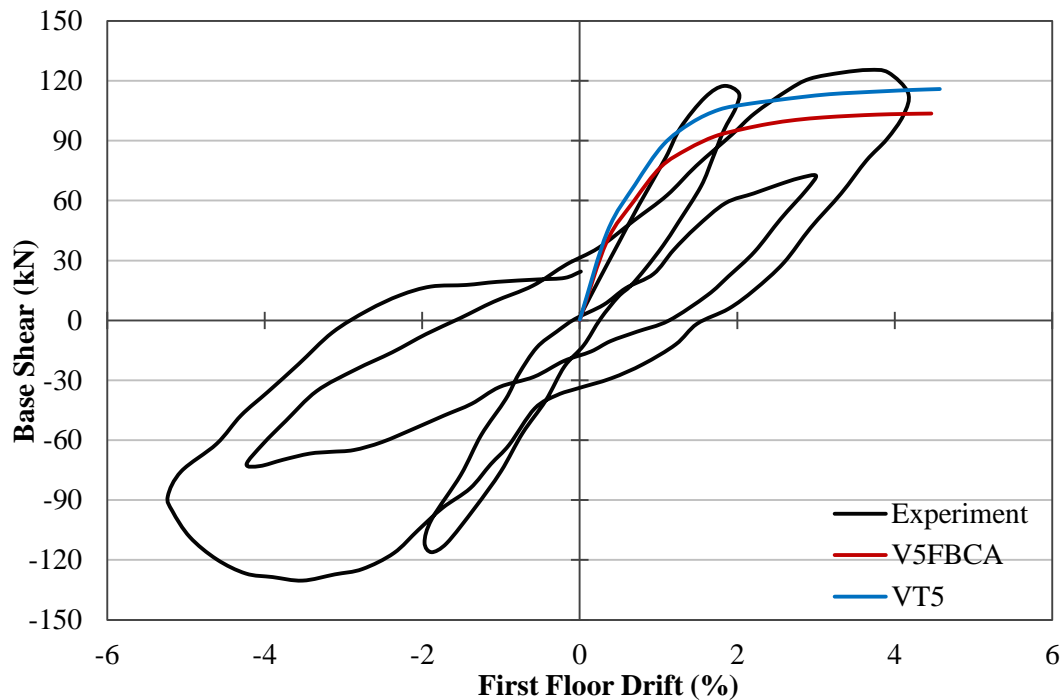
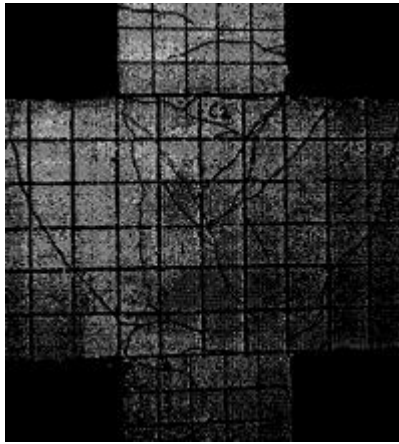


Figure 5.54: Comparison of base shear versus first floor drift response of Ghannoum and Moehle frame

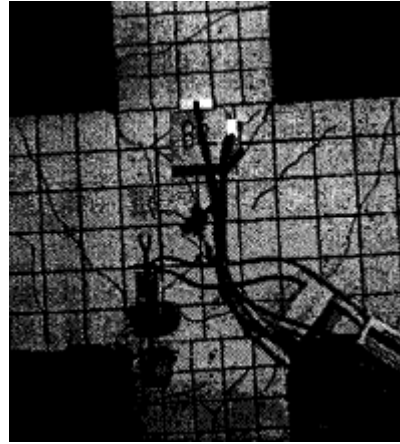
In the experiment, the interior older-type column (i.e. Column B) in the first story yielded in flexure. Then, shear failure initiated near the column base, and the column eventually developed axial failures (see Figure 5.55). Shear cracking was observed in the interior joints, with the most severe damage at the joints in the interior older-type column (i.e. Joints B1 and B2) (see Figure 5.56).



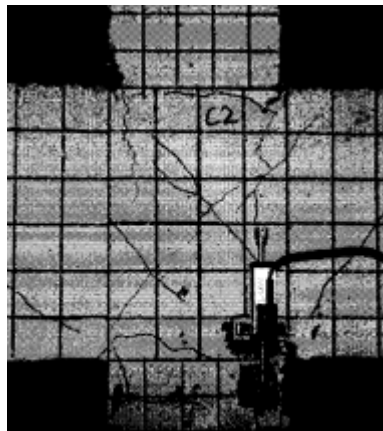
Figure 5.55: Failures of Ghannoum and Moehle frame (Ghannoum and Moehle, 2012)



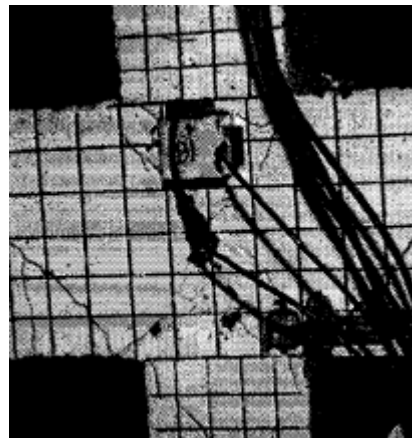
Joint C2



Joint B2



Joint C1



Joint B1

Figure 5.56: Damage of interior joints in Ghannoum and Moehle frame (Ghannoum and Moehle, 2012)

The load-displacement response predicted by V5FBCA simulated well the experimental backbone curve in terms of the strength and stiffness. The flexure damage mode was predicted for this frame, which was similar to the experimental observations. The older-type columns yielded at a drift of 1.4%. Flexural cracks formed at the base of all columns, as well as the beam ends near the east column. With increasing lateral drift, flexural cracks extended at the column bases and propagated through the depth of the beams. Figure 5.57 shows the deformed shape and cracking pattern of the frame at a drift of 5.2%. Meanwhile, Joints B1 and B2 just reached their peak strengths, and Joints C1 and C2 were approaching their peak strengths. The predicted average crack widths in the joint cores ranged from 1.2 mm to 1.6 mm. The experimental observations indicated that the joints sustained inclined cracking, and spalling in some cases.

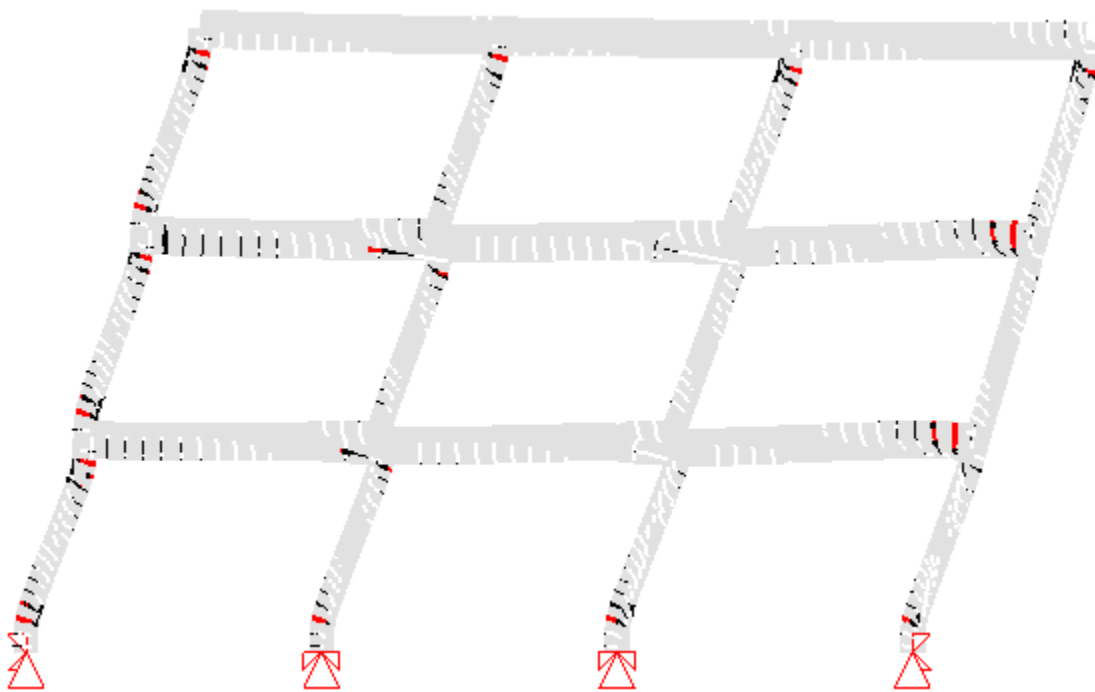


Figure 5.57: Deformed shape and cracking pattern of Ghannoum and Moehle frame

5.4.4 Pampanin et al. (2007)

An experimental program was conducted to investigate the efficiency of seismic retrofitting using fiber-reinforced polymer composites on poorly detailed reinforced concrete frames (Pampanin et al., 2007). The experiment involved testing of a two-thirds scale, three-story, three-

bay frame structure subjected to quasi-static cyclic loading and gravity loads. The frame structure prior to the retrofit was examined in this study.

The test frame was constructed with a story height of 3000 mm and an overall height of 9000 mm (see Figure 5.58). The beam center-to-center spans were 3000 mm, 1330 mm and 2330 mm. All beams were 330 mm deep and 200 mm wide. All columns were 200 mm deep and 200 mm wide. The frame was built integral with a long base above a strong floor serving as the foundation. The frame was designed in accordance with the design code provisions in the 1970s. Consequently, no transverse reinforcement was placed in the joint regions. The mechanical properties of the concrete and reinforcing steel were similar to those typically used in older structures. The material properties of the concrete and the reinforcement are listed in Table 5.35.

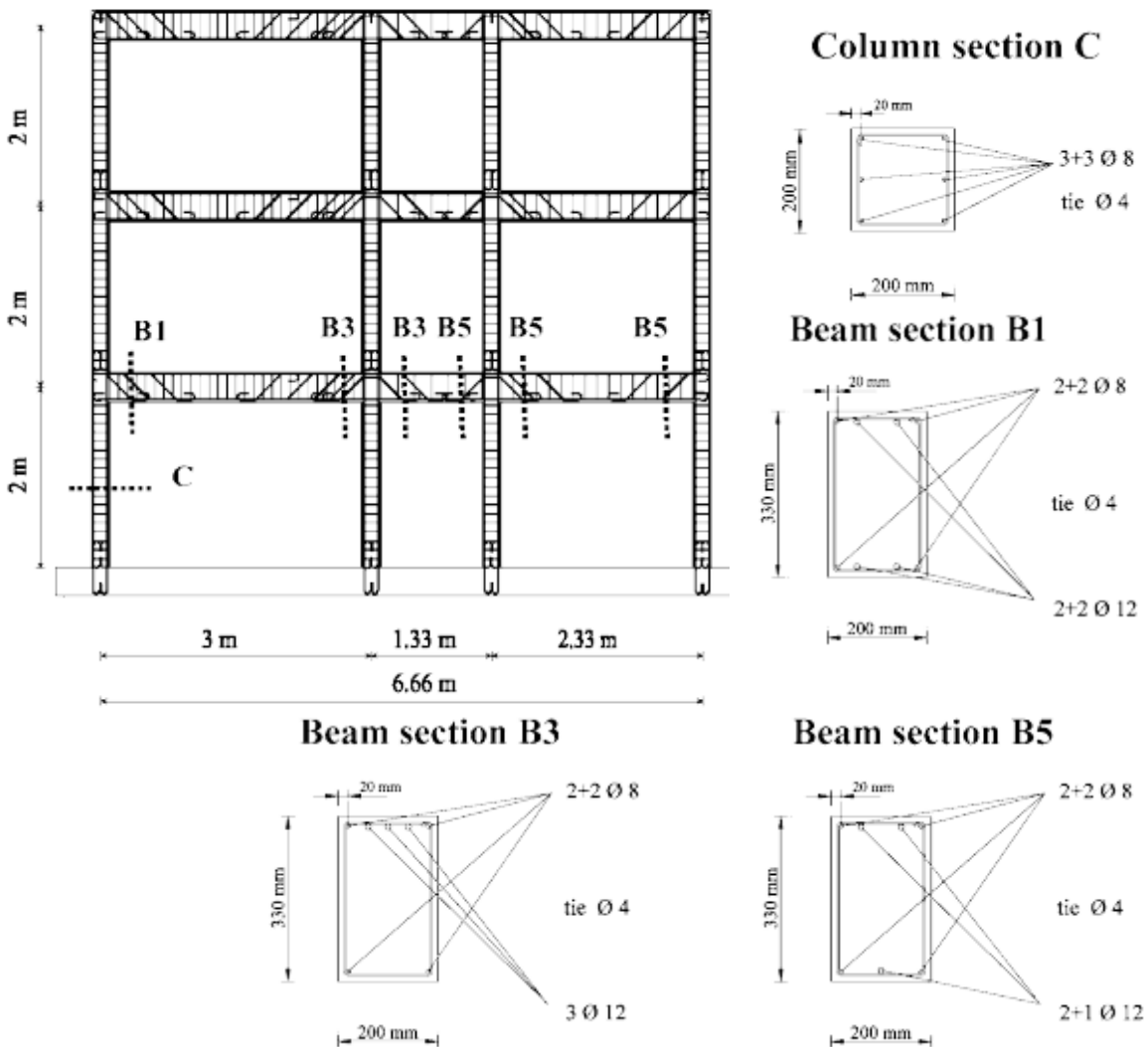


Figure 5.58: Structural details of Pampanin et al. frame (Pampanin et al., 2007)

Table 5.35: Material properties of Pampanin et al. frame

Bar Type	Reinforcement Properties							Spec.	Concrete Properties		
	d_b (mm)	F_y (MPa)	F_u (MPa)	E_s (MPa)	E_{sh}^* (MPa)	ϵ_{sh}^* ($\times 10^{-3}$)	ϵ_u^* ($\times 10^{-3}$)		f'_c (MPa)	E_c^* (MPa)	ϵ'_c^* ($\times 10^{-3}$)
D12	12.0	345	458	176000	1256	10	100	Pampanin	14.06	14757	1.91
D8	8.0	386	451	176300	722	10	100				
D4	4.0	200*	250*	151300	1744	1.32	30.0				

*: estimated

Testing of the frame involved applying reversed cyclic lateral loads and constant gravity loads as shown in Figure 5.59. The gravity loads were simulated with concrete blocks on every beam span. The lateral loads were applied by three screw jack actuators. The roof displacement was directly controlled, while displacements on the two lower floors were proportional to the mass of the concrete blocks and the floor level height. Additional information regarding this experiment can be found in Pampanin et al. (2002) and Galli (2006).

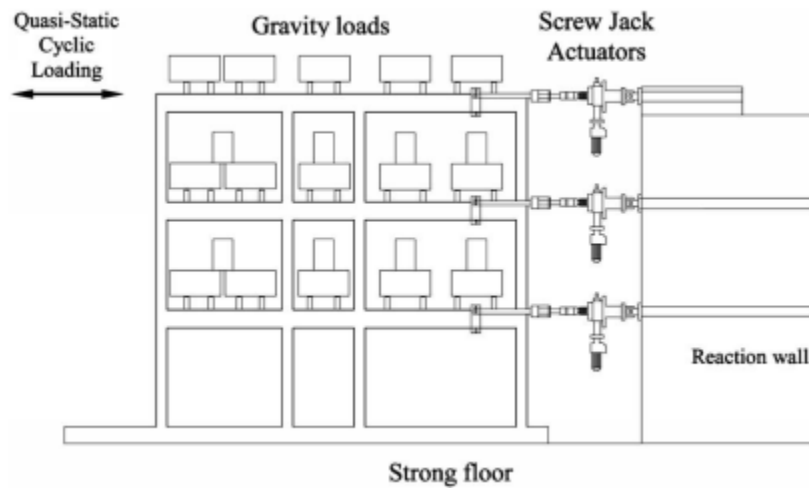


Figure 5.59: Applied Loads on Pampanin et al. Frame (Pampanin et al., 2007)

5.4.4.1 Analytical Modeling

The beams and columns were divided into a number of segments to create the frame model of the structure. The length of the column segments was approximately 100 mm, which was half of the cross-sectional depth of the column. Lengths of the beam segments were approximately 165 mm, which was half of the cross-sectional depth of the beam. Figure 5.60 shows the analytical model with loading and support restraints. There were 414 nodes, 409 members, 12 support restraints, and 4 interior joint in the model. The concrete base was not modeled in the analysis.

Nodes 1, 74, 147, and 220, located at the base of the columns, were restrained in the horizontal, vertical and rotational directions. The gravity loads carried by each span are also shown in Figure 5.60. The monotonically increasing lateral loads were modeled in a displacement-controlled mode. The displacement increments of 6.00 mm, 4.98 mm and 3.12 mm were applied at the roof level, the second level and the first level, respectively, following the recommendations of Galli (2006).

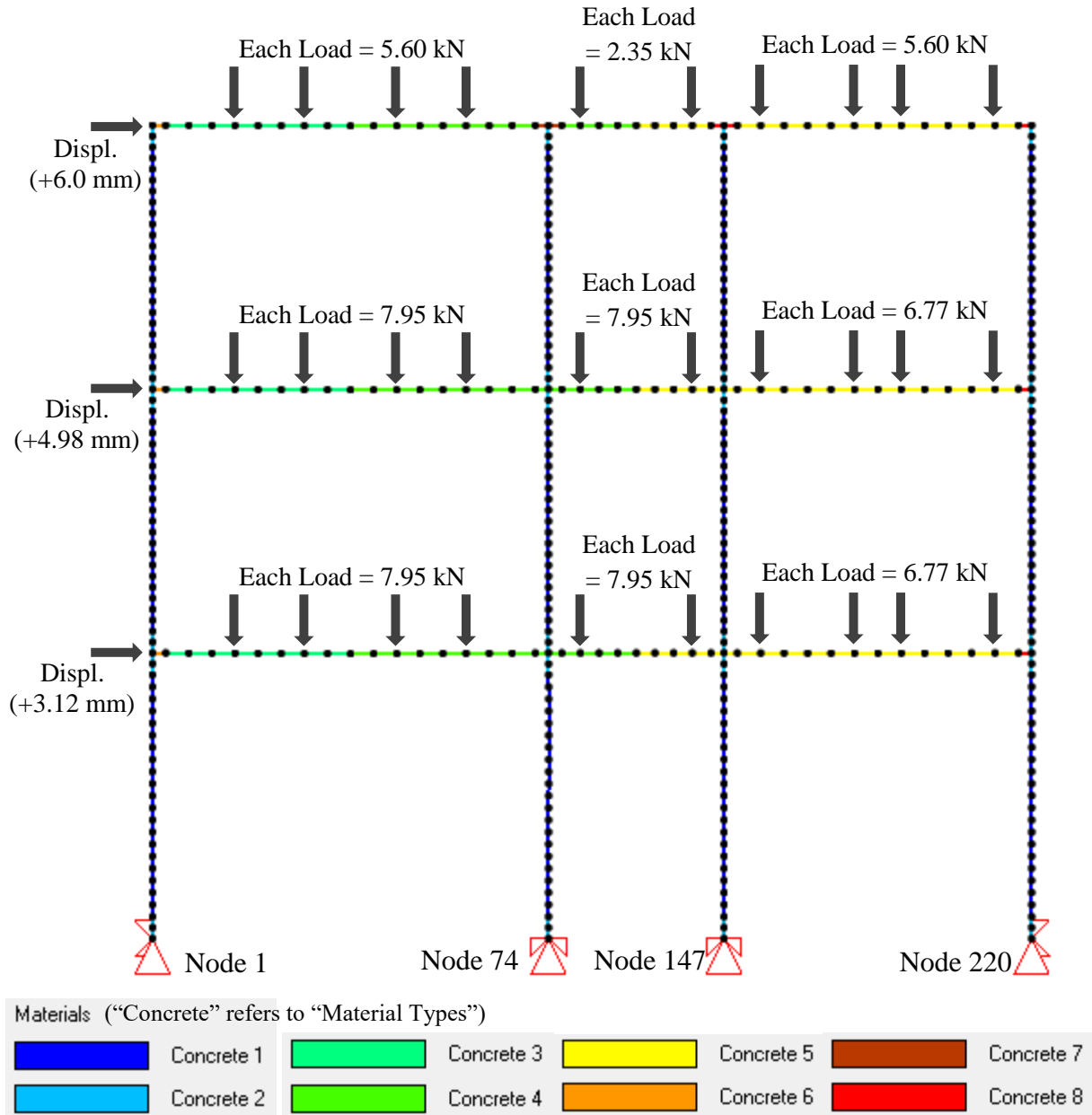


Figure 5.60: Analytical model showing dimensions, loading and support restraints of Pampanin et al. Frame

Eight member types were created to build the model. Member Type 1 was used to model the columns. Member Types 3 through 5 were used to model the beams. Member Type 2 was created with double the longitudinal reinforcement of MT1. Member Types 6, 7 and 8 were created with double the longitudinal reinforcement of MT3, MT4 and MT5, respectively. Note that there was no transverse reinforcement in MT2, MT6, MT7 or MT8 because the joints were designed in accordance with the old code provisions. Each member was divided into 20 to 24 concrete layers to perform the sectional analysis.

5.4.4.2 Comparison of the Analytical and Experimental Responses

The experimental and analytical responses of the base shear versus the top floor drift are compared in Figure 5.61.

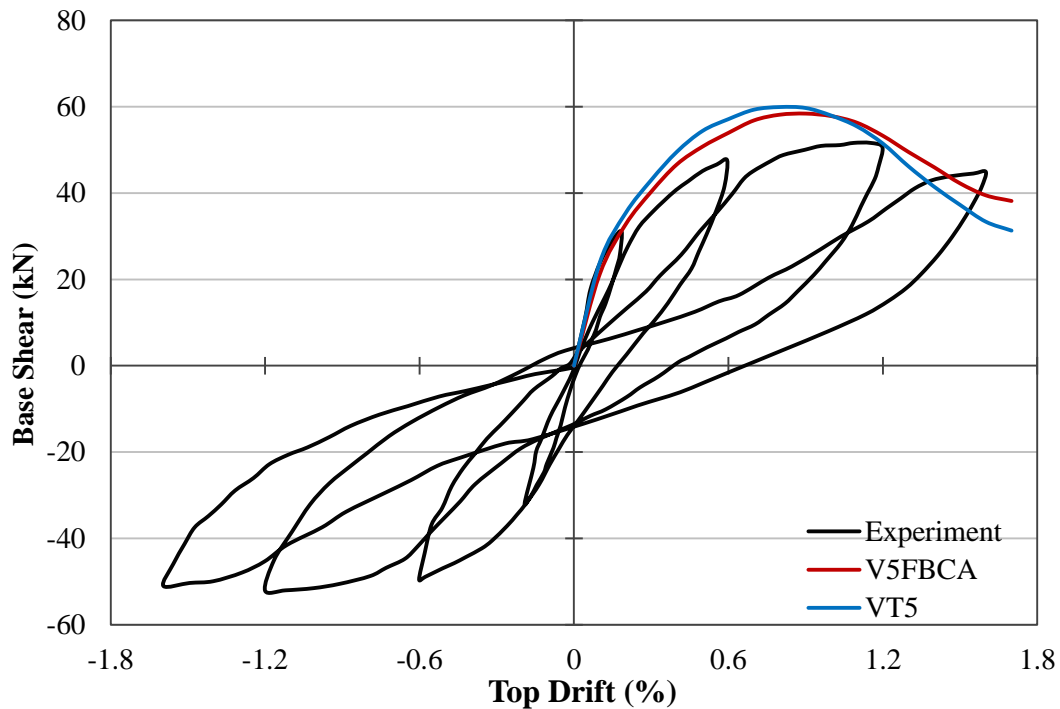


Figure 5.61: Comparison of base shear versus top drift response of Pampanin et al. frame

In the experiment, the joint panel regions showed high vulnerability. The structure exhibited an undesirable global failure mechanism due to strong-beam, weak-column design as shown in Figure 5.62. Most of the damage concentrated in exterior joints and beam-column interfaces

through the development of major flexural cracks due to the slip of the longitudinal bars. Few cracks were observed in the interior joints (see Figure 5.63).

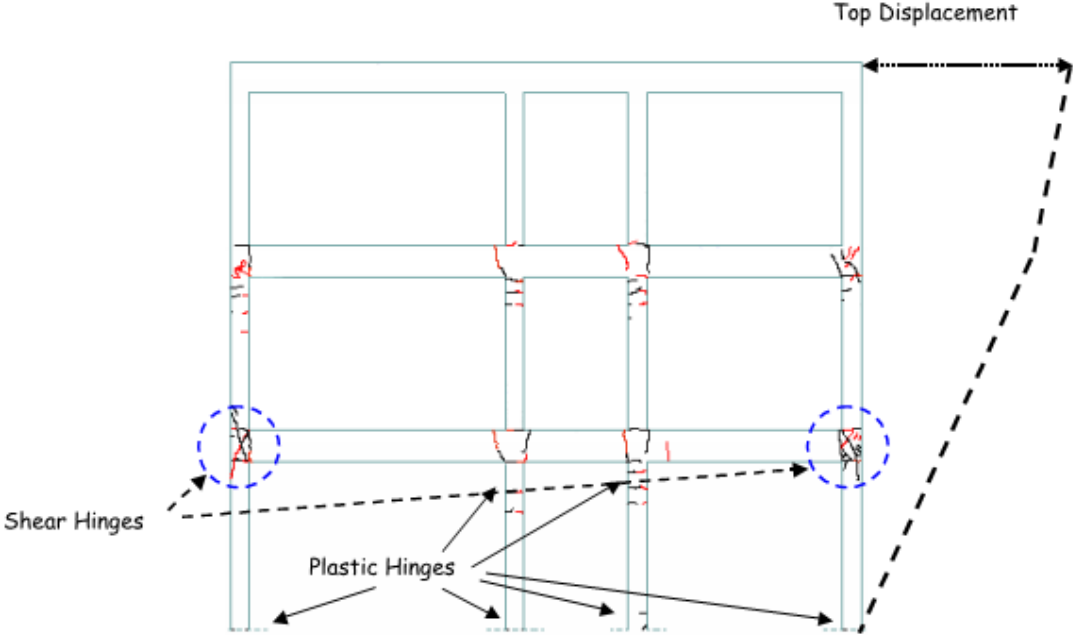


Figure 5.62: Failures of Pampanin et al. frame (Pampanin et al., 2003)

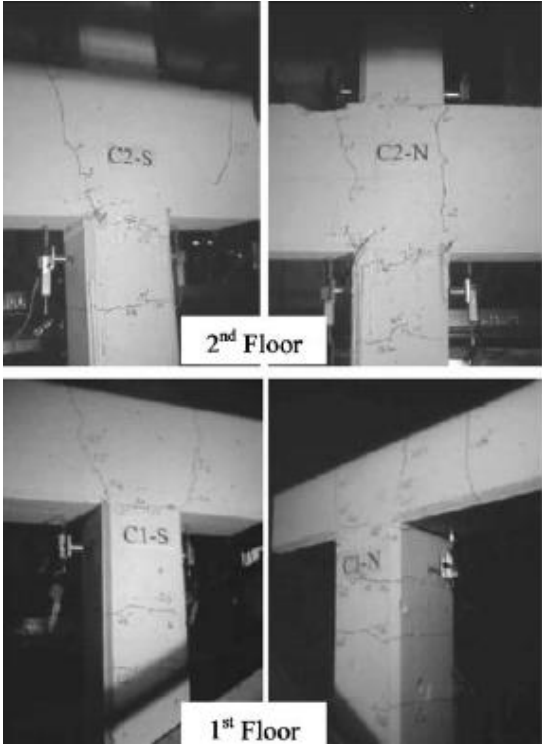


Figure 5.63: Damage of interior joints in Pampanin et al. frame (Pampanin et al., 2007)

The load-displacement response predicted by V5FBCA matched well the experimental backbone response. The program was capable of capturing shear cracking in the beams near the joint regions, and shear cracking at the base of the columns. In addition, the program predicted the flexural failure near the mid-span of the first and second story beams in the west bay. As expected, the program did not predict the major diagonal cracks in the exterior joints due to the assumption of semi-rigid joints. At a drift ratio of 1.2%, the average crack widths in the interior joints ranged from 0.2 mm to 0.4 mm, while no cracks were observed in the experiment. Figure 5.64 shows the deformed shape and cracking pattern of the frame at the end of the simulation at a drift ratio of 1.2%.



Figure 5.64: Deformed shape and cracking pattern of Pampanin et al. Frame

Overall, V5FBCA was able to capture the peak load and the stiffness of the frame structure. Cracking at the interface of the joints and in the columns were predicted successfully. Despite no transverse reinforcement used in the joint, the program predicted relative small crack width in the interior joints, matching the experimental observations.

CHAPTER 6

SUMMARY, CONCLUSIONS AND RECOMMENDATIONS

6.1 Summary

The goal of this study was to capture the impact of local joint response on the global response of frames by implementing an interior beam-column joint model into a previously-developed global frame analysis procedure, VecTor5. This nonlinear analysis program for two-dimensional reinforced concrete frame structures was originally capable of providing satisfactory simulations. The implemented joint element enabled the consideration of joint shear actions and bond slip effects taking place inside the interior joint cores. The implementation of a joint element allowed for improved simulations of global load-deflection response and local joint conditions for beam-column subassemblies and frame structures subjected to monotonic loading conditions.

The analysis procedure with the new joint element was verified with a variety of structures including nine interior beam-column joint subassemblies and three large-scale frames. As the main focus of the verification was to determine the accuracy of the implementation and the improvements over the original VecTor5, the specimens considered covered various material properties, reinforcing ratios and failure mechanisms. The analytical responses of the specimens were compared to the experimental responses in terms of load-displacement responses, failure modes, peak loads, loads at first beam yielding, crack widths, and joint panel shear distortions. In addition, a parametric study was carried out to investigate the impact of the loading type, concrete confinement effects, compression softening effects, and bond stress on the analytical load-displacement responses of the test specimens.

6.2 Conclusions

Based on the results of the analyses performed, the following conclusions and observations are reached:

1. Component-based joint models are suitable for implementation into nonlinear fiber-based frame analysis procedure, such as VecTor5.
2. Modifications of the global frame analysis procedure are required to facilitate the joint implementation.
3. Interior beam-column joints can be modeled with the specification of concrete properties, reinforcing steel properties, joint sectional properties and joint geometric properties.
4. The VecTor5 program had a tendency to overestimate the peak load and initial stiffness of beam-column joint subassemblies which exhibited significant joint damage due to the use of semi-rigid joint elements. For the nine interior joint subassemblies modeled, the ratio of predicted and observed peak load had a mean of 1.25 and a coefficient of variation of 4.5%.
5. After the new joint element implementation, the peak load and initial stiffness predictions improved. The predicted failure mechanisms, shear panel distortions, and average crack widths for the specimens examined showed good correlations with the experimental results.
6. The improved VecTor5 program with the new joint element showed reasonably good accuracy in the analysis of beam-column joint subassemblies and frame structures with interior joints. For the nine interior joint subassemblies modeled, the ratio of the predicted to observed peak load had a mean of 1.05 and a coefficient of variation of 16.3%.
7. The compression softening model exerts a significant influence on the predicted load-displacement response. This is concluded from the parametric study of the impact of the reduction factor due to the compression softening effect.
8. The tensile stresses of reinforcing bars at the joint interface were predicted with reasonably good accuracy. However, the compressive stresses in reinforcing bars were not predicted as well as the tensile stresses.
9. The frame structures analyzed showed that VecTor5 considers not only the joint responses but also the interactions or coupling effects between joints and other parts of the structure.

6.3 Recommendations for Future Research

The following recommendations are made to further improve the modeling of interior joints, and extend the concept to other types of joints and cyclic loading conditions:

1. In order to achieve improved accuracy and reliability in the analysis, additional work is required in better describing the constitutive relationships of the joint panel and the bond slip effects.
2. Reduction factors due to the compression softening effect have significant influence on the analytical load-displacement response. This study has shown that the compression softening model by Mitra and Lowes provides satisfactory analytical results. Further investigations of the effectiveness of other compression softening models would be useful.
3. The effectiveness of the strut-and-tie model employed for the joint shear panel was not assessed. Further investigations on this matter require the replacement with other models such as the Modified Compression Field Theory or the Disturbed Stress Field Model.
4. The sectional analysis of the beam and column members framing into the joint at nominal flexural strength is currently performed without the consideration of tension stiffening effect. Further investigation of the impact of the inclusion of tension stiffening models would be useful.
5. The compressive stresses of reinforcing bars at the joint interface were not predicted well. This issue is not currently addressed. Further investigations on the reason of this deficiency are required.
6. The joint formulation is currently only applicable to interior joints. To extend the formulation to exterior and knee joints, new transformation matrices (see Figure 3.3) are required to define the equilibrium and compatibility relationships. The size of the transformation matrices should be 9×9 for exterior joints, and 6×6 for knee joints.
7. The joint implementation is currently only applicable to monotonic loading. To extend the formulation to reversed cyclic loading, hysteresis models and damage parameters must be considered. Additional information is provided in Chapter 4 of Mitra (2007).

8. There are currently no explicit joint failure criteria that terminate the program upon the failure of the joints. Additional work is required to explicitly define the failure criteria to terminate the program in the case of joint failures.

REFERENCES

- Alath, S. and Kunnath, S.K., "Modeling Inelastic Shear Deformation in RC Beam-Column Joints." *Proc., 10th Conf., University of Colorado at Boulder, Boulder, Colo., May 21-24*, ASCE, New York, Vol. 2, pp. 822-825
- Altoontash, A. (2004). "Simulation and Damage Models for Performance Assessment of Reinforced Concrete Beam-Column Joints." Ph. D. Thesis, Department of Civil and Environmental Engineering, Stanford University, California, United States.
- Attaalla S.A. and Agbabian, M.S. (2004), "Performance of Interior Beam-Column Joints Cast from High Strength Concrete under Seismic Loads." *Advances in Structural Engineering*, 7(2): 147-157
- Celik, O.C. and Ellingwood, B.R. (2008), "Modeling Beam-Column Joints in Fragility Assessment of Gravity Load Designed Reinforced Concrete Frames," *Journal of Earthquake Engineering*, 12(3), 357-381
- Chak, I. and Vecchio, F. J. (2013), "User's Manual of Janus," Online Publication, 211 pp. <http://www.civ.utoronto.ca/vector/user_manuals/manual5.pdf>
- Eligehausen, R., Popov, E.P. and Bertero, V.V. (1983). "Local bond Stress-Slip Relationship of Deformed Bars under Generalized Excitations." *EERC Report 83/23*. Berkeley: University of California
- Elmorsi, M., Kianoush, M.R., and Tso, W.K. (2000). "Modeling Bond-Slip Deformations in Reinforced Concrete Beam-Column Joints." *Can. J. Civ. Eng.*, 27(3), 490-505
- Fleury, F., Reynouard, J.M., and Merabet, O. (2000). "Multicomponent Model of Reinforced Concrete Joints for Cyclic Loading." *J. Eng. Mech.*, 126(8), 804-811
- Ghannoum, W.M. and Moehle, J.P. (2012), "Shake-Table Tests of a Concrete Frame Sustaining Column Axial Failures." *ACI Structural Journal*, 109(3), 393-402

- Ghobarah, A. and Youssef, M. (2001). "Modeling of RC Beam-Column Joints and Structural Walls." *Journal of Earthquake Engineering*, 5(1), 91-111
- Guner, S. (2016), "Simplified Modeling of Frame Elements subjected to Blast Loads," *American Concrete Institute Structural Journal*, V.113, No.2, pp.363-372
- Guner, S. and Vecchio, F.J. (2012), "Simplified Method for Nonlinear Dynamic Analysis of Shear-Critical Frames," *American Concrete Institute Structural Journal*, V.109, No.5, pp.727-737
- Guner, S. and Vecchio, F.J. (2011), "Analysis of Shear-Critical Reinforced Concrete Plane Frame Elements under Cyclic Loading," *Journal of Structural Engineering*, American Society of Civil Engineers, V.137, No.8, pp. 834-843
- Guner, S. and Vecchio, F.J. (2010), "Pushover Analysis of Shear-Critical Frames: Verification and Application," *American Concrete Institute Structural Journal*, V.107, No.1, pp. 72-81
- Guner, S. and Vecchio, F.J. (2010), "Pushover Analysis of Shear-Critical Frames: Formulation," *American Concrete Institute Structural Journal*, V.107, No.1, pp. 63-71
- Guner, S. (2008), "Performance Assessment of Shear-Critical Reinforced Concrete Plane Frames." Ph.D. Thesis, Department of Civil Engineering, University of Toronto, 429 pp.
- Guner, S. and Vecchio, F.J. (2008), "User's Manual of VecTor5." Online Publication, 88 pp.
- Hakuto, S., Park, R., and Tanaka, H. (1999) "Effect of Deterioration on Bond of Beam Bars Passing through Interior Beam-Column Joints on Flexural Strength and Ductility." *ACI Structural Journal*, 96(5), 858-864
- Hanson, H.W. and Connor, H.W. (1967), "Seismic Resistance of Reinforced Concrete Beam-column Joints." *Journal of Structural Engineering Division, ASCE*, 93(ST5): 533-559.
- Hwang, S.J., and Lee, H.J. (2002), "Strength Prediction for Discontinuity Regions by Softened Strut-and-Tie Model." *Journal of Structural Engineering, ASCE*, 128(12): 1519-1526

- Kim, J. and Lafave, J.M. (2009). "Joint Shear Behavior of Reinforced Concrete Beam-Column Connections Subjected to Seismic Lateral Loading." *NSEL Report No.NSEL-202*. Department of Civil and Environmental Engineering, Urbana-Champaign: University of Illinois
- Lowes, L.N. and Alttontash, A. (2003). "Modeling Reinforced Concrete Beam-Column Joints Subjected to Cyclic Loading." *J. Strut. Eng.* 129(12), 1686-1697
- Loya, A. S., Lourenço, D. S, Guner, S., and Vecchio, F. J. (2016), "User's Manual of Janus for VecTor5," Online Publication, 25 pp. <<http://www.utoledo.edu/engineering/faculty/serhan-guner/Publications.html>>
- Mander, J.B., Priestley, M.J.N., and Park, R. (1988), "Theoretical Stress-Strain Model for Confined Concrete." *J. Strut. Eng.* 114(8), 1804-1826
- Mitra, N. and Lowes, L.N. (2007). "Evaluation, Calibration, and Verification of a Reinforced Concrete Beam-Column Joint Model." *J. Strut. Eng.* 133(1), 105-120
- Mörsch, E. (1909). *Der Eisenbetonbau*, 3rd Ed., Engineering News Publishing Co., New York (published in English as "Concrete-steel Construction").
- Noguchi, H. and Kashiwazaki, T. (1992), "Experimental Studies on Shear Performances of RC Interior Beam-Column Joints." *10th World Conf. on Earthquake Engineering*, Madrid, Spain, pp. 3163-3168
- Pampanin, S., Bolognini, D., and Pavese, A., (2007) "Performance-Based Seismic Retrofit Strategy for Existing Reinforced Concrete Frame Systems Using Fiber-Reinforced Polymer Composites", *Journal of Composites for Construction*, 11(2), 211-226
- Pampanin, S., Magenes, G., and Carr, A. (2003). "Modeling of Shear Hinge Mechanism in Poorly Detailed RC Beam-Column Joints." *Proc. FIB Symp. Concrete Structures in Seismic Regions, Federation International du Beton*, Athens, Paper No. 171
- Park, R. and Dai, R. (1988), "A Comparison of the Behavior of Reinforced Concrete Beam-Column Joints Designed for Ductility and Limited Ductility." *Bulletin of the New Zealand National Society for Earthquake Engineering*, 21(4), 255-278

Pauley, T., Park, R., and Priestley, M.J.N. (1978), "Reinforced Concrete Beam-Column Joints under Seismic Actions." *ACI Structural Journal*, Vol. 75, Iss. 11, 585-593.

Schlaich, J., Schaefer, K., and Jennewein, M. (1987). "Toward a Consistent Design of Structural Concrete." *PCI Journal*, Vol. 32, No. 3, 74-150

Scott, R.M., Mander, J.B., and Bracci, J.M. (2012), "Compatibility Strut-and-Tie Modeling: Part I - Formulation." *ACI Structural Journal*, 109(5), 635-644

Sezen, H. and Moehle, J.P. (2003), "Bond-Slip Behavior of Reinforced Concrete Members." fib – Symposium (CEB-FIP); Concrete Structures in Seismic Regions, 6-9 May 2003. Athens, Greece

Shin, M. and LaFave, J.M. (2004). "Modeling of Cyclic Joint Shear Deformation Contributions in RC Beam-Column Connections to Overall Frame Behavior." *Structural Engineering and Mechanics*, 18(5), 645-669

Shiohara, H. and Kusahara, F. (2007), "Benchmark Test for Validation of Mathematical Models for Non-linear and Cyclic Behavior of R/C Beam-column Joints." *ACI Spring Convention 2007*, Atlanta, United States.

Shiohara H. (2004), "Quadruple Flexural Resistance in R/C Beam-Column Joints" *13th World Conf. on Earthquake Engineering*, Vancouver, Canada, Paper No. 491

USGS. (2014), "U.S. Geological Survey: Earthquakes with 1,000 or More Deaths 1900-2014", http://earthquake.usgs.gov/earthquakes/world/world_deaths.php, Last Accessed September 18, 2016.

Vecchio, F.J. (2000), "The Disturbed Stress Field Model for Reinforced Concrete: Formulation." *ASCE Journal of Structural Engineering*, Vol. 126, No. 9, 1070-1077.

Vecchio, F.J. and Collins, M.P. (1988), "Predicting the Response of Reinforced Concrete Beams Subjected to Shear using the Modified Compression Field Theory." *ACI Structural Journal*, 85, 258-268

Vecchio, F.J. (1987), "Nonlinear Analysis of RC Frames Subjected to Thermal and Mechanical Loads." *ACI Structural Journal*, 84(6), 492-501.

Vecchio, F.J. and Collins, M.P. (1986), "The Modified Compression Field Theory for Reinforced Concrete Elements Subject to Shear." *ACI Structural Journal*, Vol. 83, Iss. 2, 219-231

Viathanatepa, S., Popov, E.P., and Bertero, V.V. (1979), "Effects of Generalized Loadings on Bond of Reinforcing Bars Embedded in Confined Concrete Blocks." *Rep. No. UCB/ERRC-79/22* ERRC, Univ. of California, Berkeley, CA

Walker, S.G. (2001). "Seismic Performance of Existing Reinforced Concrete Beam-Column Joints." MS thesis, University of Washington, Seattle, Washington.

Walraven, J.C. (1994), "Rough Cracks Subjected to Earthquake Loading." *J. Struct. Eng.*, 120(5), 1510-1524

Walraven, J.C. (1981), "Fundamental Analysis of Aggregate Interlock." *J. Struct. Div. ASCE*, 107(11), 2245-2270

Xue, W., Cheng, B., Zheng, R., Li, L., and Li, J. (2011), "Seismic Performance of Nonprestressed and Prestressed HPC Frames under Low Reversed Cyclic Loading." *J. Struct. Eng.* 137(11), 1254-1262

Zhao, J. and Sritharan, S. (2007), "Modeling of Strain Penetration Effects in Fiber-Based Analysis of Reinforced Concrete Structures." *ACI Structural Journal*, 104(2), 133-141